Aix - Marseille University

DOCTORAL SCHOOL

SCIENCES POUR L'INGENIEUR: MECANIQUE, PHYSIQUE MICRO & NANO-ELECTRONIQUE

P H D T H E S I S

to obtain the title of

PhD of Science

of the University of Aix - Marseille

Specialty : Fluid Mechanics

Defended by

Hugo Bufferand

Development of a fluid code for tokamak edge plasma simulation – Investigation on non-local transport.

Thesis Advisor: Eric Serre

prepared at M2P2-CNRS Laboratory, Marseille

defended on November 28, 2012

Jury :

Reviewers :	Detlev Reiter	-	Jülich Forschungzentrum
	Ulrich Stroth	-	Universität Stuttgart Institut für Plasmaforschung
Advisors :	Guido Ciraolo	-	Ecole Centrale Marseille
	Eric Serre	-	M2P2-CNRS (Marseille)
Examinators :	Philippe Ghendrih	-	CEA-IRFM (St Paul lèz Durance)
	Pascale Hennequin	-	LPP - Ecole Polytechnique (Palaiseau)
	Pierre Sagaut	-	Université Pierre et Marie Curie - Paris 6
Invited :	Stefano Lepri	-	Istituto dei Sistemi Complessi - CNR (Florence)

Contents

Introduction

The fusion reactions between light atoms are known for being the energy source of stars. An important research effort is now carried out to control and reproduce these reactions on earth. After decades of research programs and the construction of several devoted experimental reactors, the international ITER program represents a new promising step for operating the reactor as a fusion power plant. In that perspective, fusion reactions must produce more power than is supplied to heat the plasma. ITER must also prove that a fusion reactor can operate almost continuously using long and repeated discharges. In a farther future, the DEMO project will investigate ways to build a cost-effective fusion reactor prototype.

The fusion reactions take place in a plasma, a state of matter that can be described by a fully or partially ionized gas. Fusion reactions occur when enough energy is provided to atom nuclei to overcome the Coulombian barrier that tends to repeal them from each other. It is necessary to confine the particles long enough in the hot core region to obtain a sufficiently high interaction rate and a sustainable fusion reaction. This constraint is expressed by the so called Lawson criterion [1]. This is the principle of the magnetic confinement. The most favorable reaction is the Deuterium-Tritium reaction for which fusion occurs at the smallest temperature. However, the temperature required in this case still reaches 10 keV that is about 10^8 K. Moreover, in order to keep this very hot plasma far from the reactor chamber walls, magnetic fields are used to control charged particles trajectories and prevent them from impacting the solid materials.

Charged particles tend to follow magnetic field lines. A strong anistropy develops when a magnetic field is applied to a plasma and the flows parallel to the magnetic field are much larger than the cross-field ones. In particular, if the magnetic configuration is such that the magnetic field lines do not intercept the reactor chamber walls, the plasma particles evolving on these field lines should be "confined". The most common magnetic configuration implemented nowadays is the tokamak configuration. In tokamaks an helicoidal magnetic field is generated by the combined effects of external coils and induced current in the plasma itself. This magnetic configuration can be represented by nested tori flux surfaces on which the magnetic field lines spin around 1.

At some point on the edge of the confined plasma region, the magnetic field lines necessarily intercept the solid. This plasma region where the magnetic field lines are "open" is called scrape-off layer (SOL). The last closed flux surface (LCFS) constitutes the interface between the confined plasma and the SOL. Different magnetic geometries

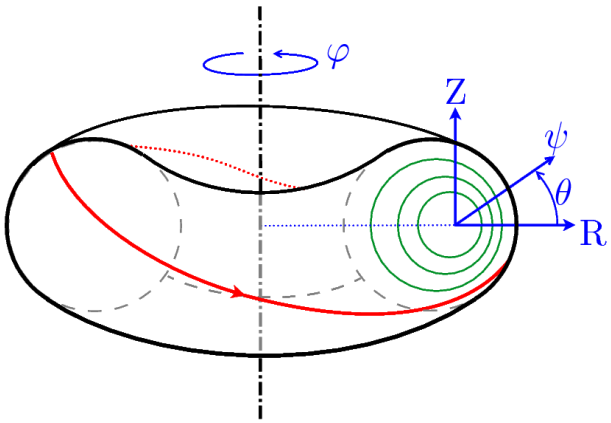

Figure 1: Tokamak configuration and toroidal coordinates definition. (φ, θ, ψ) denote the toroidal, poloidal angles and the surface label, respectively.

are implemented to control plasma-wall interaction. In the limiter configuration (see Figure 2,a), a protruding solid element intercepts the nested tori flux surfaces, opening the field lines. This element directly faces the confined plasma and must be designed to hold large heat fluxes. In the divertor configuration (see Figure 2,b), a dedicated coil creates a poloidal magnetic field in order to cancel the poloidal magnetic field generated by the plasma current. The magnetic field is zero at the X-point and the LCFS has a 8-shape. In this configuration, the open magnetic field lines intercept the solid in a region called the divertor region which is not directly in contact with the confined plasma. This configuration is thus meant to improve plasma confinement.

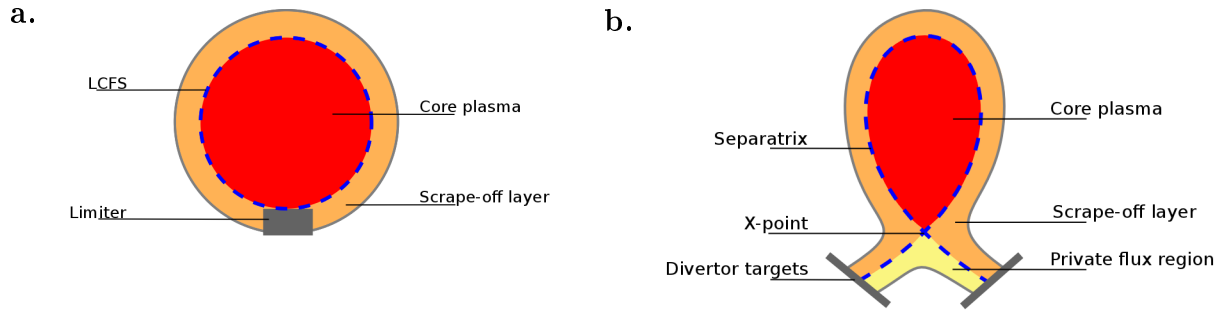

Figure 2: Different edge plasma configurations: a. Limiter configuration. b. Divertor configuration

The edge plasma is defined as the region including the scrape-off layer and the external core plasma touching the LCFS. This region is thus located at the transition between closed and open field line plasmas and governs the plasma-surface interactions. The edge plasma is also known to play a major role in plasma confinement since transport barriers may spontaneously arise near the LCFS. In particular, a high confinement mode (H-mode) characterized by a temperature and density pedestal localized at the LCFS is observed for high power. This phenomenon initially observed in divertor configuration [2] has also been

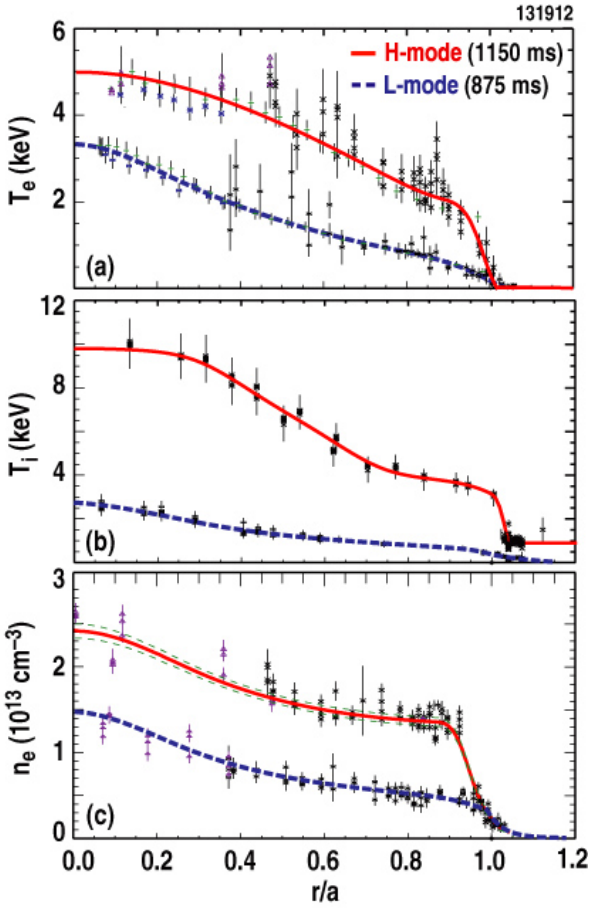

Figure 3: Radial profiles of (a) electron temperature from core plasma Thomson scattering data (triangles and x-symbols), and electron cyclotron emission (ECE, horizontal bars), (b) ion temperature from CHERS, and (c) electron density from core plasma Thomson scattering in L-mode (875 ms, dashed line) and H-mode (1150 ms, solid line). Figure from [4]

reported for limiter cases [3] and is thus quite generic. Density and temperature profiles before and after H-mode transition on DIII-D are plotted on Figure 3. The mechanisms at the origin of these barriers are still matter of debate.

In the early days of tokamak physics, the impact of the edge plasma on the core high temperature plasma has been quite underestimated. The main focus was on optimizing core plasma performances. The importance of the edge physics on the plasma confinement has slowly imposed and despite the many efforts made to decouple the edge plasma from the core, the ITER performances are now considered to be also controlled by the edge region. Several mechanisms can play a role in the core-edge coupling such as impurity contamination from the walls or flow shear near the separatrix. These effects can be deleterious (cooling effect due to radiation of impurities) or positive (creation of transport barriers). The high complexity of edge plasma physics requires resorting to numerical simulations. The great challenge of edge plasma numerical modeling is to qualitatively reproduce the transport properties observed from experiments and quantitatively estimate

particle and energy fluxes flowing in the tokamak plasma. In particular, in the scope of ITER design, a special care is taken to understand the properties of the divertor configuration. Indeed, the divertor must be optimized to control the energy flux impacting the materials, reduce the amount of impurities in the confined plasma, enable an efficient pumping of the Helium ashes. For all these phenomenons, the geometry of the divertor and plasma facing components plays a major role and despite an important effort for decades, simulating the whole tokamak edge plasma in realistic conditions remains an open problem. In this context, several codes based on fluid modeling have been developed in the fusion community such as EDGE2D, B2-EIRENE, BOUT, etc... In France, the devoted program ESPOIR funded by the French Research National Agency (ANR) aims at developing a 3D electrostatic fluid code to simulate edge plasma in realistic geometry. This project gathers the effort from plasma physics (CEA-IRFM, PIIM), applied mathematics (LATP) and high performance computing (M2P2, INRIA) laboratories.

This thesis works has been achieved in this perspective, at the interface between plasma physics and computational fluid dynamics. This work focuses on the full development of a fluid code, SOLEDGE2D (Chapter II), that must provide solutions for particle and energy transport in the edge plasma within complex and realistic 2D geometries. A *penalization technique* (Chapter II) has been developed to model plasma-wall interaction in very flexible geometries such as to treat realistic PFCs. In addition, the plasma code has been coupled with the Monte-Carlo neutral code EIRENE that implements the complex dynamic and chemistry of neutrals within the plasma (Chapter IV). This dedicated effort to properly describe the entire solid surface interacting with the plasma makes SOLEDGE2D an efficient tool to investigate crucial problematics as main chamber recycling, impurity migration in the tokamak vessel and divertor efficiency to control plasma wall interaction. The problematic of flow patterns in the edge plasma is also addressed. SOLEDGE2D simulations have for instance highlighted a broad range of plasma configurations where supersonic flows appear in the quasineutral plasma (Chapter V). In the divertor topology, the role of neutrals to prevent or trigger these transitions has been studied in details.

An issue tackled in this manuscript is the theoretical limit of the fluid description when it is applied to edge plasma modeling (Chapters III and IV). Many typical scales and processes involve in edge plasma description. The length of the magnetic field line $L_\parallel$, proportional to the physical size of the machine (major radius of the tokamak R_0) is associated with the parallel transport. The Larmor radius ρ_L, associated with the gyromotion of charged particles in a magnetic field is the typical length associated with classical cross-field transport. The particle mean free path λ_c is associated to thermalization process due to Coulombian collisions between plasma particles. Finally, the Debye length λ_D is associated to charge separation effects. In particular, charge separation occurs near the walls where electrostatic sheath develops. In the case we consider in tokamaks, the ordering differs between "hot" plasmas (core region) and "cold" plasmas (SOL) as

$$\begin{aligned} &\textbf{Hot plasma:} && \lambda_D \ll \rho_L \ll L_\parallel \ll \lambda_c \\ &\textbf{Cold plasma:} && \lambda_D \ll \rho_L \sim \lambda_c \ll L_\parallel \end{aligned} \tag{1}$$

The fluid approach being relevant for scales much greater than the collisional mean free path (Chapter I), Equation 1 shows that the fluid approach is only valid for cold plasma ($\lambda_c/L \ll 1$). The edge plasma is at the transition between cold and hot plasmas and could thus be accurately simulated with a full kinetic code. However, such approach remains numerically prohibitive (in particular, due to the requirement of modeling the fast electrons dynamic in the edge) making the fluid modeling more affordable even if not completely appropriate. Some corrections and dedicated fluid closures are proposed (Chapter III) to take the effect of weak collisionality into account. In that perspective, a dedicated work has been achieved in collaboration with statistic physicists at the CNR and at the University of Florence (Italy) to develop a 1D stochastic model taking into account collisionality in heat transfer properties. Non-local formulations for heat flux have been expressed with a generalized Fourier law, taken into account spatio-temporal memory effects with a long-range collision kernel.

Beforehand, some theoretical backgrounds used to derive SolEdge2D equations and boundary conditions are summed in Chapter I.

Chapter I

General concepts

Content

Some insights related to plasma physics are reported in this chapter. A special attention is devoted to the fluid model implemented in the edge plasma code SolEdge2D. The fluid model is derived and it is discussed in the limits of fluid closures. The reader is advised to report to the abundant literature on the subject [5, 6, 7, 8] to get more details.

This chapter starts with the description of charged particle motion. In Section I.1.1, the particle trajectory in an electro-magnetic field is computed. Section I.1.2 then describes the Coulombian collision/interaction between two charged particles. From the single particle description, the kinetic description and then to the fluid description are subsequently deduced. The fluid closures are discussed as regard to the collision properties exhibited for the Coulombian interaction in Section I.2.4. One also presents how transport associated to rapid fluctuations can be described in a diffusive way. This part justifies the model adopted all along this manuscript to treat plasma turbulent transport. Finally (Section I.5), some basic notions on sheath properties at the plasma-surface interaction are presented.

I.1 Charged particles trajectories and interactions

When an electromagnetic field is applied to an ionized gas, the charged particles evolution is driven by two independent forces due to external electromagnetic fields, the Lorentz force, and to the many electrostatic interactions among the particles themselves and described by Coulombian collisions.

I.1.1 Particles trajectories

Let us consider an orthonormal direct frame $(\vec{e}_x, \vec{e}_y, \vec{e}_z)$. At a time t, the particle is characterized by its position $\vec{x}$, velocity $\vec{v}$, mass m and charge q.

a) Magnetic confinement

The transport of charged particle in presence of an electric $\vec{E}$ and magnetic field $\vec{B}$ can be described by the Lorentz equation

$$m\frac{\partial \vec{v}}{\partial t} = q\left\{\vec{E}(\vec{x},t) + \vec{v}\times\vec{B}(\vec{x},t)\right\} \tag{I.1}$$

One has $\vec{F}_B = q\vec{v}\times\vec{B}$. Due to Relation I.2, the force induced by $\vec{F}_B$ does not work. Hence, magnetic field cannot be used to increase particle kinetic energy.

$$W_B = \vec{F_B}\cdot\vec{v} = q[\vec{v},\vec{B},\vec{v}] = 0 \tag{I.2}$$

The effect of magnetic field in the plane perpendicular to $\vec{B}$ is now considered. Assuming the magnetic field homogeneous $\vec{B} = B\vec{e}_z$, Lorentz equation becomes

$$\begin{aligned} m\frac{d\vec{v}}{dt} &= q\vec{v}\times\vec{B} \\ m\frac{d}{dt}\begin{pmatrix} v_x \\ v_y \\ v_z \end{pmatrix} &= q\begin{pmatrix} v_x \\ v_y \\ v_z \end{pmatrix}\times\begin{pmatrix} 0 \\ 0 \\ B \end{pmatrix} = qB\begin{pmatrix} v_y \\ -v_x \\ 0 \end{pmatrix} \end{aligned}$$

The magnetic field $\vec{B}$ has no effect on the parallel velocity since $dv_z/dt = 0$. For the perpendicular velocity, the following linear system of coupled equations is considered:

$$\begin{cases} \dfrac{dv_x}{dt} = \dfrac{qB}{m}v_y \\[2ex] \dfrac{dv_y}{dt} = -\dfrac{qB}{m}v_x \end{cases} \tag{I.3}$$

The cyclotronic frequency ω_c is defined as

$$\boxed{\omega_c = qB/m} \tag{I.4}$$

Reporting the second equation in the first one yields the ordinary differential equation

$$\frac{d^2v_x}{dt} + \omega_c^2 v_x = 0 \tag{I.5}$$

This equation admits solutions of the general form $v_x = v_0\sin(\omega_c t + \varphi)$. Integrating the equation for v_y, one obtains $v_y = v_0\cos(\omega_c t + \varphi)$. With such velocities, the particle motion

is decribed by an helicoidal trajectory spining around the magnetic field lines (see Figure I.1) that is to say:

$$\begin{cases} x &= -\rho_L \cos(\omega_c t + \varphi) \\ y &= \rho_L \sin(\omega_c t + \varphi) \\ z &= v_z t \end{cases} \tag{I.6}$$

with $\rho_L = v_0/\omega_c$ the Larmor radius. If T denotes the characteristic temperature such that the average velocity v_0 in the perpendicular plane is given by $v_0 = \sqrt{2k_BT/m}$, the Larmor radius expression becomes

$$\boxed{\rho_L = \sqrt{\frac{2k_BT}{m}}\frac{1}{\omega_c} = \frac{\sqrt{2k_BTm}}{qB}} \tag{I.7}$$

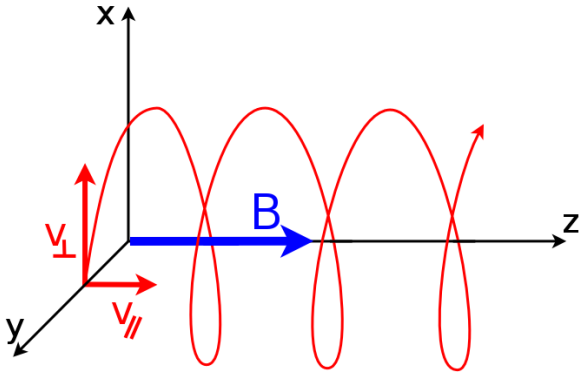

Figure I.1: Gyromotion: schematic representation of helicoidal trajectory along a magnetic field line.

When charged particles are placed in a magnetic field, they tend to follow magnetic field lines. In order to keep charged particles in a specific volume, closed field lines or more generally closed magnetic surfaces are used. This is the basic principle of magnetic confinement. The magnetic field strength must compensate the thermodynamic pressure that leads to plasma expansion. A major tokamak parameter called β expresses this balance between magnetic pressure that confines plasma and thermodynamic pressure that leads to "deconfinement".

$$\boxed{\beta = \frac{p}{p_{mag.}} = \frac{p}{B^2/2\mu_0}} \tag{I.8}$$

For the plasma to be confined, $\beta < 1$ is required. In practice, stable plasma are obtained with $\beta \approx 0.1$. One understands that if reducing β increases confinement but it also increases the cost since increasing $\vec{B}$ requires higher currents. An optimal value ensuring good confinement properties for a reasonable cost may be found.

If $\vec{B}$ is not homogeneous, Equation I.1 does not admit generally integrable solution. However, for strong magnetized system, a perturbative treatment can be used that allows

to split the motion into a fast cyclotronic motion (motion described above in an homogeneous magnetic field) and drifts due to fields inhomogeneities. This treatment known as the *adiabatic theory* is valid as long as

$$\textbf{Adiabatic theory:} \qquad \rho_L \ll \left(\frac{\|\vec{\nabla} B\|}{B} \right)^{-1} \tag{I.9}$$

and as long as the variations of magnetic and electric fields occur on a longer time scale as the gyromotion.

b) Drift velocities

One decomposes any quantity $\varphi = \{\vec{v}, \vec{B}, \vec{E}\}$ as $\varphi = \langle\varphi\rangle + \tilde{\varphi}$ with $\langle\tilde{\varphi}\rangle = 0$. The averaging operator $\langle\cdot\rangle$ is defined as the average over the gyromotion. Equation I.1 leads to:

$$m\frac{\partial}{\partial t}\Big(\langle\vec{v}\rangle + \tilde{v}\Big) = q\left\{\langle\vec{E}\rangle + \tilde{E} + \Big(\langle\vec{v}\rangle + \tilde{v}\Big) \times \Big(\langle\vec{B}\rangle + \tilde{B}\Big)\right\} \tag{I.10}$$

Averaging Equation I.10 leads to,

$$m\frac{\partial\langle\vec{v}\rangle}{\partial t} = q\left\{\langle\vec{E}\rangle + \langle\vec{v}\rangle \times \langle\vec{B}\rangle + \langle\tilde{v} \times \tilde{B}\rangle\right\} \tag{I.11}$$

and substracting I.11 from I.10, we obtain the following equation for the fluctuations:

$$m\frac{\partial\tilde{v}}{\partial t} = q\left\{\tilde{E} + \tilde{v} \times \langle\vec{B}\rangle + \langle\vec{v}\rangle \times \tilde{B} + \tilde{v} \times \tilde{B} - \langle\tilde{v} \times \tilde{B}\rangle\right\} \tag{I.12}$$

Following the *adiabatic theory*, the fluctuating velocity is assumed to be given by the cyclotronic motion equation detailed in the above paragraph a). Hence, Equation I.12 finally simplifies to

$$m\frac{\partial\tilde{v}}{\partial t} = q\left\{\tilde{v} \times \langle\vec{B}\rangle\right\} \tag{I.13}$$

This gyromotion equation is associated to the Larmor radius ρ_L given by Equation I.7. The information about the fast gyromotion is now reported into the average motion. In Equation I.11, the term $\langle\tilde{v} \times \tilde{B}\rangle$ has to be evaluated. In particular, the fluctuations of $\vec{B}$ during the gyromotion[1] are evaluated using $\tilde{B} = (\vec{\rho}_L \cdot \vec{\nabla})\langle\vec{B}\rangle$. One has thus, according to Equation I.6,

$$\begin{aligned}
\langle\tilde{v} \times \tilde{B}\rangle &= \Big\langle(\vec{\rho}_L \times \vec{\omega_c}) \times (\vec{\rho}_L \cdot \vec{\nabla})\langle\vec{B}\rangle\Big\rangle \\
&= \Big\langle\Big(\vec{\rho}_L \cdot (\vec{\rho}_L \cdot \vec{\nabla})\langle\vec{B}\rangle\Big)\,\vec{\omega}_c - \Big(\vec{\omega}_c \cdot (\vec{\rho}_L \cdot \vec{\nabla})\langle\vec{B}\rangle\Big)\,\vec{\rho}_L\Big\rangle \\
&= \langle\rho_k\rho_p\partial_p B_k\omega_i\vec{e}_i - \omega_j\rho_k\partial_k B_j\rho_i\vec{e}_i\rangle
\end{aligned}$$

[1] The gymotion is described here as a rotation of radius ρ_L around the gyrocenter. The details on how the gyrocenter is defined are not detailed in this manuscript

Since $\vec{\rho}_L = \rho_L(\cos\varphi_c\vec{e}_i + \sin\varphi_c\vec{e}_j)$, it follows that $\langle\rho_i\rho_j\rangle = \frac{1}{2}\rho_L^2\delta_{ij}$ if both indeces i and j correspond to transverse directions, $\langle\rho_i\rho_j\rangle = 0$ otherwise. For convenience, brackets will be suppressed in the followings. The parallel and perpendicular projections are made with respect to the vector $\vec{b} = \langle\vec{B}\rangle/\langle B\rangle$. Hence $\langle\tilde{v}\times\tilde{B}\rangle$ simplifies to:

$$\langle\tilde{v}\times\tilde{B}\rangle = \frac{1}{2}\rho_L^2\omega_c\left(\vec{b}(\vec{\nabla}_\perp\cdot\vec{B}_\perp) - \vec{\nabla}_\perp B\right)$$

Since $\vec{\nabla}\cdot\vec{B} = 0$, one has $\vec{\nabla}_\perp\cdot\vec{B}_\perp = -\nabla_\parallel B_\parallel = -\nabla_\parallel B$. Finally, one has

$$\langle\tilde{v}\times\tilde{B}\rangle = -\frac{1}{2}\rho_L^2\omega_c\vec{\nabla}B = -\frac{\mu}{q}\vec{\nabla}B \tag{I.14}$$

with the magnetic moment $\mu = \frac{1}{2}q\|\vec{r}\times\vec{v}\| = \frac{1}{2}q\omega_c\rho_L^2$. Equation I.11 becomes :

$$m\frac{d\langle\vec{v}\rangle}{dt} = q\left(\vec{E} + \langle\vec{v}\rangle\times\vec{B}\right) - \mu\vec{\nabla}B \tag{I.15}$$

Projecting I.15 onto the transverse plane yields

$$m\left.\frac{d\vec{v}_\perp}{dt}\right|_\perp + m\left.\frac{d(v_\parallel\vec{b})}{dt}\right|_\perp = q\left(\vec{E}_\perp + \vec{v}\times\vec{B}\right) - \mu\vec{\nabla}_\perp B \tag{I.16}$$

At first order, the first term in the LFS is neglected. For the second term,

$$\left.\frac{d(v_\parallel\vec{b})}{dt}\right|_\perp = \cancel{\frac{dv_\parallel}{dt}\vec{b}}|_\perp + v_\parallel\frac{d\vec{b}}{dt} = v_\parallel^2\nabla_\parallel\vec{b}$$

Multiplying Equation I.16 by $\times\vec{B}$ to get $\vec{v}$,

$$(mv_\parallel^2\nabla_\parallel\vec{b})\times\vec{B} = q\left(\vec{E}\times\vec{B} + B^2(v_\parallel\vec{b} - \vec{v})\right) - \mu\vec{\nabla}B\times\vec{B} \tag{I.17}$$

Finally

$$\vec{v}_\perp = \frac{\vec{E}\times\vec{B}}{B^2} + \frac{\vec{B}}{qB^2}\times\left[\mu\vec{\nabla}B + mv_\parallel^2\nabla_\parallel\vec{b}\right] \tag{I.18}$$

The first contribution $\vec{v}_E = \vec{E}\times\vec{B}/B^2$ called the electric or "*E cross B*" drift does not depend on the particle species. Consequently, it does not produce any current. The second contribution is a combination of so-called *grad-B* and curvature drifts. This velocity is mostly vertical in tokamaks and produces charge separation, electrons and ions drifting in opposite directions. This equation can be simplified in the low β limit. Indeed,

$$\begin{aligned}\nabla_\parallel\vec{b} &= \vec{b}\cdot\vec{\nabla}\vec{b} = \frac{1}{2}\vec{\nabla}(\vec{b}\cdot\vec{b}) - \vec{b}\times(\vec{\nabla}\times\vec{b})\\ &= (\vec{\nabla}\times\vec{B} - \vec{\nabla}B\times\vec{b})\times\vec{b}/B\\ &= (\vec{\nabla}\times\vec{B})\times\vec{b}/B + \vec{\nabla}_\perp B/B\end{aligned}$$

Maxwell-Ampère law $\vec{\nabla} \times \vec{B} = \mu_0 \vec{j}$ and MHD equilibrium $\vec{j} \times \vec{B} = \vec{\nabla} p$ are used to obtain the relation

$$\nabla_\parallel \vec{b} - \frac{\vec{\nabla}_\perp B}{B} = (\vec{\nabla} \times \vec{B}) \times \vec{B}/B^2 = \frac{\vec{\nabla} p}{\mu_0 B^2} \approx \frac{1}{2}\vec{\nabla}\beta$$

Equation I.18 is rewritten as

$$\boxed{\vec{v}_\perp = \frac{\vec{E} \times \vec{B}}{B^2} + \frac{\mu B + m v_\parallel^2}{q B^3} \vec{B} \times \vec{\nabla} B + \frac{m v_\parallel^2}{q \mu_0 B^4} \vec{B} \times \vec{\nabla} p} \tag{I.19}$$

where the last term is negligible in the *low-β limit*.

Concerning the parallel dynamic, projecting Equation I.15 onto the parallel direction yields

$$m \frac{d(v_\parallel \vec{b})}{dt} \cdot \vec{b} + m \frac{d\vec{v}_\perp}{dt} \cdot \vec{b} = q \vec{E}_\parallel - \mu \nabla_\parallel B \tag{I.20}$$

The first term of the LHS reduces to $m dv_\parallel/dt$ while the second gives

$$\frac{d\vec{v}_\perp}{dt} \cdot \vec{b} = \left(\vec{v} \cdot \vec{\nabla} \vec{v}_\perp\right) \cdot \vec{b} = \left\{ \left(\vec{v}_\perp \cdot \vec{\nabla}_\perp + v_\parallel \nabla_\parallel\right) \vec{v}_\perp \right\} \cdot \vec{b}$$

The first term of the RHS is proportional to $v_\perp^2$ and can be neglected.

$$\begin{aligned}
v_\parallel \left\{\nabla_\parallel \vec{v}_\perp\right\} \cdot \vec{b} &= v_\parallel \left\{ (\vec{b} \cdot \vec{\nabla}) \vec{v}_\perp \right\} \cdot \vec{b} \\
&= v_\parallel \left\{ \vec{\nabla}(\cancel{\vec{b} \cdot \vec{v}_\perp}) - \vec{v}_\perp \times (\vec{\nabla} \times \vec{b}) - \vec{b} \times (\vec{\nabla} \times \vec{v}_\perp) - (\vec{v}_\perp \cdot \vec{\nabla}) \vec{b} \right\} \cdot \vec{b} \\
&= -v_\parallel \left\{ \vec{v}_\perp \times \left(\vec{\nabla} \times \frac{\vec{B}}{B} \right) \right\} \cdot \vec{b} - v_\parallel \cancel{(\vec{v}_\perp \cdot \vec{\nabla}) b^2} \\
&= \frac{v_\parallel}{B} \left\{ \vec{v}_\perp \times \left(\vec{\nabla} B \times \vec{b} - \vec{\nabla} \times \vec{B} \right) \right\} \cdot \vec{b}
\end{aligned}$$

In the *low-β limit*, $\vec{v}_\perp \times (\vec{\nabla} B \times \vec{b})$ reduces to $\vec{v}_E \times (\vec{\nabla} B \times \vec{b})$. Hence,

$$\begin{aligned}
v_\parallel \left\{\nabla_\parallel \vec{v}_\perp\right\} \cdot \vec{b} &= \frac{v_\parallel}{B} \left\{ \vec{v}_E \times (\vec{\nabla} B \times \vec{b}) - \vec{v}_\perp \times \mu_0 \vec{j} \right\} \cdot \vec{b} \\
&= \frac{v_\parallel}{B} \left\{ \left(\cancel{\vec{v}_E \cdot \vec{b}}\right) \vec{\nabla} B - \left(\vec{v}_E \cdot \vec{\nabla} B\right) \vec{b} \right\} \cdot \vec{b} - v_\parallel \vec{v}_\perp \cdot \frac{\vec{\nabla}_\perp p}{B^2/\mu_0}
\end{aligned}$$

The last term in the RHS being proportional to β, it can be neglected and the final equation for $v_\parallel$ is given by

$$\boxed{m \frac{dv_\parallel}{dt} = q E_\parallel - \mu \nabla_\parallel B + m v_\parallel \vec{v}_E \cdot \frac{\vec{\nabla} B}{B}} \tag{I.21}$$

This equation highlights the driven mechanisms of a single particle motion along the magnetic field line. In particular:

- Electric field with a non zero parallel component. This term can be used to generate plasma current.

- Parallel gradient of magnetic field. Due to the $1/R$ structure of the magnetic field, this term generates particle bouncing and so-called *banana orbits*.

I.1.2 Coulombian interaction

This section is devoted to derive major characteristics of the Coulombian interaction such as collision time and particle mean free path.

The Coulombian interaction between two particles of charge q_1 and q_2 is given by the inverse square force

$$\vec{F}_{1\to 2} = \frac{q_1 q_2}{4\pi\epsilon_0^2}\frac{\vec{r}}{r^3} \tag{I.22}$$

where $\vec{r}$ denotes the distance between interacting particles, $\vec{r} = \vec{x}_2 - \vec{x}_1$. This central force

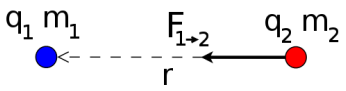

Figure I.2: Scheme of the Coulombian interaction between two particles of mass and charge (m_1, q_1) and (m_2, q_2).

problem is a "classic" of mechanics. In recall here the major properties of the particle motions. The two particles follow hyperbolic trajectories that lie in the same plane. If $\vec{v}_1$ and $\vec{v}_2$ denotes particles velocity before interacting, one may compute the velocities $\vec{v}_1'$ and $\vec{v}_2'$ after interacting. This analysis is performed in the center of mass frame represented on Figure I.3. In particular, the impact parameter b is defined as a function of $(\vec{x}_1, \vec{x}_2, \vec{v}_1, \vec{v}_2)$.

$$\begin{aligned} b = \vec{r}\cdot\vec{e}_y &= \vec{r}\cdot\frac{(\vec{r}\times\vec{v}_{12})\times\vec{v}_{12}}{rv_{12}^2} \\ &= \vec{r}\cdot\frac{(\vec{v}_{12}\cdot\vec{r})\vec{v}_{12} - v_{12}^2\vec{r}}{rv_{12}^2} \\ &= \frac{(\vec{v}_{12}\cdot\vec{r})^2 - v_{12}^2 r^2}{rv_{12}^2} \\ b(\vec{x}_1,\vec{x}_2,\vec{v}_1,\vec{v}_2) &= \frac{[(\vec{v}_2-\vec{v}_1)\cdot(\vec{x}_2-\vec{x}_1)]^2 - \|\vec{v}_2-\vec{v}_1\|^2\|\vec{x}_2-\vec{x}_1\|^2}{\|\vec{x}_2-\vec{x}_1\|\cdot\|\vec{v}_2-\vec{v}_1\|^2} \end{aligned}$$

This geometrical parameter determines the intensity of the collision between the two bodies. More precisely the deviation angle χ is linked to the impact factor by the following relation taken from [5, Section 2.8].

$$\tan\left(\frac{\chi}{2}\right) = -\frac{b_0}{b} \tag{I.23}$$

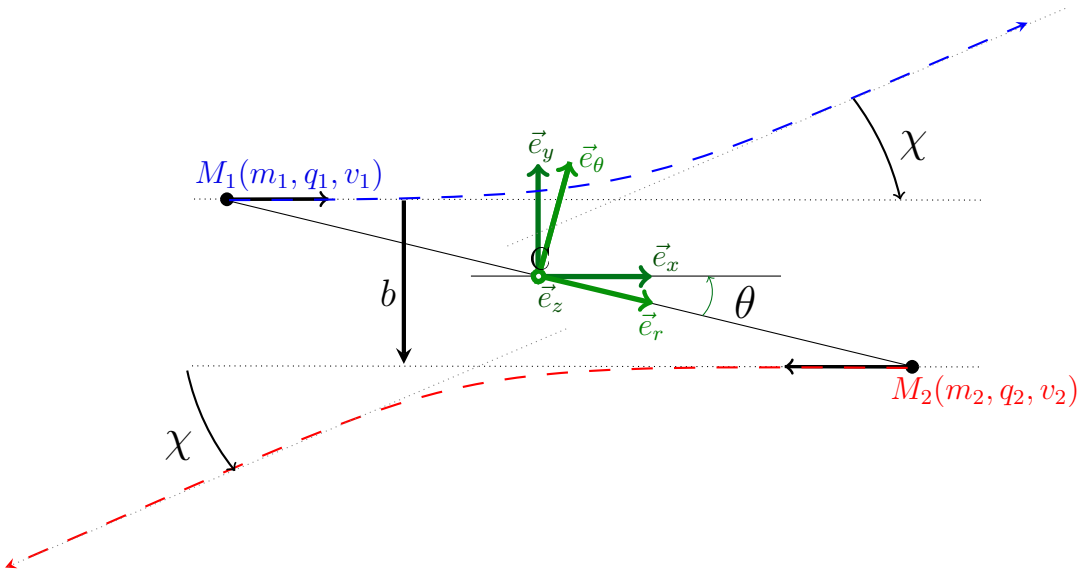

Figure I.3: Scheme of two particles colliding in the relative frame. b denotes the impact factor and χ denotes the deviation angle.

where b_0 denotes the impact factor below which the deviation is greater than 90 degrees.

$$b_0 = \frac{q_1 q_2}{4\pi\varepsilon_0^2 \mu v_{12}^2} \qquad \text{with} \qquad \mu = \frac{m_1 m_2}{m_1 + m_2} \tag{I.24}$$

So far, the problem has been treated in the plane containing the particle trajectories.

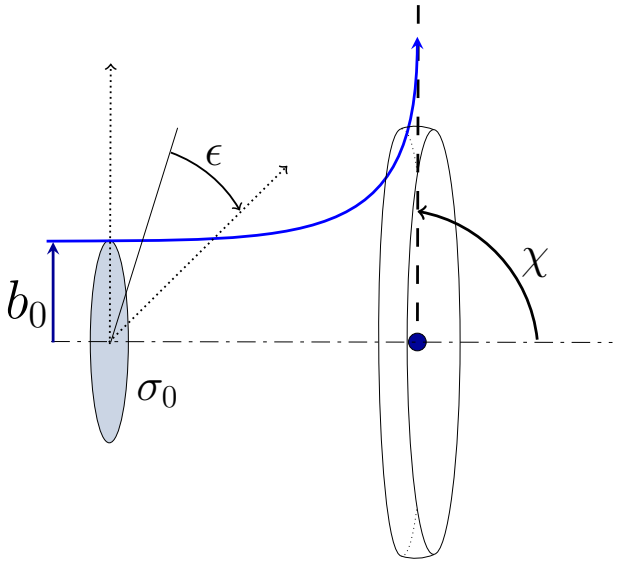

Figure I.4: Scheme of the interaction cross section σ_0 for deflection angle $\chi = 90^o$. The collision process is axisymmetric and ϵ is an angle introduced around the symmetry axis.

The 3D problem is axisymmetic and the angle ϵ is introduced to complete the description

(Figure I.4). The Coulombian interaction cross section σ_0 for large deflection (more that 90 degree) is defined as (one assumes $m_1 = m_2$ and $q_1 = q_2$):

$$\sigma_0 = \pi b_0^2 = \frac{q^4}{16\pi\varepsilon_0^4\mathcal{E}^2} \qquad \text{with} \qquad \mathcal{E} = \frac{1}{2}mv_{12}^2 \tag{I.25}$$

The particle velocity after collision can now be computed. If $\vec{v}_{1_\star}$ denotes the velocity of particle 1 in the relative frame before collision, the velocity after collision is expressed by $\vec{v}'_{1_\star} = \mathbf{R}_\chi \cdot \vec{v}_{1_\star}$ where $\mathbf{R}_\chi$ denotes the rotation around $\vec{e}_z$ of angle χ. More generally ($\vec{v}_G$ denotes the velocity of center of mass)

$$\begin{aligned} \vec{v}'_1 &= \vec{v}_G + \vec{v}'_{1_\star} \\ &= \vec{v}_G + \mathbf{R}_\chi \cdot (\vec{v}_1 - \vec{v}_G) \\ &= (\mathbb{I} - \mathbf{R}_\chi) \cdot \frac{m_1\vec{v}_1 + m_2\vec{v}_2}{m_1 + m_2} + \mathbf{R}_\chi \cdot \vec{v}_1 \end{aligned} \tag{I.26}$$

The same expression exists for $\vec{v}'_2$. Given $\vec{x}_1$ and $\vec{x}_2$ or b and ϵ, a given couple $(\vec{v}_1, \vec{v}_2)$ is associated to a unique couple $(\vec{v}'_1, \vec{v}'_2)$. $\mathcal{C}$ denotes the bijective relation linking the velocities before and after the collision. This bijection contains the characteristics of the Coulombian interaction between two particles.

To go further, let us consider the decrement of velocity for particle of type 1 in the relative frame. $\vec{v}_{1_\star}$ is originally aligned with $\vec{e}_x$. After colliding, the velocity $\vec{v}'_{1_\star}$ has a component along $\vec{e}_x$ and a component along $\vec{e}_y$. If one sums collision events over the impact parameter b, due to symmetry, the average component $\langle \vec{v}'_{1_\star} \cdot \vec{e}_y \rangle = 0$. Concerning the x-direction, the variation of velocity is evaluated during time δt (the volume of interacting particles is represented on Figure I.5. n denotes particle density)

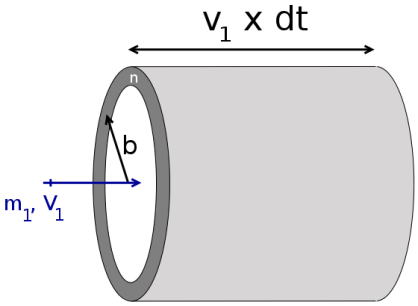

$$\begin{aligned} \delta\langle \vec{v}'_{1_\star} \cdot \vec{e}_x \rangle &= \left(\int_0^\infty v_{1_\star}(1 - \cos\chi) 2\pi b db \right) \times n v_{1_{star}} \delta t \\ &= n v_{1_\star}^2 \delta t \pi \int_0^\infty v_{1_\star} \frac{2\tan^2(\chi/2)}{1 + \tan^2(\chi/2)} 2b db \\ &= n v_{1_\star}^2 \delta t \pi \int_0^\infty v_{1_\star} \frac{2b_0^2}{b^2 + b_0^2} 2b db \\ &= 2\pi n v_{1_\star}^2 \delta t b_0^2 [\ln(b^2 + b_0^2)]_0^\infty \end{aligned}$$

Figure I.5: Elementary volume of particles that interacts during time δt with the particle of velocity $\vec{v}_1$ and with the impact factor b.

The integral diverges when $b \to \infty$ so a cut-off value for b must be found. The Debye length is used as upper integrating bound since it is the characteristic length for which Coulombian interaction is shielded. Hence,

$$\frac{\delta\langle \vec{v}'_{1_\star} \cdot \vec{e}_x \rangle}{\delta t} = 2\pi n v_{1_\star}^2 b_0^2 \ln\left(1 + \left[\frac{\lambda_D}{b_0}\right]^2\right) = 2n\sigma_0 v_{1_\star}^2 \ln\Lambda \tag{I.27}$$

From this expression, the characteristic collision time is defined as the time required to cancel the initial parallel velocity,

$$\tau_c = \frac{v_{1_\star}}{\delta\langle \vec{v}'_{1_\star} \cdot \vec{e}_x \rangle} = \frac{1}{2n\sigma_0 v_{1_\star} \ln\Lambda} \tag{I.28}$$

Likewise, one defines the collision mean free path as $\lambda_c = v_{1_\star} \cdot \tau_c$,

$$\lambda_c = \frac{1}{2n\sigma_0 \ln\Lambda} \tag{I.29}$$

In Equation I.25, σ_0 is proven to be inversely proportional to the square of particle energy in the relative frame. This energy can be linked to plasma temperature using $\mathcal{E} \sim 3/2 k_B T$. Hence, the following dependences for mean free path and collision time are obtained:

$$\boxed{\lambda_c \propto \frac{T^2}{n}} \quad \text{and} \quad \boxed{\tau_c \propto \frac{T^{3/2}}{n}} \tag{I.30}$$

I.2 From Vlasov-Landau equation to fluid equations

I.2.1 Kinetic description

The most intuitive description of the plasma consists in monitoring the position and velocity of each ion and electron constituing the plasma. The plasma dynamic can be computed by following every particle trajectory using Lorentz Equation I.1. This microscopic description can be linked to Klimontovitch description of the plasma [8] where one defines a distibution function describing the microscopic evolution of all the particles in the phase space. However, it is obviously not affordable here for any computing device; for each cube-meter of typical tokamak plasma, more than 10^{20} particles should be considered as well as the interactions between every particles that is to say 10^{40} interactions.

A statistic treatment is thus required and constitutes the kinetic description of the plasma. Indeed, if a plasma particle is described at any time t by its position $\vec{x}$ and its velocity $\vec{v}$, it is possible to define the probability density function (p.d.f.) of the particle $f(\vec{x}, \vec{v}, t)$ such as $f(\vec{x}, \vec{v}, t) d^3\vec{x} d^3\vec{v}$ is the average number of particles in the small volume $d^3\vec{x}$ about $\vec{x}$ and with a velocity within the small volume $d^3\vec{v}$ about $\vec{v}$ in the velocity space. The p.d.f. description is based on averaging over several statistical realisations of microscopical states. As any theory based on stochastic averages, it is relevant if statistical fluctuations about the average are small.

In order to study the evolution of the p.d.f. in time, one establishes the conservation equation

$$\frac{\partial f}{\partial t} + \vec{\nabla} \cdot (f\vec{V}) = 0 \tag{I.31}$$

where $\vec{V}$ represents the velocity in the phase space. Besides, since $\vec{\nabla} \cdot \vec{V} = 0$ in the phase

space, Equation I.31 can be rewritten

$$\frac{\partial f}{\partial t} + \vec{V} \cdot \vec{\nabla} f = 0 \tag{I.32}$$

Distinguishing physical space and velocity space, one obtains Boltzmann Equation:

$$\frac{\partial f}{\partial t} + \vec{v} \cdot \vec{\nabla}_x f + \vec{a} \cdot \vec{\nabla}_v f = 0 \tag{I.33}$$

where $\vec{v}$ denotes velocity in physical space and $\vec{a}$ denotes particle acceleration. For a charged particle, this acceleration is given by the Lorentz force. However, one must remember that the kinetic description is based on an averaging process over the microscopic states. Hence, the effect of the "mean" electric and magnetic field and the effect of electric and magnetic field on the microscopic states must be distinguished. The latter contribution is often refered to collision contribution since even if there is no actual collision between plasma particles, the overall effect of several microscopic interactions between charged particles shows ressemblance with the friction-diffusion process characteristic of the average motion of particles interacting through elastic collisions. The resulting equation is refered to as Vlasov-Landau equation

$$\frac{\partial f}{\partial t} + \vec{v} \cdot \vec{\nabla}_x f + \frac{q}{m}(\vec{E} + \vec{v} \times \vec{B}) \cdot \vec{\nabla}_v f = \left(\frac{\partial f}{\partial t}\right)_c \tag{I.34}$$

where $(\partial f/\partial t)_c$ denotes the effect of "collisions". The work of Landau to express this term can be found in the literature [9]. This term results in a friction-diffusion in the velocity space and is the dominant term for high density and low temperature plasmas (typically Edge plasmas). On the contrary, for hot plasmas (typically in tokamak core region), this term becomes second-order and Vlasov-Landau equation may be simplified to Vlasov equation

$$\frac{\partial f}{\partial t} + \vec{v} \cdot \vec{\nabla}_x f + \frac{q}{m}(\vec{E} + \vec{v} \times \vec{B}) \cdot \vec{\nabla}_v f = 0 \tag{I.35}$$

For cold plasma, the collisional term is the dominant one and Vlasov-Landau Equation reduces to

$$\left(\frac{\partial f}{\partial t}\right)_c = 0 \tag{I.36}$$

The solution of this equation is the well-known Maxwellian distribution. A perturbative treatment around this equilibrium distribution is then performed leading to the fluid approach. This work is addressed in the following paragraphs about fluid equations and fluid closures.

I.2.2 From kinetic to fluid equations

From the kinetic equation, it is possible to derive equations for any moment of the distribution function f. The moment of order k is defined as

$$\mathcal{M}_k(\vec{x}) = \int_{\mathcal{V}_v} \vec{v}^k f(\vec{x}, \vec{v}) d\vec{v} \tag{I.37}$$

where $\vec{v}^k = \bigotimes_{i=1}^{k} \vec{v}$.

One starts with Vlasov-Landau equation

$$\frac{\partial f}{\partial t} + \vec{v} \cdot \vec{\nabla}_x f + \frac{\vec{F}}{m} \cdot \vec{\nabla}_v f = \left(\frac{\partial f}{\partial t}\right)_C \tag{I.38}$$

where $\vec{F}$ denotes Lorentz force $\vec{F} = q(\vec{E} + \vec{v} \times \vec{B})$. Several approaches have been developped to express the collisional part of the equation. Multiplying by $\vec{v}^k$ and integrating Equation I.38 over $\vec{v}$, one obtains:

$$\int_{\mathcal{V}_v} \frac{\partial f}{\partial t} \vec{v}^k d\vec{v} + \int_{\mathcal{V}_v} \left\{ \vec{v} \cdot \vec{\nabla}_x f \right\} \vec{v}^k d\vec{v} + \int_{\mathcal{V}_v} \left\{ \frac{\vec{F}}{m} \cdot \vec{\nabla}_v f \right\} \vec{v}^k d\vec{v} = \int_{\mathcal{V}_v} \left(\frac{\partial f}{\partial t}\right)_C \vec{v}^k d\vec{v}$$

that is developped as

$$\begin{aligned} &\frac{\partial}{\partial t}\left(\int_{\mathcal{V}_v} f \vec{v}^k d\vec{v}\right) + \int_{\mathcal{V}_v} \left\{ \vec{\nabla}_x \cdot (\vec{v} f) - \cancel{f \vec{\nabla}_x \vec{v}} \right\} \vec{v}^k d\vec{v} \\ &\quad \cdots + \int_{\mathcal{V}_v} \left\{ \vec{\nabla}_v \cdot \left(\frac{\vec{F}}{m} f\right) - \cancel{f \vec{\nabla}_v \left(\frac{\vec{F}}{m}\right)} \right\} \vec{v}^k d\vec{v} \;=\; \int_{\mathcal{V}_v} \left(\frac{\partial f}{\partial t}\right)_C \vec{v}^k d\vec{v} \end{aligned}$$

The term $\vec{\nabla}_x \cdot \vec{v}$ cancels out since variables are independent. The divergence of the lorentz force in the velocity space simplifies as

$$\begin{aligned} \vec{\nabla}_v \cdot \left(\frac{\vec{F}}{m}\right) &= \frac{1}{m} \vec{\nabla}_v \cdot q\left(\vec{E} + \vec{v} \times \vec{B}\right) \\ &= \frac{q}{m} \vec{\nabla}_v \cdot \left(\vec{v} \times \vec{B}\right) \qquad \text{for } q \text{ and } \vec{E} \text{ do not depend on } \vec{v} \\ &= \frac{q}{m}\left(\vec{B} \cdot \vec{\nabla}_v \times \vec{v} - \vec{v} \cdot \vec{\nabla}_v \times \vec{B}\right) \\ &= 0 \qquad \text{for } \vec{B} \text{ does not depend on } \vec{v} \text{ and } \vec{\nabla}_v \times \vec{v} = 0 \end{aligned}$$

Going back to moment equation,

$$\frac{\partial}{\partial t}\left(\int_{\mathcal{V}_v} f\vec{v}^k d\vec{v}\right) + \int_{\mathcal{V}_v}\left\{\vec{\nabla}_x\cdot(f\vec{v}^{k+1}) - \cancel{(f\vec{v}\cdot\vec{\nabla}_x)\vec{v}^k}\right\}d\vec{v}$$
$$\cdots + \int_{\mathcal{V}_v}\left\{\vec{\nabla}_v\cdot\left(f\frac{\vec{F}}{m}\otimes\vec{v}^k\right) - \left(f\frac{\vec{F}}{m}\cdot\vec{\nabla}_v\right)\otimes\vec{v}^k\right\}d\vec{v} \;=\; \int_{\mathcal{V}_v}\left(\frac{\partial f}{\partial t}\right)_C\vec{v}^k d\vec{v}$$

Then, using $\vec{\nabla}_v\otimes\vec{v}^k = k\mathbb{I}\otimes\vec{v}^{k-1}$,

$$\frac{\partial}{\partial t}\left(\int_{\mathcal{V}_v} f\vec{v}^k d\vec{v}\right) + \vec{\nabla}_x\cdot\int_{\mathcal{V}_v} f\vec{v}^{k+1}d\vec{v} + \cancel{\int_{\partial\mathcal{V}_v} f\frac{\vec{F}}{m}\otimes\vec{v}^k d^2\vec{v}}$$
$$\cdots - \int_{\mathcal{V}_v} kf\frac{\vec{F}}{m}\otimes\vec{v}^{k-1}d\vec{v} \;=\; \int_{\mathcal{V}_v}\left(\frac{\partial f}{\partial t}\right)_C\vec{v}^k d\vec{v}$$

$f\vec{v}^k$ vanishes on the velocity space boundary assuming f has a strong decay when $\|\vec{v}\|$ tends to infinity. This property is verified for the Maxwelian distribution for which $f\sim\exp(-\|\vec{v}\|^2)$ has a stronger decay than any power law. Finally, the moment equation yields:

$$\frac{\partial\mathcal{M}_k}{\partial t} + \vec{\nabla}_x\cdot\mathcal{M}_{k+1} - k\frac{\vec{F}}{m}\otimes\mathcal{M}_{k-1} = \mathcal{C}_k \tag{I.39}$$

Since the differential operators only apply in the physical space the notation $\vec{\nabla}_x$ is replaced by $\vec{\nabla}$. The contribution linked to collisions is denoted $\mathcal{C}_k$ and is defined by Equation I.40.

$$\mathcal{C}_k = \int_{\mathcal{V}_v}\left(\frac{\partial f}{\partial t}\right)_C\vec{v}^k d\vec{v} \tag{I.40}$$

Usually, the fluid approach considers moments up to the second order. The moment of order 0 gives continuity equation, the moment of order 1 gives velocity equation and the moment of order 2 gives the pressure or energy equation. It must be noticed that the k^{th}-order moment equation contains divergence of the $(k+1)^{th}$-order moment. In the equation of the 2^{nd}-order moment, it is thus necessary to find a closure relation to express the moment of order 3 (heat flux) as a function of lower order moments. This closure relation often relies on small perturbation treatment around equilibrium and is discussed with more details in section I.2.4.

a) Continuity equation

The density n is defined as moment of order 0 and the fluid velocity $\vec{u}$ as moment of order 1:

$$n = \mathcal{M}_0 = \int_{\mathcal{V}_v} f(\vec{v})d\vec{v} \qquad ; \qquad \vec{u} = \frac{\mathcal{M}_1}{n} = \frac{1}{n}\int_{\mathcal{V}_v}\vec{v}f(\vec{v})d\vec{v} \tag{I.41}$$

From Equation I.39, the following equation for density is obtained:

$$\frac{\partial n}{\partial t} + \vec{\nabla} \cdot n\vec{u} = \mathcal{C}_0 \tag{I.42}$$

The collisions do not create or destroy particles, hence $\mathcal{C}_0 = 0$. Continuity Equation finally becomes:

$$\boxed{\frac{\partial n}{\partial t} + \vec{\nabla} \cdot n\vec{u} = 0} \tag{I.43}$$

b) Momentum equation

The equation for the moment of order 1 that is the particle flux $\Gamma = n\vec{u}$ is now derived. This equation contains the second order moment $\mathcal{M}_2$. The latter is developped as:

$$\begin{aligned}
\mathcal{M}_2 &= \int_{\mathcal{V}_v} \vec{v} \otimes \vec{v} f(\vec{v}) d\vec{v} \\
&= \int_{\mathcal{V}_{v'}} (\vec{u} + \vec{v}') \otimes (\vec{u} + \vec{v}') f(\vec{u} + \vec{v}') d\vec{v}' \\
&= n\vec{u} \otimes \vec{u} + \vec{u} \otimes \cancel{\int_{\mathcal{V}_{v'}} \vec{v}' f(\vec{u} + \vec{v}') d\vec{v}'} + \cancel{\int_{\mathcal{V}_{v'}} \vec{v}' f(\vec{u} + \vec{v}') d\vec{v}'} \otimes \vec{u} + \int_{\mathcal{V}_{v'}} \vec{v}' \otimes \vec{v}' f(\vec{u} + \vec{v}') d\vec{v}' \\
\mathcal{M}_2 &= n\vec{u} \otimes \vec{u} + \frac{\mathbf{\Pi}}{m}
\end{aligned} \tag{I.44}$$

where $\vec{v}'$ denotes the perturbation from the fluid velocity $\vec{u}$, $\vec{v}' = \vec{v} - \vec{u}$. The pressure tensor $\mathbf{\Pi}$ is defined as

$$\mathbf{\Pi} = m \int_{\mathcal{V}_v} (\vec{v} - \vec{u}) \otimes (\vec{v} - \vec{u}) f(\vec{v}) d\vec{v} \tag{I.45}$$

The isotropic pressure p is given by $p = \mathrm{Tr}(\mathbf{\Pi})/3$ such that $\mathbf{\Pi} = p\mathbb{I} + \mathbf{\Xi}$ with $\mathrm{Tr}(\mathbf{\Xi}) = 0$. Also, since Coulombian interaction is an elastic process, it conserves particle momentum in average, hence $\mathcal{C}_1 = \vec{0}$. Using Equation I.39, the following equation is obtained for fluid velocity:

$$\boxed{\frac{\partial n\vec{u}}{\partial t} + \vec{\nabla} \cdot \left(n\vec{u} \otimes \vec{u} + \frac{\mathbf{\Pi}}{m} \right) - n\frac{\vec{F}}{m} = \vec{0}} \tag{I.46}$$

The expression for $\mathbf{\Pi}$ is discussed in the section about closures I.2.4.

c) Energy equation

The total energy E_t of the fluid is defined as the integral of the kinetic energy of all particles. The total energy is thus given by the relation:

$$E_t = \int_{\mathcal{V}_v} \frac{1}{2} m\vec{v} \cdot \vec{v} f(\vec{v}) d\vec{v} \tag{I.47}$$

The definition of total energy is linked to the second moment using $\vec{v}\cdot\vec{v} = \mathrm{Tr}\left(\vec{v}\otimes\vec{v}\right)$. One obtains

$$\begin{aligned} E_t &= \frac{1}{2}m\mathrm{Tr}\left(\mathcal{M}_2\right) \\ &= \frac{1}{2}m\mathrm{Tr}\left(\vec{u}\otimes\vec{u}+\frac{\mathbf{\Pi}}{m}\right) \\ &= \frac{1}{2}m\vec{u}\cdot\vec{u}+\frac{1}{2}\mathrm{Tr}\left(p\mathbb{I}+\mathbf{\Xi}\right) \\ E_t &= \frac{1}{2}mu^2+\frac{3}{2}p \end{aligned} \tag{I.48}$$

The total energy is then splitted into:

- the fluid kinetic energy $E_c = \frac{1}{2}mu^2$
- the internal energy $U = \frac{3}{2}p$

Using Equation I.39, the following equation for total energy is obtained

$$\frac{\partial E_t}{\partial t}+\frac{1}{2}m\mathrm{Tr}\left(\vec{\nabla}\cdot\mathcal{M}_3\right)-n\vec{u}\cdot\vec{F}=\mathcal{C}_2 \tag{I.49}$$

with

$$\begin{aligned} \mathcal{M}_3 &= \int_{\mathcal{V}_v}\vec{v}^3 f(\vec{v})d\vec{v} = \int_{\mathcal{V}_{v'}}(\vec{u}+\vec{v}')^3 f(\vec{u}+\vec{v}')d\vec{v}' \\ &= n(\vec{u}\otimes\vec{u}\otimes\vec{u})+\vec{u}\otimes\frac{\mathbf{\Pi}}{m}+\frac{\mathbf{\Pi}}{m}\otimes\vec{u} \\ &\quad \cdots+\int_{\mathcal{V}_{v'}}\vec{v}'\otimes\vec{u}\otimes\vec{v}' f(\vec{u}+\vec{v}')d\vec{v}'+\int_{\mathcal{V}_{v'}}\vec{v}'\otimes\vec{v}'\otimes\vec{v}' f(\vec{u}+\vec{v}')d\vec{v}' \end{aligned}$$

The divergence is developped using

$$\begin{aligned} \mathrm{Tr}\left(\vec{\nabla}\cdot\vec{a}\otimes\vec{b}\otimes\vec{c}\right) &= \mathrm{Tr}\left(\partial_i a_i b_j c_k\right) \\ &= \partial_i a_i b_j c_j \\ &= \vec{\nabla}\cdot\left(\vec{a}\vec{b}\cdot\vec{c}\right) \end{aligned} \tag{I.50}$$

yielding

$$\mathrm{Tr}\left(\vec{\nabla}\cdot\mathcal{M}_3\right) = \vec{\nabla}\cdot\left(nu^2\vec{u}\right)+\vec{\nabla}\cdot\left(\frac{\mathrm{Tr}(\mathbf{\Pi})}{m}\vec{u}\right)+2\vec{\nabla}\cdot\left(\vec{u}\cdot\frac{\mathbf{\Pi}}{m}\right)+\frac{2}{m}\vec{\nabla}\cdot\vec{q} \tag{I.51}$$

with heat flux vector defined as

$$\vec{q}=\frac{1}{2}m\int_{\mathcal{V}_v}\|\vec{v}-\vec{u}\|^2(\vec{v}-\vec{u})f(\vec{v})d\vec{v} \tag{I.52}$$

The heat flux $\vec{q}$ that is a third order moment will be expressed as a function of lower order moments in the next section about fluid closures. Finally, the following transport equation is obtained for total energy where one identifies advection of energy, work of external forces and work of pressure forces.

$$\boxed{\frac{\partial E_t}{\partial t} + \vec{\nabla}\cdot(E_t\vec{u}) + \vec{\nabla}\cdot(\vec{u}\cdot\mathbf{\Pi}) + \vec{\nabla}\cdot\vec{q} - n\vec{u}\cdot\vec{F} = \mathcal{C}_2} \tag{I.53}$$

The kinetic energy equation is obtained by multiplying velocity equation (I.46) by $m\vec{u}$:

$$\begin{aligned} m\vec{u}\cdot\frac{\partial n\vec{u}}{\partial t} + m\vec{u}\cdot\vec{\nabla}\cdot\left(n\vec{u}\otimes\vec{u} + \frac{\mathbf{\Pi}}{m}\right) - n\vec{u}\cdot\vec{F} &= 0 \\ \frac{\partial E_c}{\partial t} + \vec{\nabla}\cdot(E_c\vec{u}) + \vec{u}\cdot\vec{\nabla}\cdot\mathbf{\Pi} - n\vec{u}\cdot\vec{F} &= 0 \end{aligned} \tag{I.54}$$

Substracting Equation I.54 from Equation I.53 yields the Equation for internal energy:

$$\boxed{\frac{\partial U}{\partial t} + \vec{\nabla}\cdot(U\vec{u}) + \mathbf{\Pi} : \left(\vec{\nabla}\otimes\vec{u}\right) + \vec{\nabla}\cdot\vec{q} = \mathcal{C}_2} \tag{I.55}$$

I.2.3 The collision operator

In the above equations, the tensor pressure $\mathbf{\Pi}$, the heat flux $\vec{q}$ and the contribution $\mathcal{C}_\in$ can be expressed from collisions properties. The algebra presented in this paragraph is inspired by the work made by *Chapman, Enskog and Cowling* summarized in the Reference [7]. The reader is invited to report to the bibliography for further information. More succinctly, this section presents the general path that makes possible to obtain a fluid closure using a perturbative treatment of the kinetic equation. A special care is taken to highlight the limits of this method.

The first step is to provide an appropriate statistical description of the Coulombian interactions that act among the particles. As described in section I.1.2, the many Coulombian interactions can be described as elastic collisions.

In that perspective, the collision term expressed in the RHS of Vlasov-Landau Equation I.34 is expressed as a source-sink term:

$$\left(\frac{\partial f}{\partial t}\right)_c \delta t d\vec{x} d\vec{v} = \left\{\begin{array}{c}\text{Number of particles in}\\ \text{the volume } d\vec{x} \text{ around } \vec{x}\\ \text{with velocity in the}\\ \text{volume } d\vec{v} \text{ around } \vec{v}\\ \textbf{produced} \text{ by encounters}\\ \text{during time } \delta t\end{array}\right\} - \left\{\begin{array}{c}\text{Number of particles in}\\ \text{the volume } d\vec{x} \text{ around } \vec{x}\\ \text{with velocity in the}\\ \text{volume } d\vec{v} \text{ around } \vec{v}\\ \textbf{“destroyed”} \text{ by}\\ \text{encounters during time } \delta t\end{array}\right\} \tag{I.56}$$

The loss of particles with velocity $\vec{v}$ due to collisions is evaluated by counting how many collisions occur between particles of velocity $\vec{v}$ with other particles during time δt. Two-body collisions are taken into account, the effects of collisions between more than two particles being considered negligible. As described in section I.1.2, a two-body collision can be entirely described by the impact factor b, the angle ϵ (see Figure I.7) and the

relative velocity between the two colliding particles $\vec{g} = \vec{v} - \vec{v}_\star$ [2]. Moreover, if the collision geometry is given (that is b and ϵ), there is a bijective relation $\mathcal{C}$ that links the particle velocities before colliding ($\vec{v}$ and $\vec{v}_\star$) and the particle velocities after impact ($\vec{v}'$ and $\vec{v}'_\star$). This relation can be determined analyticaly as done for Coulombian interaction in section I.1.2.

$$\mathcal{C}: \underset{(\vec{v},\vec{v}_\star)}{\textbf{Before impact}} \leftrightarrow \underset{(\vec{v}',\vec{v}'_\star)}{\textbf{After impact}} \tag{I.57}$$

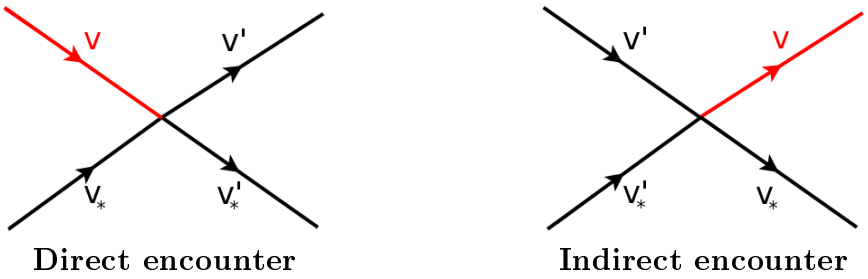

Figure I.6: Creation and destruction of particles of velocity $\vec{v}$ by collision with a particle of velocity $\vec{v}_\star$. Left: Direct collision producing a particle of velocity $\vec{v}'$. Right: Inverse collision creating a particle of velocity $\vec{v}$.

For each set of parameter, it is possible to determine a volume in the physical space in which the colliding particle of type 2 must rely to interact during time δt. This volume represented on Figure I.7 is given by $dv = g\delta t b db d\epsilon$. The number of encounters can then be determined with the formula:

$$\begin{aligned} dN^-_{enc.} &= \left\{ \begin{array}{c} \text{Number of particles} \\ \text{with velocity } \vec{v} \end{array} \right\} \times \left\{ \begin{array}{c} \text{Number of particles particles that} \\ \text{can collide with particle of velocity } \vec{v} \end{array} \right\} \\ &= f d\vec{v} d\vec{x} \times f_\star d\vec{v}_\star g \delta t b db d\epsilon \end{aligned} \tag{I.58}$$

One recovers the formula 3.5-6 of ref. [7]:

$$dN^-_{enc.} = f f_\star k d\vec{k} d\vec{v} d\vec{v}_\star d\vec{x} \delta t \tag{I.59}$$

using $g b db d\epsilon = k d\vec{k}$.

Likewise, in order to evaluate the number of collisions leading to the creation of particles with velocity $\vec{v}$, the same treatment can be done by considering what Chapman and Cowling call inverse encounters. The following formula (3.52-7) for the number of particles created is obtained:

$$dN^+_{enc.} = f' f'_\star k d\vec{k} d\vec{v} d\vec{v}_\star d\vec{x} \delta t \tag{I.60}$$

where f' and $f'_\star$ denotes the pdf of colliding particles leading to the creation of a particle

[2] If χ denotes any function associated to the particles described by the kinteic equation, $\chi_\star$ denotes the same function but associated to the particles with which the formers collide. The two classes of particles can describe the same species, however, one must keep two sets of independent variables to distinguish the two bodies colliding.

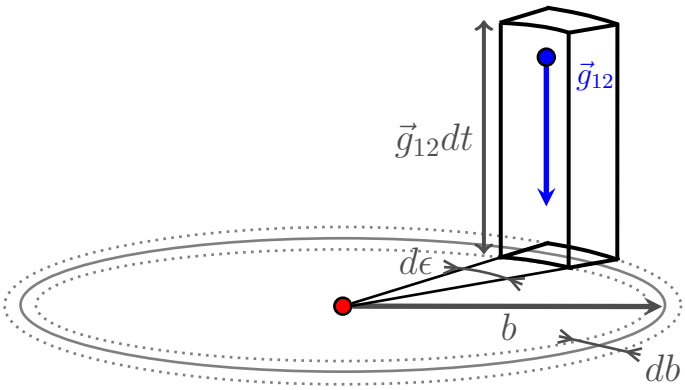

Figure I.7: Volume to consider for a two particle collision. ϵ denotes the angle of symmetry, b denotes the impact factor and $\vec{g}_{12} = \vec{v}_1 - \vec{v}_2$ the relative velocity between the particles.

with velocity $\vec{v}$. Due to the properties of the bijection I.57, it is possible to determine easily the pair of impacting velocities $(\vec{v}', \vec{v}'_\star)$ leading to after-impact velocities $(\vec{v}, \vec{v}_\star)$. Consequently, one may write in a compact form $f'f'_\star = ff_\star(\mathcal{C}(\vec{v}, \vec{v}_\star))$.

Finally, the following formula is obtained for the collision term:

$$\left(\frac{\partial f}{\partial t}\right)_{c2} \delta t d\vec{x} d\vec{v} = N^+_{enc.} - N^-_{enc.} \tag{I.61}$$

leading to

$$\boxed{\left(\frac{\partial f}{\partial t}\right)_{c2} = \iint (f'f'_\star - ff_\star) k d\vec{k} d\vec{v}_\star} \tag{I.62}$$

This relation is often refered to as Boltzmann form of the collision term. As mentionned in section I.2.5, this relation is not suited to treat Coulombian interaction for the integral does not converge when integrating b over $\mathbb{R}^+$. Some corrections must be done to cut-off the integral and take long range encounters into account.

a) The Maxwellian distribution

From Equation I.62, it is possible to express f at equilibrium. An homogeneous gas where collisions are the only mechanism inducing force is considered. The Boltzmann H-function is defined as,

$$H = \int f \ln f d\vec{v} \tag{I.63}$$

Since the system is homogeneous in space, H only depends on time. In particular,

$$\frac{\partial H}{\partial t} = \int \frac{\partial}{\partial t}(f \ln f) d\vec{v} = \int (1 + \ln f) \frac{\partial f}{\partial t} d\vec{v} \tag{I.64}$$

Reporting Equation I.62 and using some algebra described in [7],

$$\begin{aligned}\frac{\partial H}{\partial t} &= \iiint (1+\ln f)(f'f'_\star - ff_\star)k_\star d\vec{k}d\vec{v}_\star d\vec{v} \\ &= \frac{1}{4}\iiint \ln(ff_\star/f'f'_\star)(f'f'_\star - ff_\star)k_\star d\vec{k}d\vec{v}_\star d\vec{v} \end{aligned} \tag{I.65}$$

In this expression, either $ff_\star \leq f'f'_\star$ or $ff_\star \geq f'f'_\star$, the RHS of Equation I.65 is always negative. The famous Boltzmann *H-theorem* thus states $\partial_t H \leq 0$. Moreover, since H cannot tend to $-\infty$ for finiteness of energy, H must converge to a finite value leading to $\partial_t H = 0$. This steady state is characterized by so-called *local balance* that is $ff_\star = f'f'_\star$. This can be rewritten as

$$\ln f + \ln f_\star = \ln f' + \ln f'_\star \tag{I.66}$$

Hence, $\ln f$ is a summation invariant of the process. As a consequence, this invariant must express as a linear combination of the other 3 fundamental thermodynamic invariants that are: mass, momentum and energy.

$$\ln f = \alpha_1 + \vec{\alpha}_2 \cdot m\vec{v} + \alpha_3 \frac{1}{2}mv^2 \tag{I.67}$$

The constants α_i are found to match the pdf fluid moments that are density, velocity and energy. The pdf is given by the Maxwellian distribution f_M. In this equilibrium state, the temperature is defined as $U = 3/2k_BT$.

$$\boxed{f_M = n\left(\frac{m}{2\pi k_B T}\right)^{3/2} \exp\left(-\frac{m\|\vec{v}-\vec{u}\|^2}{2k_BT}\right)} \tag{I.68}$$

This expression gives the following moments:

- Density: $n = \int f_M(\vec{v})d\vec{v}$
- Velocity: $\vec{u} = \int \vec{v} f_M(\vec{v})d\vec{v}$
- Pressure: $\mathbf{\Pi} = \int (\vec{v}-\vec{u}) \otimes (\vec{v}-\vec{u}) f_M(\vec{v})d\vec{v} = k_B nT\mathbb{I}$
  Defining the isotropic pressure $p = 1/3\mathrm{Tr}(\mathbf{\Pi})$, one recovers perfect gas state law:

$$\boxed{p = k_B nT} \tag{I.69}$$

- Total energy: $E_t = \int 1/2 m_i v^2 f_M(\vec{v})d\vec{v} = 1/2 m_i n u^2 + 3/2 k_B nT$
  The well-known expression for monoatomic gas internal energy is also recovered.

$$\boxed{U = \frac{3}{2}k_B nT} \tag{I.70}$$

- Heat flux: $\vec{q} = \int \|\vec{v}-\vec{u}\|^2(\vec{v}-\vec{u}) f_M(\vec{v})d\vec{v} = \vec{0}$

I.2.4 Chapman-Enskog fluid closures

a) Chapman-Enskog ordering

In the fluid equations derived in section I.2.2, several terms have not been expressed yet. These terms are the pressure tensor $\mathbf{\Pi}$, the heat flux $\vec{q}$ and the collisional contributions $\mathcal{C}_i$. The fluid closure consists in finding an expression for these terms, expresion that only depends on the fluid variables n, $\vec{u}$ and T. These expressions can be found empirically or using a perturbative method to solve kinetic equation. The technique derived by Chapman and Enskog reported in [7] is one of these perturbative method. Let us describe how it works.

The kinetic Vlasov-Landau equation I.34 can be written as $\xi(f) = 0$ with

$$\xi(f) = J(ff_\star) + \mathcal{D}f \tag{I.71}$$

where J is the collision operator and $\mathcal{D}$ is the advection operator

$$\mathcal{D}f = \frac{\partial f}{\partial t} + \vec{v}\cdot\vec{\nabla}f + \vec{a}\cdot\vec{\nabla}_v f \tag{I.72}$$

As stated by Equation I.62,

$$J(ff_\star) = \iint (ff_\star - f'f'_\star) k d\vec{k} d\vec{v}_\star \tag{I.73}$$

The advection term is linear whereas the collisional term is bilinear in f and $f_\star$. The approach of Chapman & Enskog is to develop the density function as

$$f = \frac{1}{\varepsilon} f^{(0)} + f^{(1)} + \varepsilon f^{(2)} + \dots \tag{I.74}$$

where ε is a small parameter.

The bilinearity of the collision operator yields:

$$\begin{aligned} J(f, f_\star) &= J\left(\frac{1}{\varepsilon} f^{(0)} + f^{(1)} + \varepsilon f^{(2)} + \dots, \frac{1}{\varepsilon} f_\star^{(0)} + f_\star^{(1)} + \varepsilon f_\star^{(2)} + \dots\right) \\ &= \frac{1}{\varepsilon^2} J(f^{(0)}, f_\star^{(0)}) + \frac{1}{\varepsilon}\left(J(f^{(0)}, f_\star^{(1)}) + J(f^{(1)}, f_\star^{(0)})\right) + \dots \\ &= \frac{1}{\varepsilon^2} J^{(0)}(f^{(0)}, f_\star^{(0)}) + \frac{1}{\varepsilon} J^{(1)}(f^{(0)}, f^{(1)}, f_\star^{(0)}, f_\star^{(1)}) + \dots \end{aligned}$$

Hence the collision operator can also be decomposed according to powers of ε. In particular, one has $J^{(0)}(f, f_\star) = J(f, f_\star)$. For higher orders,

$$J^{(r)}(f^{(0)}, \dots, f^{(r)}, f_\star^{(0)}, \dots, f_\star^{(r)}) = \sum_{k=0}^{r} J(f^{(k)} f_\star^{(r-k)}) \tag{I.75}$$

Concerning the advection operator $\mathcal{D}$, the linearity gives

$$\begin{aligned} \mathcal{D}f &= \mathcal{D}\left(\frac{1}{\varepsilon}f^{(0)} + f^{(1)} + \varepsilon f^{(2)}\right) \\ &= \frac{1}{\varepsilon}\mathcal{D}^{(1)}(f^{(0)}) + \mathcal{D}^{(2)}(f^{(0)}, f^{(1)}) + \dots \end{aligned} \tag{I.76}$$

$\mathcal{D}^{(r)}$ depends only on $f^{(k)}$ with $k \leq r-1$. The kinetic equation $\xi(f) = 0$ can thus be developped as

$$\begin{aligned} \xi(f) &= J(ff_\star) + \mathcal{D}f \\ &= \frac{1}{\varepsilon^2}J^{(0)}(f^{(0)}, f_\star^{(0)}) + \frac{1}{\varepsilon}\left[J^{(1)}(f^{(0)}, f^{(1)}, \dots) + \mathcal{D}^{(1)}(f^{(0)})\right] \\ &\quad + \left[J^{(2)}(f^{(0)}, f^{(1)}, f^{(2)}, \dots) + \mathcal{D}^{(2)}(f^{(0)}, f^{(1)})\right] + \dots \\ &= \frac{1}{\varepsilon^2}\xi^{(0)}(f^{(0)}) + \frac{1}{\varepsilon}\xi^{(1)}(f^{(0)}, f^{(1)}) + \xi^{(2)}(f^{(0)}, f^{(1)}, f^{(2)}) + \dots \end{aligned} \tag{I.77}$$

Solving $\xi(f) = 0$ is then replaced by solving the system of equations

$$\xi^{(0)}(f^{(0)}) = 0 \tag{I.78}$$
$$\xi^{(1)}(f^{(0)}, f^{(1)}) = 0 \tag{I.79}$$
$$\xi^{(2)}(f^{(0)}, f^{(1)}, f^{(2)}) = 0 \tag{I.80}$$
$$\dots$$

For more details on this development, please refer to [7, chapter 7]. The first equation has a well defined solution since $\xi^{(0)}(f^{(0)}) = J(f^{(0)}f_\star^{(0)})$ is equal to zero if $f^{(0)}$ is a Maxwellian distribution (see paragraph I.2.4-a)). At this stage are set the density n, velocity $\vec{u}$ and temperature T of the fluid.

$$f^{(0)}(\vec{v}) = n\varepsilon\left(\frac{m}{2\pi k_B T}\right)^{3/2}\exp\left(-\frac{m\|\vec{v}-\vec{u}\|^2}{2k_B T}\right) \tag{I.81}$$

Since the first moments are set by $f^{(0)}$, one has

$$\forall k \geq 1,\ \forall n \in \{0,1,2\},\ \int \vec{v}^n f^{(k)}(\vec{v})d\vec{v} = 0$$

The correction terms $f^{(1)}$, $f^{(2)}$,... still have to be determined. They will produce perturbation about the equilibrium distribution leading to inhomogeneities and fluxes. These terms are derived by solving Equations (I.79,I.80,...) successively.

b) Computation of pressure tensor and heat flux - fluid closure

If $\vec{u} = 1/n\int \vec{v}f(\vec{v})d\vec{v}$ denotes the fluid velocity and $\vec{V} = (\vec{v}-\vec{u})$, the heat flux is defined as $\vec{q} = \int \vec{V}V^2 f(\vec{v})d\vec{v}$ and of the pressure tensor as $\mathbf{\Pi} = \int \vec{V}\otimes\vec{V}f(\vec{v})d\vec{v}$. From the 0^{th}-order

of Chapman-Enskog development, $f^{(0)}$ is given by the Maxwellian distribution I.81. The 0^{th} order contribution for $\vec{q}$ and $\mathbf{\Pi}$ is thus given by

$$\vec{q}^{(0)} = \frac{1}{2}m\int \vec{V}V^2\frac{f^{(0)}}{\varepsilon}d\vec{v} = \vec{0} \qquad \text{and} \qquad \mathbf{\Pi}^{(0)} = m\int \vec{V}\otimes\vec{V}\frac{f^{(0)}}{\varepsilon}d\vec{v} = p\mathbb{I} \tag{I.82}$$

where $p = k_B nT$. As expected for an equilibrium distribution, the heat flux is zero. In order to get a net heat flux, it is necessary to account for $f^{(1)}$ at least. Theoretically, one should account for highest order contributions in the development, though, if the collisionality is high, the distribution is not expected to depart much from the Maxwellian distribution hence the small parameter ε in the development is small enough to neglect $f^{(k)}$ contributions for $k \geq 2$. When the collisionality gets smaller, these contributions cannot be neglected and Chapman-Enskog development is no longer relevant. *Consequently, the following expressions obtained with Chapman-Enskog development for heat flux and pressure tensor only apply if collisionality is high*, that is $\|\mathcal{D}(f)\| \ll \|J(ff_\star)\|$ which can be expressed as:

$$\boxed{\textbf{High collisionality condition:} \qquad \nu^\star = \frac{\tau_\mathcal{D}}{\tau_c} = \frac{\lambda_\mathcal{D}}{\lambda_c} \gg 1} \tag{I.83}$$

where $\nu^\star$ is the collisionality, τ_c (resp. λ_c) is the characteristic collision time (resp. mean free path) and $\tau_\mathcal{D}$ (resp. $\lambda_\mathcal{D}$) is the characteristic time (resp. length) associated to external forces and system geometry.

In order to get $f^{(1)}$ let us solve Equation I.79:

$$\mathcal{D}^{(1)}(f^{(0)}) + J^{(1)}(f^{(0)}, f^{(1)}) = 0 \tag{I.84}$$

If the expression for $J^{(1)}$ is given by Equation I.75, an expression for $\mathcal{D}^{(1)}$ still has to be determined. The exact expression obtained by *Enskog* is given by [7, Equation 7.14-19]. In this manuscript, a simplified approach is proposed. Let us assume $\mathcal{D}^{(1)}(f^{(0)}) \approx \mathcal{D}(f^{(0)})$:

$$\mathcal{D}^{(1)}(f^{(0)}) = \frac{\partial f^{(0)}}{\partial t} + \vec{v}\cdot\vec{\nabla}f^{(0)} + \vec{a}\cdot\vec{\nabla}_v f^{(0)} \tag{I.85}$$

or

$$\mathcal{D}^{(1)}(f^{(0)}) = \frac{Df^{(0)}}{Dt} + \vec{V}\cdot\vec{\nabla}f^{(0)} + \left(\vec{a} - \frac{D\vec{u}}{Dt}\right)\cdot\vec{\nabla}_V f^{(0)} - (\vec{\nabla}_V f^{(0)}\otimes\vec{V}) : (\vec{\nabla}\otimes\vec{u}) \tag{I.86}$$

where $\vec{V} = \vec{v} - \vec{u}$ denotes the relative velocity and where the time derivative in the relative frame is given by

$$\frac{D}{Dt} = \frac{\partial}{\partial t} + \vec{u}\cdot\vec{\nabla} \tag{I.87}$$

Since $f^{(0)}$ is a function of n, $\vec{u}$ and T, the time derivative is developped, giving

$$\frac{\partial f^{(0)}}{\partial t} = \frac{\partial f^{(0)}}{\partial n}\frac{\partial n}{\partial t} + \frac{\partial f^{(0)}}{\partial \vec{u}} \cdot \frac{\partial \vec{u}}{\partial t} + \frac{\partial f^{(0)}}{\partial T}\frac{\partial T}{\partial t} \tag{I.88}$$

The time derivative are computed from fluid equations where the unknown parameters $\vec{q}$, $\mathbf{\Pi}$ and $\mathcal{C}_i$ are those obtained with $f^{(0)}$. This assumption is consistent with [7]. Since $\mathcal{C}_i(f^{(0)}) = 0$, $\vec{q}(f^{(0)}) = \vec{0}$ and $\mathbf{\Pi}(f^{(0)}) = p\mathbb{I}$, the fluid system to consider is (see fluid equations in section I.2.2).

$$\frac{\partial n}{\partial t} + \vec{\nabla} \cdot (n\vec{u}) = 0 \tag{I.89}$$

$$\frac{\partial \vec{u}}{\partial t} + (\vec{u} \cdot \vec{\nabla})\vec{u} - \vec{a} + \frac{\vec{\nabla} p}{mn} = 0 \tag{I.90}$$

$$\frac{\partial T}{\partial t} + \vec{u} \cdot \vec{\nabla} T + \frac{2}{3} T \vec{\nabla} \cdot \vec{u} = 0 \tag{I.91}$$

Equation I.90 yields $\vec{a} - D\vec{u}/Dt = \vec{\nabla} p/mn$. Reporting in Equation I.86 and using a logarithmic formulation, one has

$$\mathcal{D}^{(1)}(f^{(0)}) = f^{(0)} \left\{ \frac{D \ln f^{(0)}}{Dt} + \vec{V} \cdot \vec{\nabla} \ln f^{(0)} + \frac{\vec{\nabla} p}{mn} \cdot \vec{\nabla}_V \ln f^{(0)} - (\vec{\nabla}_V \ln f^{(0)} \otimes \vec{V}) : (\vec{\nabla} \otimes \vec{u}) \right\} \tag{I.92}$$

Since $f^{(0)}$ is given by the Maxwellian distribution,

$$\ln f^{(0)} = \text{const.} + \ln\left(\frac{n}{T^{3/2}}\right) - \frac{m\vec{V}^2}{2k_B T} \tag{I.93}$$

thus

$$\vec{\nabla}_V \ln f^{(0)} = -\frac{m\vec{V}}{k_B T} \tag{I.94}$$

Also,

$$\begin{aligned} \frac{D \ln f^{(0)}}{Dt} &= \frac{1}{n}\frac{Dn}{Dt} - \frac{3}{2T}\frac{DT}{Dt} + \frac{m\vec{V}^2}{2k_B T^2}\frac{DT}{Dt} \\ &= -\frac{n\vec{\nabla} \cdot \vec{u}}{n} + \frac{3}{2T}\left(\frac{2}{3} T \vec{\nabla} \cdot \vec{u}\right) + \frac{m\vec{V}^2}{2k_B T^2}\frac{DT}{Dt} \\ &= -\frac{m\vec{V}^2}{3k_B T}\vec{\nabla} \cdot \vec{u} \end{aligned}$$

The following simplification can be done:

$$\begin{aligned}\vec{V}\cdot\vec{\nabla}\ln f^{(0)}+\frac{\vec{\nabla}p}{mn}\cdot\vec{\nabla}_V\ln f^{(0)} &= \vec{V}\cdot\left(\vec{\nabla}\ln f^{(0)}-\frac{\vec{\nabla}p}{p}\right)\\ &= \vec{V}\cdot\vec{\nabla}\ln\left(\frac{f^{(0)}}{k_BnT}\right)\\ &= \vec{V}\cdot\left(\frac{mV^2}{2k_BT}-\frac{5}{2}\right)\vec{\nabla}\ln T\end{aligned}$$

The final expression for $\mathcal{D}^{(1)}$ is finally given by Equation I.95.

$$\mathcal{D}^{(1)}(f^{(0)})=f^{(0)}\left\{\left(\frac{mV^2}{2k_BT}-\frac{5}{2}\right)\vec{V}\cdot\vec{\nabla}\ln T+\frac{m}{k_BT}\left(\vec{V}\otimes\vec{V}-\frac{1}{3}V^2\mathbb{I}\right):(\vec{\nabla}\otimes\vec{u})\right\} \quad \text{(I.95)}$$

The expression for $\mathcal{D}^{(1}$ is now reported in Equation I.84. Given the properties of the bilinear function $J^{(1)}$, one obtains the following general solution for $f^{(1)}$ (see [7, Equation 7.31-7])

$$\boxed{f^{(1)}=-\frac{f^{(0)}}{n}\left\{\sqrt{\frac{2k_BT}{m}}\vec{A}\cdot\vec{\nabla}\ln T+\mathbf{B}:(\vec{\nabla}\otimes\vec{u})\right\}} \quad \text{(I.96)}$$

where $\vec{A}$ and $\mathbf{B}$ are two parameters depending on n, T and $\vec{V}$. Besides, $\vec{A}$ is an odd function of $\vec{V}$ components ($\vec{A}\sim\vec{V}^{2k+1}$) whereas $\mathbf{B}$ is an even function of $\vec{V}$ ($\mathbf{B}\sim\vec{V}^{2k}$). Hence the contributions of $\vec{A}$ disappear in computation of even moments such as pressure tensor whereas the contributions of $\mathbf{B}$ disappear in odd moments such as heat flux.

It is now possible to compute the heat flux $\vec{q}=\vec{q}^{(1)}$:

$$\vec{q}=\frac{1}{2}m\int V^2\vec{V}f^{(1)}(\vec{V})d\vec{V}$$

Since $\mathbf{B}$ is an even function of $\vec{V}$

$$\begin{aligned}\vec{q} &= -\frac{1}{2}m\int V^2\vec{V}\frac{f^{(0)}}{n}\sqrt{\frac{2k_BT}{m}}\vec{A}\cdot\vec{\nabla}\ln T d\vec{V}\\ &= -\frac{1}{n}\sqrt{\frac{mk_B}{2T}}\left[\int V^2\vec{V}f^{(0)}\vec{A}d\vec{V}\right]\cdot\vec{\nabla}T\end{aligned}$$

Whatever the properties of the collisions, the heat flux expresses according to the well known *Fourier's law*:

$$\boxed{\vec{q}=-\kappa\cdot\vec{\nabla}T} \quad \text{(I.97)}$$

where the heat conductivity tensor κ depends on the nature of collisions whose properties express through the parameter $\vec{A}$.

Likewise, the following expression is obtained for the pressure tensor.

$$\begin{aligned}\boldsymbol{\Pi} &= p\mathbb{I} + \boldsymbol{\Xi} \\ &= m\int \vec{V}\otimes\vec{V}\left(\frac{f^{(0)}}{\varepsilon} + f^{(1)}\right)d\vec{V} \\ &= p\mathbb{I} + m\int \vec{V}\otimes\vec{V} f^{(1)}(\vec{V})d\vec{V}\end{aligned}$$

The resulting expression for $\boldsymbol{\Xi}$ is given by Equation I.98.

$$\begin{aligned}\boldsymbol{\Xi} &= -m\int \vec{V}\otimes\vec{V} f^{(0)}\frac{1}{n}\sqrt{\frac{2k_BT}{m}}\mathbf{B} : (\vec{\nabla}\otimes\vec{u})d\vec{V} \\ &= -\frac{1}{n}\sqrt{2mk_BT}\left[\int \vec{V}\otimes\vec{V} f^{(0)}\mathbf{B}\right] : (\vec{\nabla}\otimes\vec{u})\end{aligned}$$

The pressure tensor can be expressed in term of *viscous stress* as

$$\boxed{\boldsymbol{\Xi} = -\nu : (\vec{\nabla}\otimes\vec{u})} \tag{I.98}$$

where the viscosity tensor ν depends on the collisions properties through $\mathbf{B}$.

I.2.5 Spitzer-Härm and Braginskii closures

In the previous paragraph, it has been proven that in highly collisional plasma, the heat flux is linked to the temperature gradient by a linear combination given by the heat conductivity tensor κ. The expression for κ depends on the properties of the Coulombian interaction. During the 50's, *L. Spitzer* and *R. Härm* gave an major contribution to evaluate heat conductivity in ionized gas [10, 11]. Their work differs from the *Chapman-Enskog* method in the way the Coulombian inverse-square interaction is treated. Indeed, the two-body interaction considered in *Chapman-Enskog* development implicitely applies in a range b much smaller than interparticle distance d. For Coulombian interaction, it is necessary to take into account collisions for which $b > d$, the cut-off distance to consider for b being the Debye length. The two-body collision formula given by Equation I.62 is no longer suited when $b > d$ because the particles interact with many other particles at the same time. These many simultaneous interactions are better described with an isotropization process. This process is well described by the Fokker-Planck expression that interpret collisions as a friction-diffusion process in the velocity space (see Fokker-Planck derivation for collisions in Appendix A.1). In that perspective, *Spitzer & Härm* reformulated *Chapman-Enskog* procedure where they splitted the collision term J into a close encounter contribution that is described by the two-body collision term used so far, and a far encounter contribution described by Fokker-Planck expression

$$\begin{array}{ccc}\textbf{Chapman-Enskog} & & \textbf{Spitzer-Härm} \\ J(ff_\star) & \longrightarrow & J_{b_0}(ff_\star) + K(ff_\star)\end{array} \tag{I.99}$$

where J_{b_0} is given by the same expression as J (Equation I.62) but bounding b to $[0, b_0]$ instead of $\mathbb{R}^+$:

$$J_{b_0}(ff_\star) = \int_{\vec{v}_\star}\int_{\epsilon=0}^{2\pi}\int_{b=0}^{b_0}(f'f'_\star - ff_\star)gbdbd\epsilon d\vec{v}_\star \tag{I.100}$$

Concerning K, it is given by Fokker-Plank expression where average velocity variation are computed for collisions with impact factor greater than b_0:

$$K(ff_\star) = -\sum_i \frac{\partial}{\partial v_i}(f\langle\Delta v_{i,2}\rangle) - \frac{1}{2}\sum_{i,j}\frac{\partial^2}{\partial v_i \partial v_j}(f\langle\Delta v_{i,2}\Delta v_{j,2}\rangle) \tag{I.101}$$

with for any quantity x,

$$\langle x_\star\rangle = \int_{\vec{v}_\star}\int_{\epsilon=0}^{2\pi}\int_{b=b_0}^{\lambda_D} gf_\star x bdbd\epsilon d\vec{v}_\star$$

where λ_D denotes Debye length.

Using such a formulation, *Spitzer & Härm* performed the development given by Equation I.74. This development is, as a consequence, based on the same assumption of high collisionality. The physical ingredient added by *Spitzer & Härm* to take long-range interactions does not change the conclusions of *Chapman-Enskog* development that links heat flux with temperature gradient. Moreover, after numerical integrations of collisional terms, *Spitzer & Härm* obtained the following expression for electron heat flux in ionized plasma:

$$\boxed{\vec{q}_{SH_e} = -3.16\frac{nT_e\tau_e}{m_e}\vec{\nabla}T_e = -3.16\frac{3.5\cdot 10^4}{Z(\ln\Lambda/10)}\frac{T_e^{5/2}}{m_e}\vec{\nabla}T_e} \tag{I.102}$$

and for ions

$$\boxed{\vec{q}_{SH_i} = -3.9\frac{nT_i\tau_i}{m_i}\vec{\nabla}T_i = -3.9\frac{1.5\cdot 10^6}{Z^3(\ln\Lambda/10)}\frac{T_i^{5/2}}{m_p}\vec{\nabla}T_i} \tag{I.103}$$

where $\ln\Lambda$ is the Coulomb logarithm. The numerical expressions are taken from [12] where T must be expressed in eV. The $T^{5/2}$-dependence of heat conductivity with temperature is characteristic of ionized gas. Also, due to the impact of masses, one has $\kappa_e/\kappa_i \approx \sqrt{m_i/m_e} \approx 40$. The work done by *Spitzer-Härm* does not take the effects of magnetic field into account. Thus, relations I.102-I.103 cannot be used to evaluate heat flux in the direction perpendicular to the magnetic field for which particle dynamic is ruled by cyclotronic motion. However, *Spitzer-Härm* relations apply in the direction parallel to the magnetic field, direction for which Lorentz force has no effect. With the same approach, *Spitzer & Härm* obtained a closure expression for plasma conductivity.

The temperature dependence with the parallel heat conductivity can be recovered by doing the following simple dimension analysis. The heat flux being given by $\vec{q}_\parallel = -\kappa\vec{\nabla}_\parallel T$,

energy equation is a diffusion equation yielding

$$\frac{3}{2}k_B\frac{\partial nT}{\partial t} = \frac{\partial}{\partial s}\left(\kappa\frac{\partial T}{\partial s}\right) \tag{I.104}$$

where s denotes the parallel direction coordinate. κ is thus homogeneous to $n \times \lambda^2/\tau$ where λ is the characteristic length of the diffusion process and τ the characteristic time. In our case, τ is given by the collision time τ_c and λ is given by the collision mean free path λ_c (see Equation I.30). Hence,

$$\kappa_{\parallel} = \frac{n\lambda^2}{\tau} \propto \sqrt{\frac{1}{m}}T^{5/2} \tag{I.105}$$

As mentionnend above, this formula is correct when no magnetic field is present. If a strong magnetic field applies, the typical length at which significant gradients occurs is no longer the collision mean free path but the Larmor radius. In this case, the following expression is obtained for perpendicular heat conductivity:

$$\kappa_{\perp} = \frac{n\rho_c^2}{\tau} \propto \sqrt{\frac{1}{m}}\frac{n^2}{B^2\sqrt{T}} \tag{I.106}$$

During the 60's, *S. Braginskii* [12] extended the work done *Spitzer & Härm* and performed a complete closure in presence of both electric and magnetic fields. The expression obtained by *Braginskii* for $\kappa_{\perp}$ is compatible with the above simple derivation. *Braginskii* also obtained a complete expression for the pressure tensor. Besides, since plasma is a multifluid, *Braginskii* closure also contains coupling terms between ions and electrons equations due to collisions among the different species. The expression obtained by Braginskii can be found in the literature [12, 5, 13]. One recalls that once again, the validity of Braginskii's closure is theoretically bounded to high collisional plasma.

I.3 Quasi-linear treatment of the cross-field turbulent transport

This section presents the model that justifies treating turbulent cross-field transport as effective diffusion terms. It is similar to eddy viscosity models in Reynolds Averaged Navier-Stokes (RANS). This approach refered to as *quasi-linear* treatment is commonly applied in transport codes. In particular, it is the one used in SOLEDGE2D (Chapter II).

I.3.1 Rewriting continuity equation

In tokamak plasmas, non-linear interactions give raise to small scale structures constitutive of plasma turbulence. The transport properties are drasticaly modified. In particular, the cross-field transport is strongly enhanced and the plasma confinement is thus highly

controlled by turbulence intensity. This paragraph describes how turbulence can be taken into account in a transport point of view without resolving the instrinsic nature of turbulent structures. This method is often refered as quasi-linear treatment, leading to effective turbulent diffusivities derivation.

Let us start with continuity equation (Equation I.43):

$$\frac{\partial n}{\partial t} + \vec{\nabla} \cdot n\vec{u} = 0 \tag{I.107}$$

The velocity is projected in the direction perpendicular and parallel to the magnetic field. According to the *adiabatic theory* (see Section I.1.1-a)), the velocity decomposes as $\vec{u} = u_{\parallel}\vec{b} + \vec{u}_{\perp}$ where $\vec{u}_{\perp}$ is the drift velocity where only the electric drift is considered (see Equation I.19)

$$\vec{u}_{\perp} = \frac{\vec{E} \times \vec{B}}{B^2} \tag{I.108}$$

The same procedure could be done with the other drift contributions and that simplification does not change the overall results. The electrostatic field is given from the normalized electric potential $\vec{E} = -k_B T_e \vec{\nabla}\phi/e$ and Equation I.107 is rewritten

$$\frac{\partial n}{\partial t} + \vec{\nabla} \cdot (n u_{\parallel}\vec{b}) + \vec{\nabla} \cdot \left(n D_{Bohm} \vec{b} \times \vec{\nabla}\phi \right) = 0 \tag{I.109}$$

with $D_{Bohm} = k_B T_e/(eB)$. The perpendicular convective flux term is developped

$$\begin{aligned} \vec{\nabla} \cdot \left(n D_{Bohm} \vec{b} \times \vec{\nabla}\phi \right) &= \left(\frac{n D_{Bohm}}{B} \vec{\nabla}\phi \right) \cdot (\vec{\nabla} \times \vec{B}) - \vec{B} \cdot \left(\vec{\nabla} \left\{ \frac{n D_{Bohm}}{B} \right\} \times \vec{\nabla}\phi \right) \\ &= \frac{\beta_e}{e} \vec{\nabla}\phi \cdot \vec{j} + D_{Bohm} \vec{B} \cdot \left(\vec{\nabla} \left\{ \frac{\phi}{B} \right\} \times \vec{\nabla} n \right) \end{aligned}$$

where the MHD equilibrium and Maxwell-Gauss equations are used. Curvature effects $\vec{\nabla}B/B \approx \vec{0}$ are neglected, hence in the *low-β limit*, the cross-field transport gives

$$\vec{\nabla} \cdot \left(n D_{Bohm} \vec{b} \times \vec{\nabla}\phi \right) = D_{Bohm} \vec{b} \cdot \left(\vec{\nabla}\phi \times \vec{\nabla} n \right) \tag{I.110}$$

The continuity equation hence reduces to

$$\boxed{\frac{\partial n}{\partial t} + \nabla_{\parallel}(n u_{\parallel}) + D_{Bohm} \{\phi, n\} = -\nu_K (n - n_0)} \tag{I.111}$$

where the Poisson bracket is defined by $\{F, G\} = \vec{b} \cdot \left(\vec{\nabla} F \times \vec{\nabla} G \right)$. A source term is also added in the RHS to drive the system to an equilibrium density n_0. A Krook operator is chosen to do so with a vanishing small frequency ν_K. In absence of convection, the system relaxes exponentially to the equilibrium density with a characteristic decay time $\tau_K = 1/\nu_K$

I.3.2 Multiscale expansion

In order to separate the mean field from the turbulent fluctuations, one resorts to scale separation. In this perspective, the mean field evolution is governed by long time and space scales whereas turbulence is fast and operates on smaller scales. The time variable is then decomposed into two independent variables t_0 and t_1 associated to the long time scale τ_0 and to the fast turbulent time scale τ_1, respectively. One has $t = \tau_0 t_0 + \tau_1 t_1$. The small parameter $\varepsilon_s = \tau_1/\tau_0 \to 0$ defines the scale separation. The time derivative is then expressed as

$$\frac{\partial}{\partial t} = \frac{1}{\tau_0}\left(\frac{\partial}{\partial t_0} + \frac{\tau_0}{\tau_1}\frac{\partial}{\partial t_1}\right) = \frac{1}{\tau_0}\left(\frac{\partial}{\partial t_0} + \frac{1}{\varepsilon_s}\frac{\partial}{\partial t_1}\right) \tag{I.112}$$

The same treatment as for time is performed for parallel space scales. The parallel coordinate s is expressed as $z = L_\parallel(z_0 + \varepsilon_s z_1)$ giving

$$\nabla_\parallel = \frac{1}{L_\parallel}\left(\frac{\partial}{\partial z_0} + \frac{1}{\varepsilon_s}\frac{\partial}{\partial z_1}\right) \tag{I.113}$$

The average operator $\langle\cdot\rangle$ is also defined in such a way that for any field F, $\langle F_1\rangle = 0$ and $\langle F\rangle = F_0$. Besides, the mean field F_0 is supposed to depend only on large spatio-temporal scales (z_0 and t_0) whereas the fluctutating field depends on both large and small scales. As a consequence, for any fast variable x_1, for any field F, the following relation applies:

$$\frac{\partial F_0}{\partial x_1} = 0 \tag{I.114}$$

The small parameter $\varepsilon_f \to 0$ is introduced to govern fluctuations intensity. The density field and electric potential fields are splitted between the mean field and the turbulent field such that $n = n_0 + \varepsilon_f n_1$ and $\phi = \phi_0 + \varepsilon_f \phi_1$. Assuming parallel velocity only varies on large scales $u_\parallel = u_0$, particle balance equation I.111 is developped as:

$$\begin{aligned} -(\nu_K\tau_0)n_1 \;=\; & \frac{\partial n_0}{\partial t_0} + \frac{\varepsilon_f}{\varepsilon_s}\frac{\partial n_1}{\partial t_1} + \varepsilon_f\frac{\partial n_1}{\partial t_0} \\ & + \frac{\tau_0}{L_\parallel}\left(\frac{\partial}{\partial z_0}(n_0u_0) + \frac{\varepsilon_f}{\varepsilon_s}u_0\frac{\partial n_1}{\partial z_1} + \varepsilon_f\frac{\partial}{\partial z_0}(n_1u_0)\right) \\ & + \tau_0 D_{Bohm}\left(\{\phi_0, n_0\} + \varepsilon_f\left[\{\phi_0, n_1\} + \{\phi_1, n_0\}\right] + \varepsilon_f^2\{\phi_1, n_1\}\right) \end{aligned} \tag{I.115}$$

Applying the average operator, the mean field equation for density is obtained.

$$\boxed{\frac{\partial n_0}{\partial t_0} + \frac{\tau_0}{L_\parallel}\frac{\partial}{\partial z_0}(n_0u_0) + \tau_0 D_{Bohm}\left(\{\phi_0, n_0\} + \varepsilon_f^2\Big\langle\{\phi_1, n_1\}\Big\rangle\right) = 0} \tag{I.116}$$

The effect of fluctuations on the mean field equation is given by the correlation term $\langle\{\phi_1, n_1\}\rangle$. The quasi-linear treatment consists in finding an expression for this term that only depends on the mean field variables. Substracting Equation I.116 from Equation I.115 and defining the Krook frequency $\nu_K = \varepsilon_f/\tau_0$ gives the equation for the fluctuating

density

$$\begin{aligned}\frac{\partial n_1}{\partial t_1} &+ \varepsilon_s \frac{\partial n_1}{\partial t_0} + \frac{\tau_0}{L_\parallel}\left(u_0 \frac{\partial n_1}{\partial z_1} + \varepsilon_s \frac{\partial}{\partial z_0}(n_1 u_0)\right) \\ &+ \varepsilon_s \tau_0 D_{Bohm}\left(\{\phi_0, n_1\} + \{\phi_1, n_0\}\right) \\ &+ \varepsilon_f \varepsilon_s \tau_0 D_{Bohm}\left(\{\phi_1, n_1\} - \left\langle \{\phi_1, n_1\} \right\rangle\right) = -\varepsilon_s n_1 \end{aligned} \tag{I.117}$$

I.3.3 Expression for the Poisson bracket

Let us assume the magnetic field is mostly toroidal, giving $\vec{b} \approx R_0 \vec{\nabla}\varphi$. In the (φ, θ, ψ) coordinates system, the Poisson bracket is given by:

$$\begin{aligned}\{F, G\} &= \vec{b} \cdot \left(\vec{\nabla} F \times \vec{\nabla} G\right) \\ &= R_0 \vec{\nabla}\varphi \cdot \left(\left[\frac{\partial F}{\partial \psi}\vec{\nabla}\psi + \frac{\partial F}{\partial \theta}\vec{\nabla}\theta + \frac{\partial F}{\partial \varphi}\vec{\nabla}\varphi\right] \times \left[\frac{\partial G}{\partial \psi}\vec{\nabla}\psi + \frac{\partial G}{\partial \theta}\vec{\nabla}\theta + \frac{\partial G}{\partial \varphi}\vec{\nabla}\varphi\right]\right) \\ &= R_0 \vec{\nabla}\varphi \cdot \left(\frac{\partial F}{\partial \psi}\frac{\partial G}{\partial \theta}\vec{\nabla}\psi \times \vec{\nabla}\theta + \frac{\partial F}{\partial \theta}\frac{\partial G}{\partial \psi}\vec{\nabla}\theta \times \vec{\nabla}\psi\right) \\ &= R_0 J \left(\frac{\partial F}{\partial \psi}\frac{\partial G}{\partial \theta} - \frac{\partial F}{\partial \theta}\frac{\partial G}{\partial \psi}\right)\end{aligned}$$

where J denotes the Jacobian $J = \vec{\nabla}\varphi \cdot (\vec{\nabla}\psi \times \vec{\nabla}\theta)$. The final expression for Poisson bracket can also be expressed as

$$\{F, G\} = R_0 J \left(\frac{\partial}{\partial \psi}\left(F \frac{\partial G}{\partial \theta}\right) - \frac{\partial}{\partial \theta}\left(F \frac{\partial G}{\partial \psi}\right)\right) \tag{I.118}$$

Once again, the scale separation gives $\psi = \psi_0 + \varepsilon_s \psi_1$ and $\theta = \theta_0 + \varepsilon_s \theta_1$. Reporting in the Poisson bracket expression,

$$\{F, G\} = \{F, G\}_{0,0} + \frac{1}{\varepsilon_s}\left(\{F, G\}_{1,0} + \{F, G\}_{0,1}\right) + \frac{1}{\varepsilon_s^2}\{F, G\}_{1,1} \tag{I.119}$$

where one has introduced

$$\{F, G\}_{i,j} = R_0 J \left(\frac{\partial}{\partial \psi_i}\left(F \frac{\partial G}{\partial \theta_j}\right) - \frac{\partial}{\partial \theta_j}\left(F \frac{\partial G}{\partial \psi_j}\right)\right) \tag{I.120}$$

Re-injecting expression for Poisson bracket I.120 into mean field equation I.116, the Equation for average density becomes:

$$\begin{aligned}&\frac{\partial n_0}{\partial t_0} + \frac{\tau_0}{L_\parallel}\frac{\partial}{\partial z_0}(n_0 u_0) + v_\perp^\star \{\phi_0, n_0\}_{0,0} + \ldots \\ &\quad v_\perp^\star \frac{\varepsilon_f^2}{\varepsilon_s^2}\left(\left\langle \{\phi_1, n_1\}_{1,1} \right\rangle + \varepsilon_s \left(\left\langle \{\phi_1, n_1\}_{1,0} \right\rangle + \left\langle \{\phi_1, n_1\}_{0,1} \right\rangle\right) + \varepsilon_s^2 \left\langle \{\phi_1, n_1\}_{0,0} \right\rangle\right) = 0\end{aligned} \tag{I.121}$$

with $v_\perp^\star = \tau_0 D_{Bohm} R_0 J$. In order to take fluctuations into account in mean field equation:

- the first term to consider in Equation I.121 is $\langle\{\phi_1, n_1\}_{1,1}\rangle$. This term cancels out due to periodicity and vanishing properties of fluctuating fields [3]
- the second term ($\langle\{\phi_1, n_1\}_{1,0}\rangle + \langle\{\phi_1, n_1\}_{0,1}\rangle$) is the one considered in the quasilinear study. This term expresses as

$$\begin{aligned}\Big\langle\{\phi_1, n_1\}_{1,0}\rangle + \langle\{\phi_1, n_1\}_{0,1}\Big\rangle &= -\left\langle\frac{\partial}{\partial\theta_0}\left(\phi_1\frac{\partial n_1}{\partial\psi_1}\right)\right\rangle + \left\langle\frac{\partial}{\partial\psi_0}\left(\phi_1\frac{\partial n_1}{\partial\theta_1}\right)\right\rangle \\ &= \frac{\partial}{\partial\theta_0}\left\langle n_1\frac{\partial\phi_1}{\partial\psi_1}\right\rangle - \frac{\partial}{\partial\psi_0}\left\langle n_1\frac{\partial\phi_1}{\partial\theta_1}\right\rangle \end{aligned} \tag{I.122}$$

  In particular, $\langle n_1\partial_{\theta_1}\phi_1\rangle$ and $\langle n_1\partial_{\psi_1}\phi_1\rangle$ have to be evaluated.

- the third term is neglected

At leading order (using $\varepsilon_f/\varepsilon_s \to 0$ that is to say small fluctuations for a large scale separation) the following equation for the fluctuations is obtained:

$$\frac{\partial n_1}{\partial t_1} + \frac{\tau_0 u_0}{L_\parallel}\frac{\partial n_1}{\partial z_1} + v_\perp^\star\Big(\{\phi_0, n_1\}_{0,1} + \{\phi_1, n_0\}_{0,1}\Big) + v_\perp^\star\Big(\{\phi_0, n_1\}_{1,0} + \{\phi_1, n_0\}_{0,1}\Big) = -\varepsilon_s n_1 \tag{I.123}$$

Before reporting the expression for ($\langle\{\phi_1, n_1\}_{1,0}\rangle + \langle\{\phi_1, n_1\}_{0,1}\rangle$) in the mean field equation, Equation I.123 must be solved to get an estimation for n_1 and ϕ.

I.3.4 Fourier resolution of coupled mean-field/fluctuations equations

Using $\partial_{\theta_1} F_0 = 0$ and $\partial_{\psi_1} F_0 = 0$, Equation I.123 can be rewritten

$$\frac{\partial n_1}{\partial t_1} + v_\parallel^\star\frac{\partial n_1}{\partial z_1} + v_\perp^\star\left(\frac{\partial\phi_0}{\partial\psi_0}\frac{\partial}{\partial\theta_1} - \frac{\partial\phi_0}{\partial\theta_0}\frac{\partial}{\partial\psi_1}\right)n_1 - v_\perp^\star\left(\frac{\partial n_0}{\partial\psi_0}\frac{\partial}{\partial\theta_1} - \frac{\partial n_0}{\partial\theta_0}\frac{\partial}{\partial\psi_1}\right)\phi_1 + \varepsilon_s n_1 = 0 \tag{I.124}$$

where $v_\parallel^\star$ denotes the dimensionless velocity $v_\parallel^\star = \tau_0 u_0/L_\parallel$. Let us perform the Fourier transform over the fast variables t_1, z_1, θ_1 and ψ_1. For any function f

$$f\left(\begin{array}{c} t_0, z_0, \psi_0, \theta_0, \\ t_1, z_1, \psi_1, \theta_1 \end{array}\right) = \sum_{k_\theta=-\infty}^{+\infty}\int d\omega\int dk_\parallel\int dk_\psi\, e^{i(k_\parallel z_1 + k_\psi\psi_1 + k_\theta\theta_1 - \omega t_1)}\hat{f}_{\omega,k_\parallel,k_\psi,k_\theta}(t_0, z_0, \theta_0, \psi_0) \tag{I.125}$$

[3] More precisely, $\langle\partial_{\theta_1} X\rangle = 0$ and $\langle\partial_{\psi_1} X\rangle = 0$. The average operator is an integral over the fast variables. Applying Green formula to the following expression leads to evaluate the function X on the boundary of the fast variable domain. Due to periodicity or vanishing properties, these terms always cancel out.

The linear Equation I.124 can then be expressed as

$$\left(-i\omega + ik_\parallel v_\parallel^\star + iv_\perp^\star\left(k_\theta\frac{\partial\phi_0}{\partial\psi_0} - k_\psi\frac{\partial\phi_0}{\partial\theta_0}\right) + \varepsilon_s\right)\hat{n}_1 - iv_\perp^\star\left(k_\theta\frac{\partial n_0}{\partial\psi_0} - k_\psi\frac{\partial n_0}{\partial\theta_0}\right)\hat{\phi}_1 = 0 \tag{I.126}$$

Defining $k_\perp = k_\theta\frac{\partial\phi_0}{\partial\psi_0} - k_\psi\frac{\partial\phi_0}{\partial\theta_0}$, one has $\hat{n}_1 = \mathcal{R}\cdot\hat{\phi}_1$ with

$$\begin{aligned}\mathcal{R} &= -\frac{k_\perp v_\perp^\star}{\omega - k_\parallel v_\parallel^\star - k_\perp v_\perp^\star + i\varepsilon_s}\left(\frac{k_\theta}{k_\perp}\frac{\partial n_0}{\partial\psi_0} - \frac{k_\psi}{k_\perp}\frac{\partial n_0}{\partial\theta_0}\right)\\ &= -k_\perp v_\perp^\star\frac{\omega - k_\parallel v_\parallel^\star - k_\perp v_\perp^\star - i\varepsilon_s}{\left(\omega - k_\parallel v_\parallel^\star - k_\perp v_\perp^\star\right)^2 + (\varepsilon_s)^2}\left(\frac{k_\theta}{k_\perp}\frac{\partial n_0}{\partial\psi_0} - \frac{k_\psi}{k_\perp}\frac{\partial n_0}{\partial\theta_0}\right)\end{aligned} \tag{I.127}$$

I.3.5 Determining quasilinear particle flux

Reporting Equation I.122 into the mean field continuity Equation I.121 gives

$$\frac{\partial n_0}{\partial t_0} + \frac{\tau_0}{L_\parallel}\frac{\partial}{\partial z_0}(n_0u_0) + v_\perp^\star\{\phi_0, n_0\}_{0,0} + \frac{\varepsilon_f^2}{\varepsilon_s}v_\perp^\star\left(\frac{\partial}{\partial\theta_0}\left\langle n_1\frac{\partial\phi_1}{\partial\psi_1}\right\rangle - \frac{\partial}{\partial\psi_0}\left\langle n_1\frac{\partial\phi_1}{\partial\theta_1}\right\rangle\right) = 0 \tag{I.128}$$

The quasilinear fluxes are defined as

$$\mathcal{G}_\theta = \left\langle n_1\frac{\partial\phi_1}{\partial\psi_1}\right\rangle \qquad \text{and} \qquad \mathcal{G}_\psi = -\left\langle n_1\frac{\partial\phi_1}{\partial\theta_1}\right\rangle \tag{I.129}$$

Using Fourier transform of n_1 and ϕ_1,

$$\begin{aligned}n_1\frac{\partial\phi_1}{\partial\psi_1} = &\sum_{k'_\theta=-\infty}^{+\infty}\int d\omega'\int dk'_\parallel\int dk'_\psi\sum_{k''_\theta=-\infty}^{+\infty}\int d\omega''\int dk''_\parallel\int dk''_\psi\\ &\ldots e^{i\left(-(\omega'+\omega'')t_1+(k'_\parallel+k''_\parallel)z_1+(k'_\psi+k''_\psi)\psi_1+(k'_\theta+k''_\theta)\theta_1\right)}ik''_\psi\hat{n}_{1_{\omega',k'_\parallel,k'_\psi,k'_\theta}}\hat{\phi}_{1_{\omega'',k''_\parallel,k''_\psi,k''_\theta}}\end{aligned}$$

Averaging over the fast variables t_1, z_1, θ_1 and ψ_1 contained in the exponential term leads to a product the Dirac terms $\delta(\omega'+\omega'')$, $\delta(k'_\parallel+k''_\parallel)$, $\delta(k'_\theta+k''_\theta)$ and $\delta(k'_\psi+k''_\psi)$. Finally, the quasilinear fluxes reduce to

$$\left\langle n_1\frac{\partial\phi_1}{\partial\psi_1}\right\rangle = \sum_{k_\theta=-\infty}^{+\infty}\int d\omega\int dk_\parallel\int dk_\psi\ (-ik_\psi)\hat{n}_{1_{\omega,k_\parallel,k_\psi,k_\theta}}\hat{\phi}^*_{1_{\omega,k_\parallel,k_\psi,k_\theta}} \tag{I.130}$$

where z^* denotes the complex conjugate of z. The relation $\hat{\phi}^*_{1_{\omega,k_\parallel,k_\psi,k_\theta}} = \hat{\phi}_{1_{-\omega,-k_\parallel,-k_\psi,-k_\theta}}$ holds since ϕ_1 is a real field. Likewise,

$$\left\langle n_1\frac{\partial\phi_1}{\partial\theta_1}\right\rangle = \sum_{k_\theta=-\infty}^{+\infty}\int d\omega\int dk_\parallel\int dk_\psi\ (-ik_\theta)\hat{n}_{1_{\omega,k_\parallel,k_\psi,k_\theta}}\hat{\phi}^*_{1_{\omega,k_\parallel,k_\psi,k_\theta}} \tag{I.131}$$

Using $\hat{n}_1 = \mathcal{R} \cdot \hat{\phi}_1$ and $\hat{\phi}_1 \hat{\phi}_1^* = |\hat{\phi}_1|^2$, one finds

$$\mathcal{G}_\theta = \sum_{k_\theta=-\infty}^{+\infty} \int d\omega \int dk_\parallel \int dk_\psi \; (-ik_\psi \mathcal{R}) |\hat{\phi}_1|^2$$

$$\mathcal{G}_\psi = \sum_{k_\theta=-\infty}^{+\infty} \int d\omega \int dk_\parallel \int dk_\psi \; (ik_\theta \mathcal{R}) |\hat{\phi}_1|^2$$

Reporting Equation I.127 for $\mathcal{R}$, a diffusive expression is obtained for the turbulent fluxes:

$$\mathcal{G}_\theta = -\left(\mathcal{D}_{\theta,\psi} \frac{\partial n_0}{\partial \psi_0} + \mathcal{D}_{\theta,\theta} \frac{\partial n_0}{\partial \theta_0} \right) \tag{I.132}$$

$$\mathcal{G}_\psi = -\left(\mathcal{D}_{\psi,\psi} \frac{\partial n_0}{\partial \psi_0} + \mathcal{D}_{\psi,\theta} \frac{\partial n_0}{\partial \psi_0} \right) \tag{I.133}$$

with

$$\mathcal{D}_{i,j} = \epsilon_{ij} \sum_{k_\theta=-\infty}^{+\infty} \int d\omega \int dk_\parallel \int dk_\psi \; v_\perp^\star k_i k_j |\hat{\phi}_1|^2 \frac{i(\omega - k_\parallel v_\parallel^\star - k_\perp v_\perp^\star) + \varepsilon_s}{\left(\omega - k_\parallel v_\parallel^\star - k_\perp v_\perp^\star\right)^2 + (\varepsilon_s)^2} \tag{I.134}$$

where $\epsilon_{ij} = 1$ if $i = j$, -1 otherwise. In any case, the diffusion coefficients take the form

$$\mathcal{D}_{i,j} = \int dX |\hat{\phi}_1|^2 \frac{iX + \varepsilon_s}{X^2 + \varepsilon_s^2}$$

Since the diffusion coefficient are real, the odd part of the integral vanishes giving

$$\mathcal{D}_{i,j} = \int dX |\hat{\phi}_1|^2 \frac{\varepsilon_s}{X^2 + \varepsilon_s^2} \xrightarrow[\varepsilon_s \to 0]{} \int dX |\hat{\phi}_1|^2 \pi \delta(X)$$

Using the fact that $f_\epsilon(x) = \frac{1}{\pi} \frac{\epsilon}{x^2 + \epsilon^2}$ tends to the Dirac distribution for $\epsilon \to 0$. Finally, the diffusion coefficient are given by

$$\boxed{\mathcal{D}_{i,j} = \epsilon_{ij} \sum_{k_\theta=-\infty}^{+\infty} \int d\omega \int dk_\parallel \int dk_\psi \; v_\perp^\star k_i k_j |\hat{\phi}_1|^2 \pi \delta(\omega - \omega_r)} \tag{I.135}$$

where the resonance frequency is determined by $\omega_r = k_\parallel v_\parallel^\star + k_\perp v_\perp^\star$.

The quasilinear approach leads to a diffusive expression for the tubulent transport. In particular, once the above turbulent effective diffusivities computed, the continuity

equation becomes

$$\frac{\partial n_0}{\partial t_0} + \frac{\tau_0}{L_\parallel}\frac{\partial}{\partial z_0}(n_0 u_0) + v_\perp^\star \Big\{\phi_0, n_0\Big\}_{0,0} = \frac{\varepsilon_f^2}{\varepsilon_s} v_\perp^\star \frac{\partial}{\partial \theta_0}\left(\mathcal{D}_{\theta,\psi}\frac{\partial n}{\partial \psi} + \mathcal{D}_{\theta,\theta}\frac{\partial n}{\partial \theta}\right) + \frac{\varepsilon_f^2}{\varepsilon_s} v_\perp^\star \frac{\partial}{\partial \psi_0}\left(\mathcal{D}_{\psi,\psi}\frac{\partial n_0}{\partial \psi_0} + \mathcal{D}_{\psi,\theta}\frac{\partial n_0}{\partial \theta_0}\right)$$

This equation can be written in a more compact form. The index 0 are removed for writing convenience since only mean field variables are considered.

$$\boxed{\frac{\partial n}{\partial t} + \vec{\nabla}\cdot(n u_\parallel \vec{b}) + D_{Bohm} R_0 J\Big\{\phi, n\Big\} = \vec{\nabla}\cdot\left(\mathcal{D}\cdot\vec{\nabla}_\perp n\right)} \tag{I.136}$$

where

$$\mathcal{D} = \frac{\varepsilon_f^2}{\varepsilon_s} D_{Bohm} J R_0 \begin{pmatrix} \mathcal{D}_{\theta,\theta} & \mathcal{D}_{\theta,\psi} \\ \mathcal{D}_{\psi,\theta} & \mathcal{D}_{\psi,\psi} \end{pmatrix} \quad \text{and} \quad \vec{\nabla}_\perp = \begin{pmatrix} \frac{\partial}{\partial \theta} \\ \frac{\partial}{\partial \psi} \end{pmatrix} \tag{I.137}$$

I.4 Scale separation and diffusion

In this chapter, it has been emphasized that under some conditions, transport can be taken into account through a diffusive process. The first case has been encountered in section I.2.4 where the transport of velocity and energy due to collisions has been recast in the form of two diffusive laws: the viscous stress and the Fourier's law. However, a special attention must be paid to point that these formulations have been obtained in the high collisonal limit where a strong ordering is assumed between the scale that characterizes collisions and the system size or gradient scale. The second case hase been addressed in section I.3 where it has been proven that the cross-field turbulent transport can also be described by a diffusion process. Once again, this diffusive formulation derived from the quasilinear treatment assumes a scale separation between a small scale associated with the turbulent structures and the mean field gradient scales that are assumed to be much longer.

The two phenomenons mentionned above are based on the same kind of physical system: a stochastic behavior at small scales (collisions in the first case, turbulent microstructures for the second case) and a mean field characterized by smooth and slow fluctuations on longer scales. These systems can be modeled in a synthetic forms by the Kramers-Moyal formalism [14]. Let us consider that $P(x,t)$ characterizes the probability distribution function of the quantity of interest (particles density, energy...). The microscopic stochastic process can be described by a Markov process where the probability of transition from the position x to the position x' is given by the kernel $K(x \to x')$. The

master equation giving the evolution of $P(x,t)$ is given by

$$\begin{aligned} dP(x,t) &= \left\{\begin{array}{l}\text{Probability to arrive in } x\\ \text{from } x' \text{ positions during}\\ \text{the time interval } dt\end{array}\right\} - \left\{\begin{array}{l}\text{Probability to leave } x\\ \text{to } x' \text{ positions during}\\ \text{the time interval } dt\end{array}\right\} \\ &= \int_{-\infty}^{\infty} dx' K(x' \to x) dt P(x',t) - \int_{-\infty}^{\infty} dx' K(x \to x') dt P(x,t) \end{aligned}$$

giving the master equation

$$\boxed{\frac{\partial P}{\partial t}(x,t) = \int_{-\infty}^{\infty} dx' K(x' \to x) P(x',t) - \int_{-\infty}^{\infty} dx' K(x \to x') P(x,t)} \tag{I.138}$$

At this stage, the assumption of scale separation is made. In that sense, the microscopic stochastic process is supposed to be characterized by a small scale compared to the gradient scale of the field $P(x,t)$. The scale of the microscopic process is the decay length of the kernel $K(x \to x')$. Let us suppose here that this scale can be defined; this assumption is discussed in next paragraph. The major consequence of the scale separation is that a Taylor expansion can be performed about x so as to express the first term in Equation I.138-RHS:

$$P(x',t) = P(x,t) + (x'-x)\frac{\partial P}{\partial x}(x,t) + \frac{1}{2}(x'-x)^2 \frac{\partial^2 P}{\partial x^2}(x,t) \tag{I.139}$$

Assuming Kernel symmetry, that is $K(x \to x') = K(x' \to x) \equiv K(x' \leftrightarrow x)$ traducing that the miscroscopic motion has no prefered direction, reporting Equation I.139 into Equation I.138 gives

$$\frac{\partial P}{\partial t}(x,t) = \frac{\partial P}{\partial x}(x,t) \int_{-\infty}^{\infty} dx' K(x' \leftrightarrow x)(x'-x) - \frac{\partial^2 P}{\partial x^2}(x,t)\frac{1}{2}\int_{-\infty}^{\infty} dx' K(x' \leftrightarrow x)(x'-x)^2 \tag{I.140}$$

Due to symmetry the first term vanishes giving the expected diffusive behavior for P

$$\boxed{\frac{\partial P}{\partial t}(x,t) = D\frac{\partial^2 P}{\partial x^2}(x,t)} \quad \text{with} \quad \boxed{D = \frac{1}{2}\int_{-\infty}^{\infty} dx' K(x' \leftrightarrow x)(x'-x)^2} \tag{I.141}$$

The diffusion coefficient is given by the spatial correlation characterizing to the microscopic process. Another formulation can link the diffusion coefficient with temporal correlation leading to the Green-Kubo relations [15].

Another limit relies in the convergence of the integral given in Equation I.141. Indeed, if the microscopic kernel decay is not strong enough, the above mentionned expression for the diffusion coefficient tends to infinite values. If this kernel is exponential, the integral converges and the diffusive formulation is relevant; conversely, if the kernel is Lorentzian, the integral diverges and no diffusion formulation can be used. The transport in this case can be described by super-diffusion processes that have been well studied in the literature

[16]. The underlying microscopic process is described by Levi flights where the "long range jumps" characterized by the tail of the transition distribution ensure most of the tranport. Even if the probability of transition decays with the distance covered during a jump, the decay is not strong enough and the average length of a jump is infinite. One fails in particular to define a finite mean free path for this process.

To go further, let us consider the results from statistical mechanics about the description of transport for weak departure from equilibrium. This study is based on the description of the irreversible evolution of a system driven out of thermodynamic equilibrium. A synthetic description of this study is done by Jean-Marcel Rax in [17, Chapter 11]. In the hydrodynamic regime, a distinction can be made between transport time scales in the physical space and kinetic relaxation time scales in the velocity space that are supposed to be much faster. Under this scale separation assumption, the fluxes are linked to thermodynamic forces – this theory is attributed to Lars Onsager [18] and is sometimes refered to as "4th principle of thermodynamic". For instance, a plasma is made of a mixture of species described by its electric potential ϕ, chemical potential μ, pressure p and temperature T. At equilibrium, these variables are uniform and fluxes are zero. If the system is slightly out of equilibrium, the fluxes express as a linear combination of the latter intensive quantities gradients called thermodynamic forces. If one denotes $\vec{q}$ the heat flux, $\vec{\Gamma}$ the major species mass flux, $\vec{J}$ the electric current and $\vec{\gamma}$ the impurity (minor species) mass flux, the flux are linked to the forces according to table I.1. The kinetic theory aims at expressing the different diffusivities as functions of plasma

	$\vec{\nabla}T$	$\vec{\nabla}P$	$\vec{\nabla}\phi$	$\vec{\nabla}\mu$
$\vec{q}$	Fourier's law	Joule-Thomson effect	Peltier effect	Dufour effect
$\vec{\Gamma}$	Thermo-osmosis	Darcy's law	Electro-osmosis	Osmosis
$\vec{J}$	Seebeck effect	Flow current	Ohm's law	Electrodiffusion
$\vec{\gamma}$	Soret effect	Reverse-osmosis	Electrophoresis	Fick's law

Table I.1: Onsager relations between fluxes and thermodynamic forces for slightly out of equilibrium systems

parameters. The study consists in considering the kinetic equation in the velocity space assuming hydrodynamic gradients in the physical space. Several methods exists such as linear developments, perturbative treatments, spectral methods, etc... some of them have been detailed in the above paragraphs. For plasma theory, three kinds of development must been emphasized:

- Braginskii (classical) theory where the microscopic motion is described by Coulombian "collisions" and where the magnetic field is considered homogeneous (see Section I.2.4),

- neo-classical theory where microscopic motion relies in particles orbits in inhomogeneous magnetic field. This transport is not treated in this manuscript,

- turbulent transport theory where the microscopic motion consist in turbulent micro-structures due to electric and magnetic field fluctuations (see Section I.3).

As a conclusion to this study, it has been proven that under the assumption of a scale separation between the stochastic process and the mean field fluctuations, the transport can be described with a coarse-grained diffusive law. The diffusive description fails if the stochastic process mean free path is longer than mean field gradient length. The cases where the mean free path is infinite such as in the Levi flight process are thus obviously not diffusive. Nevertheless, even if the correlation expression for diffusion converges (Equation I.141), one must ensure that the mean free path of the underlying stochastic process is smaller than gradient length to apply a diffusive treatment. Chapter II focuses on this case where the microscopic process exhibits a finite mean free path but where the latter is longer than system gradient scales. One is thus interested into recasting the closure work performed in this chapter to obtain a non-diffusive closure for weakly collisional systems.

I.5 Plasma-wall interaction - Bohm boundary conditions

When the plasma interacts with a solid, recombination processes occur. In that perspective, the solid acts as a sink for the plasma. This sink produces plasma flows. Most of the ions and electrons that recombine on the wall will latter be reinjected into the plasma as neutrals. The mass balance between the outflux of ions and electrons and the influx of neutrals is often refered to as plasma "recycling". However, the recycling process is not instantaneous and a detailed study of traping-detraping of particles coming from the plasma into the solid has to be done [19].

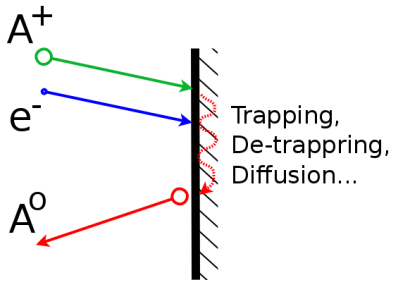

Figure I.8: The recycling mechanism. Ions and electrons impacting the wall can recombine, be trapped and diffuse in the solid. They can further be re-emitted in the plasma volume as atoms or molecultes.

Due to the difference of mobility between heavy ions and light electrons, the two species are not interacting in the same manner with the solid. The solid hence breaks the

quasineutrality and a net plasma charge is observed in a thin layer surrounding the solid called "plasma sheath". The typical thickness of the sheath is given by the Debye length λ_D. Due to the higher mobility of electrons, the solid charges negatively. The plasma sheath is thus charged positively to shield the quasineutral plasma from the negative wall. If basic features of the sheath were given by I. Langmuir in 1929 [20], it is 20 years later that D. Bohm managed to provide an explicit formulation and clear interpretation of the sheath physics [21]. K.U. Riemann also provides an interesting review on the sheath mechanisms [22].

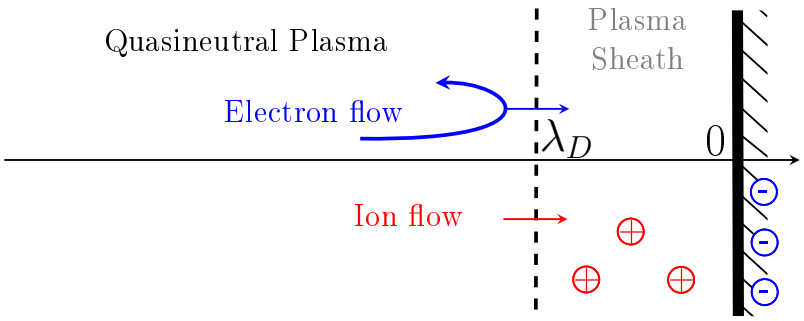

Figure I.9: Scheme of the near wall plasma region. Definition of sheath near solid surface.

The plasma geometry near the wall is represented on Figure I.9. Since the Debye length is much smaller than the collision mean free path, the sheath can be regarded as collisionless. As mentionned in the above paragraph, due to high mobility of electrons, the wall is usually charged negatively. Hence, most of the electrons are repelled from the wall surface. This does not mean that no electrons reach the wall. Besides, in order to ensure quasineutrality at steady state, there must be as many ions as electrons leaving the quasineutral plasma, hence as many ions as electrons entering the sheath. The electron distribution is supposed to be weakly modified by wall losses.

Let us derive so-called Bohm criterion in the case of cold ion plasma, i.e. $T_i \ll T_e$. This development can be found in [6, Chapter 2]. ϕ denotes the electrostatic potential, ϕ_{se} being the value of electrostatic potential at sheath entrance. Figure I.10 represents the electrostatic potential of a shielded negatively charged surface.

The fluid description is supposed to apply for electrons and that their inertia can be neglected. In this case, Equation I.46 provides the following relation between electron density and electrostatic potential

$$\nabla_{\parallel} p_e = -n_e e E_{\parallel} \tag{I.142}$$

$$k_B \nabla_{\parallel} n_e T_e = n_e e \nabla_{\parallel} \phi \tag{I.143}$$

$$\tag{I.144}$$

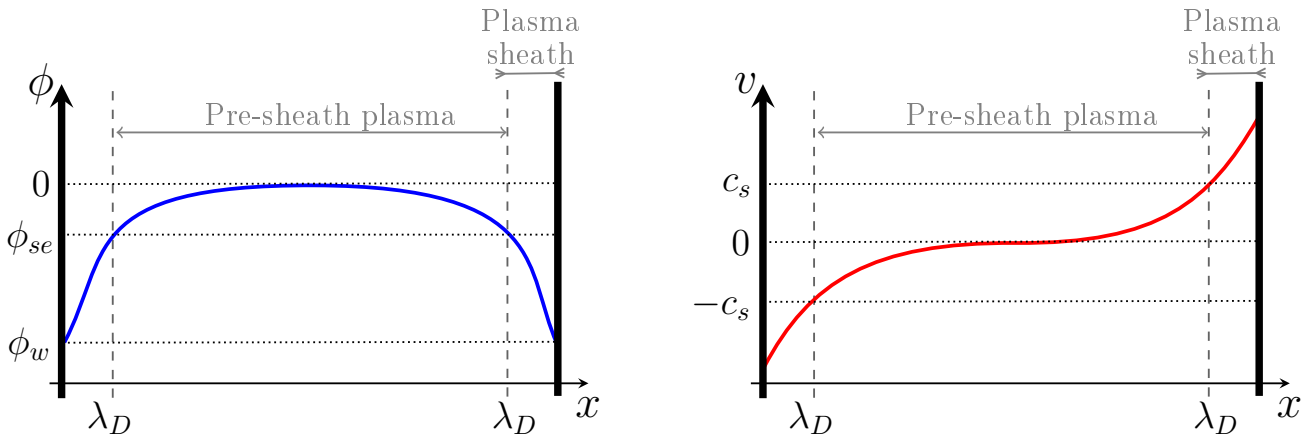

Figure I.10: Electric potential and velocity in the Scrape-off layer plasma

giving the so-called Boltzmann relation:

$$\boxed{n_e = n_{e_0} \exp\left(\frac{e(\phi - \phi_0)}{k_B T_e}\right)} \tag{I.145}$$

The reference potential is $\phi = 0$ where the ion source is located far upstream from the wall. The ions are accelerated due to the potential difference between the upstream point and the sheath entrance. Assuming $T_i = 0$ and that the acceleration is collisionless, conservation of ion energy gives

$$\frac{1}{2} m_i v^2 = -e\phi \tag{I.146}$$

Besides, the ion particle flux is constant since there is no ion source between the upstream position and the wall.

$$n_i v = \text{const.} = n_{se}\sqrt{\frac{\phi_{se}}{\phi}} \tag{I.147}$$

In the quasineutral plasma, one has $n_e = n_i$ whereas in the sheath, the relation between electron and ion density is given by Maxwell-Gauss equation

$$\vec{\nabla} \cdot \vec{E} = \frac{\rho}{\varepsilon_0} \tag{I.148}$$

that can be expressed as Poisson's Equation

$$\frac{d^2\phi}{dx^2} = -\frac{q}{\varepsilon_0}(n_i - n_e) \tag{I.149}$$

Reporting Equation I.145 and I.147,

$$\frac{d^2\phi}{dx^2} = -\frac{q}{\varepsilon_0}\left[\sqrt{\frac{\phi_{se}}{\phi}} - \exp\left(\frac{e(\phi - \phi_{se})}{k_B T_e}\right)\right] \tag{I.150}$$

Denoting $\Delta = \phi_{se} - \phi > 0$, we may expand

$$\sqrt{\frac{\phi_{se}}{\phi}} \approx 1 + \frac{1}{2}\frac{\Delta}{\phi_{se}} = 1 - \frac{1}{2}\frac{\Delta}{|\psi_{se}|}$$
$$\exp\left(\frac{\phi - \phi_{se}}{k_B T_e}\right) \approx 1 - \frac{e\Delta}{k_B T_e}$$

giving

$$\frac{d^2\Delta}{dx^2} \approx \frac{e n_{se}\Delta}{\varepsilon_0}\left(\frac{e}{k_B T_e} - \frac{1}{2|\phi_{se}|}\right) \tag{I.151}$$

This equation admits non-oscillatory solutions only if

$$\frac{e}{k_B T_e} - \frac{1}{2|\phi_{se}|} \geq 0$$

Reporting in Equation I.146, *Bohm criterion* for ions velocity at sheath entrance is obtained:

$$\boxed{v_{se} \geq c_s} \qquad \text{with} \qquad c_s = \sqrt{\frac{k_B T_e}{m_i}} \tag{I.152}$$

where c_s denotes the sound speed (speed of electro-acoustic waves). This result can be generalized for hot plasmas where $T_i \approx T_e$. In this case, the expression for sound speed is given by

$$\boxed{c_s = \sqrt{\frac{k_B(T_e + \gamma T_i)}{m_i}}} \tag{I.153}$$

where γ is a polytropic index. In particular, $\gamma = 1$ if the plasma is isothermal and $\gamma = 5/3$ if the plasma is adiabatic with isotropic pressure.

A comparison can been made between the sheath entrance and the fluid expansion into vacuum. In both cases, the presence of a strong sink drives a sonic or supersonic flow at the boundary [23]. The acceleration of the ions to the sound speed at sheath entrance is due to the difference of electrostatic potential between the stagnation plane where the ion source is located ($\phi = 0$) and the sheath entrance ($\phi = \phi_{se}$). The region where the acceleration takes place is often refered to as "pre-sheath" region.

From this analysis of sheath properties, the plasma outflux at sheath entrance is deduced:

$$\Gamma_{se} = n v_{se} \geq n c_s \approx n\sqrt{\frac{k_B(T_e + T_i)}{m_i}} \tag{I.154}$$

If the particle outflux is known, the energy outflux has still to be determined. Since the sheath is collisionless, the outgoing heat flux is necessarily convective and thus expresses as

$$\boxed{q_e = \gamma_e k_B n_e T_e \Gamma_{se}} \qquad \text{and} \qquad \boxed{q_i = \gamma_i k_B n_i T_i \Gamma_{se}} \tag{I.155}$$

where γ_e and γ_i are called sheath transmission coefficients. A kinetic approach must be

used to determined these transmission coefficients. Several formulation can be found in the literature. The following expressions can be found in [6, Chapter 25].

$$\gamma_i \approx 2.5\frac{T_i}{T_e} - \sim 0.5 \tag{I.156}$$

and

$$\gamma_e \approx \frac{2}{1-\delta_e} - 0.5\ln\left[\left(2\pi\frac{m_e}{m_i}\right)\left(1+\frac{T_i}{T_e}\right)(1-\delta_e)^{-2}\right] + \sim 0.5 \tag{I.157}$$

where δ_e is the secondary electron coefficient. On Figure I.11 are represented the values of γ as a function of T_i/T_e. For simplicity, the following value are considered in this

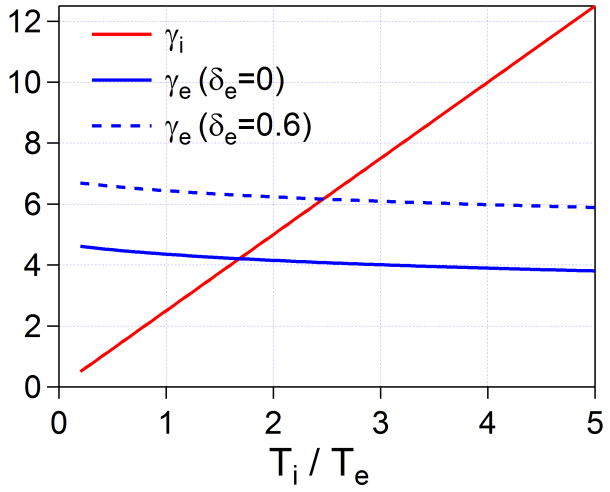

Figure I.11: Sheath transmission coefficients for Hydrogen plasma as a function of $\tau = T_i/T_e$ and secondary electron emission coefficients.

manuscript.

$$\boxed{\gamma_i = 2.5} \quad \text{and} \quad \boxed{\gamma_e = 4.5} \tag{I.158}$$

Chapter highlights

- *Three fluid equations for density, momentum and total energy are derived from the Boltzmann equation.*
- *Assuming high collisionality, closure relations are obtained for pressure tensor and heat flux. These closure expressions take the form of diffusive terms such as Fourier law where the heat conductivity is given by Spitzer-Härm relation:*

$$\vec{q} = -\kappa_0 T^{5/2} \vec{\nabla} T$$

- *Applying scale separation assumption, the turbulent transport can also be expressed by effective diffusive relations.*
- *Bohm boundary conditions model the interaction between the plasma and the solid. In particular, it states that plasma flow can be sonic or supersonic at sheath entrance.*

$$|M_{se}| \geq 1$$

Chapter II

Edge plasma simulations with the fluid code SolEdge2D

Content

The edge transport code SolEdge2D developed during this thesis is introduced. The considered fluid equations is firts presented including conservation equations for n, v, T together with appropriate boundary conditions. The multidomain algorithm incorporating the penalization technique used to model plasma-wall interactions is also presented. Finally, some illustrative simulations in cylindrical and X-point configuration are examplified.

II.1 Motivations for SolEdge2D development

Motivations are various and concern the understanding of physical mechanisms governing transport at the edge, the prediction of particles and heat fluxes at the walls for tokamak operations as well as the development of a test bed tool to develop original numerical methods on the road of developing 3D turbulent fluid code (ANR-ESPOIR). For instance, the understanding of H-mode transport barrier that develops under some conditions about the LCFS remains an open question. This plasma configuration that is nowadays well described and reproduced experimentally has never been simulated self-consistently without forcing the transport barrier formation.

In the scope of designing plasma facing components, an important effort is made to simulate precisely plasma behavior close to the wall of the tokamak chamber. This work is crucial since simulating plasma up to the wall is required to estimate impurities due to plasma-wall interaction. This kind of simulations have been reported to be quite challenging. In fact, many plasma codes are based on magnetic-field-aligned coordinates that are not suited to treat the complex geometry of the chamber wall. Contributions

concerning this issue can be found in the literature and the work made on meshing up-to-the-wall with the fluid code B2-Eirene [24] must be cited. In order to deal with this issue without resorting to mesh reshaping near the solid surface, penalization technique has been used in the transport code SolEdge2D to implement boundary conditions. This immersed technique allows to treat boundary conditions on a single magnetic-field-aligned mesh extending from the plasma into the PFCs, defined by a mask function. Numerical results show that such a technique is able to recover appropriate boundary conditions at plasma-solid interface [25], in particular the Bohm boundary condition. Such a technique opens the perspective of modifying the mask function dynamically to simulate how the plunging of a probe modifies the plasma. In a general point of view, the fact that the code takes real geometries of PFCs into account makes it particularly suited for synthetic diagnostic applications.

In this chapter, the code equations are presented as well as the penalization technique used to impose boundary conditions. One also reports some details on the algorithm and some results in various geometries.

II.2 The SolEdge2D fluid model

The basic SolEdge2D set of equations can be deduced from the fluid equations presented in Chapter I. Three fluid equations are considered per species (either ions or electrons): equation for density, velocity and temperature.

II.2.1 Continuity equation

Let us start with the 2 equations for density (see Equation I.43):

$$\frac{\partial n_e}{\partial t} + \vec{\nabla} \cdot (n_e \vec{u}_e) = S^{n_e} \tag{II.1}$$

$$\frac{\partial n_i}{\partial t} + \vec{\nabla} \cdot (n_i \vec{u}_i) = S^{n_i} \tag{II.2}$$

S^{n_α} denotes any volumic source of plasma. Assuming quasineutrality, these two equation reduces to a single equation for plasma density n that is taken to be equal to ions density.

$$\boxed{n = n_i = Z n_e} \tag{II.3}$$

Z being the number of charges per ion. The assumption of no parallel current is made leading to the simplification $u_e \approx u_i = u$ where u denotes the so-called plasma velocity. Moreover, the turbulent cross-field transport is taken into account in a diffusive way, according to the quasi-linear approach presented in section I.3. Neglecting mean field drifts, one as finally (see Equation I.136)

$$\boxed{\frac{\partial n}{\partial t} + \vec{\nabla} \cdot \left(n u_\parallel \vec{b} \right) = \vec{\nabla} \cdot \left(D \vec{\nabla}_\perp n \right) + S^n} \tag{II.4}$$

II.2.2 Momentum equation

Concerning momentum equation, Equation I.46 gives

$$m_e \frac{\partial n_e \vec{u}_e}{\partial t} + \vec{\nabla} \cdot (m_e n_e \vec{u}_e \otimes \vec{u}_e + \mathbf{\Pi}_e) = -n_e e \vec{E} + S^{\Gamma_e} \tag{II.5}$$

$$m_i \frac{\partial n_i \vec{u}_i}{\partial t} + \vec{\nabla} \cdot (m_i n_i \vec{u}_i \otimes \vec{u}_i + \mathbf{\Pi}_i) = n_i Z e \vec{E} + S^{\Gamma_i} \tag{II.6}$$

Braginskii collisional closure provides a complex expression for the pressure tensor $\mathbf{\Pi}$. In SolEdge2D, the pressure tensor is approximated by its spherical part yielding $\mathbf{\Pi} = p\mathbb{I}$. Also, the mass of electrons is neglected. Hence, projecting both equations along the magnetic field:

$$\nabla_\parallel p_e = -n_e e E_\parallel \tag{II.7}$$

$$m_i \frac{\partial n_i u_\parallel}{\partial t} + \vec{b} \cdot \vec{\nabla} \cdot (m_i n_i \vec{u}_i \otimes \vec{u}_i) + \nabla_\parallel p_i = n_i Z e E_\parallel + S^{\Gamma_i} \tag{II.8}$$

Equation II.7 gives Boltzmann adiabatic response for electronic pressure. Given $E_\parallel = -\nabla_\parallel \phi$,

$$\boxed{\nabla_\parallel \ln n_e = \frac{e \nabla_\parallel \phi}{k_B T_e} - \nabla_\parallel \ln T_e} \tag{II.9}$$

For Equation II.8, the advection term develops as:

$$\begin{aligned} \vec{b} \cdot \vec{\nabla} \cdot (m_i n_i \vec{u}_i \otimes \vec{u}_i) = {} & \vec{b} \cdot \vec{\nabla} \cdot \left(m_i n_i u_\parallel^2 \vec{b} \otimes \vec{b} \right) \\ & + 2\vec{b} \cdot \vec{\nabla} \cdot \left(m_i n_i u_\parallel \vec{b} \otimes \vec{v}_\perp \right) \\ & + \vec{b} \cdot \vec{\nabla} \cdot (m_i n_i \vec{v}_\perp \otimes \vec{v}_\perp) \end{aligned}$$

- The first term gives $\vec{\nabla} \cdot \left(m_i n_i u_\parallel^2 \vec{b} \right)$
- The second one is treated with the quasilinear approach and yields a diffusive contribution $-m_i \vec{\nabla} \cdot \left(\nu \vec{\nabla}_\perp (n_i u_\parallel) \right)$
- The third term in $v_\perp^2$ is neglected assuming $v_\perp \ll u_\parallel$

Finally, the ions velocity equation becomes

$$m_i \frac{\partial n_i u_\parallel}{\partial t} + \vec{\nabla} \cdot \left(m_i n_i u_\parallel^2 \vec{b} \right) + \nabla_\parallel p_i = m_i \vec{\nabla} \cdot \left(\nu \vec{\nabla}_\perp (n_i u_\parallel) \right) + n_i Z e E_\parallel + S^{\Gamma_i} \tag{II.10}$$

Adding Equation II.7 and II.8, one gets rid of electric field and obtains SolEdge2D equation for parallel velocity:

$$\boxed{m_i \frac{\partial n u_\parallel}{\partial t} + \vec{\nabla} \cdot \left(m_i n u_\parallel^2 \vec{b} \right) + \nabla_\parallel (p_e + p_i) = m_i \vec{\nabla} \cdot \left(\nu \vec{\nabla}_\perp (n u_\parallel) \right) + S^{\Gamma_i}} \tag{II.11}$$

with the state equations (perfect gases)

$$p_e = k_B n_e T_e = k_B Z n T_e \qquad \text{and} \qquad p_i = k_B n_i T_i = k_B n T_i \tag{II.12}$$

II.2.3 Energy equations

a) Kinetic energy equation

Since the parallel component is the only one considered for velocity, the parallel kinetic energy expresses as $E_c = \frac{1}{2} m_i n u_\parallel^2$ (since the mass of electrons is neglected, so is their kinetic energy). The equation for kinetic energy is thus obtained from velocity equation multiplying it by $u_\parallel$.

$$\begin{aligned} m_i u_\parallel \frac{\partial n u_\parallel}{\partial t} + u_\parallel \vec{\nabla} \cdot \left(m_i n u_\parallel^2 \vec{b} \right) + u_\parallel \nabla_\parallel (p_e + p_i) &= m_i u_\parallel \vec{\nabla} \cdot \left(\nu \vec{\nabla}_\perp (n u_\parallel) \right) + u_\parallel S^{\Gamma_i} \\ \frac{\partial E_c}{\partial t} + \vec{\nabla} \cdot \left(E_c u_\parallel \vec{b} \right) + \frac{1}{2} m_i u_\parallel^2 \left(\frac{\partial n}{\partial t} + \vec{\nabla} \cdot (n u_\parallel \vec{b}) \right) + u_\parallel \nabla_\parallel (p_e + p_i) &= m_i u_\parallel \vec{\nabla} \cdot \left(\nu \vec{\nabla}_\perp (n u_\parallel) \right) + u_\parallel S^{\Gamma_i} \end{aligned}$$

Reporting continuity equation

$$\frac{\partial E_c}{\partial t} + \vec{\nabla} \cdot \left(E_c u_\parallel \vec{b} \right) + u_\parallel \nabla_\parallel (p_e + p_i) = -\frac{1}{2} m_i u_\parallel^2 \vec{\nabla} \cdot \left(D \vec{\nabla}_\perp n \right) + m_i u_\parallel \vec{\nabla} \cdot \left(\nu \vec{\nabla}_\perp (n u_\parallel) \right) + u_\parallel S^{\Gamma_i} - \frac{1}{2} m_i u_\parallel^2 S^n \tag{II.13}$$

b) Internal energy equation

Then, let us consider the equation for total energy (see Equation I.53)

$$\frac{\partial E_{t_\alpha}}{\partial t} + \vec{\nabla} \cdot (E_{t_\alpha} \vec{u}_\alpha) + \vec{\nabla} \cdot (p_\alpha \vec{u}_\alpha) + \vec{\nabla} \cdot \vec{q}_\alpha - n_\alpha q_\alpha \vec{u}_\alpha \cdot \vec{E} = \mathcal{C}_{2_\alpha} + S^{E_{t_\alpha}} \tag{II.14}$$

with $E_{t_e} = \frac{3}{2} k_B n_e T_e$ and $E_{t_i} = \frac{3}{2} k_B n_i T_i + \frac{1}{2} m_i n_i u_i^2$. For the cross-field transport, the quasi-linear diffusive formulation is used once again. If $\vec{\Phi}_\perp(E_{t_e})$ is the cross-field electron energy flux, one writes

$$\begin{aligned} \vec{\Phi}_\perp(E_{t_e}) &= -\mathcal{D} \vec{\nabla}_\perp \left(\frac{3}{2} k_B n_e T_e \right) \\ &= -\frac{3}{2} k_B \left(T_e D \vec{\nabla}_\perp n_e + n_e \chi_e \vec{\nabla}_\perp T_e \right) \end{aligned} \tag{II.15}$$

This flux is splitted so as to distinguish the convective flux

$$\vec{\Phi}_{conv}(E_{t_e}) = -\frac{3}{2} k_B Z T_e D \vec{\nabla} n = \frac{3}{2} k_B T_e \vec{\Phi}_\perp(n_e)$$

where $\vec{\Phi}_\perp(n)$ denotes the cross field particle flux (see Equation II.4) from the conductive flux

$$\vec{\Phi}_{cond}(E_{t_e}) = -\frac{3}{2} k_B Z n \chi_e \vec{\nabla} T_e = -\alpha_e \vec{\nabla} T_e$$

where the standard Fourier's law is recovered. Finally, reporting Boltzmann relation for electric field, electron energy equation gives,

$$\begin{aligned}\frac{\partial}{\partial t}\left(\frac{3}{2}k_B Z n T_e\right)+\vec{\nabla}\cdot\left(\frac{3}{2}k_B Z n T_e u_\parallel \vec{b}\right)+k_B Z n T_e \vec{\nabla}\cdot(u_\parallel \vec{b}) &= \frac{3}{2}k_B Z \vec{\nabla}\cdot\left(T_e D\vec{\nabla}_\perp n + n\chi_e \vec{\nabla}_\perp T_e\right)\\ &\quad -\vec{\nabla}\cdot\left(q_{\parallel_e}\vec{b}\right)+\mathcal{C}_{2_e}+S^{U_e} \qquad \text{(II.16)}\end{aligned}$$

For the parallel heat flux, *Spitzer-Härm* collisional closure is used (see section I.2.5)

$$q_{\parallel_e} = -\kappa_e^0 T_e^{5/2}\nabla_\parallel T_e \qquad \text{(II.17)}$$

A thermalization term between the species due to ions-electrons collisions must also be added. From *Braginskii* (see [12, Equation 2.17]), this term gives

$$\mathcal{C}_{2_e} = -\mathcal{C}_{2_i} = Q_c = \frac{3m_e}{m_i}\frac{n_e}{\tau_e}(T_i - T_e) \qquad \text{(II.18)}$$

where the electron collision time computed by *Braginskii* is ([12, Equation 2.5e])

$$\tau_e = \frac{3\sqrt{m_e}T_e^{3/2}}{4\sqrt{2\pi}e^4 Z n_e \ln\Lambda} \qquad \text{(II.19)}$$

One rewrites $Q_c = \alpha n^2 T_e^{-3/2}(T_i - T_e)$ with

$$\alpha = \frac{\sqrt{m_e}}{m_i}4\sqrt{2\pi}e^4 Z^2 \ln\Lambda \qquad \text{(II.20)}$$

The final form for electron temperature equation

$$\begin{aligned}\frac{\partial}{\partial t}\left(\frac{3}{2}k_B Z n T_e\right)+\vec{\nabla}\cdot\left(\frac{3}{2}k_B Z n T_e u_\parallel \vec{b}\right)+k_B Z n T_e \vec{\nabla}\cdot(u_\parallel \vec{b}) &= \frac{3}{2}k_B Z \vec{\nabla}\cdot\left(T_e D\vec{\nabla}_\perp n + n\chi_e \vec{\nabla}_\perp T_e\right)\\ &\quad +\vec{\nabla}\cdot\left(\kappa_e^0 T_e^{5/2}\nabla_\parallel T_e\right)+\alpha\frac{n^2}{T_e^{3/2}}(T_i - T_e)+S^{U_e} \qquad \text{(II.21)}\end{aligned}$$

In order to obtain the internal energy equation for ions, kinetic energy equation is substracted from ions total energy equation. The ions total energy cross-field flux is given by

$$\begin{aligned}\vec{\Phi}_\perp(E_{t_i}) &= -\mathcal{D}\vec{\nabla}_\perp\left(\frac{3}{2}k_B n T_i+\frac{1}{2}m_i n u_\parallel^2\right)\\ &= -\frac{3}{2}k_B\left(T_i D\vec{\nabla}_\perp n + n\chi_i\vec{\nabla}_\perp T_i\right)+\frac{1}{2}m_i u_\parallel^2 D\vec{\nabla}_\perp n - m_i u_\parallel \nu\vec{\nabla}_\perp(n u_\parallel) \qquad \text{(II.22)}\end{aligned}$$

From II.14(blue) - II.13(red), denoting $E_{t_i} = U_i + E_c$:

$$\begin{aligned}\frac{\partial U_i}{\partial t}+\vec{\nabla}\cdot(U_i u_\parallel\vec{b})+\vec{\nabla}\cdot(p_i u_\parallel\vec{b})-nZneE_\parallel-u_\parallel\nabla_\parallel(p_e+p_i) &= \frac{3}{2}k_B\vec{\nabla}\cdot\left(T_i D\vec{\nabla}_\perp n+n\chi_i\vec{\nabla}_\perp T_i\right)\\ &\quad +\vec{\nabla}\cdot(\kappa_i^0 T_i^{5/2}\nabla_\parallel T_i\vec{b})-\alpha\frac{n}{T_e^{3/2}}(T_i-T_e)+S^{E_{t_i}}-u_\parallel S^{\Gamma_i}+\frac{1}{2}m_i u_\parallel^2 S^n+\mathcal{K}_i\end{aligned}$$

where the correction term $\mathcal{K}_i$ is given by

$$\mathcal{K}_i = \vec{\nabla}\cdot\left(-\frac{1}{2}m_i u_\parallel^2 D\vec{\nabla}_\perp n + m_i u_\parallel \nu \vec{\nabla}_\perp (n u_\parallel)\right) + \frac{1}{2}m_i u_\parallel^2 \vec{\nabla}\cdot\left(D\vec{\nabla}_\perp n\right) - m_i u_\parallel \vec{\nabla}\cdot\left(\nu\vec{\nabla}_\perp(n u_\parallel)\right) \tag{II.23}$$

which simplifies to

$$\boxed{\mathcal{K}_i = -m_i u_\parallel \left(\vec{\nabla}_\perp u_\parallel\right)\cdot\left(D\vec{\nabla}_\perp n\right) + m_i \nu \left(\vec{\nabla}_\perp u_\parallel\right)\cdot\left(\vec{\nabla}_\perp (n u_\parallel)\right)} \tag{II.24}$$

Finally, denoting

$$S^{U_i} = S^{E_{t_i}} - u_\parallel S^{\Gamma_i} + \frac{1}{2}m_i u_\parallel^2 S^n \tag{II.25}$$

the following equation is obtained for ions internal energy:

$$\begin{aligned}\frac{\partial}{\partial t}\left(\frac{3}{2}k_B n T_i\right) + \vec{\nabla}\cdot\left(\frac{3}{2}k_B n T_i u_\parallel \vec{b}\right) + k_B n T_i \vec{\nabla}\cdot(u_\parallel \vec{b}) = \frac{3}{2}k_B \vec{\nabla}\cdot\left(T_i D\vec{\nabla}_\perp n + n\chi_i \vec{\nabla}_\perp T_i\right) \\ + \vec{\nabla}\cdot\left(\kappa_i^0 T_i^{5/2}\nabla_\parallel T_i\right) - \alpha\frac{n^2}{T_e^{3/2}}(T_i - T_e) + S^{U_i} + \mathcal{K}_i\end{aligned} \tag{II.26}$$

II.3 Computational domain and magnetic topologies

II.3.1 SOLEDGE2D coordinates

The SOLEDGE2D equations are solved with finite-differences method on a magnetic field aligned grid. More precisely, the tokamak can be described by the magnetic coordinates (ψ, θ, φ), see Figure II.3.1 where ψ labels flux surfaces, θ denotes a generalized poloidal angle and φ the toroidal angle. SOLEDGE2D assumes toroidal symmetry hence $\partial_\varphi = 0$. The SOLEDGE2D grid is thus described by the remaining relevant coordinates (ψ, θ). The

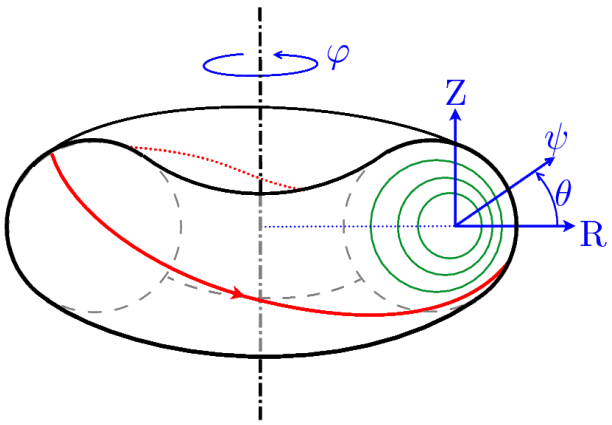

Figure II.1: Toroidal geometry and definition of toroidal coordinates. (φ, θ, ψ) denote the toroidal, poloidal angles and the surface label, respectively.

numerical grid is thus represented by a structured (ψ, θ) mesh. Each point in the lattice is given by its grid coordinates (i, j) with $i \in [\![1, N_\psi]\!]$ and $j \in [\![1, N_\theta]\!]$ where N_ψ (resp. N_θ) denotes the grid resolution in the radial (resp. poloidal) direction. The discrete coordinates $(\psi_i)_{i\in[\![1,N_\psi]\!]}$ and $(\theta_j)_{j\in[\![1,N_\theta]\!]}$ hence characterize the SOLEDGE2D lattice. Each grid point (ψ_i, θ_j) is also associated to coordinates in the physical space $(R_{i,j}, Z_{i,j})$. As a consequence, the differential operator $\vec{\nabla}$ is expressed in the (ψ, θ) frame as

$$\vec{\nabla} = \frac{\partial}{\partial\psi}\vec{e}^{\psi} + \frac{\partial}{\partial\theta}\vec{e}^{\theta} + \cancel{\frac{\partial}{\partial\varphi}\vec{e}^{\varphi}} \tag{II.27}$$

where $(\vec{e}^{\psi}, \vec{e}^{\theta}, \vec{e}^{\varphi})$ is the contravariant base associated to the (ψ, θ, φ) coordinates. These vectors are defined as

$$\vec{e}^{\psi} = \vec{\nabla}\psi = \frac{\partial\psi}{\partial R}\hat{e}_R + \frac{\partial\psi}{\partial Z}\hat{e}_Z \qquad \text{and} \qquad \vec{e}^{\theta} = \vec{\nabla}\theta = \frac{\partial\theta}{\partial R}\hat{e}_R + \frac{\partial\theta}{\partial Z}\hat{e}_Z \tag{II.28}$$

where $(\hat{e}_R, \hat{e}_Z)$ is the Cartesian orthonormal base of the poloidal plane. The different spatial derivatives such $\partial R/\partial\psi$ are specific to the magnetic geometry and constitute so-called metric coefficients. For more details on the metrics, see Appendix C.

On figure II.2 is represented an example of SOLEDGE2D grid. In this case, the magnetic configuration is made of circular nested tori. At the bottom of the machine is located the limiter (see Figure 2).

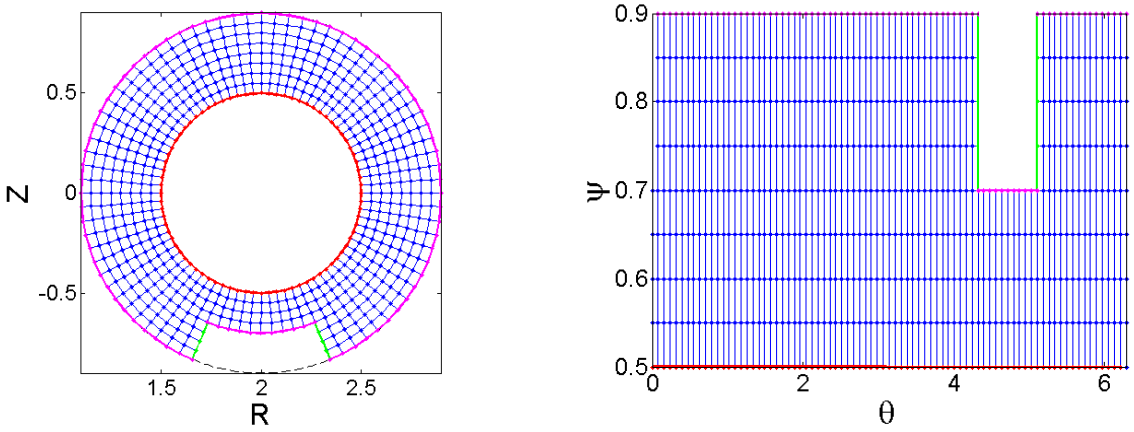

Figure II.2: Example of mesh for a circular case with a limiter at the bottom. Left: mesh in the physical space. Right: mesh in the (ψ, θ) space - in this simple case $\psi = r$ where r denotes the minor radius. Boundary conditions are figured in color: Red: Core boundary condition, Green: Bohm boundary condition, Purple: Radial wall boundary condition

The numerical scheme used in SOLEDGE2D is detailed in Appendix B.

II.3.2 Multi-domain algorithm

Complex topologies such as divertor configurations are mapped into a Cartesian frame (ψ, θ) using a multi-domain algorithm. In fact, whatever the topology of the magnetic configuration, it can be described by a set of elementary subdomains having a simple rectangular topology. A matrix of neighborhood then specifies how these elementary elements are connected to each other. This approach is also efficient for parallelization by assigning each subdomain to one processor using, here, OPENMP library.

Divertor and limiter domains are splitted as described on Figure II.3 and II.4 respectively.

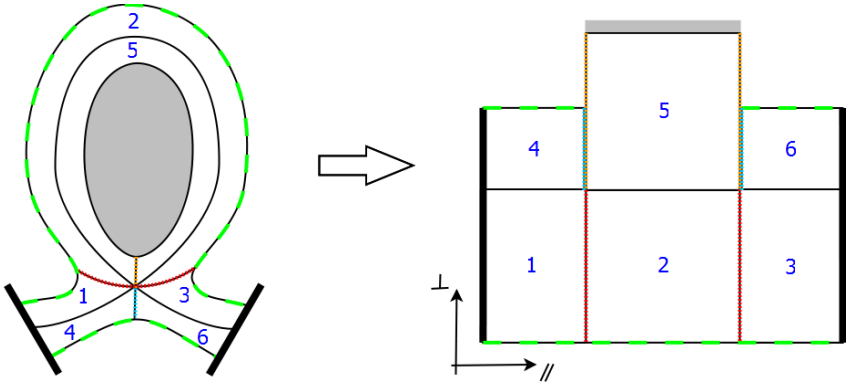

Figure II.3: Divertor configuration. Example of subdomain decomposition. Zone 5 corresponding to core plasma is periodic. This closed field line region communicates with the main-SOL region (zone 2) that extends to the divertor SOL (zones 1 & 3). The divertor SOL regions communicate with subdomains 4 and 6 that represent the private flux plasma region.

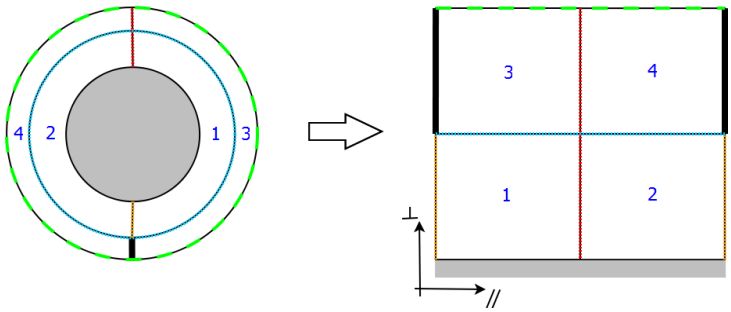

Figure II.4: Limiter configuration. Decomposition into four subdomains for parallelization. The limiter is infinitely thin. The parallel direction is described by θ, the perpendicular direction is described by ψ.

Each subdomain is provided with tables containing data fields for spatial grid, metric coefficients, plasma variables etc. Moreover, each subdomain is surrounded by ghosts cells that store the necessary information on the neighboring subdomains. These ghost cells are represented on Figure II.5 where a limiter decomposition is shown. Two cases must be considered:

- The neighbor is another subdomain. In this case, one just reports the values of the neighboring subdomain fields into the ghost cells.
- The neighbor is a boundary of the computational domain (core, wall or limiter). In this case, one uses the boundary conditions to compute the ghost cell values.

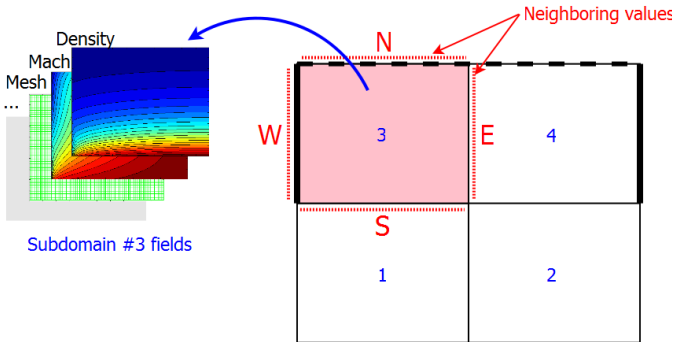

Figure II.5: Sketch of the subdomain decomposition and definition of the neighbor labels. In this example, for subdomain 3, one has North=wall, South=1, East=4 and West=limiter.

In any case, the computation of ghost cell values in parallel algorithm requires a communication step between the processors at the beginning of each iteration.

The algorithm is sketched on Figure II.6. First, a communication phase takes place between the threads to determine subdomain neighboring values. Then, the equations for density and velocity are solved using an explicit time discretization. Finally, the temperature equations that contains parallel diffusion terms that are solved implicitly. This last phase requires gathering the subdomains connected in the parallel direction into so-called *parallel areas*.

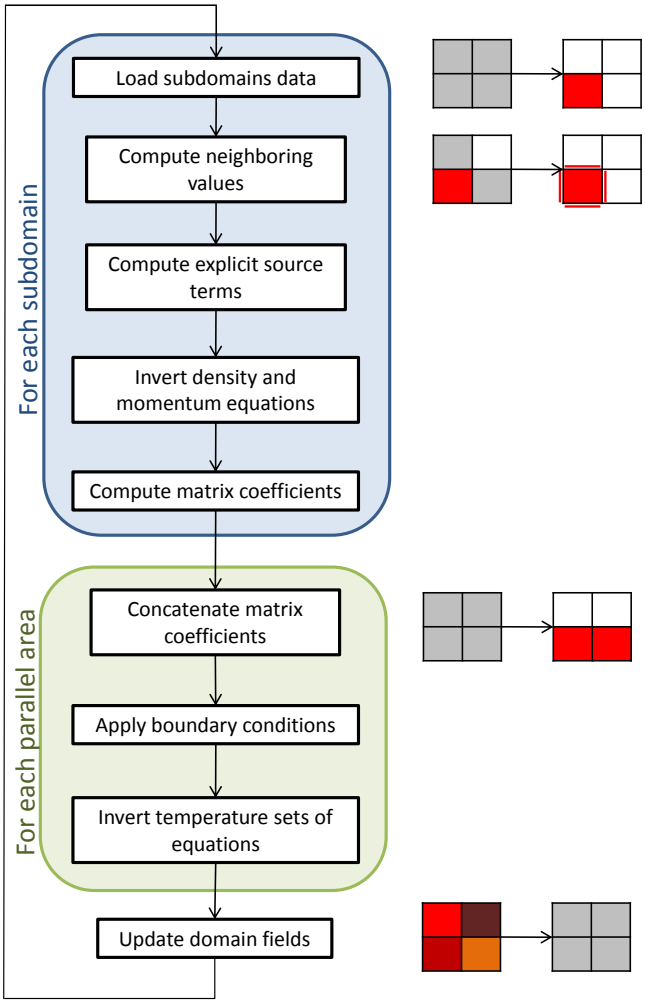

Figure II.6: Sequences of the multi-domain algorithm used to solve SolEdge2D *equations. The first explicit part is perfomed in parallel for each subdomain (density and velocity equations). The second part that contains parallel diffusion treated implicitly by a tri-diagonal matrix inversion is performed in parallel for each parallel area (cluster of subdomains connected in the parallel direction).*

II.4 Boundary conditions and penalization technique

II.4.1 Ghost-cell boundary conditions

In the standard way of imposing boundary conditions, the above mentionned "ghost cells" surrounding the subdomains are used. These ghosts cells or points are represented on Figure II.7.

The values taken for ghost points are computed from the following boundary conditions:

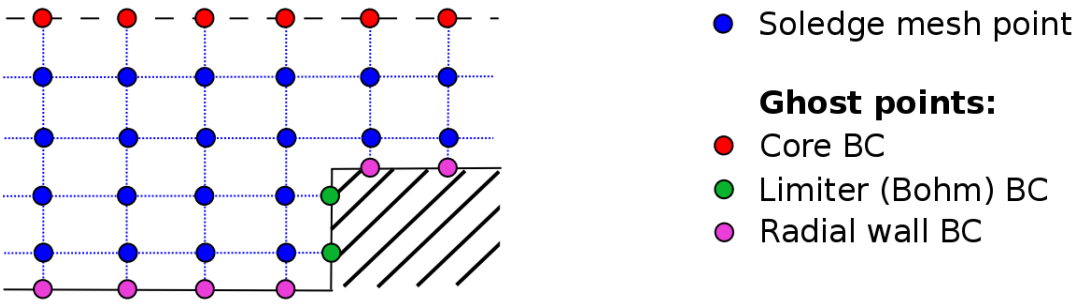

Figure II.7: Definition of ghost points to set boundary conditions. The ghost points are located at domain boundary. The horizontal direction represents the parallel (θ) direction. The vertical direction represents radial (ψ) direction.

- **Core boundary conditions:**

	density	*velocity*	T_e	T_i
Values	core density (m^{-3})	core velocity $(m^2 s^{-1})$	core electronic temperature (eV)	core ions temperature (eV)
Fluxes	particle influx (s^{-1})	Slip boundary	Electrons incoming power (MW)	Ions incoming power (MW)

Table II.1: Possible sets of boundary conditions on core side. The boundary conditions on core side control particle and energy influxes. The user can specify either the value or the flux for most quantities

- **Wall parallel boundary condition:**

According to Bohm boundary conditions I.5, ions velocity at sheath entrance must be greater or equal to sound speed. The Bohm boundary condition on ions velocity $|u_\parallel| \geq c_s$ is recast as:

```
if  |u_∥upstream| < c_s then
        |u_∥| = c_s
else
        ∇²_∥ u_∥ = 0
end
```

Concerning heat flux, sheath transmission expression are used (Equation I.155) with sheath transmission coefficients $\gamma_e = 4.5$ and $\gamma_i = 2.5$. The parallel total heat flux in the plasma equation is given by

$$\Phi_\parallel^{U_\alpha} = \frac{5}{2} k_B n u_\parallel T_\alpha - \kappa_\alpha^0 T_\alpha^{5/2} \nabla_\parallel T_\alpha \tag{II.29}$$

This flux is set to be equal to the energy flux given by sheath transmission coefficients, yielding at sheath entrance

$$\frac{5}{2}k_B n u_\parallel T_\alpha - \kappa_\alpha^0 T_\alpha^{5/2}\nabla_\parallel T_\alpha = \gamma_\alpha k_B n u_\parallel T_\alpha \tag{II.30}$$

Density is extrapolated linearly at sheath entrance to get values for ghost cells. Table II.2 sums up parallel boundary conditions.

	density	*velocity*	T_e	T_i
B.C.	$\nabla_\parallel^2 n = 0$	$\lvert u_\parallel \rvert \geq c_s$	$\nabla_\parallel T_e = -\frac{2k_B n u_\parallel}{\kappa_e^0 T_e^{3/2}}$	$\nabla_\parallel T_i = 0$

Table II.2: Parallel boundary conditions at a solid wall (Bohm + sheath transmission for energy)

- **Wall perpendicular boundary condition:**
  In the wall ghost cells radially connected to the wall, one imposes $n_{BC} = 0$, $T_{i_{BC}} = 0$ and $T_{e_{BC}} = 0$. This ensures a net diffusive flux of particles and energy oriented toward the solid. For velocity, a slip boundary condition is used.

	density	*velocity*	T_e	T_i
B.C.	$n = 0$	$\nabla_\perp u_\parallel = 0$	$T_e = 0$	$T_i = 0$

Table II.3: Wall perpendicular boundary conditions

II.4.2 Penalization technique for plasma-wall interaction

Instead of using ghost points for plasma-surface boundary-condition, an immersed boundary condition technique called *penalization* [26, 27, 28, 29] has been implemented. Indeed, the ghost-cell method presented in the above paragraph requires to adapt the mesh to the geometry of the wall (see Figure II.7). If this method is manageable for simple geometries such as square limiter, simulating complex geometries of real PFCs remains challenging. The penalization technique extends the plasma grid from the plasma into the solid. A mask function χ distinguishes the grid points in the plasma and in the solid. The objective is to modify the fluid equations in the penalized domain in such a way to recover desired boundary conditions at the interface between the plasma and the solid.

A first step was made to get Bohm boundary conditions in isothermal plasma [30]. In this contribution, the penalization technique is inspired by the physics and the fact that solid elements in plasma act as a strong plasma sinks has been used. In particular, Bohm boundary conditions can be compared to the properties of any fluid flows expanding into vacuum. In that perpective, one expects to recover these specific boundary conditions if one adds an important density sink term in the solid volume. The following penalized

system for n and $\Gamma = nu_\parallel$ is considered[1]:

$$\frac{\partial n}{\partial t} + \vec{\nabla}\cdot(nu_\parallel\vec{b}) + \frac{\chi}{\eta}(n - n_\varepsilon) = \vec{\nabla}\cdot\left(D\vec{\nabla}_\perp n\right) \tag{II.31}$$

$$\frac{\partial \Gamma}{\partial t} + \vec{\nabla}\cdot\left(\frac{\Gamma^2}{n}\vec{b}\right) + \nabla_\parallel\left(\frac{k_B(T_e+T_i)}{m_i}\right) + \frac{\chi}{\eta}\Gamma = \vec{\nabla}\cdot\left(D\vec{\nabla}_\perp \Gamma\right) \tag{II.32}$$

where η is a small parameter and the mask function χ is defined as:

$$\chi = \begin{cases} 0 & \text{in the plasma} \\ 1 & \text{in the solid} \end{cases} \tag{II.33}$$

In the plasma, $\chi = 0$ and the regular fluid equations are recovered. In the solid, since η is a small parameter, the penalized equations give at leading order $n = n_\varepsilon$ and $\Gamma = 0$. n_ε is thus the "virtual plasma density within the solid". This parameter is chosen to be very small, typically n_ε is chosen to be ten thousand times less than typical plasma density. It is proven [23] that the penalization procedure is able to ensure a near sonic Mach number at the plasma-wall interface recovering Bohm boundary condition. Let us study why.

For simplicity, in the following paragraph, one considers the region of the SOL where flows are positive. The same treatment can be done symmetrically for negative flows. The particle flux Γ and total pressure are given by

$$\begin{aligned} \Gamma &= nu_\parallel \\ &= nc_sM \end{aligned} \quad \text{and} \quad \begin{aligned} \Pi &= m_i n u_\parallel^2 + p_e + p_i \\ &= m_i n c_s^2(1+M^2) \end{aligned}$$

where $p_\alpha = k_B n T_\alpha$ and $c_s = \sqrt{k_B(T_e+T_i)/m_i}$. In this short demonstration, the system is considered *isothermal*. At steady state in the plasma domain, the penalized system of Equations II.31 can be simply rewritten as

$$\frac{\partial \Gamma}{\partial s} = S_\perp^n \quad \text{and} \quad \frac{\partial \Pi}{\partial s} = S_\perp^\Gamma \tag{II.34}$$

Hence, in the SOL plasma, the parallel gradient length for Γ is given by the typical length L_S associated to perpendicular density source. As a first assumption, the loss of pressure in the SOL due to the perpendicular source of momentum can be neglected. The total pressure is thus constant along the field line yielding,

$$\frac{L_\parallel}{\Gamma}\left(\frac{\partial \Gamma}{\partial s}\right)_{plasma} = \frac{L_\parallel}{L_S} \quad \text{and} \quad \frac{L_\parallel}{\Pi}\left(\frac{\partial \Pi}{\partial s}\right)_{plasma} = 0 \tag{II.35}$$

In the solid region, the penalization terms lead to a fast decay of flux and pressure char-

[1] Rigorously, one should denote n_η and $u_{\parallel_\eta}$ the variables of the penalized system of equation and prove that these penalized variables properly fit with the density n and velocity $u_\parallel$ in the limit $\eta \to 0$. These η-subscript are not used in the manuscript for writing convenience and clarity.

acterized by decay length L_Γ and L_Π. One writes,

$$\frac{L_\parallel}{\Gamma}\left(\frac{\partial\Gamma}{\partial s}\right)_{solid} = -\frac{L_\parallel}{L_\Gamma} \qquad \text{and} \qquad \frac{L_\parallel}{\Pi}\left(\frac{\partial\Pi}{\partial s}\right)_{solid} = -\frac{L_\parallel}{L_\Pi} \tag{II.36}$$

From Γ and Π expressions, the logarithmic derivatives give

$$\begin{aligned}\frac{\partial_s\Gamma}{\Gamma} &= \frac{\partial_s n}{n} + \frac{\partial_s M}{M} + \frac{\partial_s \cancel{c_s}}{\cancel{c_s}} \\ \frac{\partial_s\Pi}{\Pi} &= \frac{\partial_s n}{n} + 2\frac{\partial_s \cancel{c_s}}{\cancel{c_s}} + \frac{2M\partial_s M}{1+M^2}\end{aligned}$$

This system of equation can be rewritten

$$\frac{\partial_s n}{n} = -\frac{2M^2}{1-M^2}\frac{\partial_s\Gamma}{\Gamma} + \frac{1+M^2}{1-M^2}\frac{\partial_s\Pi}{\Pi} \tag{II.37}$$

$$\frac{\partial_s\mathcal{A}}{\mathcal{A}} = \frac{\partial_s\Gamma}{\Gamma} - \frac{\partial_s\Pi}{\Pi} \tag{II.38}$$

with

$$\boxed{\mathcal{A} = \frac{2M}{1+M^2}} \tag{II.39}$$

The function $\mathcal{A}$ is plotted on Figure II.8,a. Its properties are detailed in section V. Let us consider equation II.38, in standard SOL the RHS is positive since $\partial_s\Pi \approx 0$ and $\partial_s\Gamma = S_\perp^n > 0$. Hence $\partial_s\mathcal{A} > 0$ and starting from the upstream stagnation point, $\mathcal{A}$ is continuously growing. For a continuous Mach number solution, this behavior is possible only if one remains on the subsonic branch (acceptable and non-acceptable solutions are represented on Figure II.8,b).

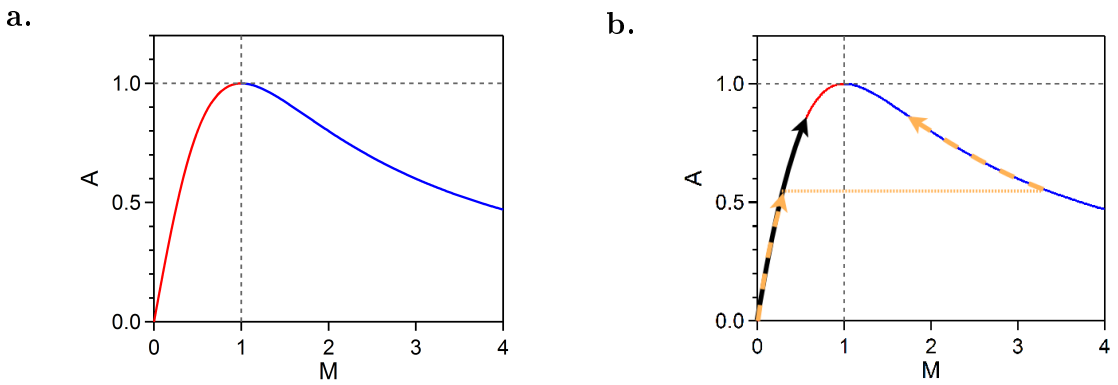

Figure II.8: a: $\mathcal{A}$ as a function of Mach number M. b: Starting from stagnation points, acceptable (solid black) and unacceptable solutions (dashed gold) for $\partial_s\mathcal{A} > 0$. The unacceptble solution breaks Mach number continuity.

Concerning density Equation II.37, reporting expressions for Γ and Π gradient scales

gives

$$\frac{L_\parallel}{n}\left(\frac{\partial n}{\partial s}\right)_{plasma} = -\frac{2M^2}{1-M^2}\frac{L_\parallel}{L_S} \tag{II.40}$$

$$\frac{L_\parallel}{n}\left(\frac{\partial n}{\partial s}\right)_{solid} = \frac{2M^2}{1-M^2}\frac{L_\parallel}{L_\Gamma} - \frac{1+M^2}{1-M^2}\frac{L_\parallel}{L_\Pi} \tag{II.41}$$

Assuming continuity of parallel density gradient[2], the two above expressions must give the same density gradient length L_n at plasma-solid interface that is

$$-\frac{L_\parallel}{L_n} = -\frac{2M^2}{1-M^2}\frac{L_\parallel}{L_S} \tag{II.42}$$

$$-\frac{L_\parallel}{L_n} = \frac{2M^2}{1-M^2}\frac{L_\parallel}{L_S}\left(\frac{L_S}{L_\Gamma} - \frac{L_S}{L_\Pi}\right) - \frac{L_\parallel}{L_\Pi} \tag{II.43}$$

giving

$$\frac{L_n}{L_S} = \frac{1-M^2}{2M^2} \tag{II.44}$$

$$\frac{L_n}{L_S} = \frac{L_\Pi}{L_S} + \left(\frac{L_\Pi}{L_\Gamma} - 1\right) \tag{II.45}$$

Given the fact that L_S is a long scale of the order $L_\parallel$ and that a strong density (resp. pressure) drop is expected at the transition, that is $L_n \ll L_S$ (resp. $L_\Pi \ll L_S$), Equation II.45 gives $L_\Pi \approx L_\Gamma$. The Mach number at the transition is given by Equation II.44:

$$\boxed{M_{pen} = \sqrt{\frac{1}{1+2\frac{L_n}{L_S}}}} \tag{II.46}$$

The Mach number remains subsonic everywhere. In the limit $L_n/L_S \to 0$, one obtains a near sonic Mach number at the transition which is compatible with Bohm boundary condition. This solution is valid if the Mach number is subsonic in the plasma. In section V, the supersonic case is addressed. The decay length of density in the penalized domain is given by the penalization parameter η. One expects $L_n \approx \eta$. The dependence of Mach number on the η parameter is studied by performing a set of 1D simulations. The radial source is set to a constant value in $S_\perp^n = S^\star$ in the whole domain (hence $L_S = L_\parallel$) and the mesh resolution is set to 1600 points. The penalized region represents 400 points in the middle of the domain. $S_\perp^\Gamma$ is set to zero. Simulation results are shown on Figure II.9. The numerical solutions are compared with the analytical solution (see section IV.1.2).

However, the analysis presented above is drastically simplified. On the numerical point of view, extra parameters such as mesh size and numerical scheme can play a role in the final value for Mach number at the transition.

[2] this assumption is discussed in details in [23, section 5.2]

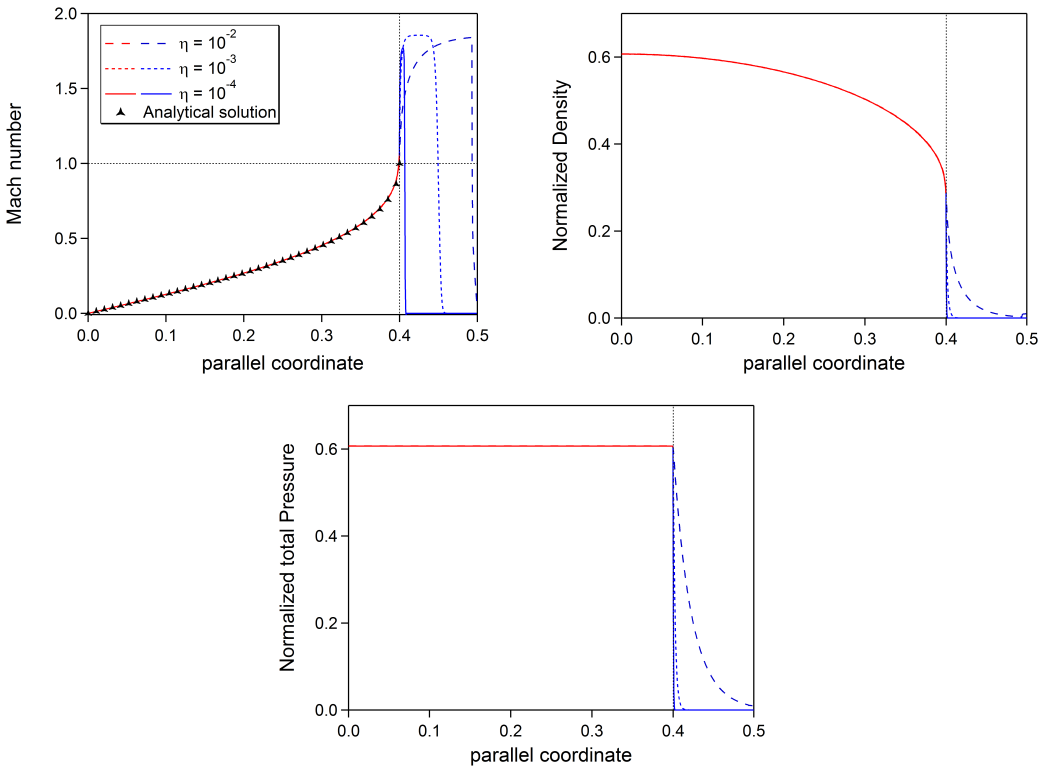

Figure II.9: Results for Mach number, density and total pressure in a 1D penalized system. The particle source S^n is set to a constant value and the analytical solution is plotted for Mach number. Results for different values of the penalization parameter η are shown. The solution in the plasma is plotted in red and the solution in the limiter is plotted in blue.

Concerning radial transport, by imposing the density to be small in the solid, the density gradient ensures that the radial diffusive flux is always oriented toward the solid. The exact formulation for boundary condition when magnetic field line intercept solid elements with grazing incidence are still debated. The radial transport properties obained with penalization at least guarantee that plasma flow is always oriented toward the solid and no plasma can flow out of the solid.

Concerning the boundary condition for temperature [25, 31], one has to set the parallel temperature gradient. This is done by adding forcing terms at the solid surface. Unlike for density where the density value is imposed in the entire solid volume, the temperature gradients are set only at the solid surface. This is a general feature when penalization is used to impose derivatives (Neumann boundary conditions). Secondary penalization masks χ_1 and χ_2 are added around the main mask χ. The χ_1 and χ_2 limiters extent is such as they start one grid point before the main penalization mask (see Figure II.10). In that sense, the first point where the gradient is penalized is in the plasma and not in the solid. Then, the secondary masks overlap the main mask on 2 or 3 grid points. One can also defines the mask $\chi_3 = \chi \backslash (\chi_1 \cup \chi_2)$.

If N_{BC}^L and N_{BC}^R denote the gradient boundary conditions that must be imposed on

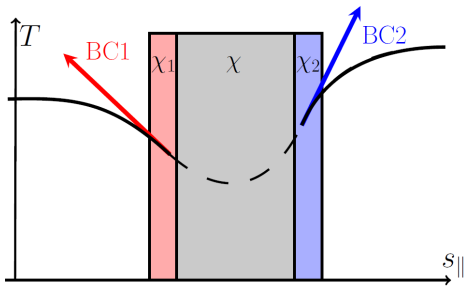

Figure II.10: Penalization masks for Neumann type boundary conditions.

the left and right side of the obstacle, the penalized temperature equation is the following,

$$\frac{\partial}{\partial t}\left(\frac{3}{2}k_B n T\right) + LHS + \frac{\chi_1}{\eta}\left(\nabla_\parallel^L T - N_{BC}^L\right) - \frac{\chi_2}{\eta}\left(\nabla_\parallel^R T - N_{BC}^R\right) + \frac{\chi_3}{\eta}\left(T - T_\varepsilon\right) = RHS \tag{II.47}$$

where LHS and RHS denote the left hand side and right hand side terms of equations II.26 and II.21. $\nabla_\parallel^L$ and $\nabla_\parallel^R$ denote left and right sided parallel gradients. When $\chi_1 = 1$ (resp. $\chi_2 = 1$) the dominant term in temperature equation gives $\nabla_\parallel^L T = N_{BC}^L$ (resp. $\nabla_\parallel^R = N_{BC}^R$) imposing the desired boundary condition. It is important to use decentered expression for gradients to guarantee that no information travels from the solid to the plasma. The last penalization term forces the temperature to be equal to T_ε in the rest of the solid. Indeed, as shown on Figure II.11, the middle part of the solid can be radially connected with the plasma. A vanishing temperature in the solid hence ensures a net radial diffusive flux oriented toward the solid.

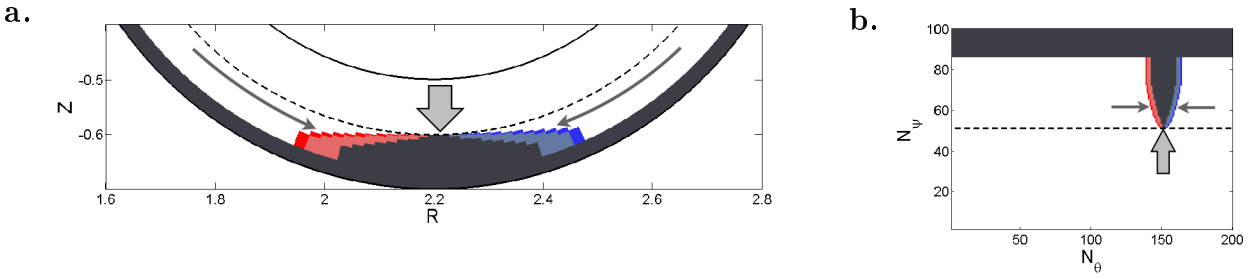

Figure II.11: Example of penalization masks for a circular flux surfaces configuration with a flat bottom limiter. a: Real space. b: (ψ, θ) space. Parallel and perpendicular flows are represented by thin an thick arrows respectively. One notices that radial flows are possible between the plasma and the limiter.

II.5 Illustrative simulations in limiter and divertor configurations

The capability of the code is illustrated here on two simulations briefly detailed.

II.5.1 MISTRAL test case in realistic Tore Supra configuration

The complex wall geometry of the machine is accurately modeled in SOLEDGE2D simulations using penalization technique. The magnetic configuration is the one used by J. Gunn to study cross field transport inhomogeneities [32]. This reference shot, that will be refered in this manuscript as MISTRAL base case, consists in adjusting magnetic configuration to change plasma-wall contact point location. The plasma is successively in contact with bottom main limiter, inboard limiters and outboard antenna limiters. The different configurations are schematized on Figure II.12 taken from [32].

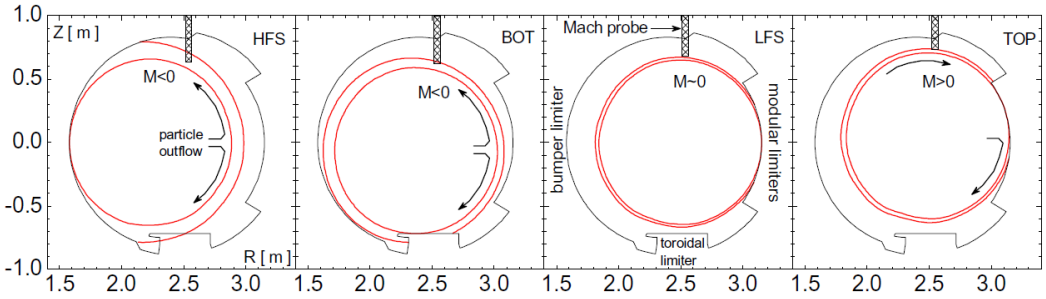

Figure II.12: From left to right these four panels show the magnetic configurations used in the experiment. Both the LCFS and the flux surface on which $1/e$ of the LCFS density was measured in each case are drawn (red lines). The main paths of the particle outflux from the core, as we postulate based on the simple model, are indicated by arrows. The sign of the parallel flow is defined to be positive when its poloidal projection is directed in the positive poloidal direction (clockwise in the R-Z plane). At the probe location positive flow is directed from the high field side towards the low field side. Shot TS#33463 ([32])

Due to the enhancement of turbulent transport on the magnetic low field side (LFS), scrape-off layer thickens when the plasma contact point is on the inboard limiter rather than when the contact point is on the outboard limiter. Indeed if one considers the continuity equation at steady state, parallel scales and perpendicular scales can be linked by

$$\begin{aligned} \vec{\nabla}\cdot(nu_{\parallel}\vec{b}) &= \vec{\nabla}\cdot(D\vec{\nabla}_{\perp}n) \\ &\Downarrow \\ \frac{nc_s}{L_{\parallel}} &\approx \frac{Dn}{\lambda_{\perp}^2} \end{aligned} \tag{II.48}$$

where $L_{\parallel}$ is the typical distance between the turbulent plasma source and the limiter. $\lambda_{\perp}$ represents SOL thickness and is thus expressed by

$$\boxed{\lambda_{\perp} = \sqrt{\frac{DL_{\parallel}}{c_s}}} \tag{II.49}$$

In the LFS configuration, the source and the limiter are at the same location hence $L_{\parallel}$ is

small involving a thin SOL. Conversely, the SOL gets thicker if the source is far from the limiter such as in the HFS configuration. The enhancement of the turbulent transport on the LFS due to ballooning also induces characteristic plasma flows captured in J. Gunn experiment by a Mach probe at the top of the machine. The arrows on Figure II.12 represent the orientation of the flows.

The experiment has been reproduced with SOLEDGE2D. The cross-field transport enhancement on the LFS has been taken into account using a peaked diffusivity profile centered on the outboard midplane. The diffusivity is represented on Figure II.13.

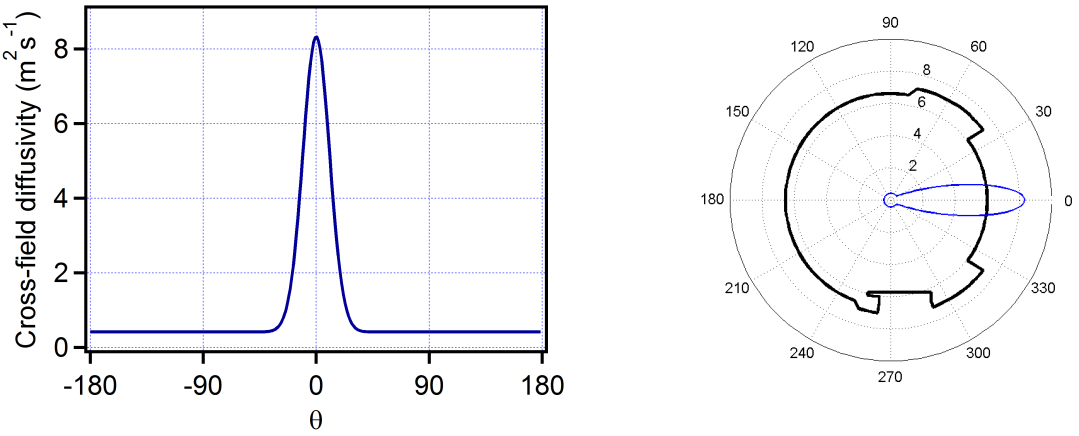

Figure II.13: The diffusivity profile as a function of the poloidal angle is given by a 30°-wide Gaussian shape centered on the outboard mid-plane. The average diffusivity $\langle D \rangle$ is 1 $m^2 s^{-1}$ and the Gaussian peaking is such as $D_{max}/D_{min} = 20$

The simulation results are represented on Figure II.14. The Mach number field is

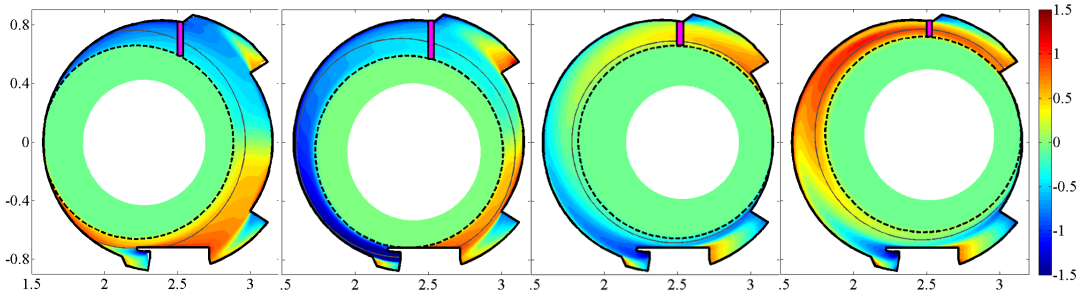

Figure II.14: Simulation results for the 4 magnetic configurations. Color background: Mach number. The SOL thickness is represented with gray lines.

represented in color and the density decay is represented with contour levels. The same trend as in the experiment is recovered. 1D plots representing density and Mach number at probe location are shown on Figure II.15. The experiental data are also represented for comparison. A qualitative agreement concerning the density decay length is once again recovered. Concerning Mach number, the simulations rather fit the experimental results close to the separatrix. A net departure is though observed in the far SOL. The

discrepencies may be linked to the presence of neutrals that are not taken into account in these simulations or related to the effects of drift velocities which are not implemented. Also, the nature of cross-field transport in the far SOL is probably not well described by the simple diffusion term used in SOLEDGE2D equations. Let us notice finally that input parameters have not been optimally tuned with respect to experiments.

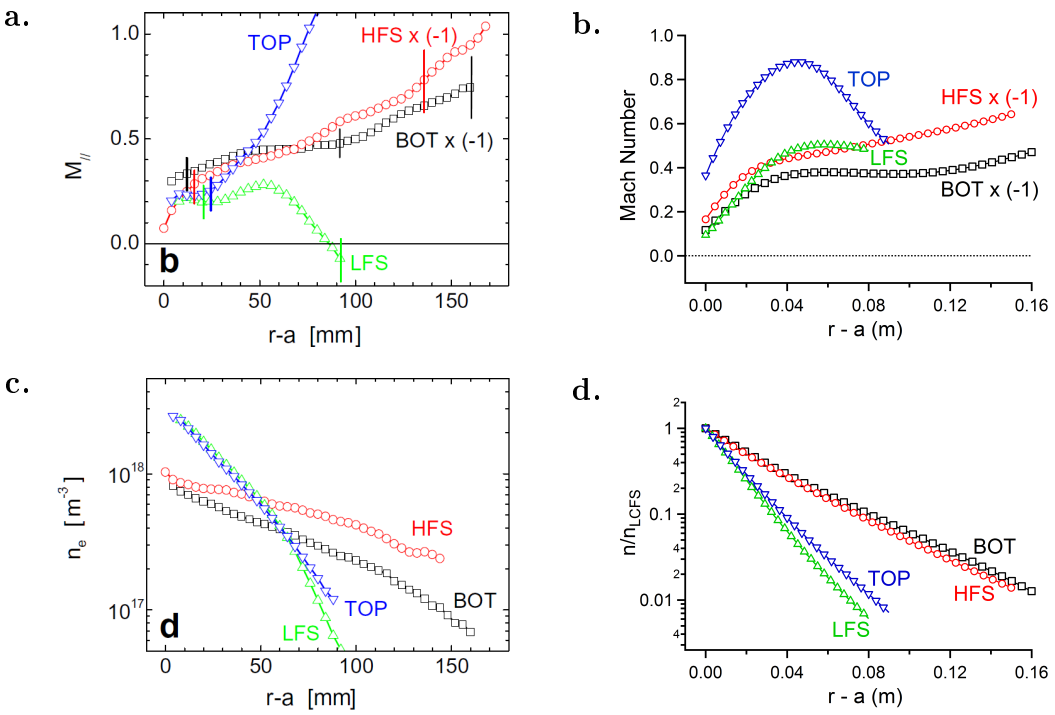

Figure II.15: Mach number at probe location (top of the machine) for the different magnetic configurations. a: experimental data. b: simulation results ; Density at probe location. c: experimental data. d: simulation results

II.5.2 Divertor simulations

Divertor simulations have been performed for several machines. Below is an example of simple X-point configuration in *JET* geometry. The Mach number and electrons temperature are represented. The realistic geometry of *JET* wall is well taken into account using the penalization technique. The typical grid size for this kind of simulation is 200 points in the radial direction and 360 points in the parallel direction. The simulation time is of the order of 10 hours on 4 processors to reach steady state.

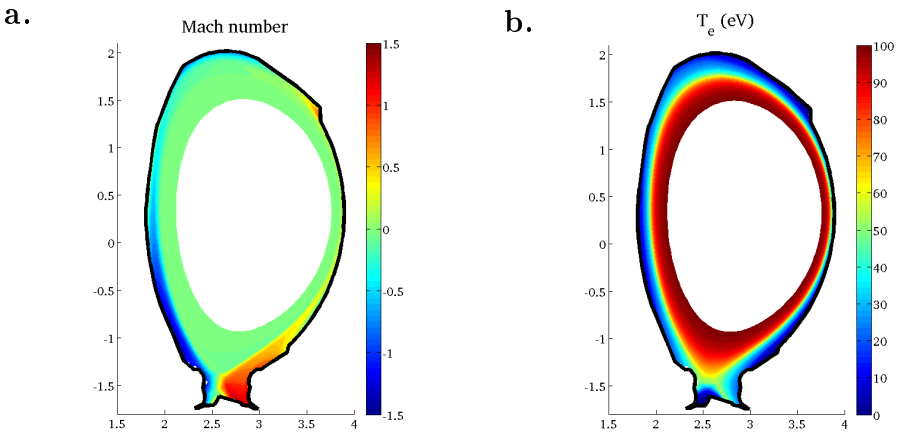

Figure II.16: JET simulations. a. Mach number. b. Electrons temperature

Many simulations have been made in the *Tore Supra - WEST* geometry. This case is a double-null configuration. The simulation domain must be divided at least in 16 subdomains to simulate this magnetic configuration. On Figure II.17 is represented the *WEST* geometry from magnetic flux surface definition to SolEdge2D subdomains. One notices the penalized areas in the square (ψ, θ) subdomains.

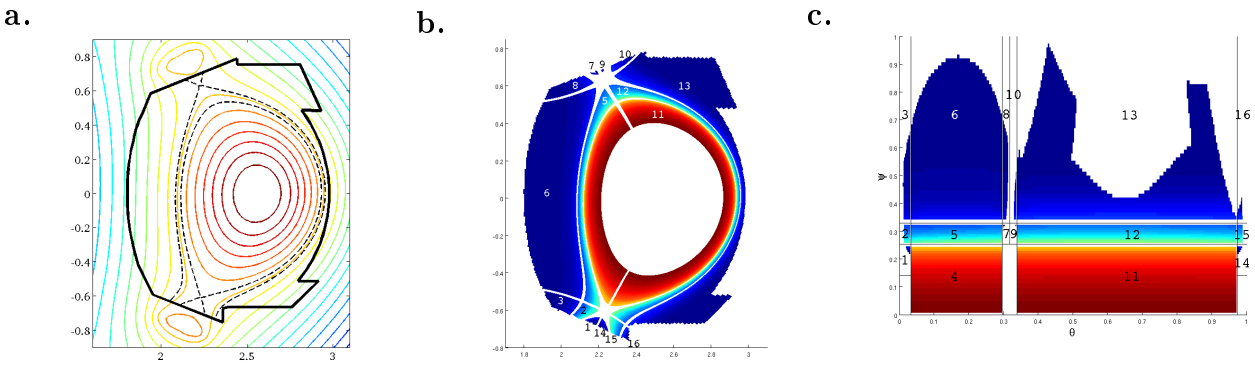

Figure II.17: WEST geometry. a: flux surfaces. Multidomain decomposition: b. Poloidal cross section in the (R,Z) plane. c. Poloidal cross section in the (ψ, θ) space. Density field is represented as color background.

II.6 In practice

SolEdge2D code is written in Fortran 90 and it is parallelized using OpenMP library.

Input parameters must be provided such as cross field diffusivities, particle and power influx, mesh etc... In order to make the code easier to use, a graphical interface has been developed in Java to automatically generate these input files. A snapshot of the infercace is shown on Figure II.18.

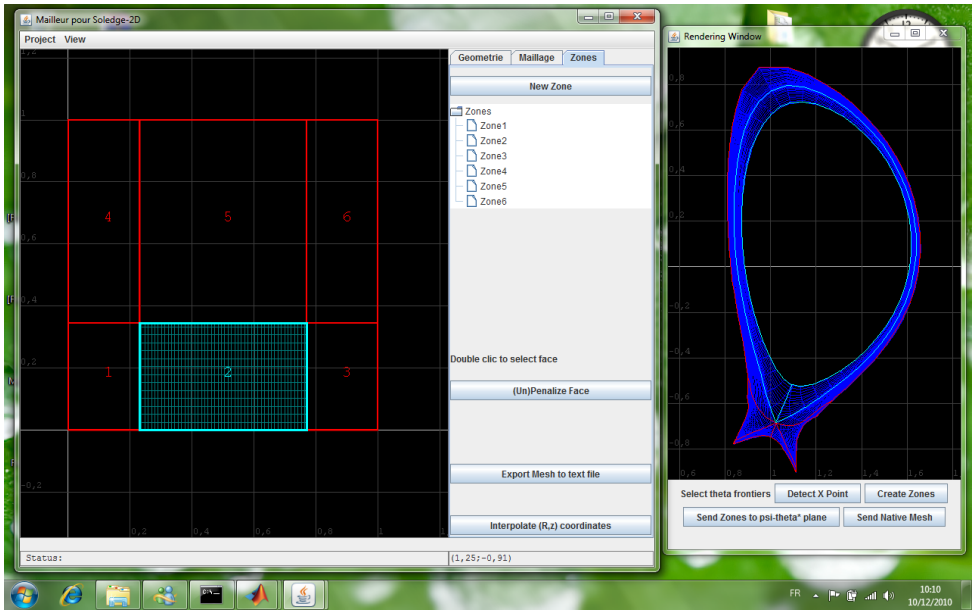

Figure II.18: Snapshot of SolEdge2D *graphical interface*

Also, Matlab routines have been developed:

- Pre-processing: Generation of meshs from magnetic flux maps.
- Post-processing: 2D and 1D plots from simulation results

These routines are to be rewritten in Java and included to the graphical interface.

Chapter highlights

- SolEdge2D *is a transport code solving equations for plasma density, parallel velocity, electrons and ions temperatures.*
- *The penalization technique used to model plasma-wall interaction makes possible to simulate the plasma up to the main chamber wall. Whatever the complexity of the wall geometry, Bohm boundary conditions are recovered.*
- *The multidomain approach enables flexibility and makes possible to simulate a broad range of magnetic configurations.*
- *The program is parallelized using* OpenMP.
- *A graphical interface developed in* Java *can be used to generate mesh and run the code.*

Chapter III

Investigations on heat flux closures in weakly collisional plasmas

Content

After a brief summary of the state-of-the-art, a stochastic 1D model is proposed to investigate energy transfer and its dependence on collisionality. A non-local expression is found and its implementation in the transport code SolEdge2D is discussed.

In section I.2.4, it has been reported that for highly collisional plasmas, the probability density function of particles velocity is given by the Maxwellian distribution f_0. Out of equilibrium, the expression for heat flux is obtained using Chapman-Enskog development about the Maxwellian. In particular, when particle mean free path is much smaller than system size, the heat flux is found to be proportional to temperature gradient and expresses according to Fourier's law:

$$q = -\kappa \nabla T \tag{III.1}$$

As far as the Coulombian interaction is considered, the mean free path increases sharply with temperature (Equation I.30).

$$\lambda_c = \tau_c \cdot v \approx 1.2 \cdot 10^{16} \frac{T_e^2}{n} \; [m] \qquad \text{with } T_e \text{ in } eV \text{ and } n \text{ in } m^{-3} \tag{III.2}$$

In the table below III.1 are given mean free path values for typical plasma parameters in the core and edge region. For some cases, the mean free path can exceed the typical length associated to the machine. Concerning the edge plasma region of interest in SolEdge2D simulations, the far scrape-off layer can be seen as collisional. Conversely, collisionality drops near the separatrix where the plasma temperature reaches hundreds eV. The hypothesis of high collisionality thus fails and the problem of heat flux closure has to be revisited to take low collisionality effects into account.

	density $[m^{-3}]$	Temperature $[eV]$	λ_c $[m]$	$\nu^\star$
Core plasma	10^{21}	10000	1200	0.05
Edge plasma	10^{19}	500	120	0.2
SOL entrance	$2 \cdot 10^{18}$	100	120	1
Far SOL	10^{17}	10	12	5

Table III.1: Typical mean free path values and collisionalities. One has chosen system size $L_\parallel = 60\ m$.

III.1 General concepts linked to weakly collisional closures

One recalls that the heat flux is given by the expression (see Equation I.52 with $\vec{v}' = \vec{v} - \vec{u}$)

$$q_\parallel = \frac{1}{2} m \int_{\mathcal{V}_v} \|\vec{v}'\|^2 v'_\parallel f(\vec{v}) d\vec{v} \tag{III.3}$$

Heat flux thus represents a measure of pdf asymmetries given by the third order moment called skewness. In the collisional case, these assymetries are small and can be linked to the temperature gradient. This is possible due to collisions that link particle velocities at one position with temperature spatial inhomogeneities in the neighboring region. In the general case, it is unlikely that such a process exists.

III.1.1 Flux limiters

In any case, for a Maxwellian distribution, the upper bound for the heat flux is provided by the one-sided flux also called "free-streaming" flux q_{FS} that represents the flux of energy carried by the particles with a positive velocity.

$$q_{FS} = \frac{1}{2} m \int_{\mathcal{V}_v, v'_\parallel > 0} \|\vec{v}'\|^2 v'_\parallel f(\vec{v}) d\vec{v} \tag{III.4}$$

that is, reporting the expression for the Maxwellian distribution

$$\boxed{q_{FS} = \sqrt{\frac{2}{\pi}} n k_B T c_s} \qquad \text{with} \qquad c_s = \sqrt{\frac{k_B T}{m}} \tag{III.5}$$

In that sense, it represents the flux associated with the maximum assymmetric distribution based on Maxwellian distribution. The opposite free streaming flux q^-_{FS} could also been defined considering particles travelling in the opposite direction. For a Maxwellian distribution that is perfectly symmetric, one finds of course $q_{Mw} = q_{FS} + q^-_{FS} = 0$. Since Spitzer-Härm expression for heat flux is based on high collisionality assumption, it is expected to fail at high temperature or low density, when particle mean free path is much longer than system size. Spitzer-Härm derivation also assumes particle distribution func-

tion to be a perturbed Maxwellian distribution so in any case, Spitzer-Härm heat flux must be less than free streaming bound. In other words, based on the existence of local thermal equilibrium, Spitzer-Härm expression enables the development of temperature gradients on scales necessarily larger than collisional mean free path.

However, in some specific configurations, kinetic simulations and experimental measurements show that "Temperature" gradients can develop on the typical system size even if this size is smaller than collision mean free path. Of course, Spitzer-Härm expression fails to describe this situation where collisionality drops and local balance no longer exists. Besides, it is irrelevant to use the term "Temperature" when refering to the quantity defined as the ratio between pressure and density in this case. The failure of Spitzer-Härm expression appears when Spitzer-Härm expression is applied to these "Temperature profiles": heat flux values greater than the permitted free streaming upper bound are obtained. In any case, an effetive heat diffusivity can be defined as

$$\kappa_{eff} = \frac{q}{\nabla T} \sim k_B n \lambda_{\nabla T} c_s \tag{III.6}$$

Spitzer-Härm expression assumes $\lambda_{\nabla T} \approx \lambda_c$ where λ_c is the collisional mean free path; it thus overestimates heat diffusivity in the above mentionned configurations where $\nu^\star \sim \lambda_{\nabla T}/\lambda_c \ll 1$.

Several attempts have been made to correct Spitzer-Härm expression to catch these low $\nu^\star$ situations. The simplest one consists in using so-called flux-limiters. Indeed, as Spitzer-Härm overestimates the flux and guessing the upper bound value (free streaming values), the flux-limited expression is defined as the weighted harmonic average between Spitzer-Härm heat flux and free streaming heat flux:

$$\boxed{q_{FL} = \left(\frac{1}{q_{SH}} + \frac{1}{\alpha_e q_{FS}} \right)^{-1}} \tag{III.7}$$

For low collisionality cases, $q_{SH} \ll q_{FS}$ and one finds $q_{FL} = q_{SH}$. Conversely, for low collisionality, Spitzer-Härm expression overestimates heat flux such as $q_{FS} \ll q_{SH}$ and $q_{FL} = \alpha_e q_{FS}$. Of course, this expression is clearly empirical and just avoids overestimating heat flux in the collisionless limit. It intrinsically assumes that heat flux tends to the Maxwellian free streaming value in the low collisionality case. In that sense, this expression refers to the Maxwellian distribution when it is no longer relevant. This asymptotic value in the collisionless case is thus prescribed and based on a misleading definition of temperature. Also, the transition from the Spitzer-Härm to the low collisionality expression is only controlled by the failure of Spitzer-Härm expression to match this prescribed collisionless asymptotic value. Comparison with kinetic simulations are performed for different plasma conditions to evaluate the weight α_e. The latter is found to vary between 0.03 and 3. Patching up a fluid expression to take kinetic effects into account cannot provide anything but raw corrections. Nevertheless, this formulation is quite convenient and likely provides an ad-hoc but reasonable correction in the $\nu^\star \leq 1$ limit. Several nu-

merical, theoretical and experimental studies [33, 6, 34] have been made to link the weight α_e with plasma properties to better control the flux limiter expression. More comments on the commonly used flux limiters can be found in the literature [35, 36, 11, 37]. Figure III.1 taken from [6, Figure 26.5] represents normalized parallel temperature profiles for different collisionalities, with and without flux limiter corrections. Spitzer-Härm and flux limiter expressions fairly match for high collisionnalities ($\nu^\star = 40$) and quite well for low collisionnalities ($\nu^\star = 2.5$) where both predict rather flat temperature profiles. The major discrepencies occur for intermediate collisionalities where the temperature gradients are steeper with the kinetic correction[1].

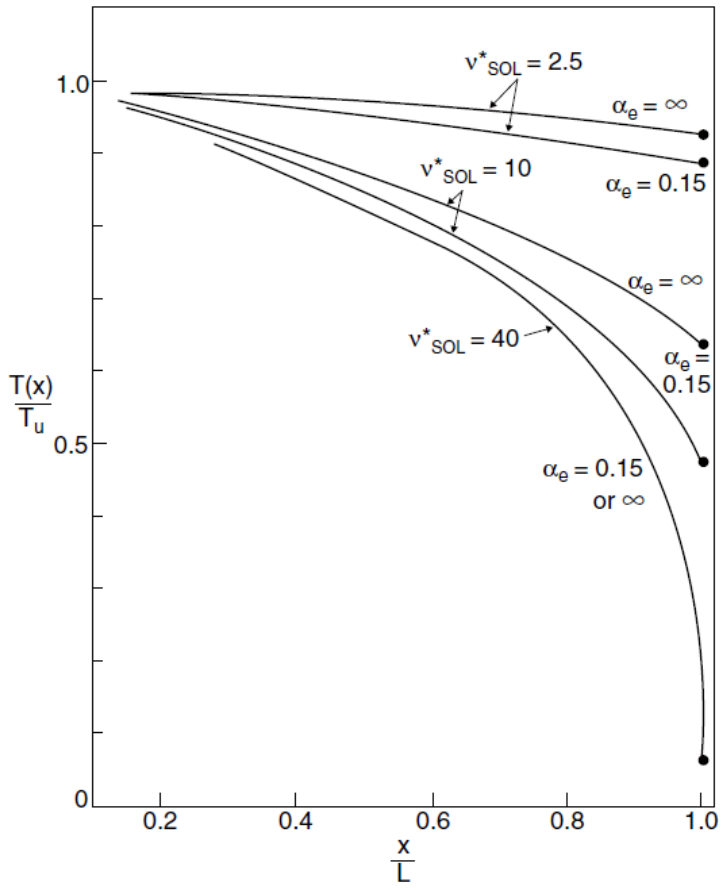

Figure III.1: Temperature profiles normalized to upstream temperature T_u for different levels of collisionality, with and without a heat limiter. The parameter α_e (Equation III.7) controls flux limiter threshold. It is clear that the effect of this heat limiter is greatest for intermediate collisionality.

[1] The transition between the collisional and collisionless regime does not occur at $\nu^\star = 1$ but for higher $\nu^\star$ because suprathermal particles $v \approx 3c_s$ play a major role in heat flux value. Since mean free path scales as $\lambda_c \propto v^4$, the suprathermal particles can be considered weakly collisional for $\nu^\star < 100$

III.1.2 Non-local formulations

A more theoretical work has been carried out in the early 80's by [38]. This work has been extended and commented afterwards [39].

III.1.3 Higher orders and kinetic models

An other effort has been done to overcome the difficult work to close heat flux expression by considering highest order equations. In the work by T. Passot [40] on Landau fluids, the set of fluid equations is closed not a the third order but at he fourth order moment. A weak departure from a bi-Maxwellian distribution is assumed to close the system. Waterbag models are also used to better describe the distribution function. In this model, the pdf is represented by a serie of N_w step functions whose bounds and values are unknowns of the waterbag system of equation. These equations are of the fluid type.

III.2 Stochastic 1D model for weakly collisional plasmas

A key issue of contemporary statistical mechanics is to understand the behaviour of systems steadily kept out of equilibrium. We propose in this section to investigate heat transport in weakly collisional plasmas with a simple stochastic model that address the key nonequilibrium effects, as the lack of local thermalization.

Indeed, a considerable insight on the nature of nonequilibrium steady states has been achieved by considering simple stochastic models that describe interaction among "particles" at the mesoscopic level. This class of systems has the invaluable advantage of being pretty straightforward to simulate by Monte-Carlo type of methods and, in some cases, to allow for an analytical solution, which is usually unfeasible in the deterministic cases. Actually, many general properties of nonequilibrium states are inferred by such simplified models thus opening the way to general concepts and approaches [41, 42]. For heat conduction problems[43, 44, 45], the simplest level of modeling amounts to consider local energies as random variables on a lattice [46]. In this context, a model that can be explicitly solved is the Kipnis-Marchioro-Presutti (KMP) lattice model, in which stochastic collisions mix the energy of neighboring particles, conserving the total energy [47]. This model is proven to satisfy Fourier's law when put in contact with two external reservoirs yielding a linear temperature profile. Energy conserving stochastic noise has been also used in lattice model systems, as natural generalizations of KMP and of the simple exclusion process [48]. In the same perspective, lattice of coupled oscillators subject to energy and momentum conserving noise have been also discussed to describe anomalous heat conduction problems and the associated steady-state correlations properties [49, 50].

In our model, the dynamics inspired by the above mentioned KMP model [47] is supplemented by interaction rules introduced to describe the salient features of Coulombian interaction and to introduce an energy-dependent thermalization mean free path.

III.2.1 Description of the model

We aim at characterizing plasma heat transport with a probabilistic model. This model is sketched in Figure III.2. At each lattice site $i = 1, \ldots, N$ we have a pair of particles of energies E_i^+ and E_i^-: the plus and the minus sign indicates particles moving in opposite directions with constant velocity. Their discrete-time dynamics consists of two steps. At each time t, we first perform a free convection of energy:

$$E_i^{\pm}(t) \longrightarrow E_{i\pm1}^{\pm}(t') \tag{III.8}$$

We assume periodic boundary conditions assumed as for a ring geometry. Taking inspiration from the KMP-model, we consider that the energy exchange mechanism between particles occurs at each lattice site i at any time t and amounts to a random redistribution of the total energy of the particles. In formulae:

$$\begin{cases} E_i^+(t+1) &= r[E_i^+(t') + E_i^-(t')] \\ &= 2rE_i(t') \\ E_i^-(t+1) &= (1-r)[E_i^+(t') + E_i^-(t')] \\ &= 2(1-r)E_i(t') \end{cases} \tag{III.9}$$

where we have defined the energy on the site i as $E_i(t) = [E_i^+(t) + E_i^-(t)]/2$ and with r a random number uniformly distributed in $[0, 1]$.

In order to include an important ingredient coming from the physics of the interactions among plasma particles, we mimic an effective Coulomb-like cross section (see section I.1.2) by assuming that the energy exchange may occur with a rate $\mathcal{P}$ inversely proportional to the square of the energy of the interacting particles. Specifically,

$$\mathcal{P} = \frac{C}{1 + (E_i/E_{\text{int}})^2} \tag{III.10}$$

where E_{int} is an energy scale, $0 < E_i < +\infty$, and C is a suitable constant. For $E_i \ll E_{\text{int}}$, the interaction probability is energy-independent meaning that low-energy particles are strongly interacting. In this asymptotic limit, Equation (III.10) is expected to yield a standard diffusion mechanism. On the other hand, for $E_i \gg E_{\text{int}}$ the collision rate vanishes and thus particles travel almost ballistically.

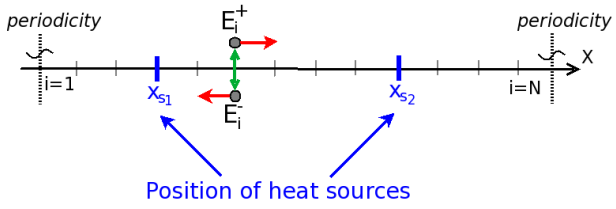

Figure III.2: Sketch of the 1D particle model. The dynamic step is represented in red and the interaction step in green.

In tokamaks, plasma particles interact with hot and cold localized sources (e.g. Fast particle heated region, hot/cold turbulent structures, etc...) that are schematized as external reservoirs. We can introduce two heat sources located at the lattice sites i_h and i_c (typically $i_h \sim N/4$ and $i_h \sim 3N/4$) and with inverse temperatures β_h, β_c, respectively. To keep the interaction rule as simple as possible and in analogy with other models of heat baths [44] we assume a strong coupling with the sources: at each time step, energies $E_i^{\pm}$, at the source sites $i = i_h, i_c$ are assigned new random values drawn from the Maxwell-Boltzmann distributions $\beta_h \exp(-\beta_h \epsilon)$ and $\beta_c \exp(-\beta_c \epsilon)$ respectively.

In the simulation hereby discussed, the update is synchronous on all lattice sites; one could make it sequential by updating randomly chosen sites from a unifom distribution, but we do not expect significant modifications w.r.t. the synchronous rule.

A related mean-field model is discussed in Appendix D.

III.2.2 Study of the equilibrium properties: characteristic thermalization scale

a) Relaxation to equilibrium

In order to study the equilibrium, we consider a domain without sources and let the system evolve starting from an arbitrary random state. Let us denote by $f(E,t)$ the distribution function of energies of all particles at time t. As an example, we consider the case such that the energies of the particles are initialized with $f(E,0)$ being a step distribution function centered on the average energy E_0 (see the curve labeled $t = 0$ in Figure III.3). As expected, after a certain number of time steps, $f(E,t)$ approaches a Maxwell-Boltzmann distribution $f_0(E) = \beta \exp(-\beta E)$ where $\beta = 1/T = 1/E_0$, see Figure III.3a. To monitor this convergence to equilibrium we considered the distance $d(t) = \langle \| f(E,t) - f_0(E) \| \rangle$. The $\| \cdot \|$ denotes $\mathcal{L}^1$ norm while $\langle \cdot \rangle$ means an average over several trajectories. At long enough times, this distance decays exponentially to zero $d = F \exp(-t/\tau_r)$, see Figure III.3b. Actually, a closer inspection of the data suggests that equilibration process occurs in two stages, compatible with a double exponential fit. We can argue that the first time scale is associated to some transient equilibration that may depend on the chosen initial conditions. What actually governs the asymptotic behavior of the relaxation to equilibrium is the final stage characterized by a time scale that we denote τ_r. Numerical evidence suggests that the latter time scale is proportional to the square of the average energy, $\tau_r \propto E_0^2$ (see the lower line in Figure III.4) . This is a consequence of the choice of the interaction rate $\mathcal{P}$ in Equation (III.10). More precisely, the relaxation time τ_r can be seen as the number of events required for probability of having interacted to be of order 1, that is for independent events $\tau_r \mathcal{P} = 1$.

b) Fluctuations around equilibrium

In the spirit of linear response theory, properties of the fluctuations of equilibrium currents yield information on transport coefficients. In the present context we are interested in the

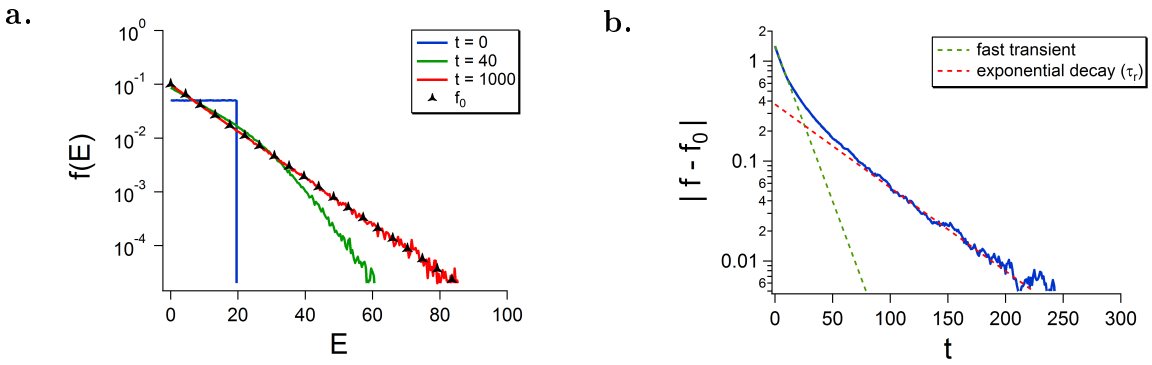

Figure III.3: Relaxation to equilibrium for $N = 1000$ particle sites, $E_0 = 10$ and $E_{int} = 5$. a: Initial (blue), transient (red) and equilibrium (green) distribution of energy. b: Distance to equilibrium distribution versus time. Blue: simulation results - Red: fit with exponential decay with decay time τ_r - Green: fast transient relaxation of initial conditions.

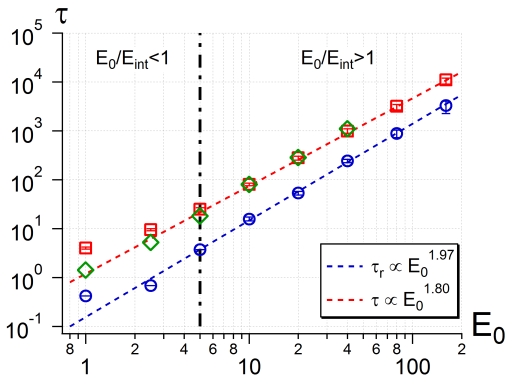

Figure III.4: Characteristic times of the interaction as a function of system average temperature E_0. Blue dots: Relaxation time to equilibrium, see Section a) - Red squares: fitting value of τ in Equation III.20 - Green diamonds: cutting time $\tau_c = 1/\omega_c$. Line: Power law fit.

correlation function of the heat current J, $c_J(\tau) = \langle J(t)J(t-\tau)\rangle$ whose time integral is related to the thermal diffusivity by the Green-Kubo formula [15]

$$D = \frac{1}{k_B T^2 N} \int_0^\infty c_J(\tau) d\tau \tag{III.11}$$

where T is the equilibrium temperature of the system defined above and N the number of sites, defining the length of the sysem. We ignore here the difference between diffusivity and conductivity since they only differ by a proportionality constant. More generally, the time behavior of c_J yields information on relaxation processes and thus on nonstationary energy transport. By Wiener-Khintchin theorem, this description is equivalent to considering the power spectrum $Sp[J](\omega) = \mathcal{F}[c_J(\tau)]$ where $\mathcal{F}$ denotes the Fourier transform.

In our model, the heat flux at site i is defined as $j_i(t) = E^+_{i-1}(t) - E^-_i(t)$ as can be found by writing the lattice continuity equation $E_i(t+1) - E_i(t) = -j_{i+1} + j_i$. The total heat flux travelling in the system is the sum of all the local contributions $J(t) = \sum_i j_i(t)$.

The application of Green-Kubo formula for open, finite systems is still matter of debate [51], so it is relevant to perform a comparison between different statistical ensembles. In a first series of experiments, we considered the microcanonical system that is with the sources turned off. In Figure III.5,a we plot the power spectra of J for different values of the system energy E_0. The data are fitted with a Lorentzian shape, i.e. $Sp[J](\omega) \approx C/(\omega^2 + \tau_c^{-2})$ assuming that the time correlation function c_J decays exponentially with a single[2] characteristic time-scale τ_c. From the data we found that $\tau_c \sim E_0^2$, see the lower line in Figure III.4, namely the same dependence of the thermalization time τ_r.

The time τ_c defines a characteristic length λ_c which represents a particle mean free path. Indeed, if a particle moves on a length smaller than λ_c (or on a time smaller than τ_c), the interaction probability is very small and the transport of energy can be considered as ballistic. On the contrary, on scales larger than λ_c, it is likely that a particle undergoes several interaction events hence reducing its correlation with its inititial conditions. The particle thermalizes and the energy transport can be thereby described as a standard diffusion process.

This observation is useful to interpret the data for the canonical case in which the system interacts with two sources both having the same temperatures $\beta_h = \beta_c$ corresponding to an average system energy equal to the value E_0 employed in the microcanonical setting. The heat flux power spectra for different values of E_0 are reported in Figure III.5,b.

At small enough energies $\lambda_c \ll N$ microcanonical and canonical spectra are almost the same (compare the lower-lying curves in Figure III.5). Conversely, for larger E_0 ($\lambda_c \sim N$) differences are significant. In particular in the presence of sources the spectra display oscillations. This is a consequence of the presence of localized thermal sources in the lattice. More precisely, the particle transit time τ_s between the sources corresponds to the characteristic time of the oscillations of the spectra. Despite this oscillating behavior, one observes at any value of E_0 a flat profile of the spectra for small frequencies, $\omega < 1/\tau_s$. This is due to the fact that particles loose memory when interacting with the sources and no correlation can be expected for times larger than $\tau_{sources}$.

Another difference between the microcanonical and the canonical cases is shown in Figure III.6. One can conclude that the Green-Kubo relation (III.11) evaluated in these two ensembles yields the same result only for small enough energies. For high value of E_0, a quasi ballistic regime where D grows proportionally to E_0^2 is observed for the microcanonical data, while the canonical data exhibit a saturation of the ballistic regime and D levels off at half of the system length $N/2$. This upper bound is reached because any particle must at least interact with the sources. These results can be found directly

[2] Admittedly, the Lorentzian fit is not very accurate for $\omega\tau_c \sim 1$. A possible improvement would be to consider a two-parameter fitting with two characteristic time-scales, somehow akin with the two relaxation stage illustrated in Figure III.3. For simplicity, we ignored this refinement henceforth.

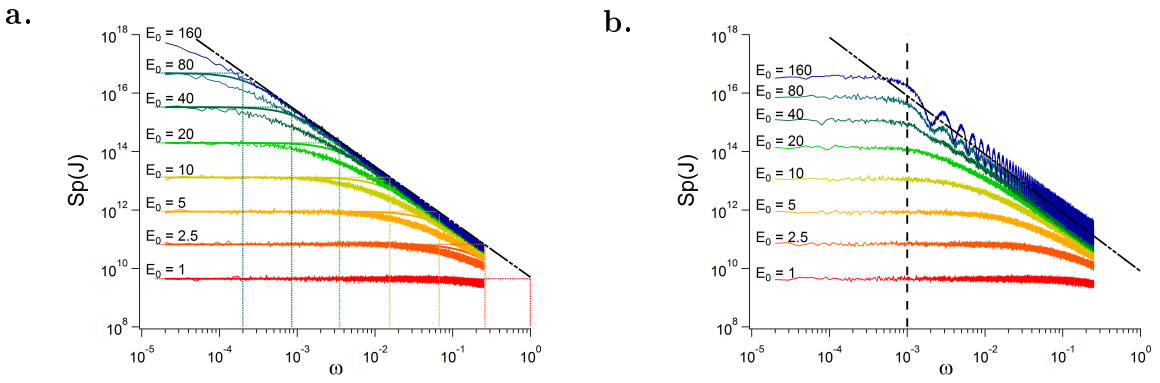

Figure III.5: Power spectrum of total heat flux for different average energies E_0. Simulation parameters: $N = 1000$ and $E_{int} = 5$. The black line represents the ω^{-2} asymptotic behavior. a: Results without sources and fits with Lorentzian. The vertical lines corresponds to the respective cutting frequency ω_c b: Results with sources. The vertical dashed line indicated the characteristic frequency associated with system size ω_{system}. Units on the vertical axis are arbitrary.

from the following algebra on Green-Kubo formula:

$$D = \frac{1}{NT^2}\int_0^\infty c_J(\tau)d\tau = \frac{1}{NT^2}\langle J^2\rangle\tau_{cor}$$

where τ_{cor} is defined as the characteristic correlation time. From equilibrium distribution of energy, the local heat flux j_i can be described by a Normal law centered on 0 and with a standard deviation of $\sqrt{2}T$ and consequently, the total heat flux $\langle J^2\rangle = \langle\sum_{i=1}^N j_i\rangle = 2NT^2$. Concerning the correlation time, one can distinguish between three cases. For small enough temperatures such that particle mean free path is shorter than the distance between the sources, the correlation time is inversely proportional to the probability rate of interaction $\tau_{cor} = 1/\mathcal{P}$. For high energies E_0, the mean free path becomes larger than the distance between sources and the correlation time is then the transit time $\tau_s = N/2$. The threshold between collisional and ballistic regime is reached for $E_0 > \sqrt{N/2}E_{int} = E_{ball}$. One finally obtains

$$D \approx \begin{cases} 1 & \text{if} \quad E_0 \ll E_{int} \\ \left(\frac{E_0}{E_{int}}\right)^2 & \text{if} \quad E_{int} < E_0 < E_{ball} \\ \frac{N}{2} & \text{if} \quad E_{ball} < E_0 \end{cases} \tag{III.12}$$

For comparison, in Figure III.6 we report also the values of D computed by nonequilibrium simulations. Those are obtained by computing the average heat current divided by the applied gradient $2(\beta_c^{-1} - \beta_h^{-1})/N$. The temperature difference is fixed to 20% of the average, to insure that the gradient is small for the considered sizes. The current can be evaluated by averaging either the energies exchanged with the sources or the above defined current, J. Equality of such two quantities (within statistical fluctuations) is checked to

ensure that the steady state is attained on the time scale of the numerical simulations (typically 10^5 time steps). It is noteworthy that the canonical Green-Kubo data accounts very accurately for the nonequilibrium measurementts of the finite system.

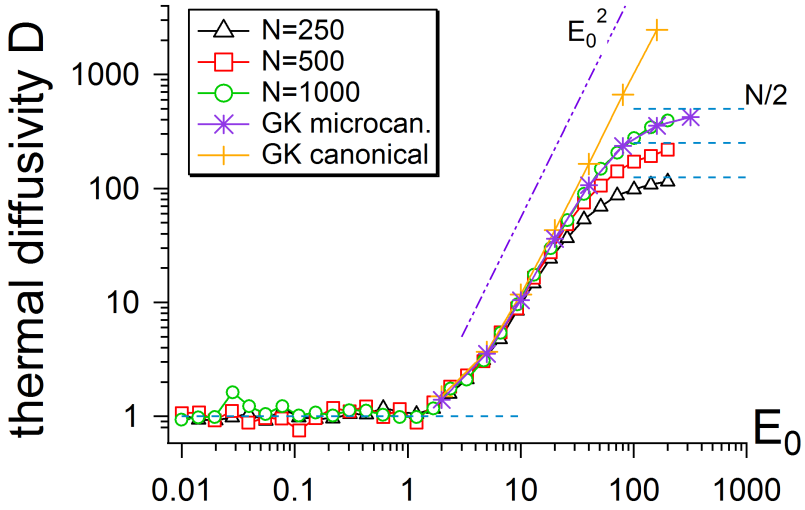

Figure III.6: Comparison of heat diffusivities computed by nonequilibrium simulations for three different lattice sizes (circles, squares and triangles) and with Kubo-Green formula ($N = 1000$, $E_{int} = 5$); stars and crosses correspond to the data with and without sources respectively. The horizontal lines mark the two asymptotic values $D \approx 1$ and $D \approx N/2$; for comparison we draw a line corresponding to $D \sim E_0^2$ (dash-dotted).

III.2.3 Generalized Fourier law

The first step to analyse the transport properties of the stochastic model is to determine whether the energy flux can be expressed using the linear–response approach. At a macroscopic level, one uses the most general linear relation between the energy current J and the local temperature gradient. Precisely, one can express the heat flux with a generalized Fourier law where J takes the form of the spatio-temporal convolution of the temperature gradient with a memory kernel K [52]

$$J(x,t) = -\int_{-\infty}^{\infty} dx' \int_{-\infty}^{t} dt' K(x-x', t-t') \frac{\partial T}{\partial x}(x',t') \tag{III.13}$$

The temporal evolution of the temperature field is given (up to some dimensional constant) by the heat equation:

$$\frac{\partial T}{\partial t}(x,t) = -\frac{\partial J}{\partial x}(x,t) \tag{III.14}$$

Making use of the Laplace-Fourier transform

$$\tilde{Y}(k,\omega) = \int_{-\infty}^{\infty} dx \int_{0}^{\infty} dt Y(x,t) e^{i(kx-\omega t)}$$

Equations III.13 and III.14 yield the relation

$$\tilde{T}(k,\omega) = \frac{\mathcal{F}[T(x,0)](k)}{i\omega - k^2\tilde{K}(k,\omega)} \tag{III.15}$$

The simplest phenomenological form of the kernel is the one in which memory decays exponentially in both time and space,

$$K(x,t) = \frac{D}{2\lambda\tau}\exp\left(-\frac{t}{\tau}\right)\exp\left(-\frac{|x|}{\lambda}\right) \tag{III.16}$$

where by τ and λ the characteristic time and space scales above which the heat transfer can be described by a diffusion process. In the definition we choose the coefficients in such a way that the usual Fourier law $J = -D\frac{\partial T}{\partial x}$ is recovered for a constant and time-independent temperature gradient. The Laplace-Fourier transform of K is thus given by

$$\tilde{K}(k,\omega) = \frac{D}{(1-i\tau\omega)(1+\lambda^2k^2)}. \tag{III.17}$$

This means that $\tilde{T}(k,\omega)$ may have poles at complex frequencies and thus that relaxation may occur in the form of damped heat waves [52]. In order to obtain some insight on what to expect from our model, let us for the moment drop the terms in λ. The Laplace-Fourier transform of the heat equation then reduces to

$$\tilde{T}(k,\omega) = \frac{\mathcal{F}[T(x,0)](k)\,(-i\omega + 1/\tau)}{-\omega^2 - i\omega/\tau + Ak^2} \tag{III.18}$$

which (assuming $\partial_t T(x,t) = 0$ for $t = 0$) is also the Laplace-Fourier transform of the telegraphist Equation [52].

$$\frac{\partial^2 T}{\partial t^2} + \frac{1}{\tau}\frac{\partial T}{\partial t} = A\frac{\partial^2 T}{\partial x^2} \tag{III.19}$$

For $\tau \ll 1$, that is to say a short mean free path, the telegraphist equation becomes the equation of diffusion with a diffusion coefficient $A\tau$. For $\tau \gg 1$, the first derivative vanishes and one finds the wave-propagation equation with a wave velocity $v = \sqrt{A}$.

III.2.4 Numerical evidences of memory effects

In this Section, we perform numerical simulations with the stochastic model to investigate if its behavior can be described by this effective formulation.

a) Equilibrium fluctuations

In this part, we study the spatio-temporal evolution of the fluctuations around equilibrium. To compare with the above hydrodynamic approach, we compute numerically the dynamical structure factor $\langle|\tilde{E}(k,\omega)|\rangle$, where $\tilde{E}(k,\omega)$ is the the spatio-temporal Fourier transform of the energy field $E_i(t)$. As usual, $\langle\cdot\rangle$ denotes the average over several realisa-

tions. One tries to fit the results obtained numerically with the formula found analytically for the time and space exponential memory Kernel. According to Equations III.15 and III.17 one obtains

$$\langle|\tilde{E}(k,\omega)|^2\rangle = \frac{T_0^2(\omega^2+1/\tau^2)}{(\omega^2-\omega_0^2)^2+(\omega/\tau)^2} \tag{III.20}$$

with

$$\omega_0^2 = \frac{D}{\tau}\frac{k^2}{1+\lambda^2 k^2} \tag{III.21}$$

To derive Equation from III.20 from III.15 we let

$$\langle|\tilde{E}(k,\omega)|^2\rangle = \langle|\tilde{T}(k,\omega)|^2\rangle$$

and assume that average over the initial random conditions of $\mathcal{F}[T(x,0)]$ yields a constant denoted by T_0.

The numerical results and fits are plotted in Figure III.7 in the case $E_0 = E_{int} = 5$. For high values of k ($k = 0.1$), i.e. at small scales, we observe a peak at finite frequency that indicates some kind of oscillating response, that is the propagation of damped temperature waves. On the contrary, at large scales ($k = 0.01$), the peak disappears and the spectrum shows a monotonic decay that signals the onset of a diffusive behavior. We have also observed that for small (large) values of E_0, i.e. at low (high) temperature, the behavior is diffusive (ballistic) for all values of k.

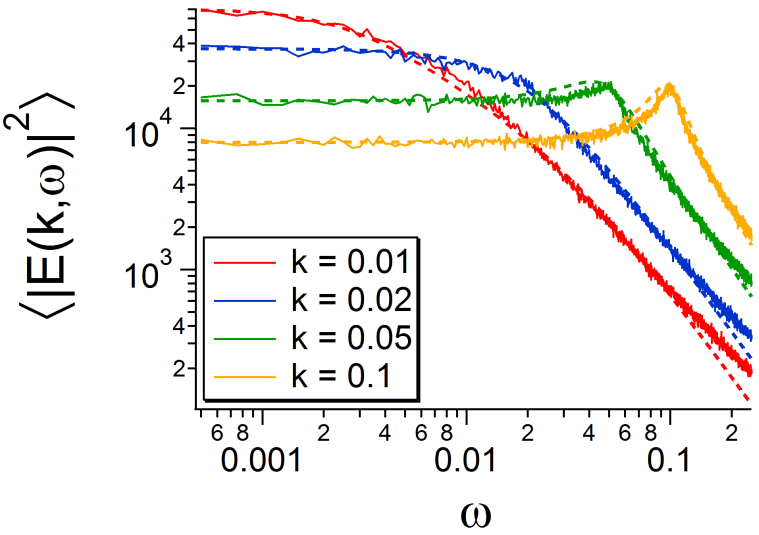

Figure III.7: Dynamical structure factor for $E_0 = 5$. One notices the resonance for high values of k denoting a ballistic transport at small scales that differs from the diffusive transport at large scales (no-resonance for low value of k). The low-frequency part of the data have been fitted with the function $B/[(\omega^2-\omega_0^2)^2+(\omega/\tau)^2]$ derived by III.20 under the approximation $\omega \ll 1/\tau$ where the numerator symplifies to a constant.

Moreover, we finds that ω_0 is approximately proportional to k. i.e. typically we are dealing with regimes where $\lambda k \ll 1$. For what τ is concerned one finds that it scales as

$\tau \sim E_0^2$, which is consistent with the data shown in Figure III.4.

b) Evolution of perturbations

The dynamics of disturbances is a typical nonstationary heat conduction problem [53, 54]. From Equation (III.18) it is expected that their propagation would display a transition from a diffusive to a wave-like propagation behavior upon increasing the energy. Numerical studies have been performed by "thermalizing" the lattice at energy E_0 according to a Maxwell-Boltzmann distribution and then heating a small domain of the lattice at the energy $1.5E_0$. Figure III.8 shows this finite amplitude perturbation propagates in space and time for different values of E_0.

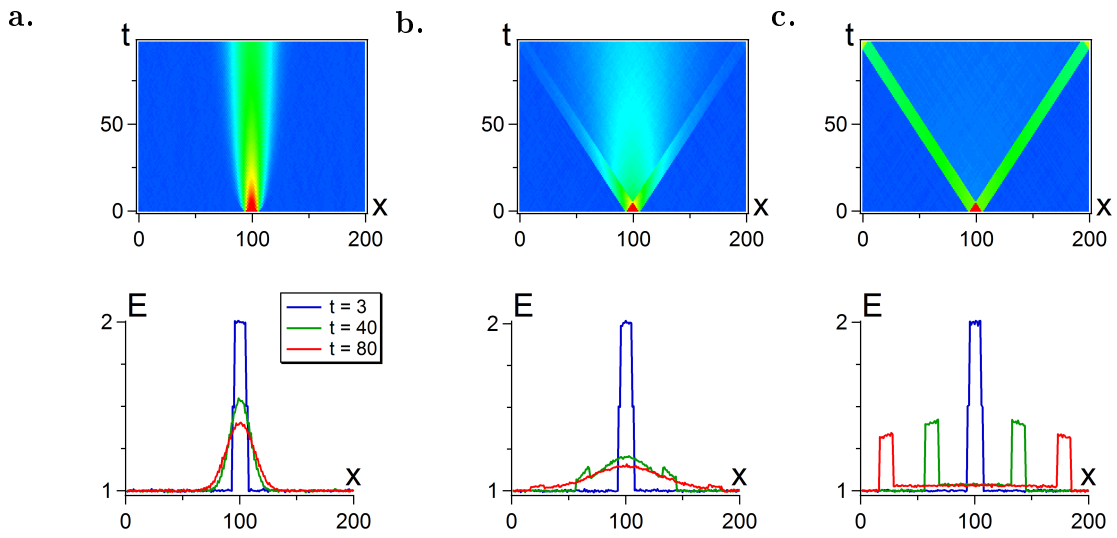

Figure III.8: Propation of a perturbation for different temperature. a: Low temperature $E_0/E_{int} = 0.2$ (diffusive transport) - b: Intermediate temperature $E_0/E_{int} = 1$ - c: High temperature $E_0/E_{int} = 4$ (ballistic transport)

It can be observed that for small values of E_0 the perturbation diffuses, whereas for $E_0/E_{int} \gg 1$ one observes the ballistic propagation of two temperature fronts, in qualitative agreement with the telegraphist Equation (III.19).

c) Temperature profiles at steady-state

In Figure III.9 we plotted three temperature profiles at steady-state for different values of the initial average temperature of the system E_0. For each case, the temperatures of the source are chosen as $E_{\text{hot}}/E_0 = 105\%$ and $E_{\text{cold}}/E_0 = 95\%$. One plots the average temperature E_i as well as the forward-going and backward-going particles temperature ($E_i^{\pm}$). One notices that for low values of temperature, one has $E_i \approx E_i^+ \approx E_i^-$ and one recovers a quasi-linear profile interpolating between the two sources temperatures that is similar to the temperature profile that could be found considering the Fourier law $J = -\kappa \nabla T$. On the countrary, when the temperature is higher, one observes a departure

between E_i^+ and E_i^- that is a consequence of the weakness of the interaction for such temperatures. This difference between E_i, E_i^+ and E_i^- can be seen as the failure of local thermal balance. In this case, the heat transport between the sources is obviously ballistic. When one considers the profile of the average temperature, one notices a quasi-linear profile in the region between the sources. However, one observes steep temperature gradients close to the sources. This suggests te existence of a boundary layer around sources position.

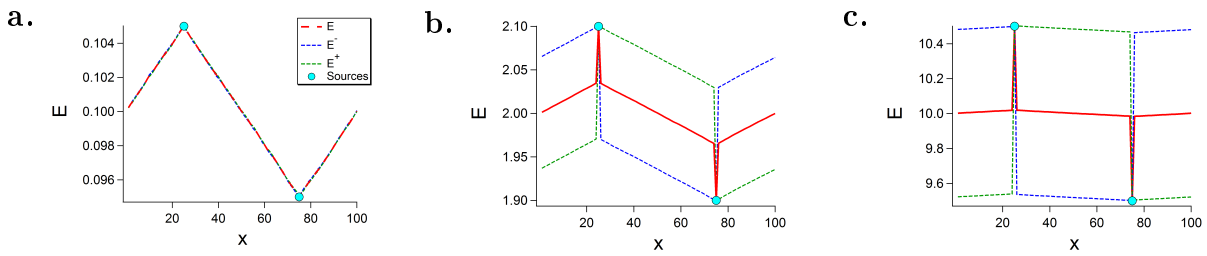

Figure III.9: Temperature profiles at steady-states with sources for different values of E_0 (a: $E_0 = 0.1$, b: $E_0 = 2$, c: $E_0 = 10$). For all cases, $E_{int} = 0.5$. On the second figure is also plotted in dashed line the solution of the heat Equation using flux expression given by Equation III.22

A possible explanation can be drawn by solving Equation (III.14) with the kernel of Equation (III.16).

$$J(x) = -\frac{D}{2\lambda}\int_{-\infty}^{\infty} dx' \exp\left(-\frac{|x-x'|}{\lambda}\right)\frac{\partial T}{\partial x}(x') \tag{III.22}$$

This expression is quite similar to the one proposed by Luciani [38] to describe heat flux for steep temperature gradients in plasma. The profiles obtained fit quite well with the steady-state solution of the stochastic model (see Figure III.9). Notice that the solution correctly reproduces the temperature drops at the sources, that could not be obtain by the standard Fourier law. More precisely, the Fourier transform of the heat equation gives according to Equation III.17

$$\frac{Dk^2}{1+\lambda^2 k^2}\tilde{T} = \tilde{S} \tag{III.23}$$

where $\tilde{S}$ denotes the Fourier transform of the sources. One notices that this equation can be rewritten as

$$T(x) = T(0) + \frac{1}{D}\int_0^x dx' \int_0^{x'} dx'' S(x'') + \frac{\lambda^2}{D}S(x) \tag{III.24}$$

where $S(x) = S_0(\delta(x-x_h)-\delta(x-x_c))$ in the case we consider here. The first contribution describes solution of the standard diffusion law. It is the dominant term if $\lambda^2 \ll D$. The second term that becomes dominant if λ is important traduces non local effects and causes the strong gradients localized near sources.

III.2.5 Spatial correlations in the nonequilibrium steady state

In this section, we consider the steady nonequilibrium state with heat sources at differrent temperatures.

Analogously to what found in other stochastic and deterministic models [48, 55, 50], we expect the onset of a non-zero heat flux to be characterized by long-range spatial correlations. In the KMP model, correlations are given by the expression (see [41])

$$C_{ij}^{x} = \begin{cases} \frac{(T_1-T_0)^2}{N+1}\frac{i}{N}\left(1-\frac{j}{N}\right) \\ \quad \text{if} \quad 0 \leq i < j \leq N \\ \\ \langle E_i \rangle^2 + 2\frac{(T_1-T_0)^2}{N+1}\frac{i}{N}\left(1-\frac{i}{N}\right) + \frac{(T_1-T_0)^2}{N(N+1)} \\ \quad \text{if} \quad 0 \leq i = j \leq N \end{cases} \tag{III.25}$$

where the spatial autocorrelation function C_{ij}^{x} is defined as

$$C_{ij}^{x} = \langle E_i E_j \rangle - \langle E_i \rangle \langle E_j \rangle \tag{III.26}$$

and $\langle E_i \rangle$ denotes the value of the mean energy at site i.

$$\langle E_i \rangle = T_0 + (T_1 - T_0)\frac{i}{N} \tag{III.27}$$

We have computed numerically C_{ij}^{x} for our model. For low values of E_0 (diffusive regime) data agrees with theoretical predictions (that are essentially equivalent in the KPM model), while for large values of $E - 0$ (ballistic regime) no spatial correlation is present (see Figure III.10).

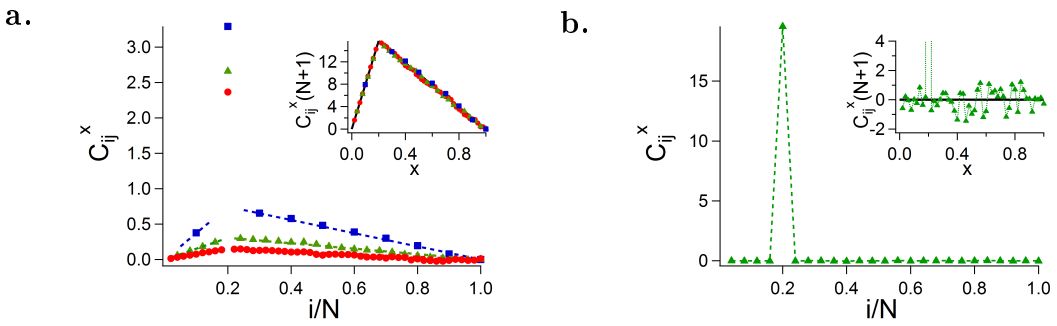

Figure III.10: Spatial correlation function close to the cold source for different value of interaction temperature (a: $E_{int} = 0.001$, b: $E_{int} = 1000$). Results show spatial correlations at low temperature (left) in good agreement with analytical model developped in reference [41] plotted with lines for different system size N. At high temperature (right), the spatial correlations disappear.. In these simulations, one has $T_1 = 10$ and $T_0 = 0.1$.

III.2.6 Discussion and heat flux expression

The stochastic model presented in this section well reproduces the transition from collisional to ballistic transport. In any case, the heat flux can be expressed according to the generalized Fourier law

$$\boxed{q = -\int_{-\infty}^{\infty} dx' \int_{-\infty}^{t} dt' K(x-x', t-t') \nabla T = -K * \nabla T} \tag{III.28}$$

where the kernel is given by

$$\boxed{K(x-x', t-t') = K_0 \exp\left(-\frac{|x-x'|}{\lambda}\right)\left(-\frac{t-t'}{\tau}\right)} \tag{III.29}$$

where λ is the collision mean free path and τ the collision time. This formulation is consistent with the non-local formulation of Luciani. The temporal correlation ingredient is added providing the possibility to catch wave like propagation of heat in the system. The impact of such an expression for heat flux in 1D systems and in SolEdge2D is now presented.

III.3 Introduction of non-local ingredients in SolEdge2D

The non-local expression for heat flux is implemented in SolEdge2D. The spatial memory kernel and the heat flux are defined as

$$q(x) = -\int dx' \frac{K_0}{\lambda} \exp\left(-\frac{|x-x'|}{\lambda}\right) \frac{\partial T}{\partial x}(x') \tag{III.30}$$

The integral bounds depend whether one considers open or closed field lines. The integration domains are represented on Figure III.11. For a closed field line, the integral bounds corresponds to the points where the field line intercept the solid. The heat flux is given in this case by Equation III.31.

$$\textbf{Non-periodic case:} \qquad q(x) = \int_{0}^{L_\parallel} dx' \mathcal{K}(x') \tag{III.31}$$

Conversely, if one condiders open field line, the domain is periodic and denoting $L_\parallel$ the magnetic field line length, the heat flux expresses as

$$\textbf{Periodic case:} \qquad q(x) = \int_{x-L_\parallel/2}^{x+L_\parallel/2} dx' \mathcal{K}(x') \tag{III.32}$$

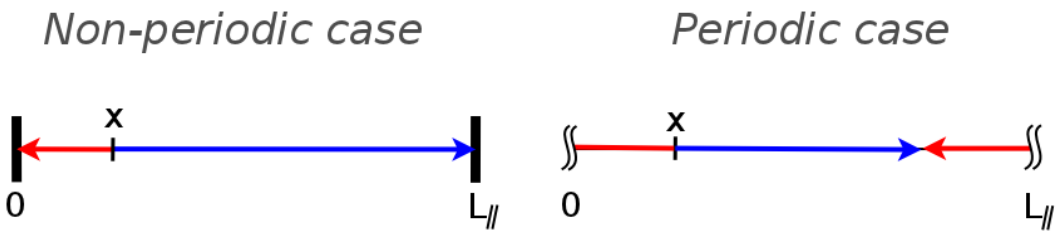

Figure III.11: Sketch of the integration domain used to compute non-local heat flux in the closed and open field line case.

A simplified heat equation is considered:

$$n\frac{\partial T}{\partial t} + \frac{\partial q}{\partial x} = S \tag{III.33}$$

This reduced equation is used to study the numerical discretization of the non-local heat flux. With centered finite differences, one has

$$\frac{\partial q}{\partial x} = \frac{q^R_{i+1} - q^L_{i-1}}{x_{i+1} - x_{i-1}}$$

with the integral expression

$$q^R_{i+1} = \sum_{j=0}^{N} K(i+1, j+1)\,(T_{j+1} - T_j) \tag{III.34}$$

$$q^L_{i-1} = \sum_{j=0}^{N} K(i-1, j)\,(T_{j+1} - T_j) \tag{III.35}$$

where N denotes the number of grid points in the parallel direction. According to the kernel definition

$$K(i,j) = -\frac{K_0}{\lambda}\exp\left(\frac{d(x_i, x_j)}{\lambda}\right) \tag{III.36}$$

$d(x_i, x_j)$ denotes the distance between the point x_i and x_j. For the closed field line case, this distance is given by $d(x_i, x_j) = |x_i - x_j|$. For the open field line case, the distance is given by the algorithm

$d(x_i, x_j) \leftarrow x_i - x_j \mod L_\parallel$
if $d(x_i, x_j) > \frac{L_\parallel}{2}$ then
    $d(x_i, x_j) \leftarrow |d(x_i, x_j) - L_\parallel| \mod \frac{L_\parallel}{2}$
end

The discrete heat Equation III.33 is rewritten using the above expressions:

$$\begin{aligned} n_i\frac{\partial T_i}{\partial t} - S_i &= \frac{1}{x_{i+1}-x_{i-1}}\sum_{j=0}^{N} K(i+1,j+1)\left(T_{j+1}-T_j\right) - K(i-1,j)\left(T_{j+1}-T_j\right) \\ &= \frac{1}{x_{i+1}-x_{i-1}}\left[\sum_{j=0}^{N}\left(K(i-1,j)-K(i+1,j+1)\right)T_j + \sum_{j=1}^{N+1}\left(K(i+1,j)-K(i-1,j-1)\right)T_j\right] \\ &= \frac{1}{x_{i+1}-x_{i-1}}\sum_{j=1}^{N}\left[K(i-1,j)-K(i+1,j+1)+K(i+1,j)-K(i-1,j-1)\right]T_j \\ &\quad + \frac{1}{x_{i+1}-x_{i-1}}\left[K(i-1,0)-K(i+1,1)\right]T_0 \\ &\quad + \frac{1}{x_{i+1}-x_{i-1}}\left[K(i+1,N+1)-K(i-1,N)\right]T_{N+1} \end{aligned} \tag{III.37}$$

In the non-periodic case, the values T_0 and T_{N+1} are determined using boundary conditions. In the periodic case, $T_0 = T_N$ and $T_{N+1} = T_1$. This system of equation is solved implicitely as

$$\boxed{\left(\frac{n_i}{\delta t}\mathbb{I} - D_{ij}\right)\cdot T_j^{t+1} = \frac{n_i T_i^t}{\delta t} + S_i} \tag{III.38}$$

where in the simple case, the matrix (D_{ij}) is given by

$$\boxed{D_{ij} = \frac{1}{x_{i+1}-x_{i-1}}\left[K(i-1,j)-K(i+1,j+1)+K(i+1,j)-K(i-1,j-1)\right]} \tag{III.39}$$

The matrix expression can be modified by boundary conditions:

- **For the periodic case:**
  Since $T_0 = T_N$ and $T_{N+1} = T_1$, the above expression is correct if $j \neq 1$ and $j \neq N$. Otherwise:

$$\begin{aligned} D_{i1} &= \frac{1}{x_{i+1}-x_{i-1}}\left[K(i-1,1)-K(i+1,2)+K(i+1,1)-2K(i-1,N)+K(i+1,1)\right] \\ D_{iN} &= \frac{1}{x_{i+1}-x_{i-1}}\left[2K(i-1,N)-K(i+1,1)+K(i+1,N)-K(i-1,N-1)-K(i+1,1)\right] \end{aligned}$$

- **For the non-periodic case:**
  the sheath transmission relation are imposed:

$$\begin{aligned} q_{cond} &= \left(\gamma_\alpha - \frac{5}{2}\right)k_B n T_\alpha u_\parallel \\ \textbf{BC:}\quad \int_0^{L_\parallel} dx' K(x-x',t-t')\nabla T_\alpha(x') &= \left(\gamma_\alpha - \frac{5}{2}\right)k_B n T_\alpha u_\parallel \end{aligned}$$

Following the expressions for the heat fluxes (Equations III.34 & III.35),

$$\begin{aligned} q_0^L &= \sum_{j=0}^{N} K(0,j)\,(T_{j+1}-T_j) \\ &= \left(\gamma_\alpha - \frac{5}{2}\right) k_B n T_\alpha u_\parallel \\ T_0 &= T_1 + \frac{1}{K(0,0)} \left\{ \sum_{j=1}^{N} K(0,j)\,(T_{j+1}-T_j) - \left[\left(\gamma_\alpha - \frac{5}{2}\right) k_B n T_\alpha u_\parallel\right]_L \right\} \end{aligned}$$

Likewise

$$\begin{aligned} q_{N+1}^R &= \sum_{j=0}^{N} K(N+1,j+1)\,(T_{j+1}-T_j) \\ &= \left(\gamma_\alpha - \frac{5}{2}\right) k_B n T_\alpha u_\parallel \\ T_{N+1} &= T_N - \frac{1}{K(N+1,N+1)} \left\{ \sum_{j=0}^{N-1} K(N+1,j+1)\,(T_{j+1}-T_j) - \left[\left(\gamma_\alpha - \frac{5}{2}\right) k_B n T_\alpha u_\parallel\right]_R \right\} \end{aligned}$$

The expression for T_{N+1} must be reported in T_0 expression. Finally, one obtains

$$\begin{aligned} T_0 &= T_1 + \beta_0 \sum_{j=2}^{N-1} \left[K_0^{j-1} - K_0^j - \frac{K_0^N (K_{N+1}^j - K_{N+1}^{j+1})}{K_{N+1}^{N+1}} \right] T_j \\ &\quad + \beta_0 \left(K_0^{N-1} - \frac{K_0^N K_{N+1}^N}{K_{N+1}^{N+1}} \right) T_N - \beta_0 \left(K_0^1 - \frac{K_0^N K_{N+1}^2}{K_{N+1}^{N+1}} \right) T_1 \\ &\quad + \beta_0 \frac{K_0^N}{K_{N+1}^{N+1}} \left[\left(\gamma_\alpha - \frac{5}{2}\right) k_B n T_\alpha u_\parallel\right]_R - \beta_0 \left[\left(\gamma_\alpha - \frac{5}{2}\right) k_B n T_\alpha u_\parallel\right]_L \\ T_{N+1} &= T_N - \beta_N \sum_{j=2}^{N-1} \left[K_{N+1}^j - K_{N+1}^{j+1} - \frac{K_{N+1}^1 (K_0^{j-1} - K_0^j)}{K_0^0} \right] T_j \\ &\quad - \beta_N \left(K_{N+1}^N - \frac{K_{N+1}^1 K_0^{N-1}}{K_0^0} \right) T_N + \beta_N \left(K_{N+1}^2 - \frac{K_{N+1}^1 K_0^1}{K_0^0} \right) T_1 \\ &\quad - \beta_N \frac{K_{N+1}^1}{K_0^0} \left[\left(\gamma_\alpha - \frac{5}{2}\right) k_B n T_\alpha u_\parallel\right]_L + \beta_N \left[\left(\gamma_\alpha - \frac{5}{2}\right) k_B n T_\alpha u_\parallel\right]_R \end{aligned}$$

with

$$\beta_0 = \frac{K_{N+1}^{N+1}}{K_0^0 K_{N+1}^{N+1} - K_0^N K_{N+1}^1} \qquad \text{and} \qquad \beta_N = \frac{K_0^0}{K_0^0 K_{N+1}^{N+1} - K_0^N K_{N+1}^1}$$

Reporting into Equation III.37 gives the expression for the matrix D'_{ij} including boundary

condition.

$$D'_{i1} = D_{i1} + \frac{K^0_{i-1} - K^1_{i+1}}{x_{i+1} - x_{i-1}} \left[1 - \beta_0 \left(K^1_0 - \frac{K^N_0 K^2_{N+1}}{K^{N+1}_{N+1}} \right) \right] + \frac{K^{N+1}_{i+1} - K^N_{i-1}}{x_{i+1} - x_{i-1}} \beta_N \left(K^2_{N+1} - \frac{K^1_{N+1} K^1_0}{K^0_0} \right) \quad \text{(III.40)}$$

$$D'_{ij} = D_{ij} + \frac{K^0_{i-1} - K^1_{i+1}}{x_{i+1} - x_{i-1}} \beta_0 \left[K^{j-1}_0 - K^j_0 - \frac{K^N_0 (K^j_{N+1} - K^{j+1}_{N+1})}{K^{N+1}_{N+1}} \right] - \frac{K^{N+1}_{i+1} - K^N_{i-1}}{x_{i+1} - x_{i-1}} \beta_N \left[K^j_{N+1} - K^{j+1}_{N+1} - \frac{K^1_{N+1} (K^{j-1}_0 - K^j_0)}{K^0_0} \right] \quad \text{(III.41)}$$

$$D'_{iN} = D_{iN} + \frac{K^0_{i-1} - K^1_{i+1}}{x_{i+1} - x_{i-1}} \beta_0 \left[K^{N-1}_0 - \frac{K^N_0 K^N_{N+1}}{K^{N+1}_{N+1}} \right] + \frac{K^{N+1}_{i+1} - K^N_{i-1}}{x_{i+1} - x_{i-1}} \left[1 - \beta_N \left(K^N_{N+1} - \frac{K^1_{N+1} K^{N-1}_0}{K^0_0} \right) \right] \quad \text{(III.42)}$$

The source term becomes

$$\mathcal{S}'_i = \mathcal{S}_i + \frac{K^0_{i-1} - K^1_{i+1}}{x_{i+1} - x_{i-1}} \beta_0 \left\{ \frac{K^N_0}{K^{N+1}_{N+1}} \left[\left(\gamma_\alpha - \frac{5}{2} \right) k_B n T_\alpha u_\parallel \right]_R - \left[\left(\gamma_\alpha - \frac{5}{2} \right) k_B n T_\alpha u_\parallel \right]_L \right\} - \frac{K^{N+1}_{i+1} - K^N_{i-1}}{x_{i+1} - x_{i-1}} \beta_N \left\{ \frac{K^1_{N+1}}{K^0_0} \left[\left(\gamma_\alpha - \frac{5}{2} \right) k_B n T_\alpha u_\parallel \right]_L - \left[\left(\gamma_\alpha - \frac{5}{2} \right) k_B n T_\alpha u_\parallel \right]_R \right\} \quad \text{(III.43)}$$

Let us consider a regular mesh with $N = 20$. The mesh length is $\delta x = L_\parallel/20$. The matrix (D_{ij}) is represented on Figure III.12 for $\lambda = L/100$ and $\lambda = L$. In the first case,

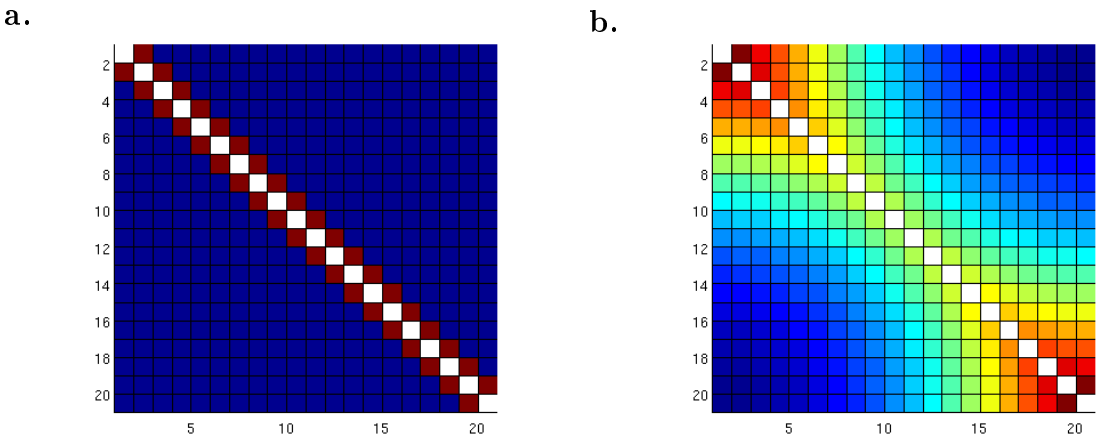

Figure III.12: Non-diagonal terms of the generalize diffusion matrix D for a 20-points grid. a: $\lambda = L/100$ standard diffusion case. b: $\lambda = L$ strong non local effects.

the mean free path is much smaller than mesh resolution and the typical tri-diagonal matrix characteristic of diffusion problems is recovered (second order):

$$\textbf{Diffusion – tri-diagonal:} \qquad D \frac{\partial^2 T}{\partial x^2} = \mathcal{S} \quad \Leftrightarrow \quad \frac{T_{i+1} - 2T_i + T_{i-1}}{2\delta x^2} = \frac{\mathcal{S}_i}{D} \quad \text{(III.44)}$$

Conversely, if the mean free path is much larger than mesh size (second case), the general diffusion matrix is non-sparse, expressing the long-range interactions and non-locality.

Numerically, the non-sparse matrix is inverted using the LAPACK library. Numerical techniques to solve the non-local problem are reported in the literature [56, 57, 58]. The method presented above may show non-physical oscillations in the temperature profiles. Further work will be necessary to properly implement that non-local form in SolEdge2D and ensure a stable behavior for the convergence.

As a preliminary results, Equation III.45 is solved

$$\frac{\partial T}{\partial t} + \frac{\partial q}{\partial x} = S_0 \tag{III.45}$$

where the heat flux is given by

$$q = -K \int dx' \exp\left(-\frac{|x - x'|}{\lambda}\right) \frac{\partial T}{\partial x}(x')$$

If a constant temperature gradient is considered, one has $q = -K\lambda\nabla T$, the "effective" diffusion coefficient is thus proportional to λ. The source S_0 is constant in the entire simulation domain and the boundary condition $q = AT^{3/2}$ are considered. This boundary condition is similar to the one obtained with sheath transmission coefficients boundary condition. This system is solved for different λ values and results are shown on Figure III.13. As λ increases, the temperature profiles get flatter since the "effective" diffusion coefficient is larger. Also, if the mean free path λ is comparable with system size L, steep temperature gradients are localized on the domain boundary. This boundary layer discontinuity is the same as the one observed in the stochastic model around dirac energy sources. Due to the non-locality of transport (lack of local thermalization), a discontinuity develops between the plasma domain and the wall that is ruled by different physical mechanisms.

III.4 Discussion on discontinuities, boundary conditions and boundary layers

In the previous paragraph, discontinuities seem to appear in the heat equation solution if non-local operators are considered. One investigates whether these discontinuities have a physical meaning or are just spurious effects due to an ill formulated expression for heat flux.

Let us recall where the discontinuity appears. In paragraph III.2.4-c), an analytical solution for the heat equation has been found in the periodic case. If the energy source is given by $S(x)$, the temperature profile, solution of the heat equation with a non-local

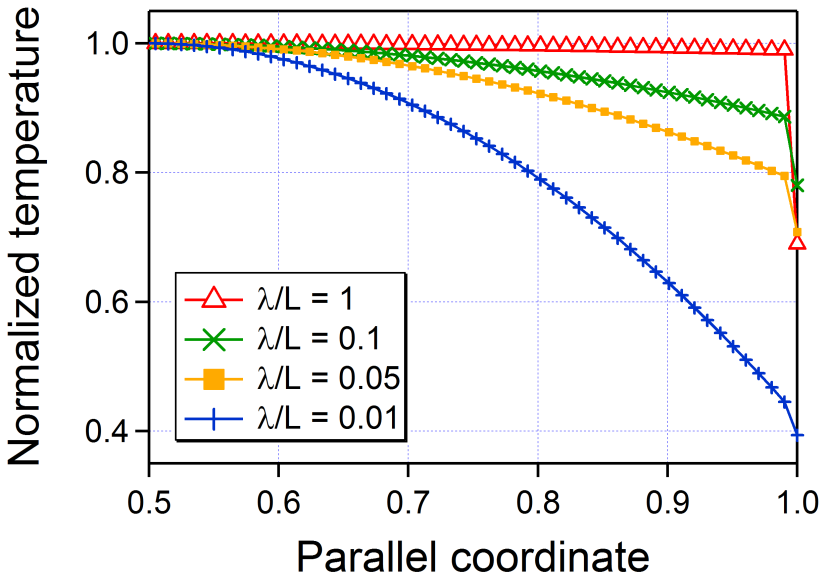

Figure III.13: Numerical results for different collisionalities. The outflux on both sides of the domain is imposed (for symmetry reason, only one side is shown). For low collisionality, notice the flat temperature profile with high temperature jump at the boundary. For high collisionality, one gets a continuous temperature drop without discontinuity at the boundary

exponential kernel heat flux is given by Equation III.24 that is

$$T(x) = T(0) + \frac{1}{D}\int_0^x dx' \int_0^{x'} dx'' S(x'') + \frac{\lambda^2}{D} S(x) \tag{III.46}$$

The continuity of the temperature field is thus conditionned by the continuity of the sources. More precisely, if discontinuous sources are considered, the last term in the above equation states that the temperature profile will be discontinuous as well. The study of the underlying stochastic model enables to exhibit the physical mechanisms leading to this discontinuity. The first ingredient, once again, is a discontinuity in the source profile. Second ingredient, the thermalization processes between the plasma particles with the sources must be stronger than the thermalization processes between the particles themselves. This can be expressed in term of thermalization scales. In particular, the thermalization scale between the particles is the collision mean free path. In the stochastic model presented in paragraph III.2.4-c), the coupling with the source if infinitely efficient and the thermalization length with the source is zero. As long as the collision mean free path is non-zero, a discontinuity occures near the source (as confirmed by Equation III.46). If the mean free path is zero, one recovers a continuous solution for temperature, even if the source is discontinuous.

In the case where sources are removed and if the flux is imposed as boundary condition instead, discontinuities are also observed at the boundary. This case is important since it is the one encountered in the SOL where the energy flux at sheath entrance is prescribed by

sheath properties. For instance, let us consider that the heat equation is solved imposing zero energy outflux at the boudary. Let us consider the domain $x \in [0,1]$ where heat equation yields at steady state

$$\frac{\partial}{\partial x}\left(\int_0^1 \exp\left(-\frac{|x-x'|}{\lambda}\right)\frac{\partial T}{\partial x}(x')dx'\right) = S(x) \tag{III.47}$$

The integral of the source is zero in order to get a steady state solution. Integrating over x and using $q(0) = 0$, the temperature gradient is the solution of the Fredholm equation of the first type:

$$\int_0^1 \exp\left(-\frac{|x-x'|}{\lambda}\right)\frac{\partial T}{\partial x}(x')dx' = Q(x) \tag{III.48}$$

with $Q(x) = \int_0^x S(x')dx'$. It is unclear whether this equation admits continuous solutions. Further investigations on Fredholm equation properties must be done at this stage. Numerical results are presented for a high and low collisonality case on Figure III.14. Whatever the resolution of the numerical grid, a discontinuity develops in the low collisionality case on the domain boundary. To what extent is this dicontinuity physical? This discontinuity issue have been reported for neutral fluids in Knudsen layers. A dedicated work has then been achieved to find appropriate boundary conditions for this kind of systems [59].

Let us go back to the kinetic description. It is unlikely that particles velocity distribution function f is discontinuous at sheath entrance. Even if they are very weak, collisions express as a diffusive operator in the velocity space ensuring continuity in the velocity space. Regularization processes transfer this continuity into the physical space. These smoothening effects can be seen as the consequence of the probabilistic description of particles. Indeed, as mentionned by Cédric Villani in [60]:

> *"Underlying kinetic theory is the modelling assumption that the gas is made of so many particles that it can be treated as a continuum. In fact there are two slightly different ways to consider f : it can be seen as an approximation of the true density of the gas in phase space (on a scale which is much larger than the typical distance between particles), or it can reflect our lack of knowledge of the true positions of particles".*

In any case, if the distribution function is continuous, so are its moments and thus temperature field (defined as second order moment and not as the "true" thermodynamic Temperature at equilibrium). The discontinuity observed with the non-local model still has to be understood properly. Comparison between fluid results with non-diffusive heat flux and kinetic simulations must be performed. This work in progress is an interesting perspective to this manuscript.

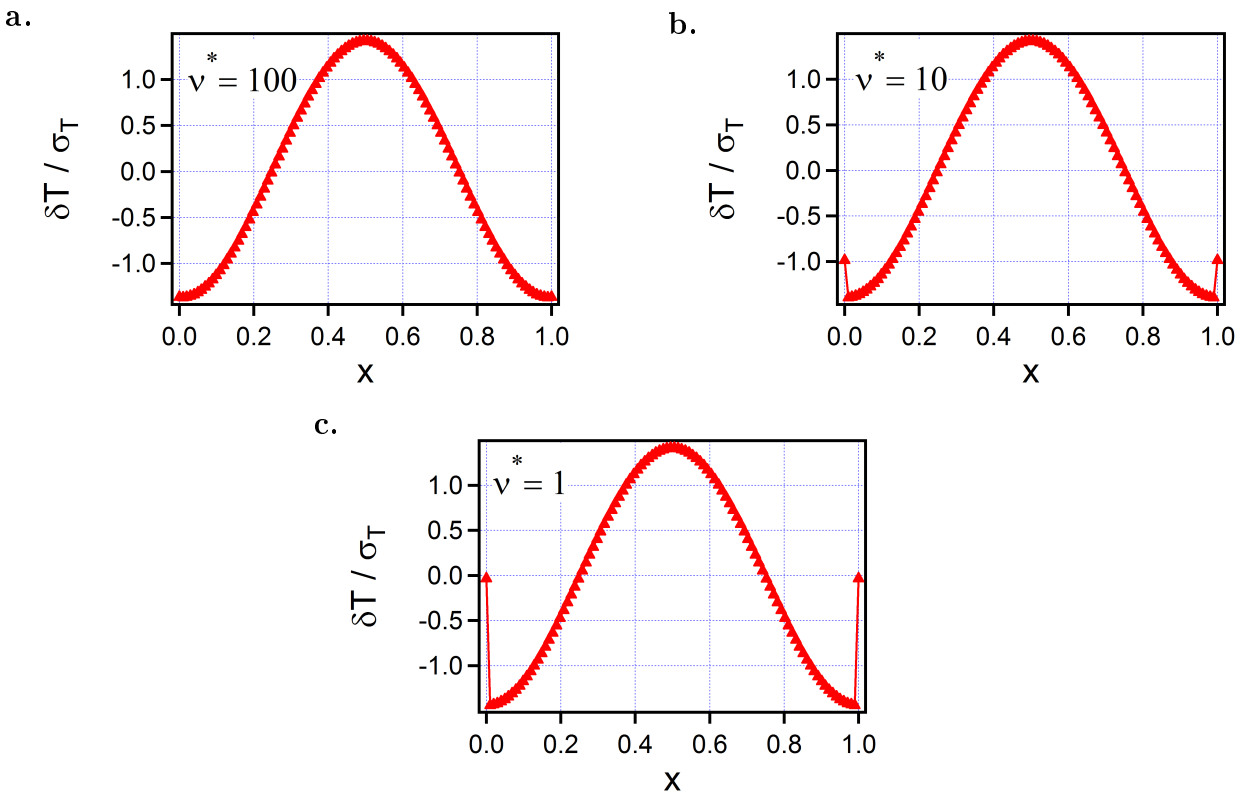

Figure III.14: Numerical results for Fredholm Equation III.48 solving heat equation with a non-local exponential kernel. The heat flux on domain boundary is set to zero. The normalized temperature fluctuations about the average temperature ($\delta T = T - \langle T \rangle$) are plotted as a function of the spatial coordinate x. The source $S(x)$ is given by $S(x) = -S_0 \cos(2\pi x)$. Simulations are performed for different collisionalities $\nu^\star = L/\lambda$ where L (resp. λ) denotes system size (resp. kernel mean free path): a. Collisional $\nu^\star = 100$; b. Intermediate $\nu^\star = 10$; c. Weakly collisional $\nu^\star = 1$. A discontinuity arises at domain boundaries when collisionality drops. For the collisional case, according to Fourier's law, the heat flux cancels out by setting temperature gradient to zeros: $q_{BC} = -\kappa \nabla T = 0$.

Chapter highlights

- *At low collisonality, the diffusive description for the collisional transport fails.*
- *Several corrections to the diffusive law can be found in the literature including flux limiter formulations.*
- *A simple stochastic model for collisional transport has been developped. The study of transport properties including temporal and spatial correlations has permitted expressing the flux in a non-local generalized Fourier's law where and exponential kernel describes temporal and spatial memory effects:*

$$q(x,t) = \int_{-\infty}^{t} dt' \exp\left(-\frac{t-t'}{\tau}\right) \int_{a}^{b} dx' \exp\left(-\frac{|x-x'|}{\lambda}\right) \nabla T(x',t')$$

  This formulation is consistent with the one formerly formulated by Luciani in its reference paper [38].

- *Discontinuities can appear in the temperature field with this formulation about sources or at domain boundaries. The physical meaning of those discontinuities is still under investigation.*

Chapter IV

Transport of neutrals

Content

The localization of ionization and radiation sources governs edge plasma physics. The study of neutrals trajectories suggests that their mean free path is of the order of the tokamak size. Using non-local formulations, a fluid description is investigated to describe neutrals transport. More precisely, a generalized diffusion law is implemented in SolEdge2D. Finally, to obtain a self-consistent description of the neutral physics SolEdge2D has been coupled with the Monte-Carlo neutral code Eirene.

IV.1 Neutrals in plasma

In section I.5, the mechanism taking place when the impinging plasma interact with a solid component has been shortly described. When plasma ions encounter the wall, a fraction recombines in the solid and can be latter re-emited in the plasma as neutral atoms or molecules. At steady state, up to 95% of the plasma flow can be re-injected in the plasma as neutrals. The transport of neutrals is governed in particular by the ions-neutral and neutral-neutral collisions. The molecules also encounters several dissociation where the molecule initial momentum is redistributed to the different chemical species resulting of the molecule dissociation. Figure IV.1 represents the typical path of a D_2 molecule in the plasma.

Several numerical methods can be used to simulate these different processes. In a first section, a simple fluid model for neutrals is presented. This model aims at capturing the overall impact of neutrals on plasma flow. In this model, only one neutral species is considered and is transported with the same kind of non-local transport formulation as those found for heat flux in the previous chapter. Secondly, one introduces the neutral code Eirene developped in Jülich that fully describes neutral collisions and chemistry using Monte-Carlo algorithm.

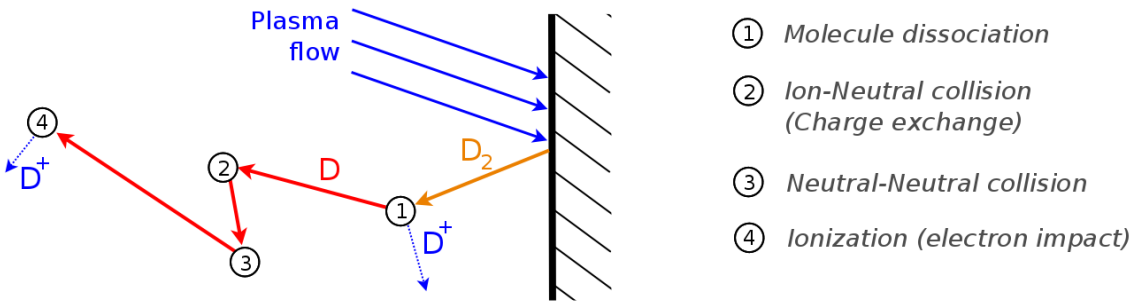

Figure IV.1: Example of neutral typical life in the plasma from molecule emission to atom ionization.

IV.1.1 The plasma density regimes - Two-points model

One of the major problem in edge plasma physics consists in evaluating heat load impacting plasma facing components. Let us consider the two points model, the first point being located upstream from the wall at the stagnation point, the second point being at sheath entrance (on the target). n_u and T_u (resp. n_t and T_t) denote the density and temperature at the upstream point (resp. on the target). $q_\parallel$ denotes the energy flux flowing along the field line. The energy source is considered to be located at the upstream point, hence $q_\parallel$ is conserved all along the SOL. The configuration is represented in Figure IV.2.

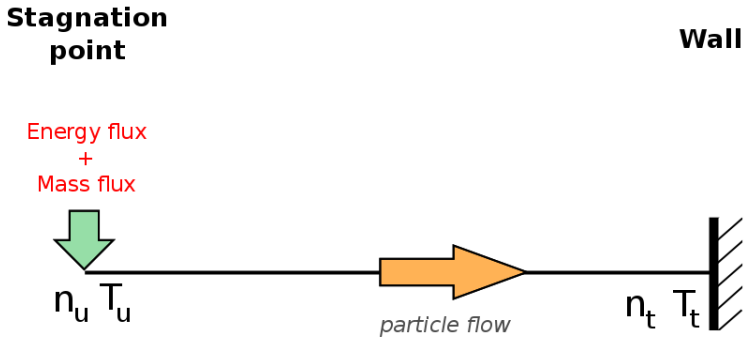

Figure IV.2: 2-points model configuration. The upstream point is located at the stagnation point. One considers here that the whole perpendicular mass and energy flux enters the SOL at the stagnation point.

The flow dependences with n_u are investigated. The unknown we consider are T_u, n_t and T_t.

For very low plasma density, ionization takes place in the core. If the heating power is high enough, the temperature needs to be quite high in the SOL to carry the heat flux and compensate for low density. In this case, due to high parallel heat conductivity, the field line are almost isothermal, giving $T_u = T_t$. If the viscosity is neglected, the total pressure is conserved at the first order. Provided Bohm criterion applies in its equality

form on the target, one has

$$2n_t T_t = n_u T_u \tag{IV.1}$$

In any case, the heat flux on the wall is given by sheath transmission coefficients (see I.5) as

$$q_\parallel = \gamma k_B n_t T_t c_{s_t} = \alpha n_t T_t^{3/2} \qquad \text{with} \qquad \alpha = \frac{\gamma k_B^{3/2}}{\sqrt{m_i}} \tag{IV.2}$$

Combining Equations IV.1, IV.2 with $T_t = T_u$, one obtains

$$\boxed{\begin{aligned} T_t = T_u &= \left(\frac{2q_\parallel}{\alpha n_u}\right)^{2/3} \\ n_t &= \frac{n_u}{2} \end{aligned}} \tag{IV.3}$$

In this regime, for a given temperature the heat flux is provided by the sheath transmission expression. This regime is thus refered in the literature as *sheath limited* regime.

When ionization takes place in the SOL, the conditions involve an increase of plasma density close to the wall and thus reduce temperature for a given energy flux. In this configuration, the energy source is still in the core whereas the particle source is located near the targets. In this two points model, the influence of ionization on velocity or plasma temperature is neglected. The neutral contribution is thus only regarded as a particle source close to the targets (see Figure IV.3). In the region upstream of the

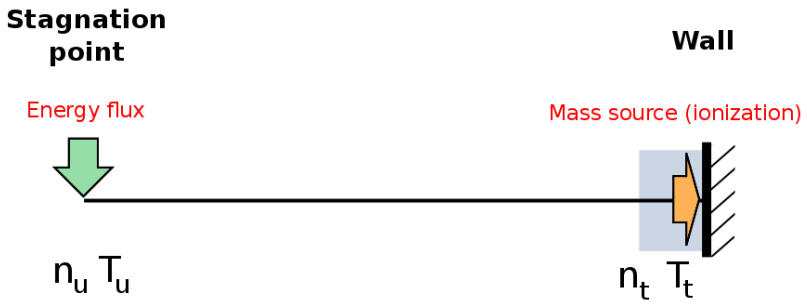

Figure IV.3: 2-points model configuration. The upstream point is located at the stagnation point. The energy source is located at the upstream point whereas the mass source due to recycling is located near the wall

ionization source, the parallel flow is close to zero and the parallel heat flux reduces to the conductive contribution:

$$q_\parallel = \cancel{\frac{5}{2} k_B n T u_\parallel} - \kappa_0 T^{5/2} \nabla_\parallel T = q_{cond.} \tag{IV.4}$$

The relation between upstream and target temperature is thus given by

$$T_t^{7/2} = T_u^{7/2} - \frac{2}{7} \frac{q_\parallel L_\parallel}{\kappa_0} \tag{IV.5}$$

or

$$T_u = T_t \left[1 + \left(\frac{T_q}{T_t} \right)^{7/2} \right]^{2/7} \tag{IV.6}$$

where one has defined

$$T_q = \left(\frac{2 q_\parallel L_\parallel}{7 \kappa_0} \right)^{2/7} \tag{IV.7}$$

If $T_q \ll T_t$, one finds $T_t = T_u$ and recovers the *sheath limited* regime. Conversely, if $T_t \ll T_q$, Equation IV.6 simplifies to

$$\boxed{T_u = T_q = \left(\frac{2}{7} \frac{q_\parallel L_\parallel}{\kappa_0} \right)^{2/7}} \tag{IV.8}$$

Using relations IV.1 and IV.2 yields

$$\boxed{T_t = \frac{4}{\alpha^2} \left(\frac{2 L_\parallel}{7 \kappa_0} \right)^{-4/7} \frac{q_\parallel^{10/7}}{n_u^2}} \tag{IV.9}$$

and

$$\boxed{n_t = \frac{\alpha^2}{8} \left(\frac{2 L_\parallel}{7 \kappa_0} \right)^{6/7} \frac{n_u^3}{q_\parallel^{8/7}}} \tag{IV.10}$$

This regime where the heat flux is constrained by the conductive flux is refered as *conductive limited* or *high recycling* regime since it appears when the ionization is located near the targets.

It is possible to express a criterion at which the transition occurs, that is $T_t \ll T_q$. Reporting the expression for T_t, one obtains

$$\begin{aligned} \frac{4}{\alpha^2} \left(\frac{q_\parallel}{T_q n_u} \right)^2 &\ll T_q \\ n_u &\ll \frac{\alpha^2}{4 q_\parallel^2} \left(\frac{2}{7} \frac{q_\parallel L_\parallel}{\kappa_0} \right)^{6/7} \end{aligned}$$

For a fixed value of $q_\parallel$, the trends for T_t and n_t are represented on Figure IV.4. For even higher value of n_u the pressure loss due to neutrals as well as the volumic source of energy generated by radiation in the neutral region lead to the *detached plasma* regime where density decreases on the target as n_u increases. This roll-over is represented as well on the Figure.

These trends are found experimentally and plotted on Figure IV.5,a where experimental results obtained for an axisymetric divertor configuration on ASDEX are represented. These density regimes are rather generic and are well recovered in the ergodic divertor configuration on Tore Supra [61], Figure IV.5,b.

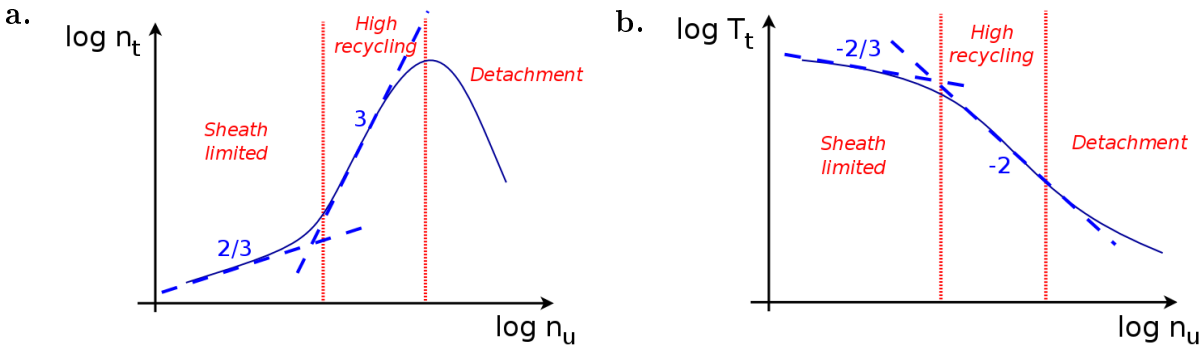

Figure IV.4: Density regimes. Variations for target density (a) and target temperature (b) as a function of upstream plasma density. The heat flux is fixed and the trend is ruled by Equations IV.3, IV.9 and IV.10.

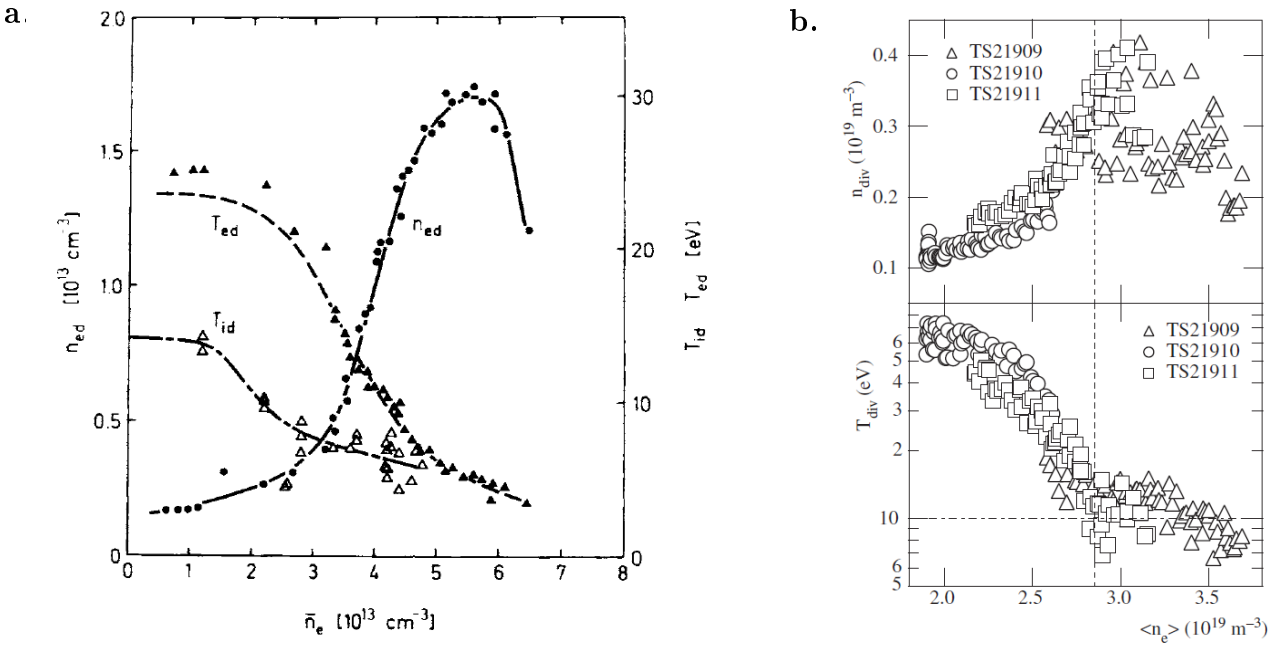

Figure IV.5: a: ASDEX, 1983. Scaling of the electron temperature and density measured by a Langmuir probe, and the ion temperature deduced from Doppler-broadened CIII radiation of the ASDEX divertor plasma with the main plasma density. The decrease in $n_{ed} \approx n_t$ at the highest density would, today, be attributed to divertor detachment. (Figure from Ref. [6]). b: density scan performed in the ergodic divertor configuration on Tore supra. One recovers the low density sheath limited regime, followed by the high recycling regime until the density rollover in the detached regime, $T_e \leq 10$ eV. (Figure from [61]).

IV.1.2 Analytical solutions

In this paragraph, simple cases that can be solved analytically are considered for both *sheath limited* and *high recycling* plasmas. Once the solutions derived, the characteristics of the two regimes are summed up for comparison.

a) Sheath limited regime

One considers the plasma steady-state along the field line. The radial particle source is supposed to be constant: $S_\perp^n = S_0$. In the sheath limited regime, the temperature is constant along the field line. Also, if the pressure loss due to flow shear is neglected, the following equations (from fluid equations, see section I.2.2) have to be solved:

$$\frac{\partial \Gamma}{\partial s} = S_0 \quad , \quad \frac{\partial \Pi}{\partial s} = 0 \tag{IV.11}$$

Integrating from stagnation point ($s = 0$) to the target ($s = L_\parallel$), one obtains:

$$\Gamma = n c_s M = S_0 s \tag{IV.12}$$

$$\Pi = n m_i c_s^2 (1 + M^2) = cst. \tag{IV.13}$$

Applying Bohm boundary conditions ($M = 1$ for $s = L_\parallel$) gives

$$n_t = \frac{S_0 L_\parallel}{c_s} \qquad n_u = 2 n_t \tag{IV.14}$$

Dividing Equations IV.12 and IV.13 gives

$$\frac{2M}{1 + M^2} = \frac{s}{L_\parallel} \tag{IV.15}$$

which yields

$$\boxed{M = \frac{L_\parallel}{s}\left[1 - \sqrt{1 - \left(\frac{s}{L_\parallel}\right)^2}\right]} \quad \text{and} \quad \boxed{n = \frac{S_0}{c_s} \frac{s^2}{L_\parallel - \sqrt{L_\parallel^2 - s^2}}} \tag{IV.16}$$

The Mach and density profiles are plotted on Figure IV.6.

b) High recycling regime

To get analytical solutions in the high recycling regime, an exponential decay for the ionization source is prescribed. The radial source of particles is set to zero. The temperature profile is ruled by equation IV.4 giving

$$\boxed{T(s) = T_u \left(1 - \left(\frac{T_q}{T_u}\right)^{7/2} \frac{s}{L_\parallel}\right)^{2/7}} \tag{IV.17}$$

with the same definition as in the previous paragraph (Equation IV.7). From continuity equation, the particle flux is given by

$$\Gamma(s) = \int_0^s S_{iz} ds' = S_0 \left[\exp\left(-\frac{L_\parallel - s}{\lambda_{iz}} \right) - \exp\left(-\frac{L_\parallel}{\lambda_{iz}} \right) \right] \tag{IV.18}$$

where an exponetial decay has been chosen for the ionization source profile. In particular, one finds

$$q_\parallel = \gamma k_B \Gamma_t T_t = \gamma k_B S_0 \left(1 - \exp\left(-\frac{L_\parallel}{\lambda_{iz}} \right) \right) T_t$$

This relation gives the temperature at the target plate hence the temperature everywhere using Equation IV.17. One also gets density on the target using Bohm boundary condition and assuming $T_e = T_i$:

$$\Gamma_t = S_0 \left(1 - \exp\left(-\frac{L_\parallel}{\lambda_{iz}} \right) \right) = n_t \sqrt{\frac{2k_B T_t}{m_i}}$$

The conservation of the total pressure gives the density profile.

$$m_i \frac{\Gamma^2}{n} + 2k_B nT = m_i \frac{\Gamma_t^2}{n_t} + 2k_B n_t T_t = \Pi_t$$

yielding

$$n = \frac{\Pi + \sqrt{\Pi^2 - 8m_i k_B T \Gamma^2}}{4k_B T} \tag{IV.19}$$

c) Comparison and summary

The typical solutions for density, temperature and Mach number are plotted for the different density regimes based on the above paragraph equations.

The main characteristics of the two regimes are summed up in Table IV.1. One notices in particular that *high recycling* regime is characterized by a strong increase of density near the targets. A strong temperature drop can also be associated to the *conduction limited/high recycling* regime.

	Sheath limited	**High recycling**
Density	monotonic decay $n_t = n_u/2$	sharp increase near the targets
Mach number	increasing all along the field line	zero almost everywhere Increase to Mach 1 localized near the target
Temperature	constant	strong gradient

Table IV.1: Density regime characteristics (summary)

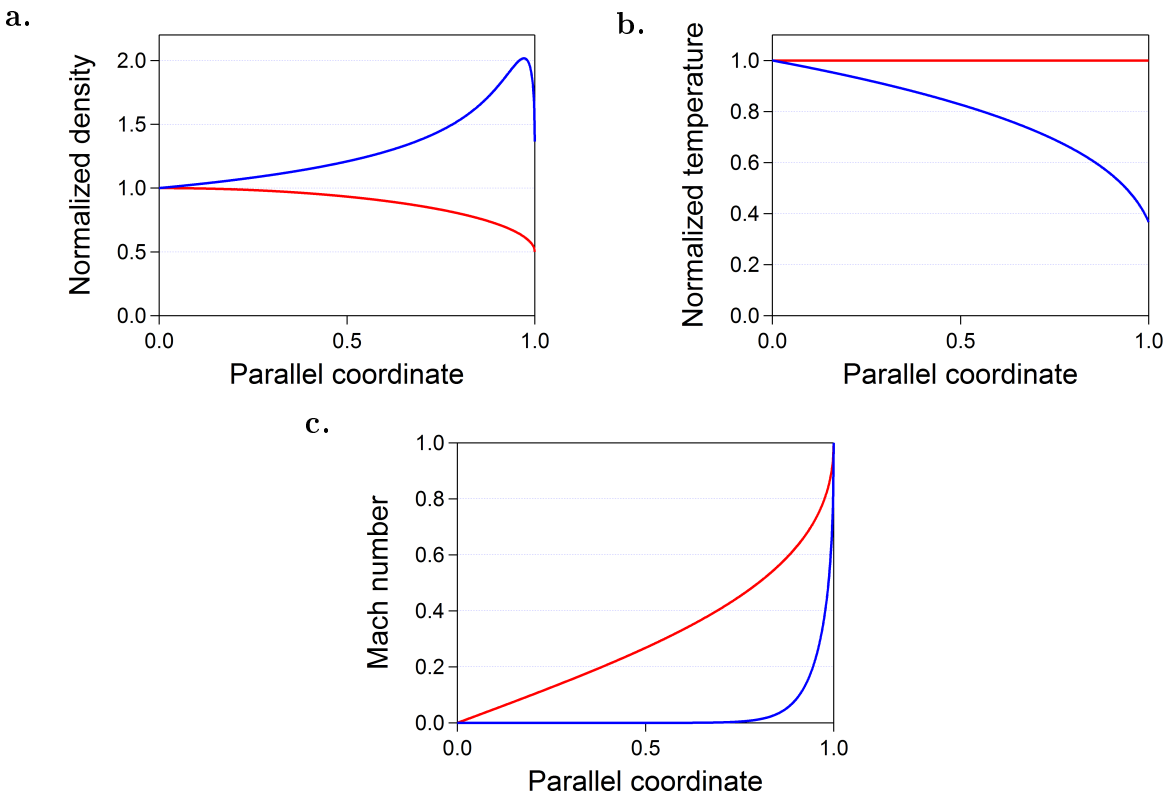

Figure IV.6: 1D simulation results. Density (a.), temperature (b.) and Mach number (c.) profiles for the sheath limited (red) and high-recycling regime (blue). The profiles are normalized to the upstream value, the upstream position being located at $s = 0$ and the target at $s = 1$, s being the normalized parallel coordinate.

IV.2 Implementation of a non-local fluid model for neutrals in SolEdge2D

In order to study the impact of neutrals on the plasma flows, it is possible to use a very simple model for neutrals. In this model, the neutrals are transported with an isotropic diffusion process. This transport implicitely assumes an underlying microscopic Brownian motion where the neutrals mean free path is smaller than the typical length considered in SolEdge2D simulations. This assumption is barely valid in typical plasmas and the transport of neutrals from their emission source to the place where they ionize is often better described by an isotropic ballistic motion. In that perspective, a non-local generalized diffusion can also be used to take weak-collisionality into account as in chapter III. Despite its overall simplicity, the diffusive model for neutrals gives a good insight on the overall mechanisms and regimes controlled by neutrals. Further details on these models can be found in the literature [62, 63].

IV.2.1 The fluid model equations

In the model considered here, the sources of neutrals are located at the surface of plasma facing components. At each time step, for each SolEdge2D mesh cell in contact with the wall, the outflux of plasma is computed and a percentage of this outflux is reinjected as a volumic source of neutrals. The percentage of reinjection is provided by the recycling coefficient $R^\star$; one typically chooses $R^\star = 95\%$. Then the neutrals are transported with the generalized Fick law and encounter ionization events whose intensity is governed by the ionization cross-section $\langle \sigma v \rangle_{iz}$. The Equation for neutrals density is the following:

$$\boxed{\frac{\partial n_n}{\partial t} - \vec{\nabla} \cdot \vec{\Gamma}_n = -S_{iz} + S_{wall}} \tag{IV.20}$$

where the ionization source is given by Equation (IV.21).

$$\boxed{S_{iz}(n_N, n, T_e) = n n_n \langle \sigma v \rangle_{iz}} \tag{IV.21}$$

where according to [13], $\langle \sigma v \rangle_{iz}$ is given by Equation IV.22 (T_e in eV) and is plotted on Figure IV.7.

$$\langle \sigma v \rangle_{iz} = 10^{-5} \frac{\sqrt{T_e/E_\infty}}{(E_\infty)^{3/2}(6.0 + T_e/E_\infty)} \exp\left(-\frac{E_\infty}{T_e}\right) \ cm^3/s \qquad \text{with} \qquad E_\infty = 13.6 \ eV \tag{IV.22}$$

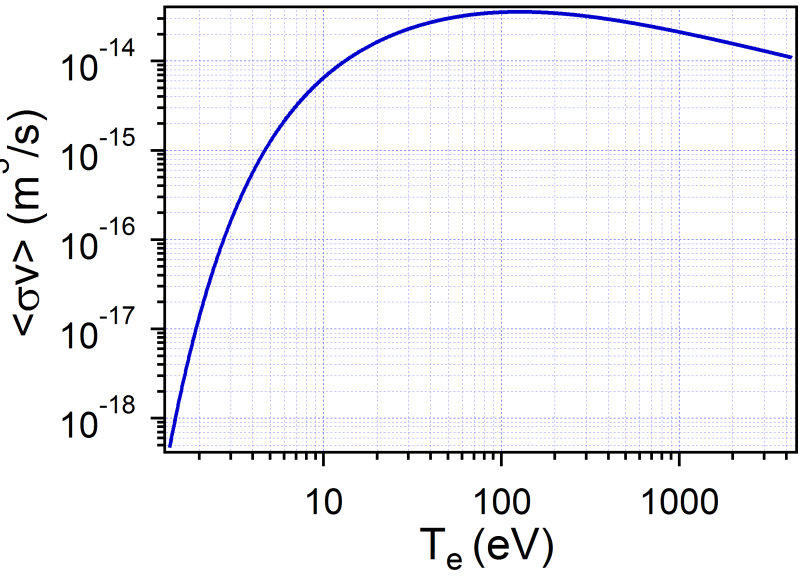

Figure IV.7: $\langle \sigma v \rangle$ as a function of T_e for Hydrogen from Equation IV.22.

The neutral flux is given by generalized Fick law

$$\boxed{\vec{\Gamma}_n = -\int_{\mathcal{V}} d\vec{x}' \int_{-\infty}^{t} dt' K(\vec{x}-\vec{x}', t-t')\vec{\nabla} n_n(\vec{x}', t') = -K * \vec{\nabla} n_n} \tag{IV.23}$$

with the kernel expression

$$K(\vec{x}-\vec{x}', t-t') = K_0 \exp\left(-\frac{\|\vec{x}-\vec{x}'\|}{\lambda}\right) \exp\left(-\frac{t-t'}{\tau}\right) \tag{IV.24}$$

where λ and τ denotes space and time correlation scales.

Notice that the ionization source S_{iz} present in Equation IV.20 gives the neutral contribution written in Equation II.4 as S^n ($S^n = S_{iz}$). The neutral diffusivity kernel is a free parameter that is set to obtain relevant penetration length for neutrals in the plasma. This parameter that is linked to neutral velocity should depend on the temperature.

On Figure IV.8 and IV.9 are displayed some SolEdge2D results in WEST geometry for the sheath limited and high recycling cases. The simulation parameters are given in Table IV.2. In these simple simulations, the characteristic correlation time and length are chosen small enough for the transport process to be diffusive. The mesh size is 100 points in the radial direction and 300 points in the parallel direction. The computation time is about 1 day on 4 processors.

	Sheath limited	**High recycling**
Core density	$2.5 \cdot 10^{18}\ m^{-3}$	$10^{20}\ m^{-3}$
Core Temperature	$200\ eV$	$200\ eV$
Cross field diffusivities	$1\ m^2 s^{-1}$	$1\ m^2 s^{-1}$
Neutrals diffusivity	$1000\ m^2 s^{-1}$	$1000\ m^2 s^{-1}$

Table IV.2: Simulation parameters for the sheath limited and high recycling simulation with the fluid model for neutrals.

The main characteristics of the two regimes are recovered. In particular, a flat temperature profile is found in the *sheath limited* regime as well as a strong temperature drop in the *high recycling* regime. In the first case, a decaying density profile is observed unlike the second case where the plasma density is peaked near the targets. Also, one remarks the slightly supersonic flow in the sheath limited case (for further details, see the dedicated section on supersonic flows in paragraph V).

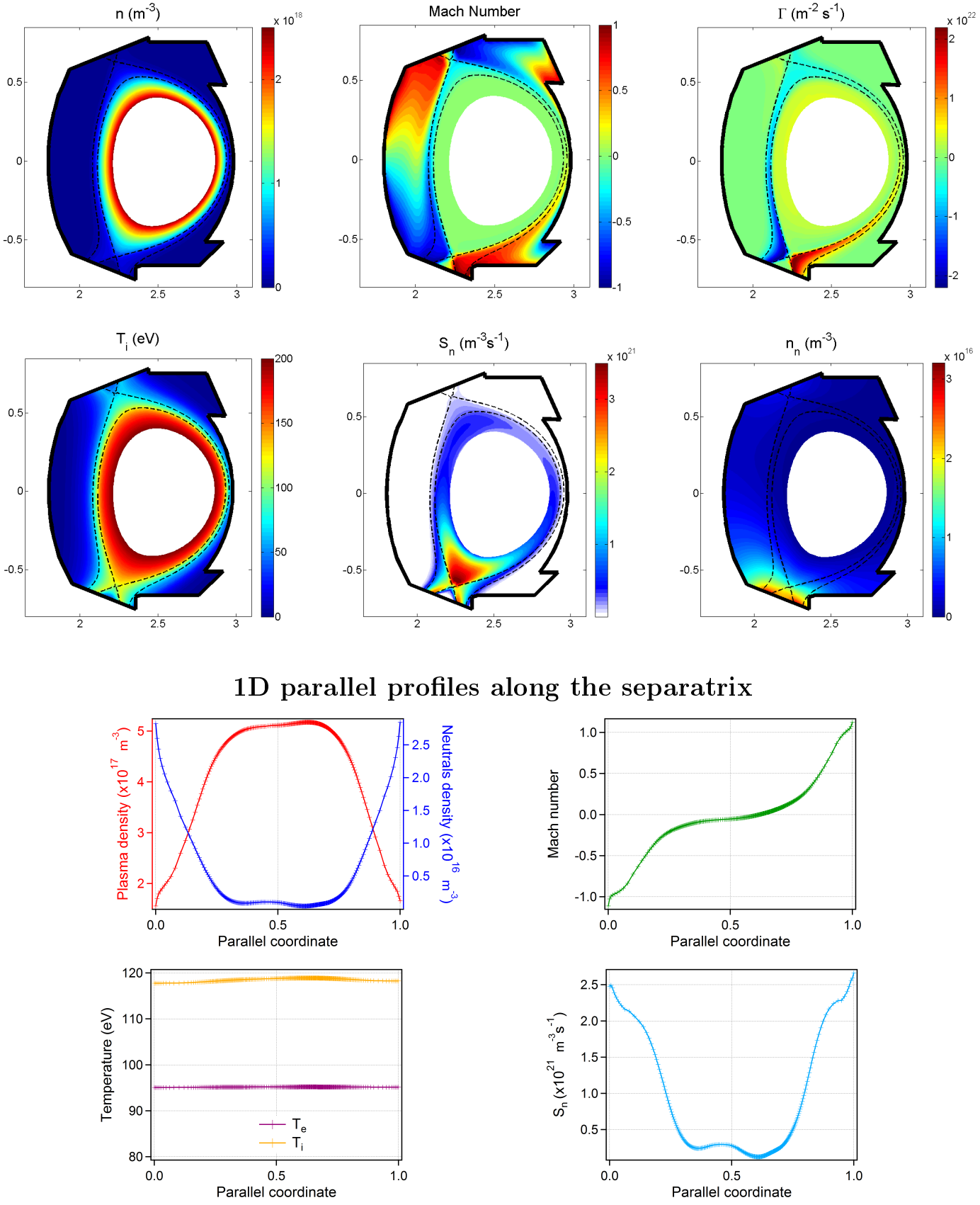

Figure IV.8: SolEdge2D *sheath limited simulation results obtained with the fluid model for neutrals*

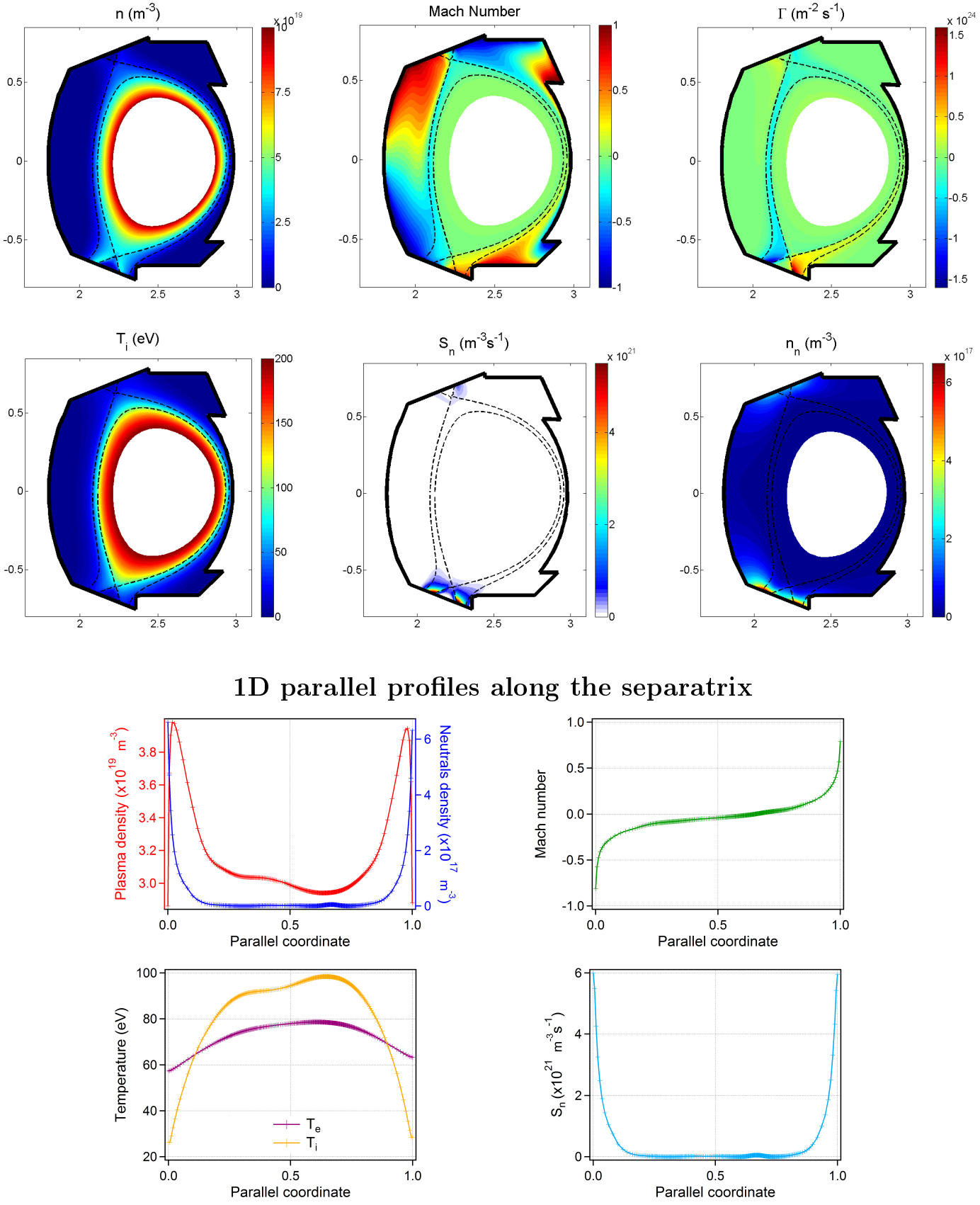

Figure IV.9: SolEdge2D *high recycling simulation results obtained with the fluid model for neutrals*

IV.3 Implementation of neutrals with the Monte-Carlo code Eirene

IV.3.1 A quick introduction to Eirene

The code Eirene has been developped at Forschungszentrum in Jülich, based on a Monte-Carlo algorithm that is known to be very effective to simulate complex randomized process. Monte-Carlo methods have the great advantage to permit a kinetic description of systems in complex geometry configurations. The Monte-Carlo procedure consists in intrepreting the Boltzmann equation as a stochastic process. In particular, test particles whose behavior is prescribed by the above mentionned stochastic process are followed and the average properties of the test particles population give the desired quantities (density, ionization source etc). In that sense, the distribution function is not directly computed. The procedure directly gives access to fluid moments taking the whole kinetic effects into account. As any random procedure, the drawback of this method is the stochastic noise that decreases as the square root of the number of test particles; a considerable number of test particles and thus a large amount of computation time may thus be required to reach a satisfactory low level of noise.

The Eirene code needs input plasma parameters that are provided here by SolEdge2D. Eirene has also been coupled with many other plasma codes such as B2 [64, 65, 66], Edge2D [67, 68, 69, 70], OEDGE [71, 72] or EMC3 [73]. In the next paragraphs, the algorithm beneath Eirene code is briefly describes. For more informations, the reader is kindly invited to refer to Eirene documentation [64, 74, 75].

Let us go back to Boltzmann equation. No external forces are taken into account. One only considers collisions with a background species whose distribution function is denoted $f_\star$ and for which the collisions cross section is denoted σ. From Boltzmann expression for collisions (Equation I.62)

$$\begin{aligned}\frac{\partial f(\vec{x},\vec{v},t)}{\partial t} + \vec{v}\cdot\vec{\nabla} f(\vec{x},\vec{v},t) &= \iiint \sigma(\vec{v}',\vec{V}';\vec{v},\vec{V})\|\vec{v}'-\vec{V}'\| f(\vec{v}') f_\star(\vec{V}') d\vec{v}' d\vec{V}' d\vec{V} \\ &\quad - \iiint \sigma(\vec{v},\vec{V};\vec{v}',\vec{V}')\|\vec{v}-\vec{V}\| f(\vec{v}) f_\star(\vec{V}) d\vec{v}' d\vec{V}' d\vec{V} + Q(\vec{x},\vec{v},t) \quad \text{(IV.25)}\end{aligned}$$

In this expression, $Q(\vec{x},\vec{v},t)$ is the net source of particles. If the background distribution function $f_\star$ is given, the above equation can be linearized to

$$\frac{\partial f(\vec{x},\vec{v},t)}{\partial t} + \vec{v}\cdot\vec{\nabla} f(\vec{x},\vec{v},t) = \int C(\vec{v}' \leftrightarrow \vec{v}) f(\vec{v}') d\vec{v}' - \nu_c f(\vec{v}) + Q(\vec{x},\vec{v},t) \qquad \text{(IV.26)}$$

where one has defined the collision frequency

$$\nu_c = \iiint \sigma(\vec{v},\vec{V};\vec{v}',\vec{V}')\|\vec{v}-\vec{V}\| f_\star(\vec{V}) d\vec{v}' d\vec{V}' d\vec{V} \qquad \text{(IV.27)}$$

and the collision kernel

$$C(\vec{v}' \leftrightarrow \vec{v}) = \iint \sigma(\vec{v}', \vec{V}'; \vec{v}, \vec{V}) \|\vec{v}' - \vec{V}'\| f_\star(\vec{V}') d\vec{V}' d\vec{V} \tag{IV.28}$$

The simplest way to model Equation IV.26 is to interpret the physical meaning of it and derive a stochastic process that mimic the same behavior. In particular, if one considers that collisions can be described by punctual events in space and time, a stochastic process that determines when collision events occur must be found. Looking at Equation IV.26, test particles with velocity $\vec{v}$ are emitted from the source $Q(\vec{x}, \vec{v}, t)$ and then follow a ballistic motion between collision events. These collisions events are described by the sink term of particles $-\nu_c f(\vec{v})$ that is characterized by its frequency ν_c. The future of the particle after the collision is determined by the collision kernel that tells the number of particles of velocity $\vec{v}'$ created from particles of velocity $\vec{v}$ during each collision event and vice versa. In particular, a distribution function can be obtained from the kernel as

$$c(\vec{v}' \leftrightarrow \vec{v}) = \frac{C(\vec{v}' \leftrightarrow \vec{v})}{\int C(\vec{v}' \leftrightarrow \vec{v}) d\vec{v}'} \tag{IV.29}$$

To sum it up, a sampling procedure is used to generate test particles from, the source $Q(\vec{x}, \vec{v}, t)$. These particles travels ballistically until a collision event occures. The events probability is determined from the collision frequency ν_c. After a collision, the velocity of the particle changes according to the distribution function $c(\vec{v}' \leftrightarrow \vec{v})$. This procedure repeats until the particle is absorbed. Indeed, in this simple version, one has only considered elastic collisions that change particle velocity but other collision events such as ionization can be considered in parallel to build a model as complex as necessary. This model follows more or less the underlying physics of the system. It is refered as analog process[1]. Numerically, the particle tracking algorithm that aims at determining particles trajectory in the simulation domain is shared by many Monte-Carlo codes and is gathered in the "geometrical" module of EIRENE. A specific work must be done concerning the computation of collision rate ν_c and the sampling of the source and of the transition kernel c. This work constitutes the "physical" module of EIRENE. It relies on atomic physics database such as HYDHEL and AMJUEL that have been built from a long and systematic experimental process.

In the above procedure, one has assumed that the distribution function for background particles is given. In practice, when considering the collisions between the neutrals and the plasma, ions are assumed to be described by a shifted Maxwellian distribution whose parameters are given by ions density, velocity and temperature. Most of the source of neutrals comes from recycling on the wall. A dedicated module is implemented to address this problem: from plama flux and properties on the wall, EIRENE considers a truncated shifted Maxwellian distribution of ions impacting the wall, the solid-particle interaction is

[1] It is sometimes useful to resort to non-analog processes such as "Russian roulette" to stop particle trajectories when they get out of the region of interest of the simulation domain. These processes optimize performances and computation time

then calculated with the Monte-Carlo TRIM code [76]. The impinging ions can either be reflected as fast particles or desorbed. In the latter case, the desorbing atoms or molecules are emitted with a temperature close to the wall temperature. The physical and chemical sputtering processes are also considered.

In the plasma volume, the electron impact processes and the heavy particles collisions can be disctinguished. The electronic collisions include ionization, dissociation and recombination. The heavy particle ones include elastic collisions and charge-exchange collisions, the latter being an elastic collision between a slow and a fast particles that exchange their charges (or velocities indifferently!).

Once the stochastic process governing test particles trajectory established, it is necessary to extract the information on the desired quantities (ionization source etc...). The quantity whose average value is equal to the desired moment is called the estimator. It exists several type of estimators. EIRENE uses the collision estimator and the track-length estimator. These estimators differ in the way they ponderate test particle trajectories in the averaging process.

Simulations are based on arbitrary triangle grids and can address any kind of geometry, independently of the magnetic configuration. EIRENE is thus a very flexible tool on the geometrical point of view. In order to couple SOLEDGE2D with EIRENE, each SOLEDGE2D cell that as a rectangular shape is splitted into two triangles to generate EIRENE grid. Then, dedicated interface routines were developped to provide plasma parameters and fluxes computed by SOLEDGE2D as input for EIRENE and send particle, momentum and energy sources computed by EIRENE back into SOLEDGE2D (see section IV.3.2). An example of EIRENE neutrals trajectory in *Tore Supra - WEST* configuration is shown on Figure IV.10. One notices the presence of H_2, H_2^+ and H molecules, the background plasma being made of H^+ ions. On this figure, one also notices that neutrals can travel on very long distance in the machine between collisions. The fact that some neutrals travel with a long mean free path justifies once again the kinetic treatment of neutral transport.

It is not necessary to re-compute neutral sources at each SOLEDGE2D time step. "Short cycling" routines can rescale previously computed sources according to plasma evolution. With such a procedure, the number of calls to EIRENE is reduced by a factor up to 10. Since rescaling sources is much faster than recomputing them with EIRENE, "short cycling" reasonably reduces computational time.

IV.3.2 Numerical aspects on the coupling

a) EIRENE mesh definition

The EIRENE mesh is based on triangle shaped cells. Each side of the triangle is given some specific properties. If the triangle is located in the middle of the plasma domain, each triangle side is associated with informations on the neighboring mesh cell. If the triangle is located near the chamber wall, the triangle edge in contact with the solid is affected with specific properties such that EIRENE identifies plasma-solid boundary. As a

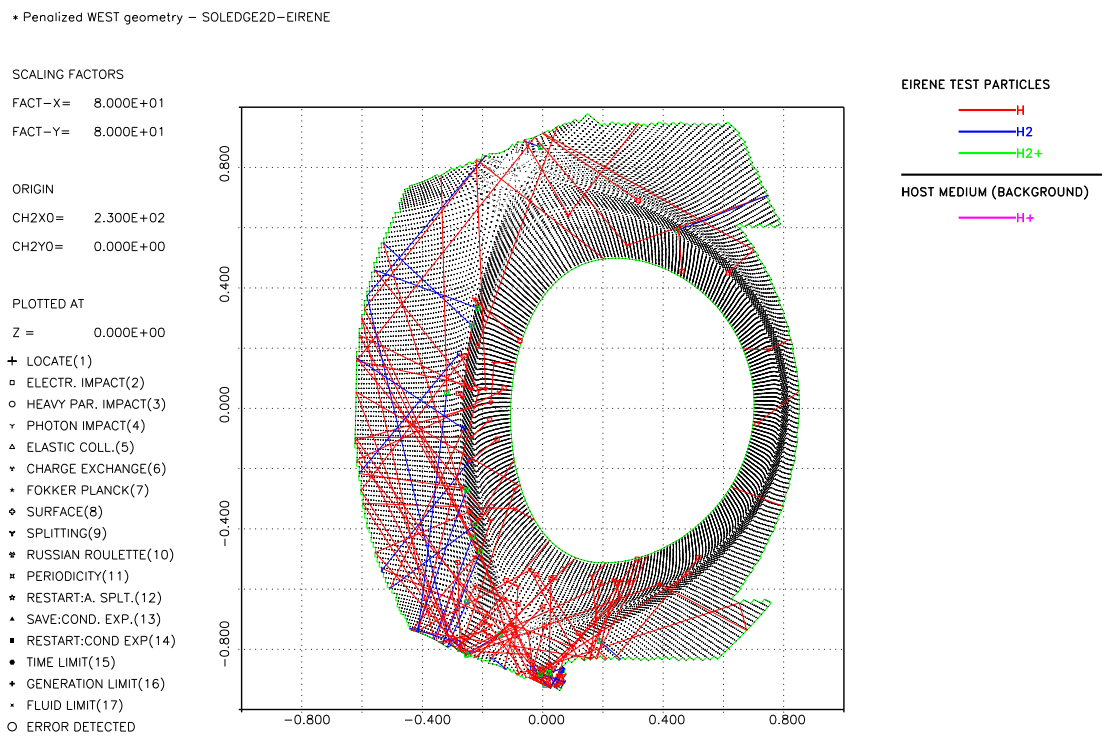

Figure IV.10: Example of EIRENE *output. Neutral trajectories in WEST geometry. The symbols represents the different events encountered by neutrals on their way.*

consequence, if the EIRENE mesh does not require to be aligned with the magnetic field, it has to be aligned with the chamber wall geometry.

Conversely, if SOLEDGE2D grid requires to be aligned with the magnetic field, no special geometrical requirement is made concerning aligning the mesh with the surface elements. In particular, with the penalization technique, the exact plasma-solid interface location is not even known. This asymptotic method just prescribes that the interface is located between two SOLEDGE2D mesh points where the mask function χ switches from 0 to 1.

In order to generate the EIRENE grid from the SOLEDGE2D grid, SOLEDGE2D virtual cells (square) are just splitted into two triangles. This regular case is represented on Figure IV.11.

If this method works well in the plasma region, a special treatment must be done near the wall since the triangles obtained after splitting SOLEDGE2D cells have no reason to be aligned with the chamber surface. An extra splitting is thus performed to get triangles aligned with the wall. The splitting method is represented on Figure IV.12. The effective position, where the wall is located if the wall-aligned triangles are not used, is also plotted. If wall-aligned triangles are not used, the wall is described by a sharp stair-shaped surface slaloming around the exact wall location, see Figure IV.12. The surface area is not the real one and it is unclear if the two way of meshing give the same results for high mesh

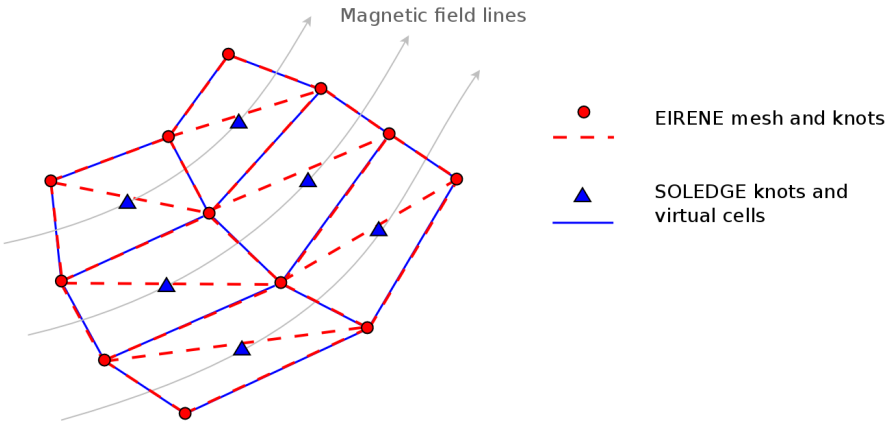

Figure IV.11: Definition of the EIRENE *grid from the* SOLEDGE2D *grid for regular cells (in the plasma region - far from the wall).*

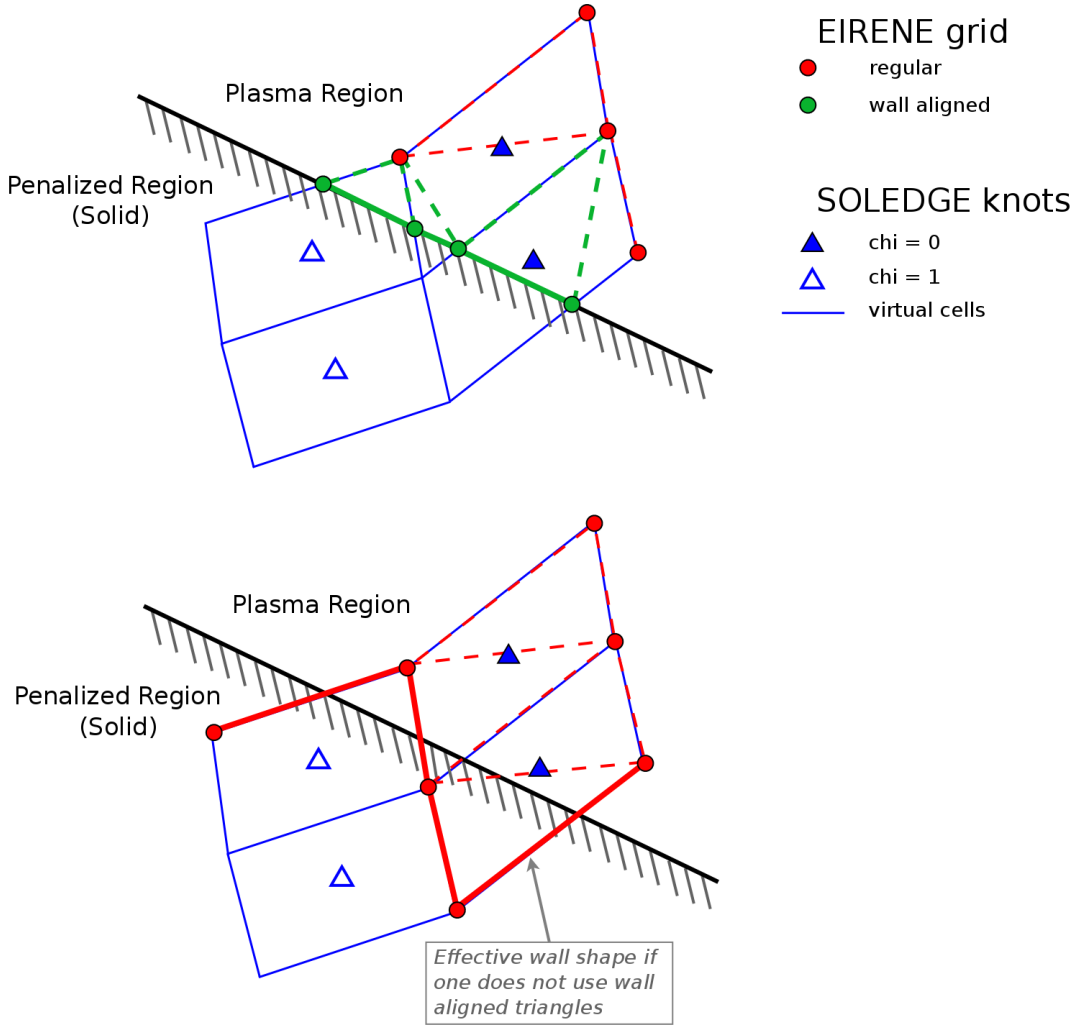

Figure IV.12: Eirene mesh definition near the wall. Top: Eirene grid using wall-aligned triangles. Bottom: Eirene grid without using wall-aligned triangle. The location of the effective surface is represented.

resolution.

b) Interpolations and extrapolations

Once the EIRENE mesh is defined, plasma quantities computed with SOLEDGE2D (such as density, temperature etc) need to be interpolated on the EIRENE grid points. This is done quite easily since EIRENE points are by construction surrounded with SOLEDGE2D points on which plasma quantities are known. However, the plasma quantitites computed with SOLEDGE2D must be extrapolated to the EIRENE grid points located on the wall. This extrapolation procedure can be reduced by using the plasma quantities computed on the nearest SOLEDGE2D point located in the plasma domain.

IV.3.3 Example of main chamber recycling investigation

The penalization technique (Section II.4.2) allows simulating recycling phenomenon within the entire chamber wall. On figure IV.13 neutral density and ionization sources are represented in a SOLEDGE2D-EIRENE simulation performed with JET geometry. In this tokamak configuration, the separatrix can be quite close to main chamber walls and the cross-field turbulent transport can bring plasma to recycle out of the divertor region. In order to highlight the phenomenon, some ballooning effects are modeled using a peaked diffusivity profile centered on the outboard mid-plane. With such an enhancement of the radial transport, one clearly observes a net ionization source in the low field side region (Figure IV.13, right).

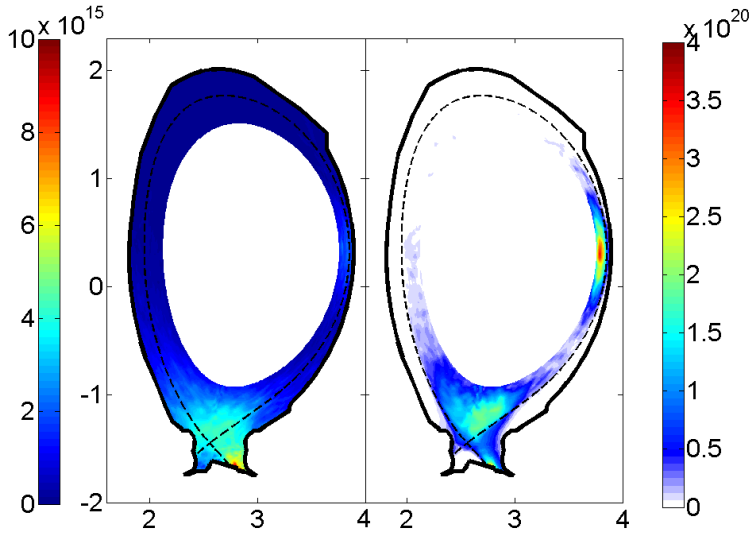

Figure IV.13: SOLEDGE2D-EIRENE *simulation results in JET geometry. Left: Atoms density – Right: Ionization source. A net ionization source is present at the outboard mid-plane due to recycling on chamber walls.*

These results are preliminary and a deeper analysis on how this main chamber recycling affects plasma flows must be carried out. A special care must be taken to evaluate the

percentage of the plasma flux recycling on main chamber walls and to define geometrical criterion to prevent this main chamber recycling contribution. Comparison of results with experimental data [77] are also required.

The simulation of the plasma up to the main chamber wall requires to estimate the amount of impurities in the plasma. Indeed, at least two mechanisms can increase the level of impurities: first, there is the direct sputtering on the main chamber wall and secondly, the impurities coming from the main chamber can be transported up to the divertor region where they can impact the divertor materials increasing the sputtering in this region. The sputtering due to impurities impact is much stronger than sputtering due to hydrogen ions impact, since impurities are much heavier. In order to evaluate these phenomena, one must couple SolEdge2D-Eirene with an impurity code.

Chapter highlights

- *The study of so-called density regimes shows that the plasma behavior is very sensitive to the position of the ionization source.*
- *As a consequence, it is extremely important to properly simulate neutrals transport. The neutrals mean free path being quite long and comparable to system size, a non-diffusive approach is used.*
- *A simple model using the generalized diffusion law presented in Chapter III is first implemented.*
- *In the diffusive limit that is assuming high collisionality for neutrals, the sheath-limited and high-recycling regime properties are recovered. The non-diffusive results are still to be investigated.*
- *A kinetic Monte-Carlo algorithm can also be used for simulating neutrals transport. This is done by the neutral code* Eirene *that has been coupled with* SolEdge2D*. The study of neutrals trajectory justifies the non-diffusive treatment. The results obtained with* Eirene *will have to be compared with the results obtained with the generalized diffusion law. The statistics on neutrals trajectories could also be used to extract the shape of the collision kernel and compare it with the prescribed exponential decay for the analytic model.*

Chapter V

Transition from subsonic to supersonic regimes in the SOL

Content

Various configurations leading to sub/supersonic transition are detailed in quasineutral plasma. In particular, the effect of the divertor topology on plasma flows is addressed. The supersonic regime is also recovered in presence of strong temperature gradients near the plasma facing components and magnetic field inhomogeneities.

The purpose of this section is to investigate the conditions required to obtain a supersonic transition in the quasi-neutral plasma. This work is based on simulation results from the fluid transport code SolEdge2D. These simulation results confirm predictions made by an analytical model developped in [23]. From this analytical model, the basic ingredients required to produce a supersonic transition are emphasized. Beside the role played by the plasma topology, the dependence with neutrals, temperature and magnetic field is also addressed.

As mentionned in Section I.5, the wall acts as a strong sink for the plasma and drives the plasma flow up to a Mach number greater than 1 at the sheath entrance. This is the so-called Bohm criterion. The flow properties at plasma wall interface are thus very similar to those of a flow in vacuum expansion where a supersonic transition in the upstream flow region is observed. To go further, the validity of Bohm criterion in its equality form will be discussed in this section. Indeed, many diagnostics such as Langmuir probes [6] use the marginal equality form of Bohm criterion to extract density or temperature measurements even if supersonic solutions in the quasi-neutral plasma are known to exist ([78],[79]).

V.1 Geometry driven transition

Two classical configurations are detailed and will be used as reference cases to develop a theoretical model that describes supersonic transition requirements. The first example is an ideal divertor configuration in slab geometry. The second one is a realistic limiter configuration based on ToreSupra's tokamak geometry. The simulations are run without neutrals and at high temperatures ($T_e \approx T_i \approx 200\ eV$ in the edge plasma). In this case, the intense parallel heat flux ensures that the temperature is almost constant on each magnetic flux surface.

V.1.1 Supersonic transition in divertor configuration

Hereinafter, an ideal divertor configuration is considered where the magnetic surfaces are computed from pendulum phase portrait. This configuration shows two symmetric X-points on the separatrix, Figure V.1,a. The following SolEdge2D equations (II.4, II.11) are solved until steady state:

$$\frac{\partial n}{\partial t} + \vec{\nabla}\cdot\left(nu_{\parallel}\vec{b}\right) = \vec{\nabla}\cdot\left(D\vec{\nabla}_{\perp}n\right)$$
$$m_i\frac{\partial nu_{\parallel}}{\partial t} + \vec{\nabla}\cdot\left(m_i n u_{\parallel}^2\vec{b}\right) + k_B\nabla_{\parallel}n(T_e+T_i) = m_i\vec{\nabla}\cdot\left(\nu\vec{\nabla}_{\perp}(nu_{\parallel})\right)$$

The Mach number at steady state is plotted on Figure V.1,b. The Mach number is observed to be supersonic in the divertor region, the transition from subsonic to supersonic flow being located at X-point position. In this simulation, boundary conditions are im-

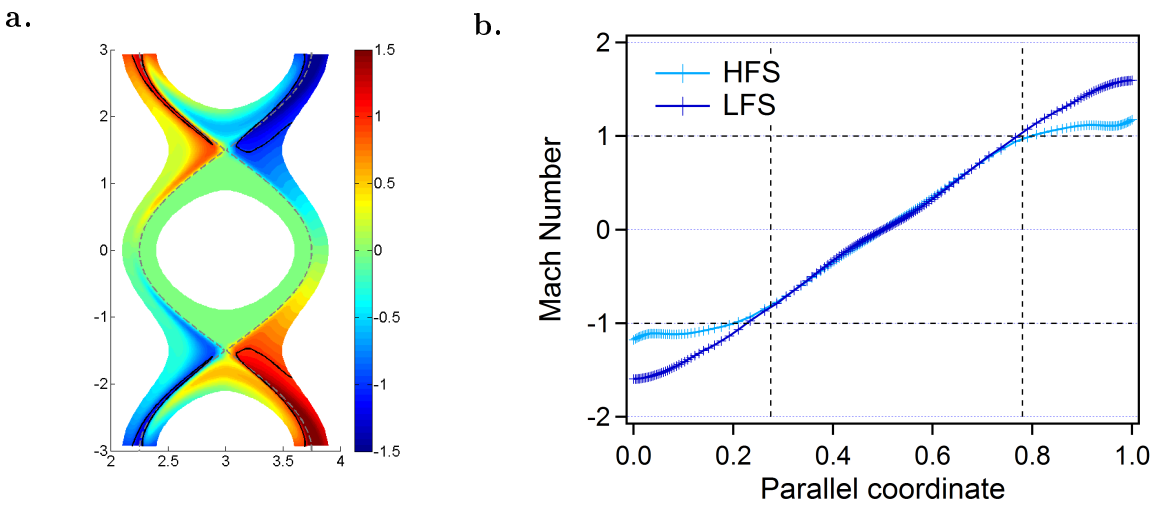

Figure V.1: SolEdge2D *simulation for an ideal slab divertor configuration. a: Mach number represented in the ideal divertor magnetic configuration (Line contour represents* $|M_{\parallel}| = 1$*. b: Mach number parallel profile in the SOL along the separatrix on the LFS and HFS. The supersonic transition is more intense on the tokamak LFS.*

posed directly in the finite-difference scheme, without using penalization technique. The same transition has been observed numerically in JET and WEST geometries [80, 81].

V.1.2 Supersonic transition in limiter configuration

One considers here a simulation of ToreSupra's tokamak geometry. The magnetic configuration corresponds to the shock #35230 and the complex geometry of the machine is taken into account using penalization technique. In this case, a transition from subsonic to supersonic flow is observed in the region located below bottom limiter. One notices that this region represented on Figure V.2 is not radially connected with the "feeding" core region.

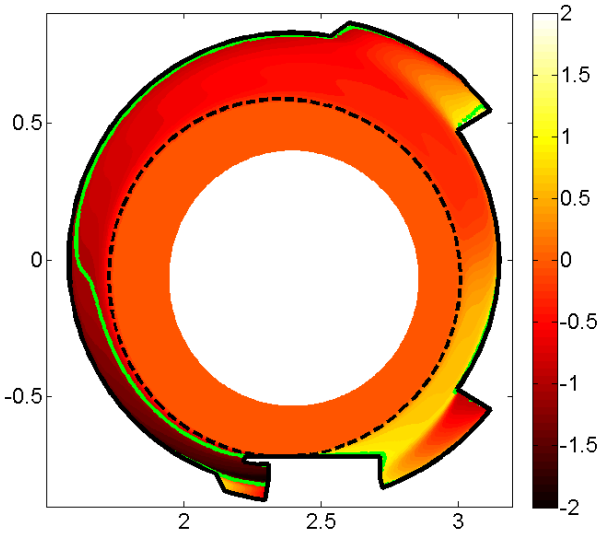

Figure V.2: SolEdge2D simulation of ToreSupra's configuration. Mach number (green line contour represents $|M_{\parallel}| = 1$

V.2 Theoretical model for supersonic transition

The study of the $\mathcal{A}$-parameter introduced by Ph. Ghendrih [23] provides good insights on the supersonic transition mechanisms. The idea is to find a reduced expression for the particle flux that depends only on the Mach number. One starts with expressing the parallel particle flux as $\Gamma_{\parallel} = nv_{\parallel} = nMc_s$. Then, one expresses the total pressure $\Pi = p + 1/2 m_i n v_{\parallel}^2 = nc_s^2(1 + M^2)$. Replacing nc_s in the expression for the particle flux and rearranging the terms lead to the following expression for $\mathcal{A}$:

$$\mathcal{A} = \frac{2M}{1 + M^2} = \frac{2\Gamma_{\parallel} c_s}{\Pi / m_i} \tag{V.1}$$

The parameter $\mathcal{A}$ is plotted on Figure V.3. One can distinguish between the subsonic branch where $\mathrm{d}\mathcal{A}/\mathrm{d}M > 0$ and the supersonic branch where $\mathrm{d}\mathcal{A}/\mathrm{d}M < 0$. A transition

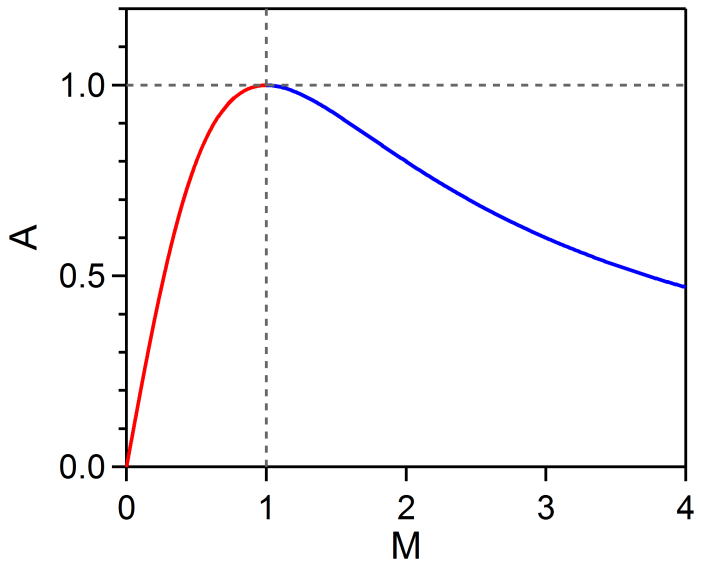

Figure V.3: Graph of function $\mathcal{A}$ as a function of the Mach number

from subsonic to supersonic regime hence requires a change in $\mathcal{A}$ derivative sign. In our case, one is interested in the variation of the Mach number along a magnetic field line. The coordinate along magnetic field line is denoted z and the operator $\nabla_\parallel$ is reduced to the derivative d/dz. One can express $\mathcal{A}$ derivative as $\mathrm{d}\mathcal{A}/\mathrm{d}M = (\mathrm{d}\mathcal{A}/\mathrm{d}z)/(\mathrm{d}M/\mathrm{d}z)$. If one has a transition from subsonic to supersonic flow along the field line (for instance let us consider that the flow is subsonic for $z < z_0$ and supersonic for $z > z_0$), the sign of $\mathrm{d}M/\mathrm{d}z$ does not change (in the case we take as an example, $\mathrm{d}M/\mathrm{d}z|_{z=z_0} > 0$). Consequently, a transition occurs if the sign of $\mathrm{d}\mathcal{A}/\mathrm{d}z$ changes. However, if this condition is necessary, it is not sufficient. Indeed a change in the sign of $\mathrm{d}\mathcal{A}/\mathrm{d}z$ can be accompanied with a change in the sign of $\mathrm{d}M/\mathrm{d}z$. This condition for transition is similar to the one encountered in fluid mechanics in a convergent-divergent nozzle [82]. In this fluid analogy, the nozzle throat correponds to the point where the sign of $\mathrm{d}\mathcal{A}/\mathrm{d}z$ changes. Let us consider an accelerating subsonic flow in the convergent part. Two cases are possible, either the nozzle throat is choked and the flow become supersonic in the divergent part of the nozzle or the nozzle throat is not choked and the flow remains subsonic and decellerates in the divergent part. In this analogy, it is the fluid properties at the outduct of the nozzle that determines whether the nozzle throat is choked or not. One will see that the same kind of rule applies in our case when boundary conditions on the divertor targets are introduced.

Let us compute the derivative $\mathrm{d}\mathcal{A}/\mathrm{d}z$ from expression given in Equation V.1:

$$\frac{\mathrm{d}_z\mathcal{A}}{\mathcal{A}} = \frac{\mathrm{d}_z\Gamma_\parallel}{\Gamma_\parallel} + \frac{\mathrm{d}_z c_s}{c_s} - \frac{\mathrm{d}_z\Pi}{\Pi} \tag{V.2}$$

One notices that variations of particle flux, total pressure and temperature along the field line compete with each other and it is quite complex to predict where a transition can occur in the general case. However, one may focus on some particular cases to highlight the physics of the transition. For instance, in the above examples, the temperature is high enough to guaranty that heat conductivity makes temperature constant along magnetic field lines. Hence, the term $\mathrm{d}_z c_s$ vanishes. Also, if the velocity shear is small and in absence of charge exchange with neutrals, parallel velocity equation gives total pressure conservation along the field line, hence the term $\mathrm{d}_z\Pi$ can be neglected over particule flux term. In this simple case, Equation V.2 thus reduces to $\mathrm{d}_z\mathcal{A} = (2m_i c_s/\Pi)\mathrm{d}_z\Gamma_\parallel$. Also, at steady state, continuity equation gives $\mathrm{d}_z\Gamma_\parallel = \mathrm{d}_r(D\mathrm{d}_r n) + S^n$. Finally, Equation V.2 becomes:

$$\frac{\mathrm{d}\mathcal{A}}{\mathrm{d}z} = \frac{2c_s}{\Pi/m_i}\left\{\vec{\nabla}\cdot(D\vec{\nabla}_\perp n) + S^n\right\} = \frac{2c_s}{\Pi/m_i}\mathcal{S}^n \tag{V.3}$$

One recalls that the supersonic transition occurs if $\mathrm{d}A/\mathrm{d}z$ sign changes. Consequently, one notices that a change in the sign of the particle source $\mathcal{S}^n$ can trigger a supersonic transition. It is then possible to investigate whether this condition is realized in our above simulations. One reminds that there is no neutral contribution in these reference cases.

In the divertor case, the key element is the SOL topology. In fact, without neutrals, Equation V.3 states that a transition can occur if the sign of $\vec{\nabla}\cdot(D\vec{\nabla}_\perp n)$ changes along the field line. This is what exactly happens when crossing the X-point on the separatrix (Figure V.4,center). The radial profiles for different z positions along the field line are plotted on Figure V.4,right. More precisely, in slab geometry, one has $\mathcal{S}^n = \vec{\nabla}\cdot(D\vec{\nabla}_\perp n) = D\partial^2_\psi n$. In the area where the SOL is connected with the core ($z < z_x$), the particle balance presents a positive source of particle from the core ($\mathcal{S}^n > 0$) and the radial density profiles are concave (usually with an exponential shape whose decay is fixed by the SOL thickness λ_n). On the contrary, in the divertor region where the SOL is connected with the private plasma region ($z > z_x$), there is no more feeding from the core and the radial density profiles take the form of a double exponential decay, both in the SOL and in the private region, with a maximum of density close to the separatrix. Hence a net outcoming radial flux develops between the considered magnetic field line and the private plasma region and $\mathcal{S}^n < 0$. A supersonic transition is thus possible. One then wonders whether the transition actually occurs. The easiest way to address this problem is to look at what happens if the transition does not occur: let us denote $\mathcal{A}_x$ (resp. $\mathcal{A}_t$) the value of $\mathcal{A}$ at X-point (resp. Target) position. In the divertor region, one has $\mathrm{d}\mathcal{A}/\mathrm{d}z < 0$ according to Equation V.3, hence $\mathcal{A}_t < \mathcal{A}_x$. Since we are on the subsonic branch of $\mathcal{A}$ (see Figure V.3), this implies $M_t < M_x \leq 1$ which is not compatible with Bohm boundary condition ($M_t \geq 1$). Hence the solution is necessarily supersonic in the divertor region, the transition taking place at X-point position and the Mach number on the target being striclty supersonic.

In the limiter case, the same pattern applies. Even if there is no X-point, one observes a transition determined by system geometry. Indeed, plasma area located below the toroidal pumped limiter is not radially connected with the core. It plays the same role as the

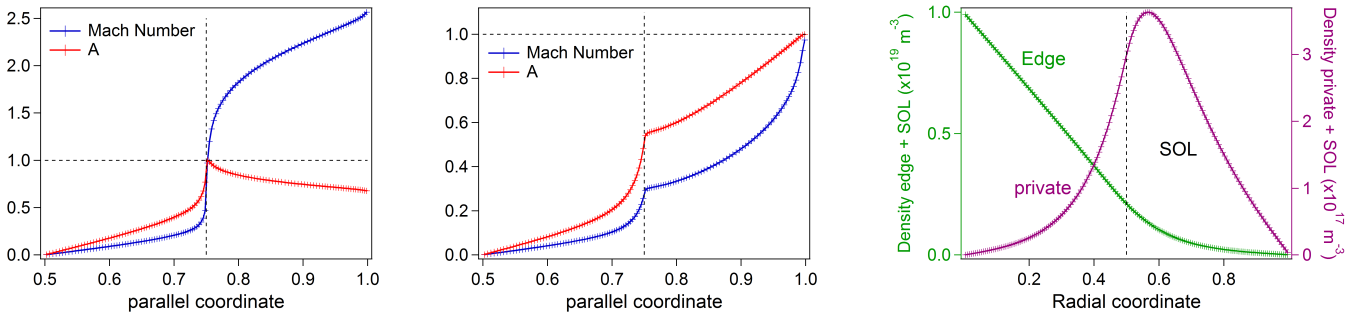

Figure V.4: Isothermal simulation with $\nu = 0$. Mach number at the separatrix: Left- without neutrals. Center- with neutrals ($R^\star = 0.9$). Right- Radial density profiles in the Core connected region and in the Private plasma connected region

divertor region in the divertor geometry. The same analysis can be done and a transition occurs along field line when passing from a core connected region to a "shadowed" region. One must notice that in this case, the magnetic field variation could have some effect on the transition, see Section V.3.

V.2.1 The effect of neutrals

A source of particles due to neutrals can compensate the loss of particles due to the perpendicular transport ans thus avoid a transition. In other words, one has to ensure that even if $\vec{\nabla} \cdot (D\vec{\nabla}_\perp n)$ is negative, $\vec{\nabla} \cdot (D\vec{\nabla}_\perp n) + S^n$ is positive. To investigate this assumption, one repeats the ideal slab divertor simulation but with the fluid neutral model turned on (Section IV.2.1). The recycling coefficient is set to $R^\star = 0.8$. The Mach number along the separatrix is plotted on Figure V.4,center with and without neutrals.

As expected, one notices that with a high enough neutral source, the supersonic transition does not occur and the Mach number reads $M_t = 1$ on target plates. Thus the transition highly depends on the tunning of the neutral model, even in this case where the neutrals are coupled to the plasma by a simple response as density source.

V.3 Temperature driven transitions

In the above section, the supersonic transition was driven by a change of topology in the divertor configuration. In order to emphasize the mechanism of the transition, one has then focused on simplified configurations where the temperature and total pressure are constant along field lines. One has observed that in the latter case, the transition can take place far from the wall. In the following part, one focuses on the effect of temperature. Indeed, when the temperature in the SOL is reduced, strong temperature gradients can take place. One must take these gradients into account and look at their consequences on the transition.

The following simulation is performed without neutrals. The absence of neutrals for low temperature is not physical but one just want to confirm the possibility of transi-

tion due to steep temperature gradients. Actually, the presence of neutrals would also contribute to sharpening temperature profiles. In presence of neutrals, the transition would be then a competition between particle source terms that tend to maintain the flow subsonic (see Section V.2.1) and the temperature gradients that tend to make the flow supersonic. A fine analysis of this interaction with neutrals is not permited by the raw neutral model used in this paper so one has prefered presenting the effect of temperature gradients without neutrals.

Let us consider the impact of temperature gradients on the parameter $\mathcal{A}$. If one neglects the variation of total pressure, the derivative of $\mathcal{A}$ along the field line is given by Equation V.4

$$\frac{\mathrm{d}A}{\mathrm{d}z} = \frac{2c_s}{\Pi/m_i}\mathcal{S}^n + \frac{\Gamma_\parallel}{c_s\Pi/m_i}\left(\frac{\mathrm{d}T_e}{\mathrm{d}z} + \frac{\mathrm{d}T_i}{\mathrm{d}z}\right) \tag{V.4}$$

Hence, one deduces that $\mathrm{d}_z\mathcal{A}$ can become negative if one has a strong drop of temperature. That is what actually happen near the target plates for low temperature plasma. Besides, this transition does not require that the sign of $\mathcal{S}^n$ changes hence this transition should be observed in a simple ideal limiter configuration at low enough temperatures. Simulation results are plotted on Figure V.5 where Mach number and temperature are represented.

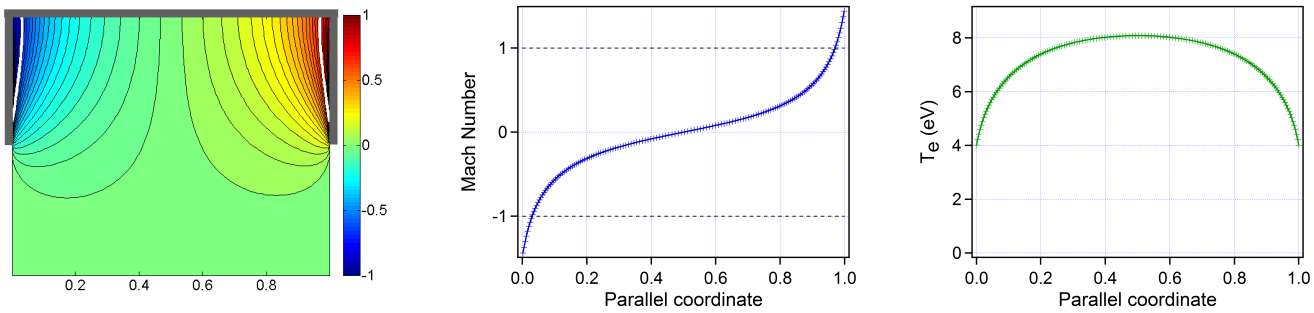

Figure V.5: Supersonic transition due to steep temperature gradients. a. Mach number in the Slab limiter configuration. The white line contour represents $|M| = 1$. b. Mach parallel profile in SOL revealing a supersonic flow near the limiter. c. Parallel temperature profile showing important temperature gradients.

On Figure V.5, one observes as expected a transition to supersonic flow near the limiter.

V.4 Magnetic field driven transitions

The effect of magnetic field can be highligthed in a simple configuration. Once again, one considers a limiter geometry but without slab approximation. One can then distinguish between a high magnetic field side (HFS) and a low magnetic field side (LFS). If one takes the magnetic field into account, in the continuity equation, the divergence of the parallel

particle flux expresses as

$$\begin{aligned} \vec{\nabla}\cdot\Gamma_{\parallel}\vec{b} &= B\frac{\partial}{\partial z}\left(\frac{\Gamma_{\parallel}}{B}\right) = \frac{\partial\Gamma_{\parallel}}{\partial z} - \Gamma_{\parallel}\frac{\partial \log B}{\partial z} \\ &= \mathcal{S}^n \qquad \text{(continuity equation)} \end{aligned} \tag{V.5}$$

Hence, in the basic configuration without temperature gradients, the variation of $\mathcal{A}$ can be described by Equation V.2 and Equation V.5 that gives,

$$\frac{\mathrm{d}\mathcal{A}}{\mathrm{d}z} = \frac{2c_s}{\Pi/m_i}\left(\mathcal{S}^n + \Gamma_{\parallel}\frac{\mathrm{d}\log B}{\mathrm{d}z}\right) \tag{V.6}$$

Hence, a transition can occur if $\Gamma_{\parallel}\mathrm{d}\log B/\mathrm{d}z < 0$. This behavior explains the differences observed in 2 limiter simulations where the limiter is successively placed at the bottom of the machine and on the HFS – see Mach number results on Figure V.6. When the limiter is at the bottom of the machine, the flow becomes supersonic on the limiter face that is exposed to the HFS plasma. In fact, this configuration meet the above required condition on the magnetic field to trigger the transition. This is not the case when the limiter is placed on the HFS of the machine.

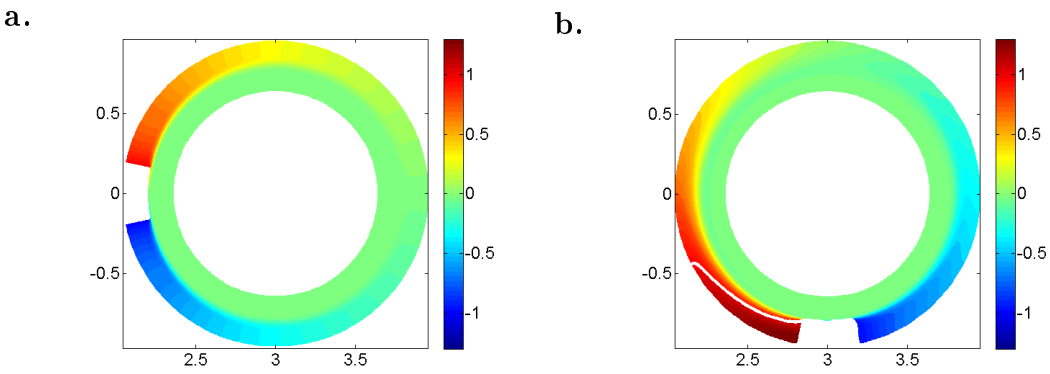

Figure V.6: Mach number for 2 different limiter configurations. The white contour line represents $|M| = 1$. a: Limiter on the HFS region. b: Limiter at the bottom. When the limiter is at the bottom, on the HFS, since the magnetic field decreases as approching the limiter, a supersonic transition is possible. This is not the case on the LFS where conversely, the magnetic field increases as approaching the limiter. When the limiter is located at the inboard mid-plane, on both side the magnetic field increases as aproching the limiter. The transition hence does not occur.

Chapter highlights

- *The hydrodynamic properties of the plasma make transition from subsonic to supersonic flow in the quasineutral plasma possible.*
- *The non-dimensionalized parameter $\mathcal{A}$ gathers the informations about how this transition is permitted or not since it occurs if $d\mathcal{A}/dz = 0$.*

$$\mathcal{A} = \frac{2M}{1+M^2} = \frac{2\Gamma c_s}{\Pi/m_i}$$

- *In particular, the supersonic transition can occur:*
  - *if the sign of the plasma source changes: this occurs in particular about the X-point in the sheath-limited regime,*
  - *if strong temperature gradients take place near the targets: This occurs in the low power, high recycling regime,*
  - *if the magnetic field is inhomogeneous.*
- *In any case, the transition is driven by the Bohm boundary condition that imposes $|M| \geq 1$ on the wall.*
- *The consequence of the supersonic transition on the flux impacting the wall is still under investigation.*

Conclusion

The SolEdge2D code development has benn motivated by various concerns from the understanding of physical mechanisms governing transport at the edge to the prediction of particles and heat fluxes at the walls for tokamak operations, as well as the development of a test bed tool to develop original numerical methods on the road of developing 3D turbulent fluid code (ANR-ESPOIR). Original numerical methods such as the penalization technique that models plasma-wall interaction for complex geometries have been validated. The penalization method enables in particular to use a largely orthogonal grid up to the main chamber wall providing a great flexibility to simply and efficiently simulate realistic tokamak configurations. Its applications to complex SOL in the limiter configuration have been published in [25]. Concerning diverted plasma simulations, realistic configurations such as *ToreSupra–WEST* and *JET* geometries are reported in this manuscript. During the code development, a special attention has been paid to guarantee numerical precision and efficiency. Some simple configurations such as the slab limiter and slab divertor for which analytical work can be done have been used to validate the code behavior. In particular, a special care has been taken to understand the many situations where spontaneous supersonic transitions take place in the quasineutral plasma. A complete description of the flow properties leading to supersonic velocity has been published in the literature [23, 83]. Also, a collaborative work has been achieved with experimentalists to understand the impact of turbulence ballooning on plasma flows in the edge region [31, 84]. Indeed, if the transport code does not directly provide informations on the turbulence (the cross field transport being set by ad hoc diffusion coefficients), it enables reproducing the overall flow pattern, simplifying the interpretation of experimental data.

Simulating the plasma up to the wall is a key issue to properly estimate where the heat load is deposited as well as where the recycling mechanisms take place. Far from the core plasma, the physics is widely controlled by the interaction between the plasma and the neutrals. In the perspective of understanding how the latter influence the edge plasma, SolEdge2D has been coupled with several neutral models. First, a fluid model where neutrals transport is ruled by a diffusion law has permitted recovering the expected density regimes. To go further, the kinetic Monte-Carlo code Eirene has been used to properly address neutrals transport and complex interaction with the plasma. Combined with the penalization technique, the neutral code Eirene makes possible to quantify the part of the main chamber wall recycling in the particle balance. These results have been presented at PSI-2012 conference in Aachen [81]. The first wall recycling phenomenon is

of major concern since it could reduce the close-divertor configuration efficiency to hold impurities far from the confined plasma. In the scope of a better understanding of the main chamber influence on the tokamak performance, the SolEdge2D-Eirene code should be coupled with an impurity code. It is indeed important to accurately quantify the amount of impurities produced on the wide main chamber surface since their concentration in the edge plasma is a key parameter to estimate sputtering and impurity production on the main plasma facing components.

In addition investigations have been carried out to find fluid closures taking weak collisionality effects into consideration. After studying the literature on this subject, a theoretical work has been achieved in collaboration with the CSDC[1] group of statical physicists in Florence. First, a deterministic model presented at Varenna international School of Plasma-Physics [85] gave some analytical results on heat propagation in a lattice. Then, a stochastic model based on Kipnitz-Marchioro-Presutti's approach has been implemented to study how microscopic energy exchange can be expressed in term of a macroscopic fluid formulation for heat flux. In the high collisionality case, the standard Fourier's law is recovered. Conversely, when collisionality drops, a non-local relation is found and an exponential kernel takes long range spatio-temporal memory effects into account. This generalized Fourier's law asymptotically recovers a ballistic transport of energy if the collisionality tends to zero. This work initially focused on parallel heat flux closure can be generalized to any process where the particle mean free path is comparable to typical system size. It has thus been applied to improve transport description in the neutral fluid model. A comparison between results obtained with the fluid model and with Eirene is a natural perspective to this work. The results obtained with the stochastic model and the generalized Fourier's law derivation can be found in [86].

During this thesis, an important numerical and theoretical work has been achieved to improve transport simulations in the edge plasma. In a near future, more quantitative simulations should be performed and compared with experimental results. A comparison with other codes shall also be done to benchmark SolEdge2D results. Finally, once the code fully validated, it will be involved in the *WEST*-tokamak program to predict heat load on the materials and evaluate impurity contamination.

[1] Center for the Study of Complex Dynamics

Bibliography

[1] J.D. Lawson. Some criteria for a power producing thermonuclear reactor. In *Proceedings of the Physical Society B (Volume 70)*, 1957. 5

[2] F. Wagner *et al.* Regime of improved confinement and high beta in neutral-beam-heated divertor discharges of the asdex tokamak. *Phys. Rev. Lett.*, 49:1408–1412, 1982. 6

[3] S. Tsuji *et al.* Observation of the limiter h mode in the jt-60 tokamak with lower-hybrid current drive. *Phys. Rev. Lett.*, 64:1023–1026, 1990. 7

[4] L. Schmitz *et al.* Reduced electron thermal transport in low collisionality h-mode plasmas in diii-d and the importance of tem/etg-scale turbulence. *Nucl. Fusion*, 52, 2012. 7

[5] J. Wesson. *Tokamaks*. IoP, 2000. 11, 17, 37, 147

[6] P.C. Stangeby. *The Plasma Boundary of Magnetic Fusion Devices*. IoP, 2000. 11, 48, 51, 78, 105, 121, 174

[7] S. Chapman and T.G. Cowling. *The Mathematical Theory of Non-uniform Gases*. Cambridge University Press, 1939. 11, 26, 27, 29, 30, 31, 32, 33, 34

[8] PPJM Schram. *Kinetic Thoery of Gases and Plasmas*. Springer, 1991. 11, 20

[9] L. Landau. Die kinetische Gleichung für den Fall Coulombscher Wechselwirkung. *Phys. Z. Sowjet.*, 10, 1936. Translation: The transport equation in the case of Coulomb interactions, in D. ter Haar, ed., *Collected papers of L.D. Landau*, pp. 163-170. Pergamon Press, Oxford, 1981. 21

[10] L. Spitzer and R. Härm. Transport phenomena in a completely ionized gas. *Phys. Rev.*, 89-5, March 1953. 35, 171

[11] R.S. Cohen, L. Spitzer, and P.M. Routly. The electrical conductivity of an ionized gas. *Phys. Rev.*, 80-2, October 1950. 35, 78

[12] S.I. Braginskii. Transport processes in a plasma. *Review of Plasma Phys.*, 1, 1965. 36, 37, 57

[13] J.D. Huba. *NRL Plasma Formulary*. Naval Research Laboratory, 2009. 37, 109

[14] C. Van Vliet. *Equilibrium and Non-Equilibrium Statistical Mechanics*. World Scientific, 2007. 44

[15] R. Kubo, M. Toda, and N. Hashitsume. *Statistical physics II: Nonequilibrium Statistical Mechanics*. Springer, 1985. 45, 82

[16] W. Paul and Baschnagel J. *Stochastic processes: From Physics to Finance*. Springer, 2000. 46

[17] J.M. Rax. *Physique des Tokamaks*. ellipses, 2011. 46

[18] L. Onsager. Reciprocal relations in irreversible processes. *Phys. Rev.*, 37:405–426, 1931. 46

[19] C. Grisolia, Horton L.D., and J.K. Ehrenberg. Modeling of hydrogen conditioning, retention and release in tore supra. *J. Nucl. Mat.*, 220:516–520, 1995. 47

[20] I. Langmuir. The interaction of electron and positive ion space charges in cathode sheaths. *Phys. Rev.*, 33:957–989, 1929. 48

[21] A. Guthrie and R.K. Wakerling. *The Characteristics of Electrical Discharges in Magnetic Fields*. New York: McGraw-Hill, 1949. 48

[22] K.U. Riemann. The bohm criterion and sheath formation. *J. Phys. D: Appl. Phys.*, 24:493–518, 1991. 48

[23] Ph. Ghendrih *et al.* Transition to supersonic flows in the edge plasma. *Plasma Phys. Control. Fusion*, 53, 2011. 50, 65, 67, 121, 123, 131

[24] M. Baelmans, P. Börner, W. Dekeyser, and Reiter D. Tokamak plasma edge modelling including the main chamber wall. *Nucl. Fusion*, 51, 2011. 54

[25] A. Paredes *et al.* Penalization technique to implement plasma facing wall-components with complex geometries in fluid simulations of the edge plasma. *J. Nucl. Mat.*, 2012 (submitted). 54, 68, 131

[26] G. Chiavassa and R. Donat. *Hyperbolic problems: theory, numerics, applications*, chapter A Penalization Technique for the Efficient Computation of Compressible Fluid Flow with Obstacles. Springer, 2008. 64

[27] P. Angot, C.-H. Bruneau, and P. Fabrie. A penalization method to take into account obstacles in viscous flows. *Numerische Mathematik*, 81:497–520, 1999. 64

[28] O.V. Vasilyev and N. K.-R. Kevlahan. Hybrid wavelet collocation - brinkman penalization method for complex geometry flows. *International Journal for numerical methods in fluids*, 40:531–538, 2002. 64

[29] B. Kadoch, D. Kolomenskiy, Ph. Angot, and K. Schneider. A volume penalization method for incompressible flows and scalar advection-diffusion with moving obstacles. *J. Comput. Phys.*, 231:4365–4383, 2012. 64

[30] L. Isoardi *et al.* Penalization modeling of a limiter in the tokamak edge plasma. *J. Comp. Phys.*, 229:2220–2235, 2010. 64

[31] A. Paredes, H. Bufferand, G. Ciraolo, F. Schwander, E. Serre, Ph. Ghendrih, and P. Tamain. A penalization technique to model plasma facing components in a tokamak with temperature variations. *J. Comp. Phys.*, 2012 (submitted). 68, 131

[32] J.P. Gunn *et al.* Evidence for the poloidally localized enhancement of radial transport in the scrape-off-layer tokamak. *J. Nucl. Mat.*, 363-365:484–490, 2007. 70

[33] A. Froese, T. Takizuka, and Yagi M. Electron parallel heat transport in the scrape-off layer using a particle-in-cell code. In *Proceedings of International TOKI conference (ITC-18)*, 2008. 78

[34] R.C. Malone, R.L. McCrory, and R.L. Morse. Indications of strongly flux-limited electron thermal conduction in laser-target experiments. *Phys. Rev. Lett.*, 34:721–724, 1975. 78

[35] M. K. Prasad and D. S. Kershaw. Nonviability of some nonlocal electron heat transport modeling. *Phys. Fluids B*, 1, 1989. 78

[36] M. Day, B. Merriman, F. Najmabadi, and R. W. Conn. The effect of heat flux limiting on divertor fluid models. *Contrib. Plasma Phys.*, 36:419, 1996. 78

[37] W. Fundamenski. Parallel heat flux limits in the tokamak scrape-off layer. *Plasma Phys. Control. Fusion*, 47:R163–R208, 2005. 78, 171

[38] J.F. Luciani and P. Mora. Nonlocal heat transport due to steep temperature gradients. *Phys. Rev. Lett.*, 51:1664–1667, 1983. 79, 89, 100, 171

[39] S.I. Krasheninnikov. On nonlocal electron heat conduction. *Phys. Fluids B*, 5:74, 1993. 79

[40] D. Borgogno, P. Hellinger, T. Passot, P.L. Sulem, and P.M. Trávnícek. Alfvén wave filamentation and dispersive phase mixing in a high-density channel: Landau fluid and hybrid simulation. *Nonlinear Processes in Geophysics*, 16:275–285, 2009. 79

[41] L. Bertini, A. De Sole, D. Gabrielli, G. Jona-Lasinio, and C. Landim. Stochastic interacting particle systems out of equilibrium. *J. Stat. Mech.*, page P07014, 2007. 79, 90

[42] T. Bodineau and B. Derrida. Cumulants and large deviation of the current through nonequilibrium steady states. *C.R. Physique*, 8:540, 2007. 79

[43] F. Bonetto, J.L. Lebowitz, and L. Rey-Bellet. Fourier's law: a challenge to theorists. In A. Fokas, A. Grigoryan, T. Kibble, and B. Zegarlinsky, editors, *Mathematical Physics 2000*, page 128. Imperial College, London, 2000. 79

[44] S. Lepri, R. Livi, and A. Politi. Thermal conduction in classical low-dimensional lattices. *Phys. Rep.*, 377:1, 2003. 79, 81

[45] A. Dhar. Heat transport in low-dimensional systems. *Advances in Physics*, 57:457–537, 2008. 79

[46] E.B. Davies. A model of heat conduction. *J. Stat. Phys.*, 18:161, 1978. 79

[47] E. Presutti C. Kipnis, C. Marchioro. Heat flow in an exactly solvable model. *J. Stat. Phys.*, 27, 1982. 79

[48] C. Giardinà, J. Kurchan, and F. Redig. Duality and exact correlations for a model of heat conduction. *J. Math. Phys.*, 48:033301, 2007. 79, 90

[49] G. Basile, C. Bernardin, and S. Olla. Momentum conserving model with anomalous thermal conductivity in low dimensional systems. *Phys. Rev. Lett.*, 96:204303, 2006. 79

[50] S. Lepri, C. Mejia-Monasterio, and A. Politi. A stochastic model of anomalous heat transport: analytical solution of the steady state. *J. Phys. A: Math. Theor.*, 42(2):025001, 2009. 79, 90

[51] A. Kundu, A. Dhar, and O. Narayan. The green–kubo formula for heat conduction in open systems. *Journal of Statistical Mechanics: Theory and Experiment*, 2009:L03001, 2009. 83

[52] Joseph D.D. and L. Preziosi. Heat waves. *Rev. Mod. Phys.*, 61(1):41–73, 1989. 85, 86

[53] F. Piazza and S. Lepri. Heat wave propagation in a nonlinear chain. *Phys. Rev. B*, 79, 2009. 88

[54] O.V. Gendelman and A.V. Savin. Nonstationary heat conduction in one-dimensional chains with conserved momentum. *Physical Review E*, 81(2):020103, 2010. 88

[55] K.K. Lin and L.S. Young. Correlations in nonequilibrium steady states of random halves models. *J. Stat. Phys.*, 128:207, 2007. 90

[56] M. K. Prasad and D. S. Kershaw. Stable solutions of nonlocal electron heat transport equations. *Phys. Fluids B*, 3, 1991. 96

[57] D. Colombant and W. Manheimer. Numerical fluid solutions for nonlocal electron transport in hot plasmas: Equivalent diffusion versus nonlocal source. *J. Comp. Phys.*, 229:4369–4381, 2010. 96

[58] J.W. James. *Implementation and Application of Non-local parallel heat flow in magnetized plasmas*. PhD thesis, Utah State University, 2007. 96

[59] M. Torrilhon and H. Struchtrup. Boundary conditions for regularized 13-moments-equations for micro-channel-flows. *J. Comput. Phys.*, 227:1982–2011, 2008. 98

[60] C. Villani. *A review of mathematical topics in collisional kinetic theory*. Elsevier, 2002. 98

[61] Ph. Ghendrih *et al.* Progress in ergodic divertor operation on tore supra. *Nucl. Fusion*, 42:1221–1250, 2002. 104, 105

[62] M.Z. Hasan, R.W. Conn, and G.C. Pomraning. Application of diffusion theory to neutral atom tranport in fusion plasmas. *Nucl. Fusion*, 27, 1987. 108

[63] E.L. Vold, F. Najmabadi, and R.W. Conn. Fluid model equations for the tokamak plasma edge. *Phys. Fluids B*, 3:3132–3152, 1991. 108

[64] D. Reiter, M. Baelmans, and P. Börner. The EIRENE and B2-EIRENE codes. *Fusion Sci. Technol.*, 47:172–186, 2005. 113

[65] A.V. Chankin *et al.* Solps modelling of asdex upgrade h-mode plasma. *Plasma Phys. Control. Fusion*, 48:839, 2006. 113

[66] R. Schneider, X. Bonnin, K. Borrass, D.P. Coster, H. Kastelewicz, D. Reiter, and B.J. Rozhansky, V.A. Braams. Plasma edge physics with b2-eirene. *Contrib. Plasma Phys.*, 46:3–191, 2006. 113

[67] W. Fundamenski *et al.* Progress in edge plasma transport modeling on jet. *Contrib. Plasma Phys.*, 48:190–195, 2008. 113

[68] D. Moulton, W. Fundamenski, S. Wiesen, G. Corrigan, P. Belo, G. Maddison, C. Giroud, and JET-EFDA Contributors. Edge2d-eirene modelling of the inter-elm phase of h-mode plasmas on jet. *J. Nucl. Mat.*, 415:S509–S512, 2011. 113

[69] D. Moulton, W. Fundamenski, S. Wiesen, G. Corrigan, P. Belo, G. Maddison, C. Giroud, and JET-EFDA Contributors. Progress in Edge2d-Eirene modelling of nitrogen seeded jet plasmas. *JET EFDA CP*, 2010. *(preprint)*. 113

[70] C. Guillemaut *et al.* Edge2d-eirene modelling of divertor detachment in jet high triangularity l-mode plasmas in carbon and be/w environment. *JET EFDA CP*, 2012. *(preprint)*. 113

[71] P.C. Stangeby *et al.* Interpretive modeling of simple-as-possible-plasma discharges on diii-d using the oedge code. *J. Nucl. Mat.*, 313-316:883–887, 2003. 113

[72] J.D. Elder *et al.* Oedge modeling of ^{13}c deposition in the inner divertor of diii-d. *J. Nucl. Mat.*, 337-339:79–83, 2005. 113

[73] D. Harting, S. Wiesen, H. Frerichs, D. Reiter, P. Börner, and Y. Feng. Validating the 3d edge code emc3-eirene against 2d simulations with edge2d-eirene for jet single null configurations. *J. Nucl. Mat.*, 415:S540–S544, 2011. 113

[74] J. Reiter. Eirene website (links to code manuals). http://www.eirene.de/, 2009. 113

[75] V. Kotov, D. Reiter, and A.S. Kukushkin. *Numerical Study of the ITER Divertor Plasma with the B2-EIRENE Code Package*. Forschungszentrum, Zentralbibliothek, 2007. 113

[76] J. Ziegler. Trim and srim website (links to code manuals). http://www.srim.org/, 2012. 115

[77] B. Labombard *et al.* Cross-field plasma transport and main-chamber recycling in diverted plasmas on ALCATOR C-MOD. *Nucl. Fusion*, 40:2041–2060, 2000. 119

[78] P.C. Stangeby. Subsonic and supersonic divertor solutions. *Plasma Phys. Control. Fusion*, 33:677–683, 1991. 121

[79] P.J. Harbour and A. Loarte. Departures from sonic flow at the sheath on a divertor target or limiter. *Contrib. Plasma Phys.*, 34:312–316, 1994. 121

[80] E. Serre *et al.* Numerical modeling of the impact of geometry and wall components on transport in the tokamak edge. *Contrib. Plasma Phys.*, 52, 2012. 123

[81] H. Bufferand *et al.* Near wall plasma simulation with penalisation technique with tranport code soledge2d-eirene. *J. Nucl. Mat.*, 2012 (submitted). 123, 131

[82] A. Bonnet and J. Luneau. *Aérodynamique : Théories de la Dynamique des Fluides*. Editions Cépaduès, 1989. 124

[83] H. Bufferand *et al.* Study of supersonic transitions in the quasineutral edge plasma with the transport code SOLEDGE2D. *Plasma Phys. Control. Fusion*, 2012 (in preparation). 131

[84] H. Bufferand, G. Ciraolo, and L. Isoardi *et al.* Application of soledge-2d code to complex sol configurations and analysis of mach probe measurements. *J. Nucl. Mat.*, 415:589–592, 2011. 131

[85] H. Bufferand, G. Ciraolo, P. Ghendrih, P. Tamain, F. Bagnoli, S. Lepri, and R. Livi. One-dimensional particle models for heat transfer analysis. *Journal of Physics: Conference Series*, 260:012005, 2010. 132

[86] H. Bufferand, G. Ciraolo, Ph. Ghendrih, S. Lepri, and Livi. R. Particle model for nonlocal heat transport in fusion plasmas. *Phys. Rev. E*, 2012 (submitted). 132

[87] A. Harten, B. Engquist, S. Osher, and S. Chakravarthy. Uniformly high order accurate essentially non-oscillatory schemes, iii. *Journal of Computational Physics*, 71:231–303, 1987. 150

[88] X.D. Liu, S. Osher, and T. Chan. Weighted essentially nonoscillatory schemes. *Journal of Computational Physics*, 115:200–212, 1994. 150

[89] R. Donat and A. Marquina. Capturing shock reflections: An improoved flux formula. *Journal of Computational Physics*, 125:42–58, 1996. 150

[90] N. Črnjarić-Žic, S. Maćešić, and B. Crnković. Efficient implementation of weno schemes to nonuniform meshes. *Annali dell'Universita di Ferrara*, 53, 2007. 152

[91] W. Chi-Shu. Essentially non-oscillatory and weighted essentially non-oscillatory schemes for hyperbolic conservation laws. *Technical report*, 1997. 152

[92] U.M. Ascher, S.J. Ruuth, and B.T.R. Wetton. Implicit-explicit methods for time-dependent partial differential equations. *Journal of Numerical Analysis*, 32-3:797–823, 1995. 155

[93] I. Higueras and T. Roldan. Positivity-preserving and entropy-decaying imex methods. In *Ninth International Conference Zaragoza-Pau on Applied Mathematics and Statistics*, 2005. 155

[94] L. Pareschi and G. Russo. Implicit-explicit runge-kutta schemes and applications to hyperbolic systems with relaxation. *Journal of Scientific Computing*, 2003. 155

[95] D.J. Bond. Approximate calculation of the thermal conductivity of a plasma with an arbitrary temperature gradient. *J. Phys. D: Appl. Phys.*, 14, 1981. 172, 180

[96] M.H. Shirazian and L.C. Steinhauer. Kinetic-theory description of electron heat transfer in a plasma. *Phys. Fluids*, 24, May 1981. 172, 180

List of Figures

List of Tables

Appendix A

Complementary notes on collisions

A.1 Fokker-Planck expression for collisional term

The collisional term gives the rate of particules whose velocity changes from $\vec{v'}$ to $\vec{v}$ because of collisions.

$$\left(\frac{\partial f}{\partial t}\right)_c = \frac{f(\vec{x},\vec{v},t+\mathrm{d}t) - f(\vec{x},\vec{v},t)}{\mathrm{d}t}$$

In order to estimate it, it can be useful to introduce the function $\psi(\vec{v},\vec{\Delta v})$ that gives the probability that a particule of velocity $\vec{v}$ has a $\vec{\Delta v}$ velocity increment during a time unit. Hence, the expression of $\mathrm{d}f(\vec{x},\vec{v},t)$,

$$f(\vec{x},\vec{v},t+\mathrm{d}t) = \iiint_{\mathcal{V}} f(\vec{x},\vec{v}-\vec{\Delta v},t)\psi(\vec{v}-\vec{\Delta v},\vec{\Delta v})\ \mathrm{d}\vec{\Delta v}^3 \tag{A.1}$$

One can approximate this term using a Taylor series cut at the second order,

$$\begin{aligned} f(\vec{x},\vec{v}-\vec{\Delta v},t)\psi(\vec{v}-\vec{\Delta v},\vec{\Delta v}) &= f(\vec{x},\vec{v},t)\psi(\vec{v},\vec{\Delta v}) \\ &\quad - \sum_\alpha \frac{\partial}{\partial v_\alpha}(f\psi)\Delta v_\alpha + \frac{1}{2}\sum_{\alpha,\beta}\frac{\partial^2}{\partial v_\alpha \partial v_\beta}(f\psi)\Delta v_\alpha \Delta v_\beta + o(\Delta v^2) \end{aligned}$$

It is now possible to express the collisional term as follow,

$$\begin{aligned} \left(\frac{\partial f}{\partial t}\right)_c &= -\sum_\alpha \frac{\partial}{\partial v_\alpha}\left(f(\vec{x},\vec{v},t)\iiint_{\mathcal{V}}\psi(\vec{v},\vec{\Delta v})\frac{\Delta v_\alpha}{\Delta t}\mathrm{d}\vec{\Delta v}^3\right) \\ &\quad + \frac{1}{2}\sum_{\alpha,\beta}\frac{\partial^2}{\partial v_\alpha \partial v_\beta}\left(f(\vec{x},\vec{v},t)\iiint_{\mathcal{V}}\psi(\vec{v},\vec{\Delta v})\frac{\Delta v_\alpha \Delta v_\beta}{\Delta t}\mathrm{d}\vec{\Delta v}^3\right) \end{aligned} \tag{A.2}$$

One can notice that the integrals can be expressed thanks to the average deviation rate and deviation cross-products rate calculated in [5],

$$\langle \Delta v_\alpha \rangle = \iiint_{\mathcal{V}} \psi \frac{\Delta v_\alpha}{\Delta t}\mathrm{d}\vec{\Delta v}^3$$

and

$$\langle \Delta v_\alpha \Delta v_\beta \rangle = \iiint_{\mathcal{V}} \psi \frac{\Delta v_\alpha \Delta v_\beta}{\Delta t} \mathrm{d}\vec{\Delta} v^3$$

This leads to the **Fokker-Planck** expression of the collision term:

$$\boxed{\left(\frac{\partial f}{\partial t}\right)_c = -\sum_\alpha \frac{\partial}{\partial v_\alpha}(\langle \Delta v_\alpha \rangle f) + \frac{1}{2}\sum_{\alpha,\beta} \frac{\partial^2}{\partial v_\alpha \partial v_\beta}(\langle \Delta v_\alpha \Delta v_\beta \rangle f)} \tag{A.3}$$

The 1D-tensor $\langle \Delta v_\alpha \rangle$ and the 2D-tensor $\langle \Delta v_\alpha \Delta v_\beta \rangle$ are called the Fokker-Planck coefficients. One can notice that the terms in $\langle \Delta v_\alpha \Delta v_\beta \rangle$ play the role of diffusion coefficients in the velocity space.

Appendix B

Numerical scheme

In this appendix, one describes the numerical method that is used to solve SolEdge2D equations:

$$\frac{\partial n}{\partial t} + \vec{\nabla} \cdot \Gamma_{\parallel} \vec{b} = \vec{\nabla} \cdot \left(D \vec{\nabla}_{\perp} n \right) \tag{B.1}$$

$$\frac{\partial \Gamma_{\parallel}}{\partial t} + \vec{\nabla} \cdot \left(\frac{\Gamma_{\parallel}^2}{n} + n \frac{T_e + T_i}{m_i} \right) \vec{b} + \left(n \frac{T_e + T_i}{m_i} \right) \vec{\nabla} \cdot \vec{b} = \vec{\nabla} \cdot \left(\nu \vec{\nabla}_{\perp} \Gamma_{\parallel} \right) \tag{B.2}$$

$$\begin{aligned} \frac{\partial}{\partial t} \left(\frac{3}{2} n T_{\alpha} \right) + \vec{\nabla} \cdot \left(\frac{3}{2} \Gamma_{\parallel} T_{\alpha} \vec{b} \right) + n T_{\alpha} \vec{\nabla} \cdot \left(\frac{\Gamma_{\parallel}}{n} \vec{b} \right) = \vec{\nabla} \cdot \left(\kappa_{\alpha}^{0} T_{\alpha}^{5/2} \nabla_{\parallel} T_{\alpha} \vec{b} \right) \\ + \vec{\nabla} \cdot \left(\frac{3}{2} D T_{\alpha} \vec{\nabla}_{\perp} n + \frac{3}{2} \xi_{\alpha} n \vec{\nabla}_{\perp} T_{\alpha} \right) \end{aligned} \tag{B.3}$$

The numerical method is based on finite difference scheme. The spatial discretization will be addressed firstly, followed by the time discretization.

B.1 Spatial discretization

B.1.1 Advection terms

In this section, one considers the advective part of the equations; the system considered is the following:

$$\begin{cases} \partial_t n + \vec{\nabla} \cdot \Gamma \vec{b} = 0 \\ \partial_t \Gamma + \vec{\nabla} \cdot \left(\frac{\Gamma^2}{n} + \frac{n(T_e + T_i)}{m_i} \right) \vec{b} = 0 \\ \partial_t n T_e + \vec{\nabla} \cdot \left(\Gamma T_e \vec{b} \right) + \gamma n T_e \vec{\nabla} \cdot \left(\frac{\Gamma}{n} \vec{b} \right) = 0 \\ \partial_t n T_i + \vec{\nabla} \cdot \left(\Gamma T_i v \vec{b} \right) + \gamma n T_i \vec{\nabla} \cdot \left(\frac{\Gamma}{n} \vec{b} \right) = 0 \end{cases} \tag{B.4}$$

a) Re-writing in a conservative form

This set of equation corresponds to Euler equations for an adiabatic gas. In the following, one uses gas constant $\gamma = 2/3$ and one introduces the variables corresponding to entropies

S_e and S_i for these adiabatic gases.

$$S_e = \frac{p_e}{n^\gamma} = \frac{T_e}{n^{\gamma-1}} \qquad S_i = \frac{p_i}{n^\gamma} = \frac{T_i}{n^{\gamma-1}} \tag{B.5}$$

Considering the adiabaticity of the system, one expects entropy equations to be easily expressed in a conservative form. In fact, the above equations can be rewritten in a flux form:

$$\begin{cases} \partial_t n + \vec{\nabla} \cdot \Gamma \vec{b} = 0 \\ \partial_t \Gamma + \vec{\nabla} \cdot \left(\frac{\Gamma^2}{n} + \frac{n^\gamma (S_e + S_i)}{m_i} \right) \vec{b} = 0 \\ \partial_t S_e + \vec{\nabla} \cdot \left(\frac{\Gamma S_e}{n} \vec{b} \right) = 0 \\ \partial_t S_i + \vec{\nabla} \cdot \left(\frac{\Gamma S_i}{n} \vec{b} \right) = 0 \end{cases} \tag{B.6}$$

Finally, if one introduces the expression of the divergence (see Appendix C on expression of differential operators),

$$\vec{\nabla} \cdot X \vec{b} = B \mathcal{G} \frac{\partial}{\partial \theta} \left(\frac{X}{B} \right)$$

the above system can be rewritten as

$$\partial_t \vec{U} + \partial_\theta \vec{F} = 0 \tag{B.7}$$

where

$$\vec{U} = \frac{1}{B\mathcal{G}} \begin{pmatrix} n \\ \Gamma \\ S_e \\ S_i \end{pmatrix} \quad \text{and} \quad \vec{F} = \frac{1}{B} \begin{pmatrix} \Gamma \\ \frac{\Gamma^2}{n} + \frac{n^\gamma (S_e + S_i)}{m_i} \\ S_e \frac{\Gamma}{n} \\ S_i \frac{\Gamma}{n} \end{pmatrix} \tag{B.8}$$

Many numerical schemes have been developed to solve 1D equations of the form given by Equation B.7. Given the fact that due to the strong gradients appearing in velocity and density fields at the interaction between the plasma and solid surfaces, it is necessary to use a numerical scheme able to handle discontinuities. The ENO (Essentially Non-Oscillatory) scheme developped by [87] and WENO (Weighted Essentially Non Oscillatory) scheme developped by [88] are well suited to this kind of problem. A modified version of these schemes developped by [89] have thus been implemented in SolEdge2D.

b) Donat-Marquina's formulation

In this part, one does not analyse scheme properties. For further details, refer to the given reference. One just states the algorithm implemented in the code. The numerical scheme described by [89] can be summed up as follow. The finite difference discretization of Equation B.7 gives

$$\frac{\partial \vec{U}}{\partial t} = \frac{\vec{F}^M_{i+\frac{1}{2}} - \vec{F}^M_{i-\frac{1}{2}}}{\theta_{i+\frac{1}{2}} - \theta_{i-\frac{1}{2}}} \tag{B.9}$$

where one uses Donat and Marquina's discrete expression for the flux:

$$\vec{F}^M_{i+\frac{1}{2}} = \vec{F}^M(\vec{U}^l_{i+\frac{1}{2}}, \vec{U}^r_{i+\frac{1}{2}}) \tag{B.10}$$

$$\vec{F}^M_{i-\frac{1}{2}} = \vec{F}^M(\vec{U}^l_{i-\frac{1}{2}}, \vec{U}^r_{i-\frac{1}{2}}) \tag{B.11}$$

The variables $\vec{U}^{r,l}_{i+\frac{1}{2}}$ and $\vec{U}^{r,l}_{i-\frac{1}{2}}$ are computed according to the WENO procedure presented in paragaph c).

Then the expression of the flux $\vec{F}^M$ is based on spectral eigen modes properties of the linear system of Equations B.7:

$$\partial\vec{U} + \partial_\theta \vec{F}(\vec{U}) = 0$$

One computes the Jacobian of the flux $A(\vec{U}) = \partial\vec{F}/\partial\vec{U}$:

$$A(\vec{U}) = \mathcal{G}\begin{pmatrix} 0 & 1 & 0 & 0 \\ -\frac{\Gamma^2}{n^2} + \frac{\gamma n^{\gamma-1}(S_e+S_i)}{m_i} & \frac{2\Gamma}{n} & \frac{n^\gamma}{m_i} & \frac{n^\gamma}{m_i} \\ -\frac{S_e}{n}\frac{\Gamma}{n} & \frac{S_e}{n} & \frac{\Gamma}{n} & 0 \\ -\frac{S_i}{n}\frac{\Gamma}{n} & \frac{S_i}{n} & 0 & \frac{\Gamma}{n} \end{pmatrix} \tag{B.12}$$

The eigenvalues of this matrix are $\vec{\lambda}(\vec{U}) = \mathcal{G}[v, v, v+c_s, v-c_s]$ where c_s is the sound speed in adiabatic gas and $v = \Gamma/n$,

$$c_s = \sqrt{(\gamma+1)\frac{(T_e+T_i)}{m_i}} \tag{B.13}$$

Then one expresses left and right eigenvectors:

$$L(\vec{U}) = \frac{1}{\alpha+\beta+\delta}\begin{pmatrix} \delta & 0 & \frac{\delta}{\alpha} & -1-\frac{\beta}{\alpha} \\ \beta & 0 & -1-\frac{\delta}{\alpha} & \frac{\beta}{\alpha} \\ \frac{\alpha}{2} - \frac{v(\alpha+\beta+\delta)}{2c_s} & \frac{\alpha+\beta+\delta}{2c_s} & 1/2 & 1/2 \\ \frac{\alpha}{2} + \frac{v(\alpha+\beta+\delta)}{2c_s} & -\frac{\alpha+\beta+\delta}{2c_s} & 1/2 & 1/2 \end{pmatrix} \tag{B.14}$$

and

$$R(\vec{U}) = \begin{pmatrix} 1 & 1 & 1 & 1 \\ v & v & v+c_s & v-c_s \\ 0 & -\alpha & \beta & \beta \\ -\alpha & 0 & \delta & \delta \end{pmatrix} \tag{B.15}$$

where

$$\begin{cases} \alpha = \gamma\frac{T_e+T_i}{n^\gamma} \\ \beta = \frac{T_e}{n^\gamma} \\ \delta = \frac{T_i}{n^\gamma} \end{cases} \tag{B.16}$$

One computes the "sided" local variables

$$\begin{cases} \vec{\Omega}^l &= L(\vec{U}^l)\cdot\vec{U}^l \\ \vec{\Omega}^r &= L(\vec{U}^r)\cdot\vec{U}^r \end{cases} \tag{B.17}$$

and the "sided" local fluxes

$$\begin{cases} \vec{\phi}^l &= L(\vec{U}^l)\cdot\vec{F}(\vec{U}^l) \\ \vec{\phi}^r &= L(\vec{U}^r)\cdot\vec{F}(\vec{U}^r) \end{cases} \tag{B.18}$$

Then, one computes the "modified sided" fluxes with a flux-limiter Roe scheme:

for $k = 1, \ldots, 4$
  if $\lambda_k(\vec{U}^l) \times \lambda_k(\vec{U}^r) > 0$ then
    if $\lambda_k(\vec{U}^l) > 0$ then
      $\phi_k^+ = \phi_k^l$
      $\phi_k^- = 0$
    else
      $\phi_k^- = 0$
      $\phi_k^+ = \phi_k^r$
    endif
  else
    $\alpha_k = \max\{|\lambda_k(\vec{U}^l)|, |\lambda_k(\vec{U}^r)|\}$
    $\phi_k^+ = 0.5(\phi_k^l + \alpha_k\Omega_k^l)$
    $\phi_k^- = 0.5(\phi_k^r - \alpha_k\Omega_k^r)$
  endif
endfor

Finally, one computes the Marquina fluxes that we use in Equation B.9

$$\vec{F}^M(\vec{U}^l, \vec{U}^r) = \vec{\phi^+}\cdot R(\vec{U}^l) + \vec{\phi^-}\cdot R(\vec{U}^r) \tag{B.19}$$

c) WENO scheme

The WENO scheme used in SolEdgeED must be able to deal with non-uniform grid. The formulation used is inspired from [90, 91]. The WENO2 scheme is impleted giving:

$$U^l_{i+\frac{1}{2}} = \omega_0^i(\theta_{i+\frac{1}{2}})p_0^i(\theta_{i+\frac{1}{2}}) + \omega_1^i(\theta_{i+\frac{1}{2}})p_1^i(\theta_{i+\frac{1}{2}}) \tag{B.20}$$

and

$$U^r_{i+\frac{1}{2}} = \omega_0^{i+1}(\theta_{i+\frac{1}{2}})p_0^{i+1}(\theta_{i+\frac{1}{2}}) + \omega_1^{i+1}(\theta_{i+\frac{1}{2}})p_1^{i+1}(\theta_{i+\frac{1}{2}}) \tag{B.21}$$

The interpolating polynoms being defined for $s = \{0, 1\}$ by

$$p_s^i(\theta) = b_{s,0}^i + b_{s,1}^i(\theta - \theta_{i+\frac{1}{2}}) \tag{B.22}$$

with

$$b^i_{0,0} = U_{i-1} + (2\theta_{i+\frac{1}{2}} - \theta_{i-\frac{3}{2}} - \theta_{i-\frac{1}{2}})\frac{U_i - U_{i-1}}{\theta_{i+\frac{1}{2}} - \theta_{i-\frac{3}{2}}} \quad ; \quad b^i_{0,1} = 2\frac{U_i - U_{i-1}}{\theta_{i+\frac{1}{2}} - \theta_{i-\frac{3}{2}}}$$
$$b^i_{1,0} = U_i + (\theta_{i+\frac{1}{2}} - \theta_{i-\frac{1}{2}})\frac{U_{i+1} - U_i}{\theta_{i+\frac{3}{2}} - \theta_{i-\frac{1}{2}}} \quad ; \quad b^i_{1,1} = 2\frac{U_{i+1} - U_i}{\theta_{i+\frac{3}{2}} - \theta_{i-\frac{1}{2}}}$$

The weights $\omega_0(\theta)$ and $\omega_1(\theta)$ are computed using for $s = \{0, 1\}$

$$\omega^i_s = \frac{\alpha^i_s(\theta)}{\alpha^i_0(\theta) + \alpha^i_1(\theta)} \tag{B.23}$$

with

$$\alpha^i_s(\theta) = \frac{C^i_s(\theta)}{(\epsilon + IS^i_s)^2} \tag{B.24}$$

The variable ϵ is a small number (usually $\epsilon = 10^{-6}$) avoiding division by zero. The variables IS^i_s evaluate interpolating polynoms sharpness and are computed from polynoms slopes:

$$IS^i_s = (b^i_{s,1})^2(\theta_{i+\frac{1}{2}} - \theta_{i-\frac{1}{2}})^2 \tag{B.25}$$

The factors $C^i_s(\theta)$ depends on the mesh. The following expressions are used to compute fluxes at the point $\theta_{i+\frac{1}{2}}$:

$$C^i_0(\theta_{i+\frac{1}{2}}) = \frac{\theta_{i+\frac{3}{2}} - \theta_{i+\frac{1}{2}}}{\theta_{i+\frac{3}{2}} - \theta_{i-\frac{3}{2}}} \quad ; \quad C^i_1(\theta_{i+\frac{1}{2}}) = \frac{\theta_{i+\frac{1}{2}} - \theta_{i-\frac{3}{2}}}{\theta_{i+\frac{3}{2}} - \theta_{i-\frac{3}{2}}}$$
$$C^{i+1}_0(\theta_{i+\frac{1}{2}}) = \frac{\theta_{i+\frac{5}{2}} - \theta_{i+\frac{1}{2}}}{\theta_{i+\frac{5}{2}} - \theta_{i-\frac{1}{2}}} \quad ; \quad C^{i+1}_1(\theta_{i+\frac{1}{2}}) = \frac{\theta_{i+\frac{1}{2}} - \theta_{i-\frac{1}{2}}}{\theta_{i+\frac{5}{2}} - \theta_{i-\frac{1}{2}}}$$

B.1.2 Diffusion terms

The diffusion terms that are used either in the perpendicular transport terms or in the parallel heat transport term are discretized with a centered second order finite difference scheme. The diffusion coefficients are evaluated on virtual middle-points. Hence, the terms $\partial_\theta D \partial_\theta U$ or $\partial_\psi D \partial_\psi U$ are computed by the following relation (x represents either θ or ψ):

$$\begin{aligned}\frac{\partial}{\partial x}\left(D\frac{\partial U}{\partial x}\right) &= U_{i+1}\frac{D_{i+1} + D_i}{2}\frac{x_i - x_{i-1}}{dx3} \\ &\quad -U_i\left(\frac{D_{i+1} + D_i}{2}\frac{x_i - x_{i-1}}{dx3} + \frac{D_i + D_{i-1}}{2}\frac{x_{i+1} - x_i}{dx3}\right) \\ &\quad +U_{i-1}\frac{D_i + D_{i-1}}{2}\frac{x_{i+1} - x_i}{dx3}\end{aligned} \tag{B.26}$$

with

$$dx3 = 0.5(x_{i+1} - x_{i-1})(x_{i+1} - x_i)(x_i - x_{i-1}) \tag{B.27}$$

For non-orthogonal grids, one also has to compute cross-derivative terms such of the form $\partial_\theta D \partial_\psi U$ or $\partial_\psi D \partial_\theta U$. These terms are evaluated with a double centered method, for instance:

$$\begin{aligned} \frac{\partial}{\partial\theta}\left(D\frac{\partial U}{\partial\psi}\right) &= \frac{1}{\theta_{j+1}-\theta_{j-1}}\left(\left(D\frac{\partial U}{\partial\psi}\right)_{j+1} - \left(D\frac{\partial U}{\partial\psi}\right)_{j+1}\right) \\ &= \frac{1}{\theta_{j+1}-\theta_{j-1}}\left(D^i_{j+1}\frac{U^{i+1}_{j+1}-U^{i-1}_{j+1}}{\psi^{i+1}-\psi^{i-1}} - D^i_{j-1}\frac{U^{i+1}_{j-1}-U^{i-1}_{j-1}}{\psi^{i+1}-\psi^{i-1}}\right) \end{aligned} \tag{B.28}$$

The behavior of the diffusion scheme has been tested on a non-orthogonal grid and has shown rather satisfactory results. One must mention that it has not been verified that the discretization of non-orthogonal terms guarantee conservation and stability of the solution.

B.2 Time discretization

Let us evaluate characteristic times associated to the different contributions in SolEdge2D Equations:

- **Advection terms**: The characteristic speed of advection is the isothermal ($\gamma = 0$ in Equation B.13) sound speed $c_s = \sqrt{(T_e + T_i)/m_i}$. The characteristic time for advection is then (N_z denotes here the number of points in the θ-direction).

$$\tau_{adv} = \frac{\Delta s}{c_s} \approx \frac{R_0 q \Delta\theta}{c_s} = \frac{2\pi R_0 q}{N_z c_s}$$

  For realistic value of temperature ($T_e = T_i = 200\ eV$), major radius ($R_0 = 3\ m$), safety factor ($q = 4$) and let say 200 points in the poloidal direction, one obtains a typical advection time $\tau_{adv} \approx 10^{-6}\ s$.

- **Perpendicular transport**: The characteristic time associated with the various diffusion processes can be evaluated as

$$\tau_\perp = \frac{\Delta L_\perp^2}{D} = \frac{L_\perp^2}{N_x^2 D}$$

  For realistic values of $D = 1\ m^2/s$, $L_\perp = 0.1\ m$ and for 100 points in the radial direction one obtains $\tau_\perp = 10^{-6}\ s$.

- **Parallel heat transport**: The characteristic time associated with the parallel heat conduction is

$$\tau_q = \frac{3}{2}k_B n \frac{\Delta s^2}{\kappa_0 T^{5/2}} \approx \frac{3}{2}k_B n \frac{q^2 R_0^2 4\pi^2}{N_z^2 \kappa_0 T^{5/2}}$$

  For typical values $n = 10^{19}\ m^{-3}$, $\kappa_0 = 10^{-11}\ W m^{-1} K^{-7/2}$, $T = 200\ eV = 1.73E6\ K$, one obtains $\tau_q \approx 10^{-9}\ s$.

The advection and perpendicular transport hence correspond to slowly varying contributions that will be solved explicitely. Conversely, the parallel heat transport is 1000 times faster and will be solved implicitely. The penalization terms are also stiff terms that are solved implicitely. One then solves the system given by Equation B.29 where $\mathcal{E}$ denotes explicitely solved contributions, $\mathcal{D}$ denotes parallel heat transport terms and $\mathcal{P}$ the penalization terms.

$$\frac{\partial X}{\partial t} = \mathcal{E} + \mathcal{D} + \mathcal{P} \tag{B.29}$$

The time scheme is based on so called IMEX scheme [92, 93, 94] that aims at optimizing stability and precision for partial equations mixing explicit and implicit treatment. The temporal scheme retained is based on a second-order IMEX scheme that uses Adams-Bashforth scheme for explicit terms and Crank-Nicolson scheme for heat transport terms, these two schemes being second order in time. However, in order to ensure the positivity of the solution, the penalization terms have to be solved with backward Euler implicit scheme that is only first order in time. The temporal scheme is given by Equation B.30.

$$\frac{X^{n+1} - X^n}{\Delta t} = \underbrace{\frac{3}{2}\mathcal{E}^n - \frac{1}{2}\mathcal{E}^{n-1}}_{\text{Adams-Bashforth}} + \underbrace{\frac{1}{2}\left(\mathcal{D}^{n+1} + \mathcal{D}^n\right)}_{\text{Crank-Nicolson}} + \mathcal{P}^{n+1} \tag{B.30}$$

Appendix C

Metric coefficients in SOLEDGE2D

C.1 Covariant and contraviant base

For any set of 3D coordinates (u^1, u^2, u^3) it is possible to define a covariant base $(\mathbf{e}_1, \mathbf{e}_2, \mathbf{e}_3)$. If one denotes $\mathbf{R}$ the position vector in the 3D space, the covariant base is defined as:

$$\mathbf{e}_1 = \frac{\partial \mathbf{R}}{\partial u^1} \quad , \quad \mathbf{e}_2 = \frac{\partial \mathbf{R}}{\partial u^2} \quad , \quad \mathbf{e}_3 = \frac{\partial \mathbf{R}}{\partial u^3} \tag{C.1}$$

This base is not necessarilly orthogonal and one denotes $g_{ij} = \mathbf{e}_i \cdot \mathbf{e}_j$ and $h_i = g_{ii}$. Any vector $\mathbf{X}$ can be expressed in the covariant base according to Equation C.2:

$$\mathbf{X} = X^1\mathbf{e}_1 + X^2\mathbf{e}_2 + X^3\mathbf{e}_3 \tag{C.2}$$

One can also define the contravariant base $(\mathbf{e}^1, \mathbf{e}^2, \mathbf{e}^3)$ such as $\mathbf{e}^i \cdot \mathbf{e}_j = \delta_{ij}$. One can deduce that the contravariant base is given by the relation

$$\mathbf{e}^1 = \nabla u^1 \quad , \quad \mathbf{e}^2 = \nabla u^2 \quad , \quad \mathbf{e}^3 = \nabla u^3 \tag{C.3}$$

One also denotes the scalar product $g^{ij} = \mathbf{e}^i \cdot \mathbf{e}^j$ and $h^i = g^{ii}$. Likewise, any vector $\mathbf{X}$ can be expressed in the contravariant base as

$$\mathbf{X} = X_1\mathbf{e}^1 + X_2\mathbf{e}^2 + X_3\mathbf{e}^3 \tag{C.4}$$

Using the definition $\mathbf{e}_i \cdot \mathbf{e}^j = \delta_{ij}$, one deduces that $X_i = \mathbf{X} \cdot \mathbf{e}_i$ and $X^i = \mathbf{X} \cdot \mathbf{e}^i$.

C.2 Curvilinear coordinates in 2D

One considers the cylindrical coordinates (R, z, φ) associated to the covariant base $(\mathbf{e}_R, \mathbf{e}_z, \mathbf{e}_\varphi)$ and to the contravariant base $(\mathbf{e}^R, \mathbf{e}^z, \mathbf{e}^\varphi)$. This base is linked to the orthonormal base $(\hat{e}_R, \hat{e}_z, \hat{e}_\varphi)$ by the relation $(\mathbf{e}^R, \mathbf{e}^z, \mathbf{e}^\varphi) = (\nabla R, \nabla z, \nabla \varphi) = (\hat{e}_R, \hat{e}_z, \hat{e}_\varphi / R)$. Each point of the grid is given by its coordinates (R, z, φ) and for each point, the magnetic

field is given as:

$$\mathbf{B} = B^R \hat{e}_R + B^z \hat{e}_z + B^\varphi \hat{e}_\varphi$$

One considers the curvilinear coordinates (ψ, θ, φ). One assumes that the iso-ψ surfaces are orthogonal to the magetic field, hence $B \cdot \nabla\psi = 0$. One has

$$\begin{aligned} \mathbf{B} &= B^\psi \mathbf{e}_\psi + B^\theta \mathbf{e}_\theta + B^\varphi \mathbf{e}_\varphi \\ &= B_\psi \nabla\psi + B_\theta \nabla\theta + B_\varphi \nabla\varphi \end{aligned}$$

Since $\mathbf{B} \cdot \nabla\psi = 0$, one has $B^\psi = 0$.

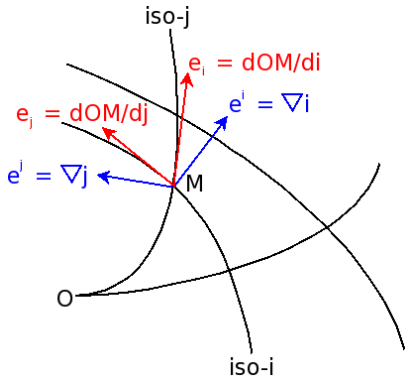

Figure C.1: Definition of covariant and contravariant vectors

C.3 Gradient

The gradient is defined as follow,

$$\nabla X = \left(\frac{\partial X}{\partial u^i} \right) \mathbf{e}^i$$

where one has denoted $u^1 = \psi$, $u^2 = \theta$ and $u^3 = \varphi$. One projects the gradient operator along the magnetic field and uses the following definition of parallel and perpendicular components:

$$\forall \mathbf{A}, \quad \mathbf{A} = \mathbf{A}_\perp + \mathbf{b} A_\parallel$$

with $\mathbf{b}^2 = 1$ and $\mathbf{b} \cdot \mathbf{A}_\perp = 0$. Thus, $A_\parallel = \mathbf{b} \cdot A$. Applying to ∇, one has

$$\nabla X = \nabla_\perp X + \mathbf{b} \nabla_\parallel X$$

with

$$\begin{aligned}\nabla_{\parallel} X &= \mathbf{b}\cdot\nabla X \\ &= \frac{1}{B}B^i(\nabla X)_i \\ &= \frac{1}{B}B^i\frac{\partial X}{\partial u^i} \\ &= \frac{1}{B}\mathbf{B}\cdot\nabla u^i\frac{\partial X}{\partial u^i}\end{aligned}$$

Since we assume φ-axisymmetry, one has $\partial_\varphi = 0$. Also as mentionned above, $\mathbf{B}\cdot\nabla\psi = 0$. The only remaining terms in parallel gradient expression is thus,

$$\nabla_{\parallel} X = \frac{\mathbf{B}\cdot\nabla\theta}{B}\frac{\partial X}{\partial\theta}$$

One can express the above expression using projection of magnetic field along the cylindrical base using the chain rule

$$\begin{aligned}\nabla\theta &= \frac{\partial\theta}{\partial R}\nabla R + \frac{\partial\theta}{\partial z}\nabla z \\ &= \frac{\partial\theta}{\partial R}\hat{e}_R + \frac{\partial\theta}{\partial z}\hat{e}_z\end{aligned}$$

Hence the expression

$$\nabla_{\parallel} X = \frac{1}{B}\left(\frac{\partial\theta}{\partial R}B_R + \frac{\partial\theta}{\partial z}B_z\right)\frac{\partial X}{\partial\theta}$$

C.4 Divergence

C.4.1 Divergence of a magnetic field aligned vector

First, let us separate the perpendicular and parallel terms using

$$\begin{aligned}\nabla\cdot\mathbf{A} &= \nabla\cdot(\mathbf{A}_\perp + \frac{\mathbf{B}}{B}A_{\parallel}) \\ &= \nabla\cdot\mathbf{A}_\perp + \frac{A_{\parallel}}{B}\nabla\cdot\mathbf{B} + \mathbf{B}\cdot\nabla\left(\frac{A_{\parallel}}{B}\right) \\ \nabla\cdot\mathbf{A} &= \nabla\cdot\mathbf{A}_\perp + B\nabla_{\parallel}\left(\frac{A_{\parallel}}{B}\right)\end{aligned}$$

Hence one has:

$$\nabla\cdot(A_{\parallel}\mathbf{b}) = B\nabla_{\parallel}\left(\frac{A_{\parallel}}{B}\right)$$

C.4.2 Perpendicular terms

In Soledge2D equations, $\mathbf{A}_\perp$ is usually a diffusive perpendicular flux that can be expressed as

$$\mathbf{A}_\perp = -D\nabla_\perp X = -D(\nabla X - \mathbf{b}\nabla_\parallel X)$$

One need to express $\nabla \cdot \mathbf{A}_\perp = -\nabla \cdot (D(\nabla X - \mathbf{b}\nabla_\parallel X))$. Let us work on the divergence operator. One need to recall how to express covariant base as a function of contravariant base:

$$\mathbf{e}_i = \frac{\mathbf{e}^j \times \mathbf{e}^k}{\mathbf{e}^i \cdot (\mathbf{e}^j \times \mathbf{e}^k)} = \frac{\nabla u^j \times \nabla u^i}{\mathcal{J}}$$

where

$$\mathcal{J} = \mathbf{e}^i \cdot (\mathbf{e}^j \times \mathbf{e}^k) = [\mathbf{e}_i \cdot (\mathbf{e}_j \times \mathbf{e}_k)]^{-1} = J^{-1}$$

Hence,

$$\frac{\mathbf{e}_i}{J} = \nabla u^j \times \nabla u^k = \nabla \times (u^j \nabla u^k)$$

One writes divergence of $\mathbf{A}$ as

$$\begin{aligned}
\nabla \cdot \mathbf{A} &= \nabla \cdot (A^i \mathbf{e}_i) \\
&= \nabla \cdot \left(J A^i \frac{\mathbf{e}_i}{J} \right) \\
&= J A^i \nabla (\nabla \times (u^j \nabla u^k)) + \frac{\mathbf{e}_i}{J} \cdot \nabla (J A^i) \\
\nabla \cdot \mathbf{A} &= J^{-1} \mathbf{e}_i \cdot \nabla (J A^i)
\end{aligned}$$

Since $\nabla = \mathbf{e}^i \partial_{u^i}$, one has

$$\nabla \cdot \mathbf{A} = \frac{1}{J} \frac{\partial J A^i}{\partial u^i}$$

If $\mathbf{A} = -D\nabla_\perp X$, one has to express $(\nabla_\perp X)^i$. One knows that $(\nabla X)_i = \partial_{u^i} X$. Thus,

$$\begin{aligned}
\nabla_\perp X &= \nabla X - \mathbf{b}\nabla_\parallel X \\
&= \frac{\partial X}{\partial u^i} \mathbf{e}^i - b^i \mathbf{e}_i \nabla_\parallel X
\end{aligned}$$

so

$$\begin{aligned}
(\nabla_\perp X)^i &= \mathbf{e}^i \cdot \nabla_\perp X \\
&= \left(\frac{\partial X}{\partial u^j} \right) \mathbf{e}^j \cdot \mathbf{e}^i - b^i \nabla_\parallel X
\end{aligned}$$

where

$$\mathbf{e}^j \cdot \mathbf{e}^i = \nabla u^i \cdot \nabla u^j$$

$$b^i = \mathbf{b} \cdot \nabla u^i$$

One can now take the properties of the curvilinear system used here ($\partial_\varphi = 0$ and $b^\psi = 0$). For divergence, one has

$$\nabla \cdot \mathbf{A} = \frac{1}{J}\left(\frac{\partial J A^\theta}{\partial \theta} + \frac{\partial J A^\psi}{\partial \psi}\right)$$

And for perpendicular gradient,

$$\left\{\begin{array}{rcl} (\nabla_\perp X)^\theta & = & \frac{\partial X}{\partial \theta}\nabla\theta^2 + \frac{\partial X}{\partial \psi}\nabla\theta\cdot\nabla\psi - \frac{\mathbf{B}\cdot\nabla\theta}{B}\nabla_\parallel X \\ (\nabla_\perp X)^\psi & = & \frac{\partial X}{\partial \psi}\nabla\psi^2 + \frac{\partial X}{\partial \theta}\nabla\theta\cdot\nabla\psi \end{array}\right.$$

where one expresses

$$\left\{\begin{array}{rcl} \nabla\theta^2 & = & \left(\frac{\partial\theta}{\partial R}\right)^2 + \left(\frac{\partial\theta}{\partial z}\right)^2 \\ \nabla\psi^2 & = & \left(\frac{\partial\psi}{\partial R}\right)^2 + \left(\frac{\partial\psi}{\partial z}\right)^2 \\ \nabla\theta\cdot\nabla\psi & = & \frac{\partial\theta}{\partial R}\frac{\partial\psi}{\partial R} + \frac{\partial\theta}{\partial z}\frac{\partial\psi}{\partial z} \end{array}\right.$$

and

$$\frac{1}{J} = \nabla\psi\cdot\nabla\theta\times\nabla\varphi = \left|\begin{array}{ccc} \partial_R\psi & \partial_R\theta & 0 \\ \partial_z\psi & \partial_z\theta & 0 \\ 0 & 0 & 1/R \end{array}\right| = \frac{1}{R}\left(\frac{\partial\psi}{\partial R}\frac{\partial\theta}{\partial z} - \frac{\partial\psi}{\partial z}\frac{\partial\theta}{\partial R}\right)$$

$$\frac{1}{J} = \nabla\psi\cdot\nabla\theta\times\nabla\varphi = \frac{1}{R}\left(\frac{\partial\psi}{\partial R}\frac{\partial\theta}{\partial z} - \frac{\partial\psi}{\partial z}\frac{\partial\theta}{\partial R}\right)$$

One can reformulate perpendicular gradient expressions considering the fact that ones want a projection in the magnetic flux surface (along $\mathbf{e}_\theta$) and a projection perpendicular to the magnetic flux surface (along $\nabla\psi = \mathbf{e}^\psi$). One has

$$\nabla_\perp X = (\nabla_\perp X)^\theta \mathbf{e}_\theta + (\nabla_\perp X)^\psi \mathbf{e}_\psi$$

with

$$\begin{array}{rcl} \mathbf{e}_\psi & = & a\mathbf{e}^\psi + b\mathbf{e}_\theta \\ \mathbf{e}_\psi\cdot\mathbf{e}^\psi & = & 1 = a\mathbf{e}^\psi\cdot\mathbf{e}^\psi \quad \Rightarrow \quad a = \dfrac{1}{\nabla\psi^2} \\ \mathbf{e}_\psi\cdot\mathbf{e}^\theta & = & 0 = a\mathbf{e}^\psi\cdot\mathbf{e}^\theta + b \quad \Rightarrow \quad b = -\dfrac{\nabla\psi\cdot\nabla\theta}{\nabla\psi^2} \end{array}$$

hence

$$\nabla_\perp X = \left((\nabla_\perp X)^\theta - (\nabla_\perp X)^\psi \frac{\mathbf{e}^\psi\cdot\mathbf{e}^\theta}{\mathbf{e}^\psi\cdot\mathbf{e}^\psi}\right)\mathbf{e}_\theta + \frac{(\nabla_\perp X)^\psi}{\mathbf{e}^\psi\cdot\mathbf{e}^\psi}\mathbf{e}^\psi$$

For diffusive tranport, one defines the diffusivity within the surface (D_θ) and perpendicular to the surface (D^ψ) such as the turbulent flux Φ is given by

$$\Phi = -D_\theta\left((\nabla_\perp X)^\theta - (\nabla_\perp X)^\psi \frac{\mathbf{e}^\psi\cdot\mathbf{e}^\theta}{\mathbf{e}^\psi\cdot\mathbf{e}^\psi}\right)\mathbf{e}_\theta - D^\psi\frac{(\nabla_\perp X)^\psi}{\mathbf{e}^\psi\cdot\mathbf{e}^\psi}\mathbf{e}^\psi$$

One computes its coordinates in the covariant base

$$\begin{aligned}(\Phi)^\theta &= \Phi\cdot\mathbf{e}^\theta = -D_\theta(\nabla_\perp X)^\theta - (D^\psi - D_\theta)(\nabla_\perp X)^\psi \frac{\mathbf{e}^\psi\cdot\mathbf{e}^\theta}{\mathbf{e}^\psi\cdot\mathbf{e}^\psi}\\ &= -D^\psi(\nabla\theta\cdot\nabla\psi)\partial_\psi X - \left(D_\theta(\nabla\theta^2 - \mathcal{G}^2) + (D^\psi - D_\theta)\frac{(\nabla\theta\cdot\nabla\psi)^2}{\nabla\psi^2}\right)\partial_\theta X\\ (\Phi)^\psi &= \Phi\cdot\mathbf{e}^\psi = -D^\psi(\nabla_\perp X)^\psi\\ &= -D^\psi\left(\nabla\psi^2\partial_\psi X + (\nabla\theta\cdot\nabla\psi)\partial_\theta X\right)\end{aligned}$$

with

$$\mathcal{G} = \frac{\mathbf{B}\cdot\nabla\theta}{B} = \left(B_R\frac{\partial\theta}{\partial R} + B_z\frac{\partial\theta}{\partial z}\right)$$

C.4.3 General expression for magnetic fields aligned terms

For magnetic field, one has $\nabla\cdot\mathbf{B} = 0$. However, it can be useful not to make this assumption and to consider $\mathbf{B}$ as a field without specific properties. Hence, the divergence of a vector aligned on $\mathbf{B}$ becomes:

$$\begin{aligned}\nabla\cdot\left(A_\parallel\mathbf{B}\right) &= B\nabla_\parallel\left(\frac{A_\parallel}{B}\right) + \frac{A_\parallel}{B}\nabla\cdot\mathbf{B}\\ &= B\nabla_\parallel\left(\frac{A_\parallel}{B}\right) + \frac{A_\parallel}{B}\frac{1}{J}\frac{\partial JB^i}{\partial u^i}\\ \nabla\cdot\left(A_\parallel\mathbf{B}\right) &= B\nabla_\parallel\left(\frac{A_\parallel}{B}\right) + \frac{A_\parallel}{B}\frac{1}{J}\frac{\partial J\mathbf{B}\cdot\nabla\theta}{\partial\theta}\end{aligned}$$

C.5 Continuity equation

C.5.1 Using the metric

Let us rewrite continuity equation taking the metric coefficients into account.

$$\frac{\partial n}{\partial t} + \nabla\cdot\Gamma = 0 \tag{C.5}$$

That gives, according to the above expressions

$$\frac{\partial n}{\partial t} + B\nabla_\parallel\left(\frac{\Gamma_\parallel}{B}\right) + \nabla\cdot\Gamma_\perp = 0$$

$$\frac{\partial n}{\partial t} + B\nabla_\parallel\left(\frac{\Gamma_\parallel}{B}\right) + \frac{1}{J}\left(\frac{\partial J\Gamma_\perp^\theta}{\partial\theta} + \frac{\partial J\Gamma_\perp^\psi}{\partial\psi}\right) = 0$$

$$\frac{\partial n}{\partial t} + B\mathcal{G}\frac{\partial}{\partial\theta}\left(\frac{\Gamma_\parallel}{B}\right) + \frac{1}{J}\left(\frac{\partial J\Gamma_\perp^\theta}{\partial\theta} + \frac{\partial J\Gamma_\perp^\psi}{\partial\psi}\right) = 0$$

with

$$\begin{aligned}\Gamma_\perp^\theta &= -D^\psi g^{\theta\psi}\partial_\psi n - \left(D_\theta(h^\theta - \mathcal{G}^2) + (D^\psi - D_\theta)\frac{g^{\theta\psi 2}}{h^\psi}\right)\partial_\theta n \\ \Gamma_\perp^\psi &= -D^\psi\left(h^\psi\partial_\psi n + g^{\theta\psi}\partial_\theta n\right)\end{aligned}$$

C.5.2 Non-Dimensionalized equation

One rewrite the equation with non-dimensionalized variables $n^\star = n/n_0$, $\Gamma^\star = \Gamma_\parallel/(n_0 c_0)$, $\theta^\star = \theta/2\pi$, $\psi^\star = (\psi - \psi_{min})/\Delta\psi_0$, $\mathcal{G}^\star = \mathcal{G}R_0$, $\nabla\theta^\star = \frac{a\nabla\theta}{2\pi}$ and $\nabla\psi^\star = \frac{a\nabla\psi}{\Delta\psi_0}$

$$\frac{n_0}{\tau_0}\frac{\partial n^\star}{\partial t^\star} + B\mathcal{G}^\star\frac{n_0 c_0}{2\pi R_0}\frac{\partial}{\partial\theta^\star}\left(\frac{\Gamma^\star}{B}\right) + \frac{1}{J}\left(\frac{\partial J\Gamma_\perp^\theta/2\pi}{\partial\theta^\star} + \frac{\partial J\Gamma_\perp^\psi/\Delta\psi_0}{\partial\psi^\star}\right) = 0$$

One defines $\tau_0 = 2\pi R_0/c_0$ hence,

$$\frac{\partial n^\star}{\partial t^\star} + B\mathcal{G}^\star\frac{\partial}{\partial\theta^\star}\left(\frac{\Gamma^\star}{B}\right) + \frac{2\pi R_0}{n_0 c_0}\frac{1}{J}\left(\frac{\partial J\Gamma_\perp^\theta/2\pi}{\partial\theta^\star} + \frac{\partial J\Gamma_\perp^\psi/\Delta\psi_0}{\partial\psi^\star}\right) = 0$$

where

$$\begin{aligned}\frac{2\pi R_0}{n_0 c_0}\frac{\Gamma_\perp^\theta}{2\pi} &= \frac{2\pi R_0}{n_0 c_0 2\pi}\left\{-D^\psi\frac{2\pi\Delta\psi_0}{a^2}g^{\theta\psi^\star}\frac{n_0}{\Delta\psi_0}\partial_{\psi^\star}n^\star\right. \\ &\quad \left. - \left(D_\theta\left(\frac{2\pi}{a}\right)^2(h^{\theta^\star} - \left(\frac{a}{2\pi R_0}\right)^2\mathcal{G}^{\star 2}) + (D^\psi - D_\theta)\left(\frac{2\pi}{a}\right)^2\frac{(g^{\theta\psi^\star})^2}{h^{\psi^\star}}\right)\frac{n_0}{2\pi}\partial_{\theta^\star}n^\star\right\} \\ &= -\frac{2\pi R_0}{a}\frac{D^\psi}{c_0 a}g^{\theta\psi^\star}\partial_{\psi^\star}n^\star \\ &\quad - \left(\frac{2\pi R_0}{a}\frac{D_\theta}{c_0 a}(h^{\theta^\star} - \left(\frac{a}{2\pi R_0}\right)^2\mathcal{G}^{\star 2}) + \frac{2\pi R_0}{a}\left(\frac{D^\psi}{c_0 a} - \frac{D_\theta}{c_0 a}\right)\frac{(g^{\theta\psi^\star})^2}{h^{\psi^\star}}\right)\partial_{\theta^\star}n^\star\end{aligned}$$

$$\boxed{\Gamma_\perp^{\theta\,\star} = -\frac{\mathrm{A}}{\mathrm{Pe}^\psi}g^{\theta\psi^\star}\partial_{\psi^\star}n^\star - \left(\frac{\mathrm{A}}{\mathrm{Pe}_\theta}(h^{\theta^\star} - \frac{1}{\mathrm{A}^2}\mathcal{G}^{\star 2}) + \left(\frac{\mathrm{A}}{\mathrm{Pe}^\psi} - \frac{\mathrm{A}}{\mathrm{Pe}_\theta}\right)\frac{(g^{\theta\psi^\star})^2}{h^{\psi^\star}}\right)\partial_{\theta^\star}n^\star}$$

and

$$\frac{2\pi R_0}{n_0 c_0}\frac{\Gamma_\perp^\psi}{\Delta\psi_0} = \frac{2\pi R_0}{n_0 c_0\Delta\psi_0}\left\{-D^\psi\left(\left(\frac{\Delta\psi_0}{a}\right)^2 h^{\psi^\star}\frac{n_0}{\Delta\psi_0}\partial_{\psi^\star}n^\star + \frac{2\pi\Delta\psi_0}{a^2}g^{\theta\psi^\star}\frac{n_0}{2\pi}\partial_{\theta^\star}n^\star\right)\right\}$$

$$\boxed{\Gamma_\perp^{\psi\star} = -\frac{\mathrm{A}}{\mathrm{Pe}^\psi}\left(h^{\psi^\star}\partial_{\psi^\star}n^\star + g^{\theta\psi^\star}\partial_{\theta^\star}n^\star\right)}$$

with

$$\mathrm{A} = \frac{2\pi R_0}{a} \quad , \quad \mathrm{Pe}^\psi = \frac{ac_0}{D^\psi} \quad , \quad \mathrm{Pe}_\theta = \frac{ac_0}{D_\theta} \tag{C.6}$$

and continuity equation becomes

$$\boxed{\frac{\partial n^\star}{\partial t^\star} + B\mathcal{G}^\star \frac{\partial}{\partial \theta^\star}\left(\frac{\Gamma^\star}{B}\right) + \frac{1}{J}\left(\frac{\partial J\Gamma_\perp^{\theta\,\star}}{\partial \theta^\star} + \frac{\partial J\Gamma_\perp^{\psi\,\star}}{\partial \psi^\star}\right) = 0} \tag{C.7}$$

C.6 Momentum equation

C.6.1 Using the metric

Momentum equation is the following

$$m_i \frac{\partial \Gamma_\parallel}{\partial t} + m_i \mathbf{b}\cdot\nabla\cdot\left(\frac{\Gamma_\parallel^2}{n}\mathbf{b}\otimes\mathbf{b}\right) + \nabla_\parallel p = S_\perp \tag{C.8}$$

One needs to evaluate the quantity $\mathbf{b}\cdot\nabla\cdot(X\mathbf{b}\otimes\mathbf{b})$. One has:

$$\begin{aligned}\mathbf{b}\cdot\nabla\cdot(X\mathbf{b}\otimes\mathbf{b}) &= \mathbf{b}\cdot\left[X\mathbf{b}\cdot(\nabla\otimes\mathbf{b}) + (\nabla\cdot(X\mathbf{b}))\,\mathbf{b}\right]\\ &= \nabla\cdot(X\mathbf{b}) + X\mathbf{b}\cdot(\nabla\otimes\mathbf{b})\cdot\mathbf{b}\end{aligned}$$

Then using the gradient definition

$$\nabla\otimes\mathbf{A} = \mathbf{A}_{,i}\otimes\mathbf{e^i} \qquad \text{with} \qquad \mathbf{A}_{,i} = \frac{\partial\mathbf{A}}{\partial u^i} = \frac{\partial A_j}{\partial u^i}\mathbf{e^j} + A_j\frac{\partial \mathbf{e^j}}{\partial u^i}$$

Using $b^\psi = 0$ and $\partial_\phi = 0$, the expression $\mathbf{b}\cdot(\nabla\otimes\mathbf{b})\cdot\mathbf{b}$ can be reduced to

$$\begin{aligned}\mathbf{b}\cdot(\nabla\otimes\mathbf{b})\cdot\mathbf{b} &= b^k\mathbf{e_k}\cdot\left(\frac{\partial b_j}{\partial u^i}\mathbf{e^i}\otimes\mathbf{e^j}\right)\cdot b^l\mathbf{e_l} + b^k\mathbf{e_k}\cdot\left(b_j\frac{\partial\mathbf{e^j}}{\partial u^i}\otimes\mathbf{e^i}\right)\cdot b^l\mathbf{e_l}\\ &= b^ib^j\frac{\partial b_j}{\partial u^i} + b^kb^ib_j\mathbf{e_k}\cdot\frac{\partial\mathbf{e^j}}{\partial u^i}\\ &= \frac{\partial b^i}{\partial u^i} - b_j\frac{\partial b^ib^j}{\partial u^i} + b_j\frac{\partial b^ib^j}{\partial u^i} - b_j\mathbf{e^j}\cdot\frac{\partial b^kb^i\mathbf{e_k}}{\partial u^i}\\ &= \frac{\partial b^i}{\partial u^i} - \frac{\partial b^i}{\partial u^i} + b^ib_j\mathbf{e^j}\cdot\frac{\partial b^k\mathbf{e_k}}{\partial u^i}\\ &= b^i\mathbf{b}\cdot\frac{\partial\mathbf{b}}{\partial u^i}\\ \mathbf{b}\cdot(\nabla\otimes\mathbf{b})\cdot\mathbf{b} &= 0\end{aligned}$$

Back to momentum equation, one has

$$m_i\frac{\partial\Gamma_\parallel}{\partial t} + m_iB\nabla_\parallel\left(\frac{1}{B}\frac{\Gamma_\parallel^2}{n}\right) + \nabla_\parallel p + \nabla\cdot\phi_\perp = 0$$

$$m_i\frac{\partial\Gamma_\parallel}{\partial t} + m_iB\nabla_\parallel\left(\frac{1}{B}\frac{\Gamma_\parallel^2}{n}\right) + \nabla_\parallel\left(n(T_e+T_i)\right) + \frac{1}{J}\left(\frac{\partial J\phi_\perp^\theta}{\partial\theta} + \frac{\partial J\phi_\perp^\psi}{\partial\psi}\right) = 0$$

$$m_i\frac{\partial\Gamma_\parallel}{\partial t}+\left(B_R\frac{\partial\theta}{\partial R}+B_z\frac{\partial\theta}{\partial z}\right)\left\{m_i\frac{\partial}{\partial\theta}\left(\frac{1}{B}\frac{\Gamma_\parallel^2}{n}\right)+\frac{1}{B}\frac{\partial}{\partial\theta}\left(n(T_e+T_i)\right)\right\}+\frac{1}{J}\left(\frac{\partial J\phi_\perp^\theta}{\partial\theta}+\frac{\partial J\phi_\perp^\psi}{\partial\psi}\right)=0$$

with

$$\begin{aligned}\phi_\perp^\theta/m_i &= -\nu^\psi g^{\theta\psi}\partial_\psi\Gamma_\parallel-\left(\nu_\theta(h^\theta-\mathcal{G}^2)+(\nu^\psi-\nu_\theta)\frac{(g^{\theta\psi})^2}{h^\psi}\right)\partial_\theta\Gamma_\parallel\\ \phi_\perp^\psi/m_i &= -\nu^\psi\left(h^\psi\partial_\psi\Gamma_\parallel+g^{\theta\psi}\partial_\theta\Gamma_\parallel\right)\end{aligned}$$

C.6.2 Non-Dimensionalized equation

One rewrite the equation with non-dimensionalized variables $n^\star=n/n_0$, $\Gamma^\star=\Gamma_\parallel/(n_0c_0)$, $\theta^\star=\theta/2\pi$, $\psi^\star=(\psi-\psi_{min})/\Delta\psi_0$, $\mathcal{G}^\star=\mathcal{G}R_0$, $\nabla\theta^\star=\frac{a\nabla\theta}{2\pi}$, $\nabla\psi^\star=\frac{a\nabla\psi}{\Delta\psi_0}$

$$\frac{m_in_0c_0}{\tau_0}\frac{\partial\Gamma^\star}{\partial t^\star}+B\mathcal{G}^\star\frac{m_in_0c_0^2}{2\pi R_0}\left\{\frac{\partial}{\partial\theta^\star}\left(\frac{1}{B}\frac{\Gamma^{\star2}}{n^\star}\right)+\frac{1}{B}\frac{\partial}{\partial\theta^\star}\left(n^\star({T_e}^\star+{T_i}^\star)\right)\right\}+\frac{1}{J}\left(\frac{\partial J\phi_\perp^\theta/2\pi}{\partial\theta^\star}+\frac{\partial J\phi_\perp^\psi/\Delta\psi_0}{\partial\psi^\star}\right)=0$$

with $c_0=\sqrt{k_BT_0/m_i}$,

$$\frac{\partial\Gamma^\star}{\partial t^\star}+B\mathcal{G}^\star\left\{\frac{\partial}{\partial\theta^\star}\left(\frac{1}{B}\frac{\Gamma^{\star2}}{n^\star}\right)+\frac{1}{B}\frac{\partial}{\partial\theta^\star}\left(n^\star({T_e}^\star+{T_i}^\star)\right)\right\}+\frac{2\pi R_0}{m_in_0c_0^2}\frac{1}{J}\left(\frac{\partial J\phi_\perp^\theta/2\pi}{\partial\theta^\star}+\frac{\partial J\phi_\perp^\psi/\Delta\psi_0}{\partial\psi^\star}\right)=0$$

where

$$\begin{aligned}\frac{2\pi R_0}{m_in_0c_0^2}\frac{\phi_\perp^\theta}{2\pi} &= \frac{2\pi R_0}{n_0c_0^2 2\pi}\left\{-\nu^\psi\frac{2\pi\Delta\psi_0}{a^2}g^{\theta\psi\star}\frac{n_0c_0}{\Delta\psi_0}\partial_{\psi^\star}\Gamma^\star\right.\\ &\quad\left.-\left(\nu_\theta\left(\frac{2\pi}{a}\right)^2(h^{\theta\star}-\left(\frac{a}{2\pi R_0}\right)^2\mathcal{G}^{\star2})+(\nu^\psi-\nu_\theta)\left(\frac{2\pi}{a}\right)^2\frac{(g^{\theta\psi\star})^2}{h^{\psi\star}}\right)\frac{n_0c_0}{2\pi}\partial_{\theta^\star}\Gamma^\star\right\}\\ &= -\frac{2\pi R_0}{a}\frac{\nu^\psi}{c_0a}g^{\theta\psi\star}\partial_{\psi^\star}\Gamma^\star\\ &\quad-\left(\frac{2\pi R_0}{a}\frac{\nu_\theta}{c_0a}(h^{\theta\star}-\left(\frac{a}{2\pi R_0}\right)^2\mathcal{G}^{\star2})+\frac{2\pi R_0}{a}\left(\frac{\nu^\psi}{c_0a}-\frac{\nu_\theta}{c_0a}\right)\frac{(g^{\theta\psi\star})^2}{h^{\psi\star}}\right)\partial_{\theta^\star}\Gamma^\star\end{aligned}$$

$$\boxed{\phi_\perp^{\theta\,\star}=-\frac{\mathrm{A}}{\mathrm{Re}^\psi}g^{\theta\psi\star}\partial_{\psi^\star}\Gamma^\star-\left(\frac{\mathrm{A}}{\mathrm{Re}_\theta}(h^{\theta\star}-\frac{1}{\mathrm{A}^2}\mathcal{G}^{\star2})+\left(\frac{\mathrm{A}}{\mathrm{Re}^\psi}-\frac{\mathrm{A}}{\mathrm{Re}_\theta}\right)\frac{(g^{\theta\psi\star})^2}{h^{\psi\star}}\right)\partial_{\theta^\star}\Gamma^\star}$$

and

$$\frac{2\pi R_0}{n_0c_0}\frac{\phi_\perp^\psi}{\Delta\psi_0}=\frac{2\pi R_0}{n_0c_0\Delta\psi_0}\left\{-\nu^\psi\left(\left(\frac{\Delta\psi_0}{a}\right)^2h^{\psi\star}\frac{n_0c_0}{\Delta\psi_0}\partial_{\psi^\star}\Gamma^\star+\frac{2\pi\Delta\psi_0}{a^2}g^{\theta\psi\star}\frac{n_0c_0}{2\pi}\partial_{\theta^\star}\Gamma^\star\right)\right\}$$

$$\boxed{\phi_\perp^{\psi\star}=-\frac{\mathrm{A}}{\mathrm{Re}^\psi}\left(h^{\psi\star}\partial_{\psi^\star}\Gamma^\star+g^{\theta\psi\star}\partial_{\theta^\star}\Gamma^\star\right)}$$

with

$$\mathrm{Re}^\psi=\frac{ac_0}{\nu^\psi}\quad,\qquad\mathrm{Re}_\theta=\frac{ac_0}{\nu_\theta}\tag{C.9}$$

and momentum equation becomes

$$\boxed{\frac{\partial \Gamma^\star}{\partial t^\star} + B\mathcal{G}^\star \frac{\partial}{\partial \theta^\star}\left(\frac{1}{B}\frac{\Gamma^{\star 2}}{n^\star}\right) + \mathcal{G}^\star \frac{\partial}{\partial \theta^\star}\left(n^\star(T_e^\star + T_i^\star)\right) + \frac{1}{J}\left(\frac{\partial J\phi_\perp^{\theta\,\star}}{\partial \theta^\star} + \frac{\partial J\phi_\perp^{\psi\,\star}}{\partial \psi^\star}\right) = 0} \tag{C.10}$$

C.7 Temperature equation

C.7.1 Using the metric

Temperature equation is the following

$$\frac{3}{2}k_B\frac{\partial nT}{\partial t} + \nabla\cdot(\frac{3}{2}k_BT\mathbf{\Gamma}) + k_BnT\nabla\cdot\left(\frac{\mathbf{\Gamma}}{n}\right) = -\nabla\cdot\mathbf{q} + Q_c \tag{C.11}$$

That gives, according to the above expressions

$$\frac{3}{2}k_B\frac{\partial nT}{\partial t} + B\nabla_\parallel\left(\frac{1}{B}\frac{3}{2}k_BT\Gamma_\parallel\right) + \nabla\cdot\phi^{\text{conv}}{}_\perp + \nabla\cdot\Phi_\perp^{\text{chaleur-turb}} + nk_BTB\nabla_\parallel\left(\frac{\Gamma_\parallel}{Bn}\right) = -B\nabla_\parallel\left(\frac{q_\parallel}{B}\right) + Q_c$$

$$\frac{3}{2}k_B\frac{\partial nT}{\partial t} + B\nabla_\parallel\left(\frac{3}{2B}k_BT\Gamma_\parallel\right) + k_BnTB\nabla_\parallel\left(\frac{\Gamma_\parallel}{Bn}\right) + \frac{1}{J}\left(\frac{\partial J\phi_\perp^\theta}{\partial\theta} + \frac{\partial J\phi_\perp^\psi}{\partial\psi}\right)$$
$$\cdots + \frac{1}{J}\left(\frac{\partial J\Phi_\perp^\theta}{\partial\theta} + \frac{\partial J\Phi_\perp^\psi}{\partial\psi}\right) = B\nabla_\parallel\left(\frac{\kappa_0T^{5/2}\nabla_\parallel T}{B}\right) + Q_c$$

$$\frac{3}{2}k_B\frac{\partial nT}{\partial t} + B\mathcal{G}\left\{\frac{3}{2}k_B\frac{\partial}{\partial\theta}\left(\frac{\Gamma_\parallel T}{B}\right) + k_BnT\frac{\partial}{\partial\theta}\left(\frac{\Gamma_\parallel}{Bn}\right)\right\} + \frac{1}{J}\left(\frac{\partial J\phi_\perp^\theta}{\partial\theta} + \frac{\partial J\phi_\perp^\psi}{\partial\psi}\right)$$
$$\cdots + \frac{1}{J}\left(\frac{\partial J\Phi_\perp^\theta}{\partial\theta} + \frac{\partial J\Phi_\perp^\psi}{\partial\psi}\right) = B\mathcal{G}\frac{\partial}{\partial\theta}\left(\frac{\kappa_0T^{5/2}}{B}\mathcal{G}\frac{\partial T}{\partial\theta}\right) + Q_c$$

with

$$\begin{aligned}
\phi_\perp^\theta &= -\frac{3}{2}k_BT\left\{D^\psi g^{\theta\psi}\partial_\psi n + \left(D_\theta(h^\theta - \mathcal{G}^2) + (D^\psi - D_\theta)\frac{(g^{\theta\psi})^2}{h^\psi}\right)\partial_\theta n\right\} \\
&= \frac{3}{2}k_BT\Gamma_\perp^\theta \\
\phi_\perp^\psi &= -\frac{3}{2}k_BT\left\{D^\psi\left(h^\psi\partial_\psi n + g^{\theta\psi}\partial_\theta n\right)\right\} \\
&= \frac{3}{2}k_BT\Gamma_\perp^\psi
\end{aligned}$$

and

$$\begin{aligned}\Phi_\perp^\theta &= -\frac{3}{2}k_B n\left\{\chi^\psi g^{\theta\psi}\partial_\psi T + \left(\chi_\theta(h^\theta - \mathcal{G}^2) + (\chi^\psi - \chi_\theta)\frac{(g^{\theta\psi})^2}{h^\psi}\right)\partial_\theta T\right\}\\ \Phi_\perp^\psi &= -\frac{3}{2}k_B n\left\{\chi^\psi\left(h^\psi\partial_\psi T + g^{\theta\psi}\partial_\theta T\right)\right\}\end{aligned}$$

C.7.2 Non-Dimensionalized equation

One rewrite the equation with non-dimensionalized variables $n^\star = n/n_0$, $\Gamma^\star = \Gamma_\parallel/(n_0 c_0)$, $\theta^\star = \theta/2\pi$, $\psi^\star = (\psi - \psi_{min})/\Delta\psi_0$, $\mathcal{G}^\star = \mathcal{G}R_0$, $\nabla\theta^\star = \frac{a\nabla\theta}{2\pi}$ and $\nabla\psi^\star = \frac{a\nabla\psi}{\Delta\psi_0}$

$$\begin{aligned}&\frac{k_B n_0 T_0}{\tau_0}\frac{3}{2}\frac{\partial n^\star T^\star}{\partial t^\star} + B\mathcal{G}^\star\frac{k_B n_0 c_0 T_0}{2\pi R_0}\left\{\frac{3}{2}\frac{\partial}{\partial\theta^\star}\left(\frac{\Gamma^\star T^\star}{B}\right) + n^\star T^\star\frac{\partial}{\partial\theta^\star}\left(\frac{\Gamma^\star}{Bn^\star}\right)\right\}\\ &\qquad\cdots + \frac{1}{J}\left(\frac{\partial J\phi_\perp^\theta/2\pi}{\partial\theta^\star} + \frac{\partial J\phi_\perp^\psi/\Delta\psi_0}{\partial\psi^\star}\right) + \frac{1}{J}\left(\frac{\partial J\Phi_\perp^\theta/2\pi}{\partial\theta^\star} + \frac{\partial J\Phi_\perp^\psi/\Delta\psi_0}{\partial\psi^\star}\right) =\\ &\qquad B\mathcal{G}^\star\frac{T_0}{(2\pi R_0)^2}\frac{\partial}{\partial\theta^\star}\left(\kappa_0 T_0^{5/2}\frac{T^{\star 5/2}}{B}\mathcal{G}^\star\frac{\partial T^\star}{\partial\theta^\star}\right) + Q_c\end{aligned}$$

$$\begin{aligned}&\frac{3}{2}\frac{\partial n^\star T^\star}{\partial t^\star} + B\mathcal{G}^\star\left\{\frac{3}{2}\frac{\partial}{\partial\theta^\star}\left(\frac{\Gamma^\star T^\star}{B}\right) + n^\star T^\star\frac{\partial}{\partial\theta^\star}\left(\frac{\Gamma^\star}{Bn^\star}\right)\right\}\\ &\qquad\cdots + \frac{3}{2}\frac{1}{J}\left(\frac{\partial JT^\star\Gamma_\perp^{\theta\,\star}}{\partial\theta^\star} + \frac{\partial JT^\star\Gamma_\perp^{\psi\,\star}}{\partial\psi^\star}\right) + \frac{2\pi R_0}{k_B n_0 c_0 T_0}\frac{1}{J}\left(\frac{\partial J\Phi_\perp^\theta/2\pi}{\partial\theta^\star} + \frac{\partial J\Phi_\perp^\psi/\Delta\psi_0}{\partial\psi^\star}\right) =\\ &\qquad B\mathcal{G}^\star\frac{\partial}{\partial\theta^\star}\left(\frac{1}{\mathrm{Pe}_\parallel^{\mathrm{T}}}\frac{T^{\star 5/2}}{B}\mathcal{G}^\star\frac{\partial T^\star}{\partial\theta^\star}\right) + Q_c{}^\star\end{aligned}$$

with

$$\mathrm{Pe}_\parallel^{\mathrm{T}} = \frac{k_B n_0 c_0 2\pi R_0}{\kappa_0 T_0^{5/2}}$$

where

$$\begin{aligned}\frac{2\pi R_0}{k_B n_0 c_0 T_0}\frac{\Phi_\perp^\theta}{2\pi} &= \frac{2\pi R_0}{k_B n_0 c_0 T_0 2\pi}\frac{3}{2}k_B n\left\{-\chi^\psi\frac{2\pi\Delta\psi_0}{a^2}g^{\theta\psi\star}\frac{T_0}{\Delta\psi_0}\partial_{\psi^\star}T^\star\right.\\ &\quad\left.-\left(\chi_\theta\left(\frac{2\pi}{a}\right)^2(h^{\theta\star} - \left(\frac{a}{2\pi R_0}\right)^2\mathcal{G}^{\star 2}) + (\chi^\psi - \chi_\theta)\left(\frac{2\pi}{a}\right)^2\frac{g^{\theta\psi\star 2}}{h^{\psi\star}}\right)\frac{T_0}{2\pi}\partial_{\theta^\star}T^\star\right\}\\ &= -\frac{3}{2}n^\star\left\{\frac{2\pi R_0}{a}\frac{\chi^\psi}{c_0 a}g^{\theta\psi\star}\partial_{\psi^\star}T^\star\right.\\ &\quad\left.+\left(\frac{2\pi R_0}{a}\frac{\chi_\theta}{c_0 a}(h^{\theta\star} - \left(\frac{a}{2\pi R_0}\right)^2\mathcal{G}^{\star 2}) + \frac{2\pi R_0}{a}\left(\frac{\chi^\psi}{c_0 a} - \frac{\chi_\theta}{c_0 a}\right)\frac{g^{\theta\psi\star 2}}{h^{\psi\star}}\right)\partial_{\theta^\star}T^\star\right\}\end{aligned}$$

$$\boxed{\Phi_\perp^{\theta\,\star} = -\frac{3}{2}n^\star\left\{\frac{\mathrm{A}}{\mathrm{Re}^\psi\mathrm{Pr}^\psi}g^{\theta\psi\star}\partial_{\psi^\star}T^\star + \left(\frac{\mathrm{A}}{\mathrm{Re}_\theta\mathrm{Pr}_\theta}(h^{\theta\star} - \frac{1}{\mathrm{A}^2}\mathcal{G}^{\star 2}) + \left(\frac{\mathrm{A}}{\mathrm{Re}^\psi\mathrm{Pr}^\psi} - \frac{\mathrm{A}}{\mathrm{Re}_\theta\mathrm{Pr}_\theta}\right)\frac{g^{\theta\psi\star 2}}{h^{\psi\star}}\right)\partial_{\theta^\star}T^\star\right\}}$$

and

$$\frac{2\pi R_0}{k_B n_0 c_0 T_0}\frac{\phi_\perp^\psi}{\Delta\psi_0} = \frac{2\pi R_0}{k_B n_0 c_0 T_0 \Delta\psi_0}\frac{3}{2}k_B n\left\{-\chi^\psi\left(\left(\frac{\Delta\psi_0}{a}\right)^2 h^{\psi\star}\frac{T_0}{\Delta\psi_0}\partial_{\psi^\star}T^\star + \frac{2\pi\Delta\psi_0}{a^2}g^{\theta\psi\star}\frac{T_0}{2\pi}\partial_{\theta^\star}T^\star\right)\right\}$$

$$\boxed{\Phi_\perp^{\psi\star} = -\frac{3}{2}n^\star\frac{\mathrm{A}}{\mathrm{Re}^\psi\mathrm{Pr}^\psi}\left(h^{\psi\star}\partial_{\psi^\star}T^\star + g^{\theta\psi\star}\partial_{\theta^\star}T^\star\right)}$$

with

$$\mathrm{Pr}^\psi = \frac{\chi^\psi}{\nu^\psi} \quad , \quad \mathrm{Pr}_\theta = \frac{\chi_\theta}{\nu_\theta}$$

and Temperature equation becomes

$$\begin{aligned}&\tfrac{3}{2}\tfrac{\partial n^\star T^\star}{\partial t^\star} + B\mathcal{G}^\star\left\{\tfrac{3}{2}\tfrac{\partial}{\partial\theta^\star}\left(\tfrac{\Gamma^\star T^\star}{B}\right) + n^\star T^\star\tfrac{\partial}{\partial\theta^\star}\left(\tfrac{\Gamma^\star}{Bn^\star}\right)\right\} = \\ &\quad -\tfrac{3}{2}\tfrac{1}{J}\left(\tfrac{\partial JT^\star\Gamma_\perp^{\theta\,\star}}{\partial\theta^\star} + \tfrac{\partial JT^\star\Gamma_\perp^{\psi\,\star}}{\partial\psi^\star}\right) - \tfrac{1}{J}\left(\tfrac{\partial J\Phi_\perp^{\theta\,\star}}{\partial\theta^\star} + \tfrac{\partial J\Phi_\perp^{\psi\,\star}}{\partial\psi^\star}\right) + B\mathcal{G}^\star\tfrac{\partial}{\partial\theta^\star}\left(\tfrac{1}{\mathrm{Pe}_\parallel^{\mathrm{T}}}\tfrac{T^{\star 5/2}}{B}\mathcal{G}^\star\tfrac{\partial T^\star}{\partial\theta^\star}\right) + Q_c{}^\star\end{aligned}$$

Perpendicular correction term for ion temperature equation

For ion temperature equation, an extra term is present in the RHS term to ensure total energy conservation. This term is the following:

$$S_{U_i} = m_i\phi_\perp^{\mathbf{\Gamma}}\cdot\nabla_\perp\left(\frac{\Gamma_\parallel}{n}\right) - m_i\frac{\Gamma_\parallel}{n}\mathbf{\Gamma}_\perp\cdot\nabla\left(\frac{\Gamma_\parallel}{n}\right)$$

Since we already know the covariant coordinates for the fluxes ($\phi_\perp^\theta$ and $\phi_\perp^\psi$), the scalar product can be computed for example as

$$\phi_\perp^{\mathbf{\Gamma}}\cdot\nabla_\perp\left(\frac{\Gamma_\parallel}{n}\right) = \phi_\perp^{\Gamma,\theta}\left(\nabla_\perp\frac{\Gamma_\parallel}{n}\right)_\theta + \phi_\perp^{\Gamma,\psi}\left(\nabla_\perp\frac{\Gamma_\parallel}{n}\right)_\psi$$

One need to determine contravariant coordinates for the perpendicular gradient. One has

$$\begin{aligned}(\nabla_\perp X)_i &= \nabla_\perp X\cdot\mathbf{e}_i \\ &= \left(\frac{\partial X}{\partial u^i}\mathbf{e}^i - \mathbf{b}\nabla_\parallel X\right)\cdot\mathbf{e}_i \\ &= \frac{\partial X}{\partial u^i} - \frac{1}{B}\left(B^\theta\mathbf{e}_\theta + B^\varphi\mathbf{e}_\varphi\right)\cdot\mathbf{e}_i\nabla_\parallel X \\ (\nabla_\perp X)_i &= \frac{\partial X}{\partial u^i} - \frac{\mathbf{B}\cdot\nabla\theta}{B}(\mathbf{e}_\theta\cdot\mathbf{e}_i)\nabla_\parallel X\end{aligned}$$

Hence

$$
\begin{aligned}
S_{U_i} &= m_i\left(-\nu^{\psi}g^{\theta\psi}\partial_{\psi}\Gamma_{\parallel}-\left(\nu_{\theta}(h^{\theta}-\mathcal{G}^2)+(\nu^{\psi}-\nu_{\theta})\frac{(g^{\theta\psi})^2}{h^{\psi}}\right)\partial_{\theta}\Gamma_{\parallel}\right)\times\left(\frac{\partial}{\partial\theta}\left(\frac{\Gamma_{\parallel}}{n}\right)-\frac{\mathbf{B}\cdot\nabla\theta}{B}h_{\theta}\nabla_{\parallel}\left(\frac{\Gamma_{\parallel}}{n}\right)\right)\\
&\quad+m_i\left(-\nu^{\psi}\left(h^{\psi}\partial_{\psi}\Gamma_{\parallel}+g^{\theta\psi}\partial_{\theta}\Gamma_{\parallel}\right)\right)\times\left(\frac{\partial}{\partial\psi}\left(\frac{\Gamma_{\parallel}}{n}\right)-\frac{\mathbf{B}\cdot\nabla\theta}{B}g_{\theta\psi}\nabla_{\parallel}\left(\frac{\Gamma_{\parallel}}{n}\right)\right)\\
&\quad-m_i\frac{\Gamma_{\parallel}}{n}\left(-D^{\psi}g^{\theta\psi}\partial_{\psi}n-\left(D_{\theta}(h^{\theta}-\mathcal{G}^2)+(D^{\psi}-D_{\theta})\frac{(g^{\theta\psi})^2}{h^{\psi}}\right)\partial_{\theta}n\right)\times\left(\frac{\partial}{\partial\theta}\left(\frac{\Gamma_{\parallel}}{n}\right)-\frac{\mathbf{B}\cdot\nabla\theta}{B}h_{\theta}\nabla_{\parallel}\left(\frac{\Gamma_{\parallel}}{n}\right)\right)\\
&\quad-m_i\frac{\Gamma_{\parallel}}{n}\left(-D^{\psi}\left(h^{\psi}\partial_{\psi}X+g^{\theta\psi}\partial_{\theta}X\right)\right)\times\left(\frac{\partial}{\partial\psi}\left(\frac{\Gamma_{\parallel}}{n}\right)-\frac{\mathbf{B}\cdot\nabla\theta}{B}g_{\theta\psi}\nabla_{\parallel}\left(\frac{\Gamma_{\parallel}}{n}\right)\right)
\end{aligned}
$$

And if one takes above non-dimensionalized expresion, one has:

$$
\begin{aligned}
{S_{U_i}}^{\star} &= \frac{2\pi R_0}{k_B n_0 c_0 T_0}S_{U_i}\\
&= \frac{2\pi R_0}{k_B n_0 c_0 T_0}m_i\left\{-\nu^{\psi}\frac{2\pi\Delta\psi_0}{a^2}g^{\theta\psi\star}\frac{n_0c_0}{\Delta\psi_0}\partial_{\psi^\star}\Gamma^\star-\left(\nu_{\theta}\left(\frac{2\pi}{a}\right)^2\left(h^{\theta\star}-\left(\frac{a}{2\pi R_0}\right)^2\mathcal{G}^{\star 2}\right)+\left(\frac{2\pi}{a}\right)^2(\nu^{\psi}-\nu_{\theta})\frac{g^{\theta\psi\star 2}}{h^{\psi\star}}\right)\right.\\
&\quad\left.\times\frac{n_0c_0}{2\pi}\partial_{\theta^\star}\Gamma^\star\right\}\times\left\{\frac{c_0}{2\pi}\left(1-\left(\frac{a}{2\pi R_0}\right)^2\mathcal{G}^{\star 2}h_{\theta}{}^{\star}\right)\partial_{\theta^\star}\left(\frac{\Gamma^\star}{n^\star}\right)\right\}\\
&\quad+\frac{2\pi R_0}{k_B n_0 c_0 T_0}m_i\left\{-\nu^{\psi}\left(\left(\frac{\Delta\psi_0}{a}\right)^2h^{\psi\star}\frac{n_0c_0}{\Delta\psi_0}\partial_{\psi^\star}\Gamma^\star+\frac{2\pi\Delta\psi_0}{a^2}g^{\theta\psi\star}\frac{n_0c_0}{2\pi}\partial_{\theta^\star}\Gamma^\star\right)\right\}\\
&\quad\times\left\{\frac{c_0}{\Delta\psi_0}\left(\partial_{\psi^\star}\left(\frac{\Gamma^\star}{n^\star}\right)-\left(\frac{a}{2\pi R_0}\right)^2\mathcal{G}^{\star 2}g_{\theta\psi}{}^{\star}\partial_{\theta^\star}\left(\frac{\Gamma^\star}{n^\star}\right)\right)\right\}\\
&\quad-\frac{2\pi R_0c_0}{k_B n_0 c_0 T_0}m_i\frac{\Gamma^\star}{n^\star}\left\{-D^{\psi}\frac{2\pi\Delta\psi_0}{a^2}g^{\theta\psi\star}\frac{n_0}{\Delta\psi_0}\partial_{\psi^\star}n^\star-\left(D_{\theta}\left(\frac{2\pi}{a}\right)^2\left(h^{\theta\star}-\left(\frac{a}{2\pi R_0}\right)^2\mathcal{G}^{\star 2}\right)\right.\right.\\
&\quad\left.\left.+\left(\frac{2\pi}{a}\right)^2(D^{\psi}-D_{\theta})\frac{g^{\theta\psi\star 2}}{h^{\psi\star}}\right)\times\frac{n_0}{2\pi}\partial_{\theta^\star}n^\star\right\}\times\left\{\frac{c_0}{2\pi}\left(1-\left(\frac{a}{2\pi R_0}\right)^2\mathcal{G}^{\star 2}h_{\theta}{}^{\star}\right)\partial_{\theta^\star}\left(\frac{\Gamma^\star}{n^\star}\right)\right\}\\
&\quad-\frac{2\pi R_0c_0}{k_B n_0 c_0 T_0}m_i\frac{\Gamma^\star}{n^\star}\left\{-D^{\psi}\left(\left(\frac{\Delta\psi_0}{a}\right)^2h^{\psi\star}\frac{n_0}{\Delta\psi_0}\partial_{\psi^\star}n^\star+\frac{2\pi\Delta\psi_0}{a^2}g^{\theta\psi\star}\frac{n_0}{2\pi}\partial_{\theta^\star}n^\star\right)\right\}\\
&\quad\times\left\{\frac{c_0}{\Delta\psi_0}\left(\partial_{\psi^\star}\left(\frac{\Gamma^\star}{n^\star}\right)-\left(\frac{a}{2\pi R_0}\right)^2\mathcal{G}^{\star 2}g_{\theta\psi}{}^{\star}\partial_{\theta^\star}\left(\frac{\Gamma^\star}{n^\star}\right)\right)\right\}\\
&= 3\left\{-\frac{\mathrm{A}}{\mathrm{Re}^{\psi}}g^{\theta\psi\star}\partial_{\psi^\star}\Gamma^\star-\left(\frac{\mathrm{A}}{\mathrm{Re}_{\theta}}\left(h^{\theta\star}-\frac{1}{A^2}\mathcal{G}^{\star 2}\right)+\left(\frac{\mathrm{A}}{\mathrm{Re}^{\psi}}-\frac{\mathrm{A}}{\mathrm{Re}_{\theta}}\right)\frac{g^{\theta\psi\star 2}}{h^{\psi\star}}\right)\partial_{\theta^\star}\Gamma^\star\right\}\\
&\quad\times\left(1-\frac{1}{A^2}\mathcal{G}^{\star 2}h_{\theta}{}^{\star}\right)\partial_{\theta^\star}\left(\frac{\Gamma^\star}{n^\star}\right)+3\left\{-\frac{\mathrm{A}}{\mathrm{Re}^{\psi}}\left(h^{\psi\star}\partial_{\psi^\star}\Gamma^\star+g^{\theta\psi\star}\partial_{\theta^\star}\Gamma^\star\right)\right\}\times\left(\partial_{\psi^\star}\left(\frac{\Gamma^\star}{n^\star}\right)-\frac{1}{A^2}\mathcal{G}^{\star 2}g_{\theta\psi}{}^{\star}\partial_{\theta^\star}\left(\frac{\Gamma^\star}{n^\star}\right)\right)\\
&\quad-3\frac{\Gamma^\star}{n^\star}\left\{-\frac{\mathrm{A}}{\mathrm{Pe}^{\psi}}g^{\theta\psi\star}\partial_{\psi^\star}n^\star-\left(\frac{\mathrm{A}}{\mathrm{Pe}_{\theta}}\left(h^{\theta\star}-\frac{1}{A^2}\mathcal{G}^{\star 2}\right)+\left(\frac{\mathrm{A}}{\mathrm{Pe}^{\psi}}-\frac{\mathrm{A}}{\mathrm{Pe}_{\theta}}\right)\frac{g^{\theta\psi\star 2}}{h^{\psi\star}}\right)\partial_{\theta^\star}n^\star\right\}\\
&\quad\times\left(1-\frac{1}{A^2}\mathcal{G}^{\star 2}h_{\theta}{}^{\star}\right)\partial_{\theta^\star}\left(\frac{\Gamma^\star}{n^\star}\right)-3\frac{\Gamma^\star}{n^\star}\left\{-\frac{\mathrm{A}}{\mathrm{Pe}^{\psi}}\left(h^{\psi\star}\partial_{\psi^\star}n^\star+g^{\theta\psi\star}\partial_{\theta^\star}n^\star\right)\right\}\times\left(\partial_{\psi^\star}\left(\frac{\Gamma^\star}{n^\star}\right)-\frac{1}{A^2}\mathcal{G}^{\star 2}g_{\theta\psi}{}^{\star}\partial_{\theta^\star}\left(\frac{\Gamma^\star}{n^\star}\right)\right)
\end{aligned}
$$

$$
\boxed{{S_{U_i}}^{\star}=3\left(\phi_{\theta}^{\Gamma^\star}-{\Gamma_{\theta}}^{\star}\right)\left(1-\frac{1}{A^2}\mathcal{G}^{\star 2}h_{\theta}{}^{\star}\right)\partial_{\theta^\star}\left(\frac{\Gamma^\star}{n^\star}\right)+3\left(\phi_{\psi}^{\Gamma^\star}-{\Gamma_{\psi}}^{\star}\right)\left(\partial_{\psi^\star}\left(\frac{\Gamma^\star}{n^\star}\right)-\frac{1}{A^2}\mathcal{G}^{\star 2}g_{\theta\psi}{}^{\star}\partial_{\theta^\star}\left(\frac{\Gamma^\star}{n^\star}\right)\right)}
$$

One inverts the Jacobian to compute $\mathbf{e}_{\theta}\cdot\mathbf{e}_i$ and one uses $\mathbf{e}_{\theta}=a/2\pi\mathbf{e}_{\theta}{}^{\star}$ and $\mathbf{e}_{\psi}=a/\Delta\psi_0\mathbf{e}_{\psi}{}^{\star}$.

$$
\begin{pmatrix} h_{\theta} & g_{\theta\psi}\\ g_{\theta\psi} & h_{\psi}\end{pmatrix}=\begin{pmatrix} h^{\theta} & g^{\theta\psi}\\ g^{\theta\psi} & h^{\psi}\end{pmatrix}^{-1}
$$

Appendix D

One-dimensional particle model for heat flux analysis

D.1 Introduction

Heat transport in the presence of a temperature gradient imposed by heat reservoirs is a classical problem in the physics of plasmas, that has been tackled over decades by different approaches. In order to improve heat transfer modeling in weakly collisional plasma, the development of so called "toy models" is of a great interest. These models have the goal of catching the specificities of different regimes of heat transfer in the simplest way. In this paper, we focus on heat transfer in the direction parallel to the magnetic field in tokamak plasma. These plasmas are known to be weakly collisional, however, the computation of the heat flux in these plasma often relies on Spitzer-Härm expression [10] of the heat flux that is based on a strong collisionality assumption. In fact, this closure equation is used in the fluid approximation where local balance should be verified. In order to account for the departure from local balance at high temperature, the Spitzer-Härm formulation is sometime adjusted. Many examples of these flux limiter corrections adjusting the flux expression to work at low collisionalities can be found in the literature [38, 37]. In this manuscript we aim at revisiting this problem by considering very simple models that epitomize the minimal ingredients for reproducing some general properties that are known to characterize the diffusive as well as the ballistic regimes typical of heat transfer in plasmas.

Far from a complex kinetic treatment, our models rely on particles that move along a closed magnetic field line and that exchange energy with each other. They can also interact with heat sources. In our approach, the properties of the tokamak magnetic field line are simplified and we consider that the magnetic field is constant on the field line. By comparison with a tokamak, one can consider that all the particles are passing and trapped particles are not considered. The models implemented in this work can be sorted in two categories. The first ones that will be presented in section D.2 consider particles traveling with a constant velocity. The second ones illustrated in section D.3 assume that particle velocities are linked to their respective energy following the relation

$v = A\sqrt{E}$. We further show that these two models can be related one to another by a suitable relation.

This particle models could be studied in parallel with the kinetic treatment performed two decades ago to study transition from strongly collisional to collisionless regime [95, 96].

D.2 Models with constant particle velocity

The domain considered in the following model is a periodic line of length L where a heat source of energy E_{s1} is located at x_{s_1} and another one of energy E_{s2} is located at x_{s_2}. On this line, $2 \times N$ particles are uniformly spread on the mesh $\{x_i\}_{i\in[\![1,N]\!]}$, with $x_i = iL/N$. Hence, on each node of the grid x_i are located two particles. One is travelling forward with velocity v^+, one is travelling backward with velocity v^- with $|v^+| = |v^-| = v$. E_i^+ and E_i^- denote the forward $(+)$ and backward $(-)$ moving particle volumic energies, respectively. The energy $\mathcal{E}$ of a particle is given by the relation $\mathcal{E} = \mathcal{V}E = S\delta x E$, where $\mathcal{V} = S\delta x$ is the volume of a particle, S is the arbitrary surface of the particle pependicular to the direction considered so far and δx is the characteristic length of a particle equal to the mesh length $\delta x = L/N$.

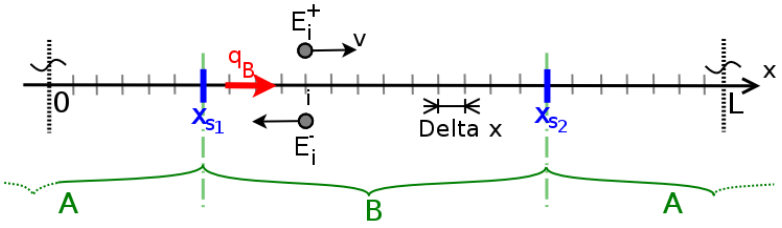

Figure D.1: Sketch of the domain

The evolution law of the system relies on two steps: a *dynamic step* $(t \to t + 1/2)$ when the particles jump from one node to the closest neighboring node according to the sign of their velocity, and an *interaction step* $(t + 1/2 \to t + 1)$ during which the $+$ and $-$ particles that are located on the same node exchange part of their energy. The evolution is given by Equations D.1 where the $t + 1/2$ step is denoted with a prime and the $t + 1$ step is denoted with two primes.

$$\begin{array}{cc} \textbf{Dynamic step} & \textbf{Interaction step} \\ \left\{ \begin{array}{rcl} E_i^{+\prime} & = & E_{i-1}^{+} \\ E_i^{-\prime} & = & E_{i+1}^{-} \end{array} \right. & \left\{ \begin{array}{rcl} E_i^{+\prime\prime} & = & E_i^{+\prime} + \frac{E_i^{-\prime} - E_i^{+\prime}}{\alpha} \\ E_i^{-\prime\prime} & = & E_i^{-\prime} + \frac{E_i^{+\prime} - E_i^{-\prime}}{\alpha} \end{array} \right. \end{array} \tag{D.1}$$

α is a number that quantify the exchanged amount of energy between the particles. If $\alpha = 2$, the energy of the two particles after the interaction is the same. In this case, one can say that the interaction is total. Moreover, when the particles pass through the nodes $x_{i_{s1}}$ and $x_{i_{s2}}$ where the heat sources are located, they take the energy of the source. In stationary conditions, we have for all i, $E_i^{\pm\prime\prime} = E_i^{\pm}$. Hence, using Equations (D.1),

the solution can be obtained by iterating equations (D.2) with the "boundary conditions" $E^{\pm}_{i_{s1}} = E_{s1}$ and $E^{\pm}_{i_{s2}} = E_{s2}$.

$$\left\{ \begin{array}{rcl} E_i^+ & = & E_{i-1}^+ + \Delta E_i \\ E_i^- & = & E_{i+1}^- - \Delta E_i \end{array} \right. \quad \text{with} \quad \Delta E_i = \frac{E_{i+1}^- - E_{i-1}^+}{\alpha} \tag{D.2}$$

From recursive serie analysis, one can prove that the solution takes the form $E_i^+ = ai+b$ and $E_i^- = ci + d$. Reporting these expressions in Equations D.2 and considering the boundary conditions, one obtains the value of a, b, c and d:

$$\left\{ \begin{array}{rcl} E_i^+ & = & \frac{E_{s1}-E_{s2}}{i_{s1}-i_{s2}+(2-\alpha)} \cdot i + \frac{E_{s2}\cdot i_{s1} - E_{s1}\cdot i_{s2} + E_{s1}\cdot(2-\alpha)}{i_{s1}-i_{s2}+(2-\alpha)} \\ E_i^- & = & \frac{E_{s1}-E_{s2}}{i_{s1}-i_{s2}+(2-\alpha)} \cdot i + \frac{E_{s2}\cdot i_{s1} - E_{s1}\cdot i_{s2} + E_{s2}\cdot(2-\alpha)}{i_{s1}-i_{s2}+(2-\alpha)} \end{array} \right. \quad \text{for } i \in [\![i_{s1}, i_{s2}]\!] \tag{D.3}$$

It is also possible to compute the energy exchanged with the source at each time step. For instance, for source s_1, this energy increment is given by the relation

$$\delta\mathcal{E} = \mathcal{V} \cdot \left(2E_{s1} - E_{i_{s1}}^{+\prime} - E_{i_{s1}}^{-\prime}\right) = \mathcal{V}\left(2E_{s1} - E_{i_{s1}-1}^{+} - E_{i_{s1}+1}^{-}\right) \tag{D.4}$$

Also, since $E_{s1} = E_{i_{s1}}^- = E_{i_{s1}}^+$, the expression of the $\delta\mathcal{E}$ can be expressed as

$$\delta\mathcal{E} = \mathcal{V} \cdot \left\{ (E_{i_{s1}}^- - E_{i_{s1}-1}^+) + (E_{i_{s1}}^+ - E_{i_{s1}+1}^-) \right\} \tag{D.5}$$

One notices from Equation D.2 that the quantity $\xi_i = E_{i-1}^+ - E_i^-$ verifies $\xi_{i+1} = \xi_i = \xi$. This quantity is conserved wherever the particles interact with each other and do not interact with the sources. These subdomains are denoted with the letter A and B on Figure D.1. Consequently, the energy exchanged with the source s_1 can also be written as $\delta E = \mathcal{V}(-\xi_A + \xi_B)$. If we divide this energy by the time step $\delta t = \delta x / v$ and by the surface S, one can determine the heat flux q by

$$q = \frac{\delta\mathcal{E}}{S \cdot \delta t} = v(-\xi_A + \xi_B) = q_A + q_B \tag{D.6}$$

Using Equations D.3 gives the following expression for q_B

$$q_B = v \cdot \xi_B = v(E_{i_{s1}}^+ - E_{i_{s1}+1}^-) = v \cdot \frac{(E_{s1} - E_{s2})\,(1-\alpha)}{i_{s1} - i_{s2} + (2-\alpha)} \tag{D.7}$$

Besides, one can calculate the energy gradients,

$$\nabla E^{\pm} = \frac{E_{i+1}^{\pm} - E_i^{\pm}}{x_{i+1} - xi} = \frac{1}{\delta x} \cdot \frac{E_{s1} - E_{s2}}{i_{s1} - i_{s2} + (2-\alpha)} \tag{D.8}$$

Reporting equation D.8 into Equation D.7 gives

$$q_B = -(\alpha - 1) \cdot \delta x \cdot v \cdot \nabla E^{\pm} \tag{D.9}$$

As noticed previously, the case where $\alpha = 2$ is of particular interest since it implies a ther-

malization between the + and − particles. This condition guarantees local equilibrium, i.e. $E_i^+ = E_i^-$. This balance leads to defining the temperature as $T \sim E^{\pm}$. The heat flux is then expressed by the standard Fourier law for heat conduction : $q = -v\delta x \nabla T = -\kappa \nabla T$. Moreover, this expression is compatible with the standard derivation of heat conductivity [6]:

$$\kappa = k_B n \lambda v_{th} \tag{D.10}$$

where λ is the mean free path, v_{th} is the thermal speed, k_B is Boltzmann constant and n is the plasma density. In the case where $\alpha = 2$, the equivalent mean free path is δx since thermalization occurs at the lattice scale. v plays the role of the thermal speed.

For $\alpha \neq 2$, $E_i^+ \neq E_i^-$ and it is not possible to define local balance at the mesh scale. However, if we define $\bar{E} = (E^+ + E^-)/2$, we have a Fourier's like expression for the heat flux that is $q = -v(\alpha - 1)\delta x \ \nabla \bar{E}$. In this case, we have $\kappa = v(\alpha - 1)\delta x$. To be coherent with the usual derivation of heat capacity, one should find that the equivalent mean free path in this case is $\lambda = (\alpha - 1)\delta x$. In fact, the interaction rule guarantees an exponential decay to equilibrium after a characteristic number of interactions $n = \alpha - 1$ and thus a characteristic decay length compatible with the above expression for the mean free path.

For α going to infinity, the + and − particles almost do not interact with each other. A standard collisionless regime is then expected. Indeed, using Equations D.3, one can find directly that $\nabla E^{\pm} \to 0$. Hence, in the domain B of Figure D.1 for instance, we have $E_{s1} = E^+ \neq E^- = E_{s2}$ and there is no local equilibrium. As expected, the mean free path tends to infinity and the particle behavior is ballistic. Moreover, making $\alpha \to \infty$ in Equation D.7 gives $q = v(E_{s1} - E_{s2})$ which is compatible with the ballistic expression of heat flux.

On Figure D.2 are plotted results for $\alpha = 2$ and $\alpha = 30$. In the first case, one can notice that $E^+ = E^- = \bar{E}$ that defines local equilibrium.

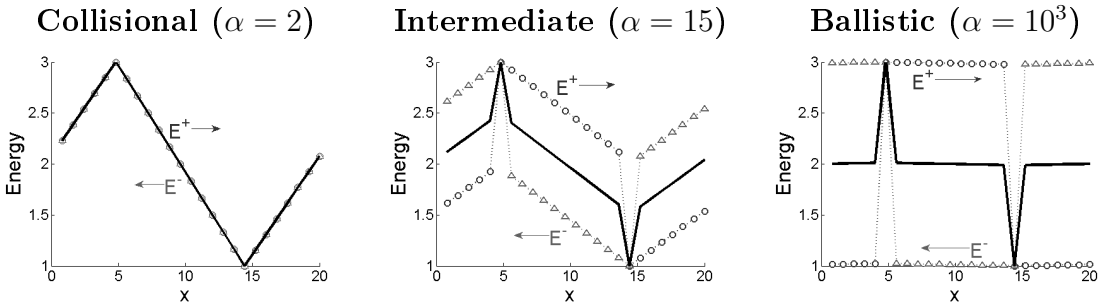

Figure D.2: Simulations performed with constant velocity for different values of α. E^+ (circles), E^- (triangles) and $\bar{E}$ (solid thick line). The sources are located at $x = 5$ and $x = 15$. Their respective energies are 3 and 1. The length of the domain is 20. The number of particles is 2×50

To go further, since the quantity $\lambda = (\alpha - 1)\delta x$ plays the role of mean free path, it can be interesting to introduce also a dependance of α on the energy. This is done by

considering the following law for α:

$$\alpha_i = 2 \cdot \left(\frac{\max(E_i^+, E_i^-)}{E_{\text{ref}}} \right)^r \tag{D.11}$$

In this expression, E_{ref} is chosen small enough to ensure that the energy ratio is always larger than one such that $\alpha > 2$. r is a positive real number. The idea is to consider the case where $\alpha \gg 1$ yielding the approximation $\lambda = \delta x(\alpha - 1) \approx 2\delta x \left(\max(E_i^+, E_i^-)/E_{\text{ref}}\right)^r \propto {E_i}^r$. For plasma physics, the case where $r = 2$ is of particular interest since Coulombian interactions between plasma particles give a mean free path proportional to the energy square. The assumption $\alpha \gg 1$ does not imply that collisionless cases are the only ones considered. Indeed, as long as $\lambda \ll L \Leftrightarrow (\alpha - 1) \ll N$ where L is the domain legnth anf N the number of interactions undergone by a particle as it travels through the domain, the model can be supposed to be collisional.

We are interested in finding analytical solutions for this system. We will solve it in the domain B on Figure D.1 where $E^+ > E^-$. The system to solve is then

$$\begin{cases} E_i^+ &= E_{i-1}^+ + \frac{E_{i+1}^- - E_{i-1}^+}{2 \cdot (E_{i-1}^+ / E_{\text{ref}})^r} = E_{i-1}^+ + \varepsilon \cdot (E_{i+1}^- - E_{i-1}^+) \\ E_i^- &= E_{i+1}^- - \frac{E_{i+1}^- - E_{i-1}^+}{2 \cdot (E_{i-1}^+ / E_{\text{ref}})^r} = E_{i+1}^- - \varepsilon \cdot (E_{i+1}^- - E_{i-1}^+) \end{cases} \tag{D.12}$$

where $\varepsilon = 1/\alpha \ll 1$. One must notice that the numerator of the exchange term can be developped as

$$\begin{aligned} E_{i+1}^- - E_{i-1}^+ &= E_{i+1}^- - E_i^+ + (E_i^+ - E_{i-1}^+) \\ &= E_{i+1}^- - E_i^+ + \varepsilon \cdot (E_{i+1}^- - E_{i-1}^+) \\ &\approx E_{i+1}^- - E_i^+ = \xi = \text{constant} \end{aligned}$$

Hence, the problem is reduced to solving recursive Equation D.13 for E_i^+:

$$E_i^+ = E_{i-1}^+ + \frac{B}{(E_{i-1}^+)^r} \quad \text{with} \quad B = \xi \cdot E_{\text{ref}}^r / 2 \tag{D.13}$$

An approximate solution is

$$E_i^+ = \left(E_{s1}^{1+r} + (i - i_{s1}) \cdot B \cdot (1 + r) \right)^{\frac{1}{1+r}} \tag{D.14}$$

The unknown B is determined using $\xi = E_i^- - E_{i-1}^+ = 2B/E_{\text{ref}}^r$ and $E_{i_{s2}}^- = E_{s2}$. Reporting in Equation D.14 for $i = i_{s2} - 1$, one find

$$2B/E_{\text{ref}}^r = E_{s2} - \left(E_{s1}^{1+r} + (i_{s2} - 1 - i_{s1}) \cdot B \cdot (1 + r) \right)^{\frac{1}{1+r}} \tag{D.15}$$

Solving equation D.15 gives B, ξ and finally the heat flux q. The simulation results are compared with the analytical solution on Figure D.3. One expects to find a good

agreement between the simulation results and the analytical solution in the cases where $\alpha \gg 1$. For the first case, we have chosen $E_{\text{ref}} = 0.5$, $E \in [2,\ 5]$ and $r = 2$ hence $\alpha \in [16,\ 100] \gg 1$. The hottest particles will thus require about 100 interactions to thermalize. The number of particles used in the simulation is $N = 2 \times 3000$. Consequently, each particle undergoes 3000 interactions when it covers the domain. Since $3000 \gg 100$, this case can then be considered as a collisional case, that is $\lambda \ll L$. In fact, on Figure D.3,a, one can notice that for all i, $E_i^+ \approx E_i^-$. In the second case, we choose the same parameters except that we limit the number of particles to 300. Thus, the relation $\lambda \sim L$ applies and the case is not collisional. One can notice the departure between E^+ and E^- on Figure D.3,b

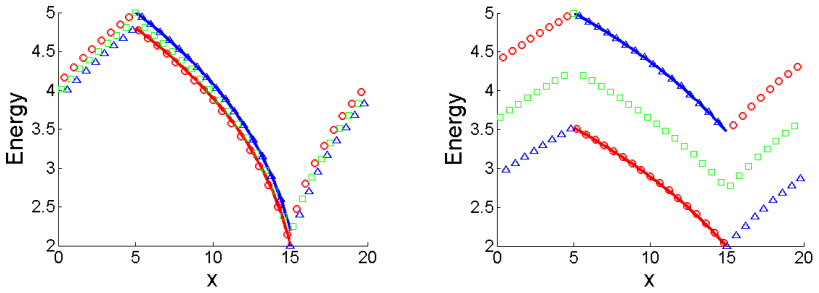

(a) (b)

Figure D.3: Simulation results with $\alpha \propto \max(E^+, E^-)^2$. $E_{s_1} = 5$ and $E_{s_2} = 2$. (a): Energy profiles obtained when the simulation is performed with 2×3000 particles and guarantee that for all i, $1/\alpha \ll 1$ and $\lambda \ll L$. (b): The simulation is performed with 2×300 particles for $\lambda \sim L$. Simulations results are plotted with symbols: E^+ (triangles), E^- (circles) and $\bar{E}$ (squares). Analytical estimations corresponding to Equation (D.14) are plotted with lines.

D.3 Models with non-constant velocity

Unlike the previous models where the velocity of particles is constant, a dependancy of velocity on the energy is added such that $v^{\pm} = A\sqrt{E^{\pm}}$. The previous energy can now be seen as the particle's kinetic energy. In the following simulations, we consider the same domain as described on Figure D.1. Particles are randomly placed in the domain with a given initial energy. One half is moving forward and one half is moving backward. The algorithm detects when two particles meet or when they meet the sources. In that case, particles exchange part of their energy with the same rules as those described in the previous section. The particle's velocity modules are recalculated and their velocity sign is conserved. Since the sign of velocity is unchanged, particles exchange energy with the two source alternatively. The U-turn is not allowed since making the two traveling directions equally probable would lead to defining an automatic local equilibrium. As a consequence, some fluctuations apart, the rate of interaction with the two sources is the same. This interaction rate is also characteristic of the rate with which particles interact with each

other. Analytical solutions are more difficult to obtain for this kind of model since there is no well defined lattice for solving the recursive equations. However, in the collisional case where $E^+ \approx E^-$, an approximate solution can be found by solving Equations (D.1,D.12) on the lattices $\{x_i^+\}$ and $\{x_i^-\}$, see Figure D.4, where

$$\left\{ \begin{array}{rcl} |x_{i+1}^+ - x_i^+| & = & |\delta t \cdot v_i^+| = \delta t \cdot A\sqrt{E_i^+} \\ |x_i^- - x_{i-1}^-| & = & |\delta t \cdot v_i^-| = \delta t \cdot A\sqrt{E_i^-} \end{array} \right. \tag{D.16}$$

Since $E_i^+ \approx E_i^-$, one has $\forall i,\ \Delta x_i^+ \approx \Delta x_{i-1}^-$ and one can define the lattice $x_i \sim x_i^+ \sim x_i^-$, see Figure D.4. To determine the values of x_i for all i, one has to solve $\Delta x_i = A\delta t\sqrt{E_i}$ constrained by $\sum_N \Delta x_i = L$ where the values of E_i are given by the solutions found in the previous section. One has to remember that this approach is only valid for the collisional cases.

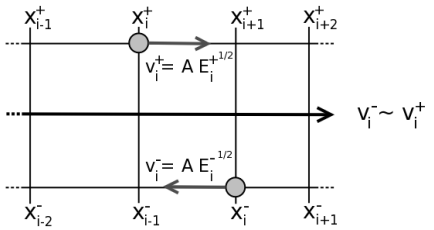

Figure D.4: Lattice definitions in the collisional approximation for non-constant velocity

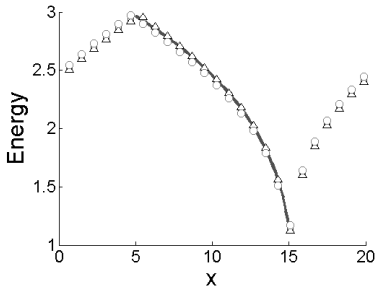

Figure D.5: Energy profiles in the non-constant velocity case for $r = 2$. Simulation results: E^+ (triangles), E^- (circles) and $\bar{E}$ (squares). Line: analytical estimation. Number of particles: 2×500.

In particular, one finds $\{x_i\}$ in the case where the mean free path depends on the energy. From Equation D.14, the energy is given by the relation

$$E_i = (a + b \cdot i)^{1/(1+r)} \tag{D.17}$$

where $a = E_{s_1}^{1+r} - Bi_{s_1}(1+r)$ and $b = B(1+r)$. In the following, we just focus on the domain B defined on Figure D.1. In order to determine the value of x_i, we use the approximation $\Delta x_i/\Delta i \approx \mathrm{d}x/\mathrm{d}i$. Hence,

$$\begin{array}{rcl} \mathrm{d}x & = & A\delta t(a + b \cdot i)^{\frac{1}{2(1+r)}}\mathrm{d}i \\ x_i - x_{s1} & = & A\delta t \int_{i_{s1}}^{i}(a + b \cdot i)^{\frac{1}{2(1+r)}}\mathrm{d}i \\ x_{s2} - x_{s1} & = & A\delta t \int_{i_{s1}}^{i_{s2}}(a + b \cdot i)^{\frac{1}{2(1+r)}}\mathrm{d}i \end{array} \tag{D.18}$$

The solution of these equations is

$$\left\{\begin{array}{rcl} x_i &=& c + d(a + b\cdot i)^{\frac{3+2r}{2(1+r)}} \\ i &=& \frac{1}{b}\left(\frac{x_i - c}{d}\right)^{\frac{2(1+r)}{3+2r}} - \frac{a}{b} \end{array}\right. \tag{D.19}$$

c and d can be determined using $x_{i_{s1}} = x_{s_1}$ and $x_{i_{s2}} = x_{s_2}$. Reporting the expression of i in Equation D.17 gives

$$E_i = \left(\frac{x_i - c}{d}\right)^{\frac{2}{3+2r}} \tag{D.20}$$

Since in the collisional case, one has $E(x_{s1}) = E_{s1}$ and $E(x_{s2}) = E_{s2}$, the constant can be determined and the energy is finally given by Equation D.21.

$$E = \left(E_{s1}^{1/\beta} + \frac{E_{s2}^{1/\beta} - E_{s1}^{1/\beta}}{x_{s2} - x_{s1}}\,(x - x_{s1})\right)^{\beta} \qquad \text{with} \qquad \beta = \frac{2}{3+2r} \tag{D.21}$$

In this collisional case where a lattice has been determined, the heat flux can be calculated as in the previous section, see Equation D.7. The velocity is now a function of the temperature:

$$\begin{array}{rcl} q &=& \frac{\mathcal{V}\cdot(E_i^+ - E_{i+1}^-)}{S\cdot\delta t} = \ell\cdot A\sqrt{E_i}\frac{E_i^+ - E_i^-}{x_{i+1} - x_i} \\ &=& -A\cdot\ell\cdot(\alpha - 1)\sqrt{\bar{E}}\nabla\bar{E} \end{array} \tag{D.22}$$

In Figure D.5, a comparison between simulation results in the collisional case for $r = 2$ and the above analytical estimation is plotted. The $+$ and $-$ particles energy are shown. One notices that these two variables are almost equal which justifies the above approximations.

We also study the dependance of the heat flux on the energy in the case $r = 2$. To do so, the number of particles is kept constant equal to 500. The energy of the source is chosen as $E_{s_1} = 1.05 \times E_0$ and $E_{s_2} = 0.95 \times E_0$ where E_0 is a parameter that describes the energy of the system. We choose $E_{\text{ref}} = 0.8$ and simulations are performed for values of E_0 between 2 and 200. A particle undergoes approximately $N_{\text{inter}} = 500$ interactions as it travels from one source to the other. Since α represents the number of interactions necessary to thermalize, the regime is expected to be collisional for $\alpha = 2(E_0/E_{\text{ref}})^2 < 500$. To make it clearer, we define the collisionality ν^* as $\nu^* = N_{\text{inter}}/\alpha$. We are in a collisional regime if $\nu^* > 1$ that is $E_0 < 13$. For $E_0 > 13$, the regime is ballistic. The distance between the source is denoted $\mathcal{L}$. For each case, one computes the average gradient of $\bar{E}$. On Figure D.6,a is plotted the equivalent heat condictivity $\kappa = q/\bar{E}$ as a function of E_0. On Figure D.6,b is plotted $q\mathcal{L}/(E_{s_1} - E_{s_2})$.

On Figure D.6,a we notice that for low energies we have $q \propto E_0^{5/2}(E_{s2} - E_{s1})/\mathcal{L}$. Besides, for low energies, we have $\nabla T \approx (E_{s_2} - E_{s_1})/\mathcal{L}$ thus $q \propto E_0^{5/2}\nabla T$. This characteristic of the collisional Spitzer-Härm regime. For high energy, we have $q \propto \sqrt{E_0}(E_{s_2} - E_{s_2})/\mathcal{L} \sim v_{th}(E_{s_2} - E_{s_2})$. This is characteristic of the ballistic regime. The transtion occurs for $\nu^* = 1$, as expected. On Figure D.6,b we notice that with the defini-

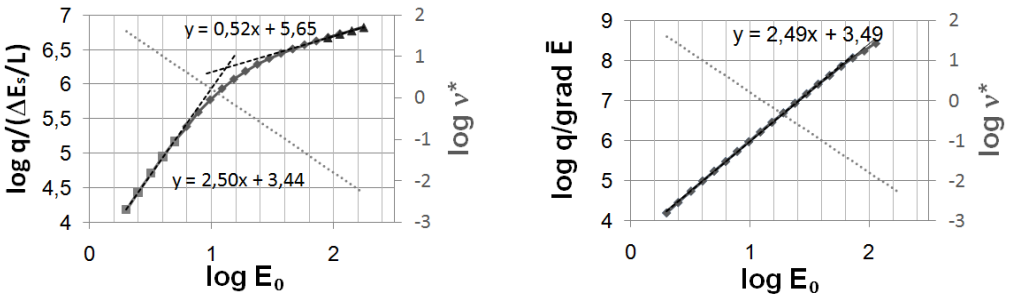

(a) (b)

Figure D.6: (a). $q/\{(E_{s_1} - E_{s_2})/L\}$ as a function of the energy of the system E_0. Simulation results (symbols) exhibiting the transition from conductive to ballistic regime. Power law fittings are represented with lines. (b). Effective heat conductivity $\kappa = q/\nabla \bar{E}$ as a function of the energy of the system E_0, simulation results (symbols), power law fitting (line) exhibiting $\kappa \propto E_0^{5/2}$. The collisionality is plotted with dot-line.

tion of $\bar{E} = (E^+ + E^-)/2$, we recover the Spitzer-Härm like law for the heat flux, even in the collisionless case ($\nu^* < 1$).

D.4 Models with two velocity classes

One considers the same model has the one presented in section **??** except instead of having just particles moving 1 step forward and 1 step backward, one adds "suprathermal" particles which move two step forward and backward at each time step. The latter particles hence travel twice faster as the formers. After the dynamic step, the energy is redistributed on each lattice site according to the law

$$E \leftarrow (1-\alpha)E + \alpha \bar{E} \tag{D.23}$$

where

$$\bar{E} = \frac{1}{4}\left(E^+ + E^- + E^{2+} + E^{2-}\right) \tag{D.24}$$

where E^{2+} and E^{2-} denotes the energy of suprathermal particles. Since all the particles do not have the same velocity, one has two class of particles which do not have the same collisionality. One expects that the above results obtained with a single class of velocity will not apply in the range of α for which the slow particles are collisional and the fast one are ballistic. Indeed, one reproduces the same experiment as in section D.3 and plots heat conductivity $\kappa = q/\nabla E$ as a function of E. The results are represented on Figure D.7. One notices that in the above mentionned range for which the two class of particles do not have the same collisional behavior, the heat conductivity drops and do not follow the same law on the whole temperature range as in the single class case. It is thus not possible to obtain a simple expression $q = \kappa \nabla \bar{E}$ with $\kappa \propto \bar{E}^\gamma$. This example with two classes of particles emphasize the necessity to use so-called flux limiters in the temperature range corresponding to the transition from collisional regime to ballistic regime.

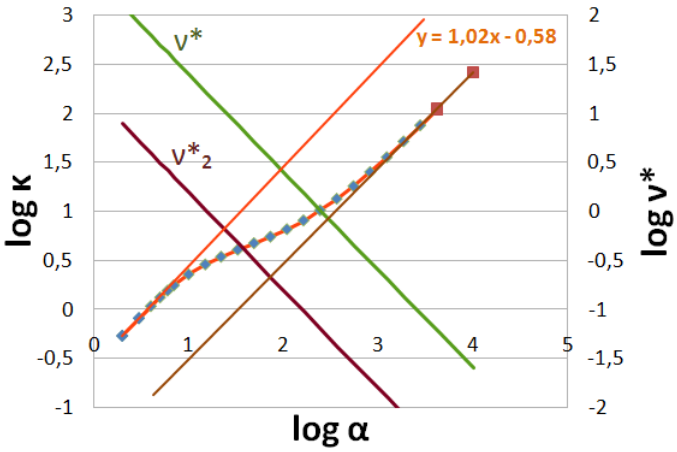

Figure D.7: Heat conductivity as a function of temperature for the two classes of velocity system. The drop of heat conductivity in the intermediate range of temperature is characteristic of the flux limited regime. One represents the collisionality of the two classes of particles. The flux limited region corresponds to $\nu_2^\star < 1$ *and* $\nu^\star > 1$.

D.5 Conclusions

The analysis of simple models where energy transfer takes place exhibits the well-known Spitzer-Härm diffusive behavior in the collisional regime. Also, the transition from collisional to ballistic behavior was observed as the equivalent mean free path of the particles increased. This transition can be compared with the one observed with a kinetic treatment limited to considering 4 moments of the distribution function [95, 96]. In the present "toy-model", no distinction is made between thermal and suprathermal particles. A perspective of this work could be to introduce this ingredient to investigate flux-limiter formulations that are used when thermal particles are collisional and suprathermal particles are ballistic.